National Technical University of Athens
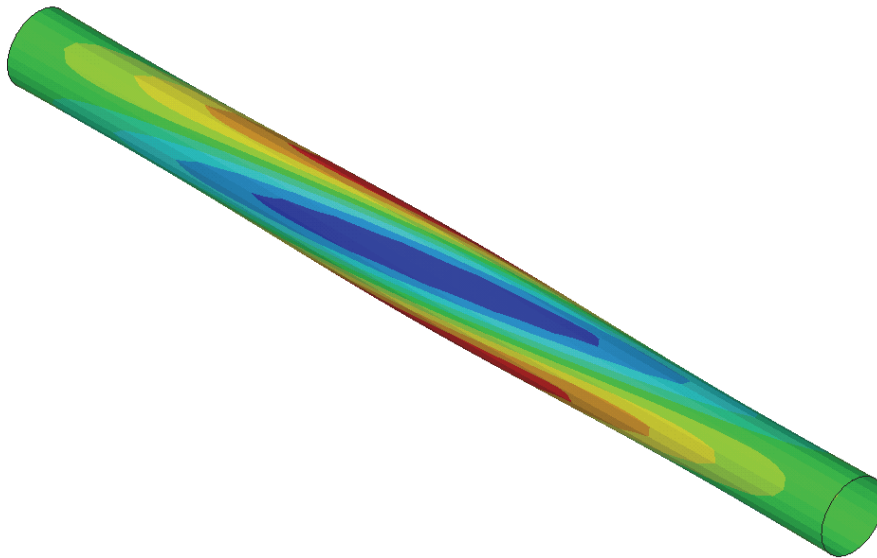School of Naval Architecture and Marine Engineering
Shipbuilding Technology Laboratory

Diploma Thesis

Experimental and Numerical Study of Composite Shafts

Elias Bilalis
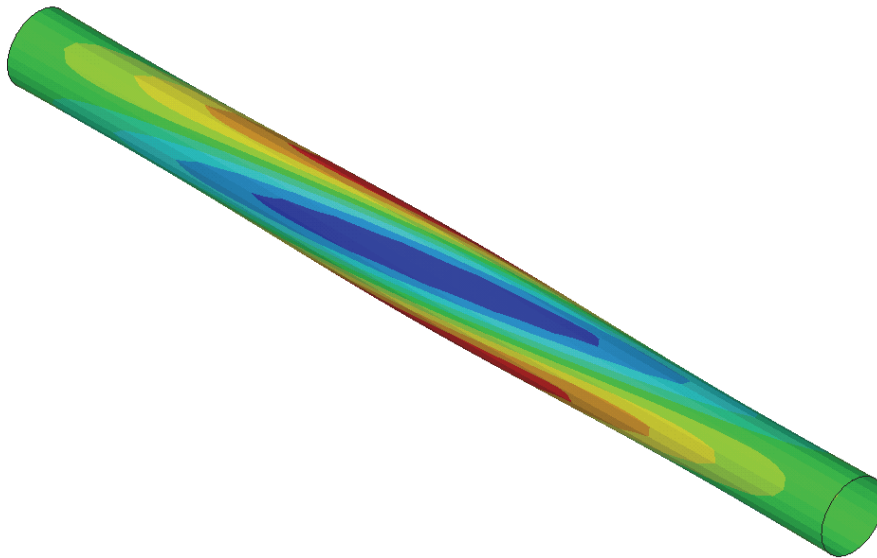

Thesis Supervisor: Professor N. Tsouvalis

June 2016

National Technical University of Athens
School of Naval Architecture and Marine Engineering
Shipbuilding Technology Laboratory

Diploma Thesis

Experimental and Numerical Study of Composite Shafts

Elias Bilalis

Thesis Supervisor: Professor N. Tsouvalis
Committee Member: Professor M. Samuelides
Committee Member: Assistant Professor C. Papadopoulos

June 2016

Dedicated to my friend Eni, whom I shall never forget.

Acknowledgements

Abstract

Composite materials are becoming increasingly the materials of choice for a number of products and applications, due to their light weight and high strength. Aviation, automotive and marine industries are investing a lot in the study and the development of composite materials in order to use them more extensively in the various structures of their respective fields.

The use of composite materials for the manufacturing of power transmission shafts attracts particular interest. Especially for the marine sector, apart from their high strength and light weight, composite shafts offer the advantages of high fatigue and corrosion resistance.

The efficient design of composite shafts is a challenging task, because of the general problem of understanding composite materials mechanical behavior and their failure modes and mechanisms, due to their anisotropic nature. The use of simulation programs that utilize the Finite Element Method (FEM), like ANSYS, helps in coping with the aforementioned challenge.

In the context of this work several finite element models are developed for the simulation of the mechanical behavior of composite shafts. The calibration and validation of the finite element models is pursued by the comparison of their results with experimental data acquired from the industry and from a torsion test conducted for the needs of the present thesis

The first finite element model simulates a Glass Fiber Reinforced Polymer (GFRP) shaft, for which experimental data from a torsion test are acquired from the industry. Initially, layered shell elements are used for the development of the model. Eigenvalue buckling analysis and nonlinear buckling analysis are conducted. The dominant failure mode is determined, as well as the critical buckling load, which is quite accurately calculated, compared to the experimental failure load. The calculated stresses also present a correct pattern. However, the model calculates a significantly higher rotational stiffness of the shaft than the experimentally extracted one. For the investigation of this discrepancy a steel shaft of the same geometry is modelled. The results of the numerical solution match the results of the existing analytical solutions indicating that the aforementioned discrepancy is limited to the composite shaft model. Furthermore, a homogeneous model of the composite shaft is developed using again shell elements. The shaft is modeled as single-layered, with the single layer having the equivalent mechanical properties of the multilayered composite, calculated according to the mechanics of composite materials. This model yields in general results very similar to the layered shell model. Additionally, the shaft is modelled using layered solid elements. The results of this model are almost identical to the layered shell model ones. Finally, the effect of the mechanical and geometrical properties to the rotational stiffness and the buckling load of the shaft is investigated, indicating the great importance of their accurate knowledge.

The second finite element model simulates a Carbon Fiber Reinforced Polymer (CFRP) shaft, which features the mechanical and geometrical properties of the shaft tested. The measured magnitudes during the torsion test were the applied torque, the angle of rotation of the rotating end of the shaft with respect to the fixed end and strains on several selected positions for the identification of the rotational buckling modeshape. After the assessment of the experimental results, a model of the shaft is developed using layered shell elements. Eigenvalue buckling analysis and nonlinear buckling analysis are conducted. Still, the model predicts a significantly higher rotational stiffness than the one extracted by the experimental data. The effect of the

mechanical and geometrical properties of the shaft on the rotational stiffness is investigated as well, leading to conclusions similar to the ones derived from the GFRP shaft case. Afterwards, the experimental and numerical strains are compared and the observed convergences and discrepancies are assessed. The model yields encouraging results concerning the strains and the most dominant to evolve buckling modeshape. Finally, a modal analysis of the shaft is conducted in order to determine whether the in-service rotational speed of the shaft is close to the mechanical resonance frequency. The results of the analysis show that over the operational range of the shaft, natural frequency resonance is avoided.

Περίληψη

Τα σύνθετα υλικά επιλέγονται όλο και περισσότερο ως υλικά κατασκευής διάφορων προϊόντων και εφαρμογών, λόγω του χαμηλού τους βάρους και της υψηλής τους αντοχής. Η αεροπορική βιομηχανία, η αυτοκινητοβιομηχανία και η ναυπηγική βιομηχανία επενδύουν αρκετά στη μελέτη και την εξέλιξη των σύνθετων υλικών, προκειμένου να τα αξιοποιήσουν στις διάφορες κατασκευές των κλάδων τους.

Η χρήση σύνθετων υλικών για την κατασκευή αξόνων μετάδοσης ισχύος παρουσιάζει ιδιαίτερο ενδιαφέρον. Ιδιαίτερα για τον κλάδο της ναυπηγικής, πέρα από την υψηλή αντοχή και το μικρό βάρος, οι άξονες από σύνθετα υλικά προσφέρουν υψηλή αντοχή σε κόπωση και σε διάβρωση.

Η αποτελεσματική σχεδίαση αξόνων από σύνθετα υλικά ενέχει προκλήσεις που πηγάζουν από το γενικότερο πρόβλημα της κατανόησης της μηχανικής συμπεριφοράς των σύνθετων υλικών και των τρόπων και των μηχανισμών αστοχίας τους, λόγω της ανισοτροπικής τους φύσης. Η χρήση προγραμμάτων προσομοίωσης που αξιοποιούν τη Μέθοδο των Πεπερασμένων Στοιχείων, όπως το ANSYS, συμβάλει στην αντιμετώπιση των παραπάνω προκλήσεων.

Στην παρούσα εργασία αναπτύσσονται μοντέλα πεπερασμένων στοιχείων για την προσομοίωση της μηχανικής συμπεριφοράς αξόνων από σύνθετα υλικά. Η ρύθμιση και η αξιολόγηση των μοντέλων επιτυγχάνεται μέσω της σύγκρισης των αποτελεσμάτων τους με πειραματικά δεδομένα από τη βιομηχανία και από μία πειραματική δοκιμή στρέψης που διενεργήθηκε για τις ανάγκες της παρούσας διπλωματικής.

Το πρώτο μοντέλο πεπερασμένων στοιχείων εστιάζει σε έναν άξονα από σύνθετο υλικό με ενισχυτικές ίνες γυαλιού και εποξική ρητίνη, για τον οποίο είναι διαθέσιμα πειραματικά αποτελέσματα από δοκιμή στρέψης από τη βιομηχανία. Αρχικά, χρησιμοποιούνται πολυστρωματικά στοιχεία κελύφους (layered shell elements) για την ανάπτυξη του μοντέλου. Διενεργείται ανάλυση ιδιοτιμών λυγισμού και μη γραμμική ανάλυση λυγισμού και προσδιορίζεται ο κυριότερος τρόπος αστοχίας και το φορτίο λυγισμού, το οποίο υπολογίζεται με καλή ακρίβεια σε σχέση με το αντίστοιχο πειραματικό φορτίο αστοχίας. Λογική εξέλιξη και τιμές παρουσιάζουν και οι υπολογιζόμενες τάσεις. Ωστόσο, το μοντέλο υπολογίζει σημαντικά υψηλότερη στρεπτική ακαμψία του άξονα σε σχέση με την πειραματική τιμή της. Για τη διερεύνηση αυτής της ασυμφωνίας μοντελοποιείται ένας χαλύβδινος άξονας ίδιας γεωμετρίας. Τα αποτελέσματα της αριθμητικής λύσης ταυτίζονται με τα αποτελέσματα των διαθέσιμων αναλυτικών λύσεων υποδεικνύοντας ότι η παραπάνω ασυμφωνία περιορίζεται στη μοντελοποίηση του άξονα από σύνθετα υλικά. Στη συνέχεια αναπτύσσεται ένα «ομογενές» μοντέλο του άξονα από σύνθετο υλικό πάλι με τη χρήση στοιχείων κελύφους, όπου ο άξονας μοντελοποιείται σαν να αποτελείται από υλικό μίας στρώσης, το οποίο έχει τις ισοδύναμες μηχανικές ιδιότητες του πολύστρωτου υλικού, υπολογισμένες σύμφωνα με την μηχανική των σύνθετων υλικών. Τα αποτελέσματα αυτού του μοντέλου είναι πολύ κοντά στα αποτελέσματα του πολύστρωτου μοντέλου. Επιπλέον, μοντελοποιείται ο ίδιος άξονας χρησιμοποιώντας πολυστρωματικά τρισδιάστατα στοιχεία. Τα αποτελέσματα αυτού του μοντέλου σχεδόν συμπίπτουν με τα αποτελέσματα του μοντέλου με τα πολυστρωματικά στοιχεία κελύφους. Τέλος, ελέγχεται η επίδραση των μηχανικών και γεωμετρικών ιδιοτήτων του άξονα στην στρεπτική ακαμψία και στο φορτίο λυγισμού, αναδεικνύοντας την μεγάλη σημασία της ακριβούς γνώσης τους.

Το δεύτερο μοντέλο πεπερασμένων στοιχείων εστιάζει σε έναν άξονα από σύνθετο υλικό με ενισχυτικές ίνες άνθρακα και εποξική ρητίνη, ο οποίος διαθέτει τη γεωμετρία και τις μηχανικές ιδιότητες του άξονα στον οποίο διενεργήθηκε η δοκιμή στρέψης. Κατά τη δοκιμή στρέψης μετρήθηκε η εφαρμοζόμενη ροπή, η γωνία στροφής του στρεφόμενου άκρου του άξονα σε σχέση με το σταθερό και οι παραμορφώσεις σε επιλεγμένα σημεία για τον προσδιορισμό της ιδιομορφής του στρεπτικού λυγισμού του άξονα. Κατόπιν της αξιολόγησης των πειραματικών αποτελεσμάτων, αναπτύσσεται το μοντέλο του άξονα με χρήση πολυστρωματικών στοιχείων κελύφους και διενεργείται ανάλυση ιδιοτιμών λυγισμού και μη γραμμική ανάλυση λυγισμού. Και σε αυτήν την περίπτωση ωστόσο, το μοντέλο υπολογίζει σημαντικά υψηλότερη στρεπτική ακαμψία από την αντίστοιχη πειραματική. Διερευνήθηκε, επίσης, η επίδραση των μηχανικών και γεωμετρικών ιδιοτήτων του άξονα στη στρεπτική ακαμψία, οδηγώντας σε όμοια συμπεράσματα με την περίπτωση του άξονα με τις ενισχυτικές ίνες γυαλιού. Στη συνέχεια γίνεται σύγκριση των πειραματικών παραμορφώσεων με τις αριθμητικές και αξιολογούνται οι παρατηρούμενες συγκλίσεις και αποκλίσεις. Το μοντέλο δίνει ενθαρρυντικά αποτελέσματα για τις παραμορφώσεις και την πιο πιθανή ιδιομορφή στρεπτικού λυγισμού. Τέλος, εκτελείται μία ανάλυση ιδιοσυχνοτήτων του άξονα προκειμένου να διαπιστωθεί εάν η πιθανή ταχύτητα περιστροφής λειτουργίας του άξονα βρίσκεται κοντά στην ιδιοσυχνότητα του. Το αποτέλεσμα της ανάλυσης οδηγεί στο συμπέρασμα ότι ο συγκεκριμένος άξονας δεν κινδυνεύει από συντονισμό στις πιθανές ταχύτητες περιστροφής λειτουργίας.

Contents

CHAPTER 1
INTRODUCTION TO COMPOSITE SHAFT TECHNOLOGY

1.1 A short introduction to composite materials and their use in marine applications

Because of their light weight and high strength, composite materials are becoming increasingly the materials of choice for a number of products and applications. Today composite materials can be found in military planes, helicopters, satellites, commercial planes, recreational boats, fast-food restaurant tables and chairs, and many sporting goods. They are also commonly used to repair bodies of automobiles. In comparison to conventional materials, such as metals, composite materials can be lighter and stronger. For this reason, composite materials are used extensively in aerospace applications. Composites are created by combining two or more solid materials to make a new material that has properties that are superior to those of the individual components. Composite materials consist of two main ingredients: matrix material and fibers. Fibers are embedded in matrix materials, such as plastics, aluminum or other metals, or ceramics. Glass, graphite, and silicon carbide fibers are examples of fibers used in construction of composite materials. The strength of fibers is increased when embedded in a matrix material, and the composite material created in this manner is lighter and stronger. Moreover, in a single material, once a crack starts due to either excessive loading or imperfections in the material, the crack will propagate to the point of failure. On the other hand, in a composite material, if one or a few fibers fail, it does not necessarily lead to failure of other fibers or the material as a whole. Furthermore, the fibers in a composite material can be oriented in a certain direction or many directions to offer more strength in the direction of expected loads. Therefore, composite materials are designed for specific load applications. For instance, if the expected load is uniaxial, meaning that it is applied in a single direction, then all the fibers are aligned in the direction of the expected load. For applications expecting multidirectional loads, the fibers are aligned in different directions to make the material equally strong in various directions (Moaveni, 2007).

Especially in the marine sector, conventional fiberglass composites have dominated the small craft and recreational boating industry, for more than 40 years, due to their advantages over different materials used for ship construction (Smith, 1990). Figure 1.1 represents a typical modern fiberglass recreational powerboat. From the 1950s to the 1990s, advances in composite materials and fabrication techniques used in the composite craft industry have helped reduce production costs and improve product quality. Although every boat builder employs unique production procedures that they feel are proprietary, general industry trends can be traced over time, as illustrated in Figure 1.2 (Greene, 1999).

Fig. 1.1. A modern 29ft fiberglass powerboat.
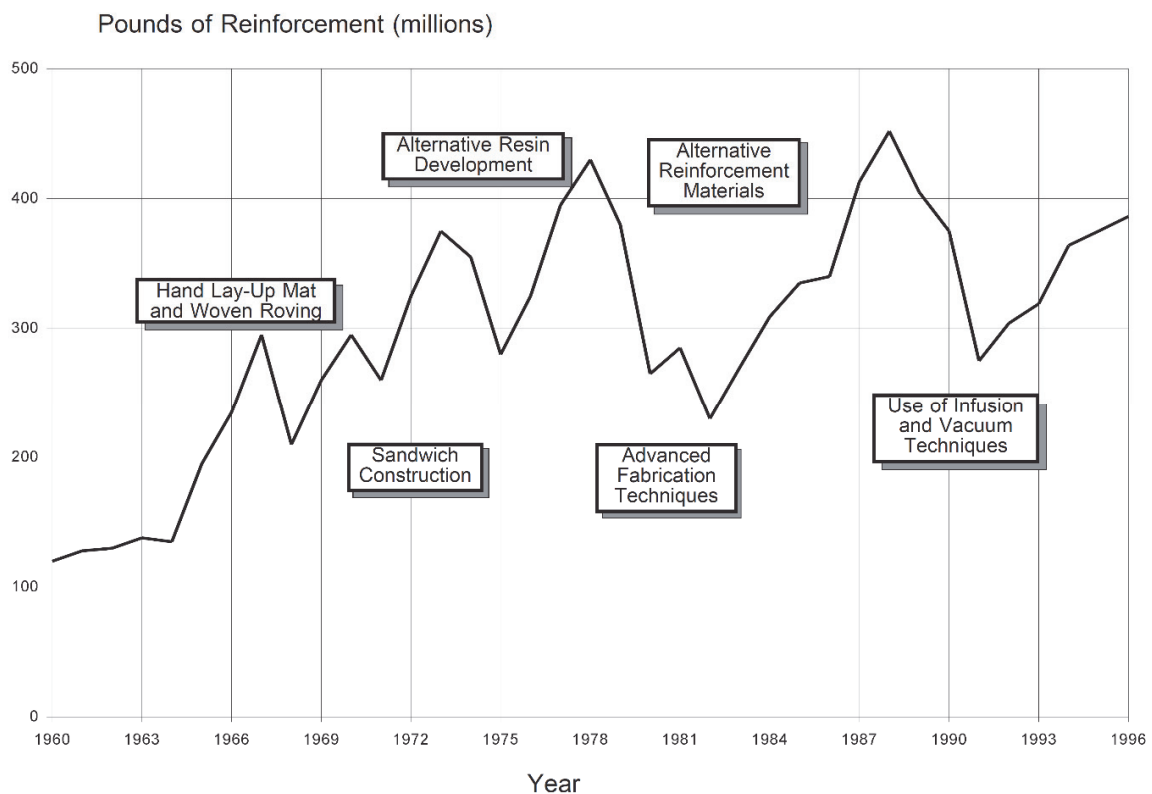
Fig. 1.2. Annual shipment of reinforced thermoset and thermoplastic resin composites for the marine industry with associated construction developments. [Data source: SPI Composites Institute (1960-1973 Extrapolated from overall data)]

According to the aforementioned advances in composites technology and fabrication, the shipbuilding industry has already started to incorporate composite materials in new ship construction and to replace specific steel components with composite ones in existing ships (Shenoi & Wellicome, 1993). Composite bulkheads, decks and superstructures are among these applications. The advantage of high strength to weight and high stiffness to weight ratio and the flexibility they offer to the designer for adjusting their strength so as to meet certain performance requirements, has turned them to be very attractive and promising, especially with the design of future structures. Figures 1.3 to 1.5 present some indicative applications of composite materials on ships and marine structures and Figure 1.6 presents a summary of the diverse range of new applications for composites in warships and ships in general.

16

Fig. 1.3. Two Visby-class corvettes of the Swedish Navy built from sandwich composite panels having face skins of hybrid carbon- and glass fiber polymer laminate covering a PVC foam core.
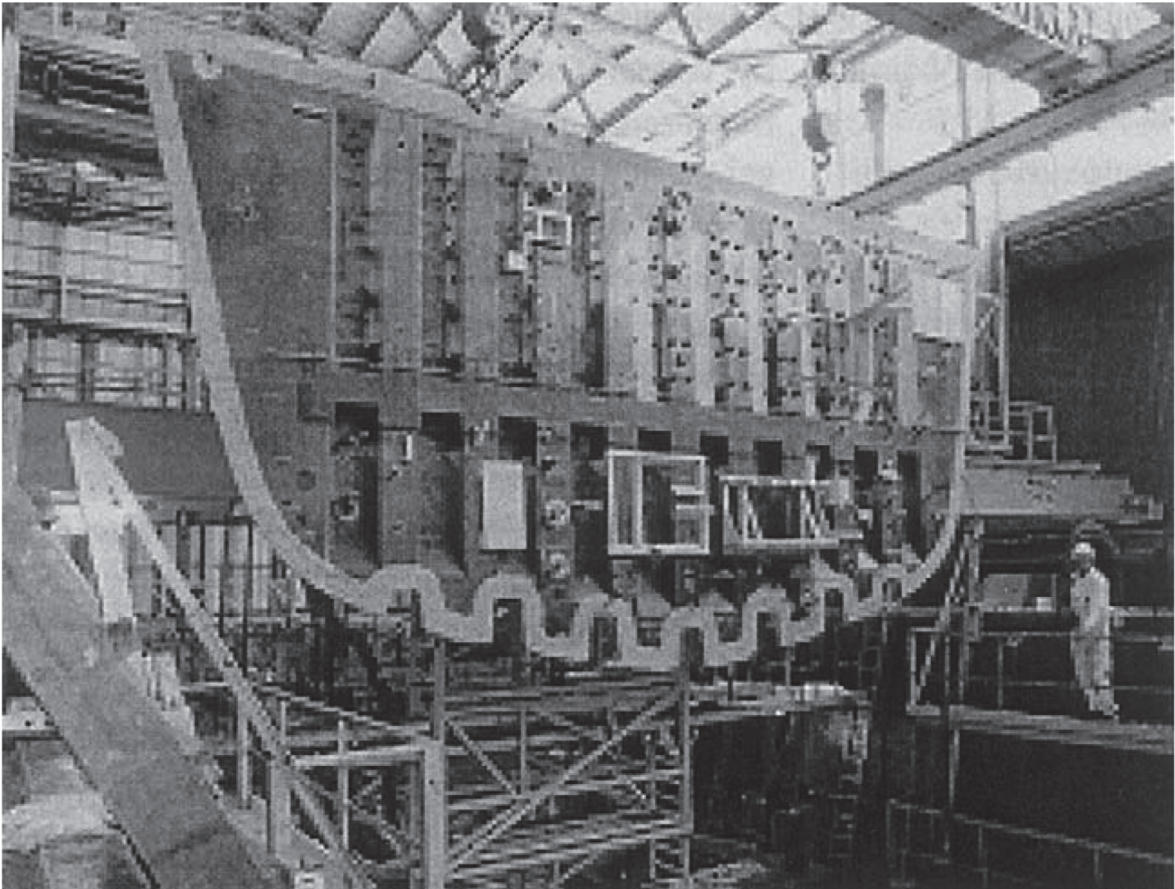
Fig. 1.4. Composite bulkhead manufactured for application on a steel ship.

Fig. 1.5. La Fayette class frigate of the French Navy. Among the first large warships fitted with a composite superstructure. In particular, the aft section of the superstructure, including the helicopter hanger, is made of GRP-sandwich composite panels.
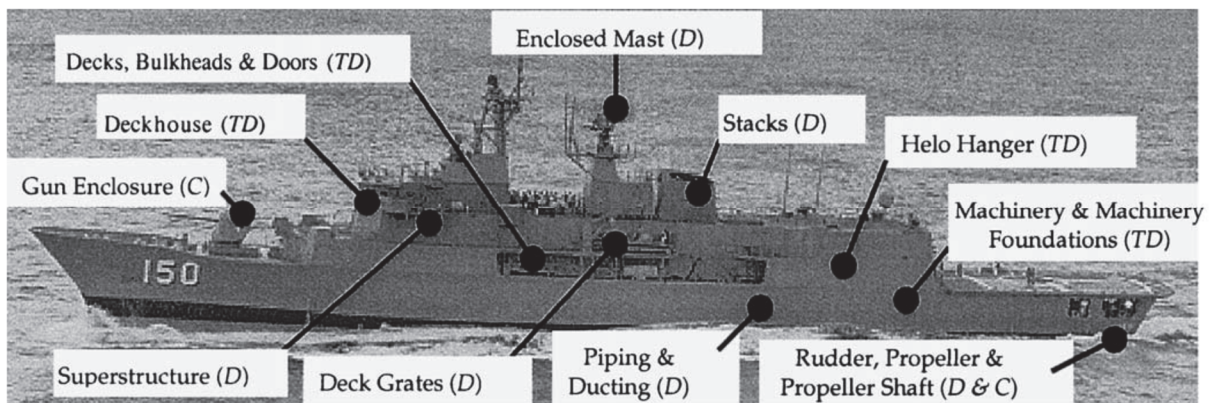
Fig. 1.6. Applications of composite structures to naval ships and ships in general.

A key component investigated to be replaced by composite materials is the propulsion shaft. The massive steel shafts on large ships comprise up to 2% (or ~100-200 tons) of the ship's total weight. The composite shafts of glass and carbon reinforcing fiber in an epoxy matrix have the potential to be 25-80% lighter than the traditional steel shafts of similar size. Ship designers expect a composite shaft to also suppress the transmission of noise from machinery and propellers due to the intrinsic damping properties of composite materials. Hence the acoustic signature of the vessel would be reduced which is important for naval warfare ships. Being non-magnetic, composite shafts will also reduce the magnetic signature of a vessel (Mouritz, Gellert, Burchill, & Challis, 2001). Additionally, composite shafts offer the advantages of corrosion

resistance, low bearing loads due to their light weight, higher fatigue resistance, greater flexibility, and improved life-cycle cost (Greene, 1999).

The development of composite propeller shafts was not as advanced as for other aforementioned marine structures until recently (last ten years). Fabrication, performance, durability and maintenance issues needed to be resolved before composites would become strong candidate materials for propeller shafts in ships. All these issues are rapidly being solved during the last decade. A remaining issue, however, is the efficient design of composite shafts, which finds its roots in the general problem of understanding composite material mechanical behavior and their failure modes and mechanisms. Additionally, the material characterization, i.e. the definition of the mechanical properties, of a composite material can be a difficult task due to its special characteristics.

Designing a composite shaft and a composite material in general, requires not only the design of the geometry but also the design of the material itself, considering that the matrix-fiber-layup combinations are infinite. Traditionally, due to the lack of knowledge about the composite material behavior, the design of a composite structure was achieved based on the use of empirical data and some experimental results. However, the high cost of experimental characterization of composites along with the enormous range of the possible combinations restricted the knowledge base and application range of composite materials in a large scale.

In the recent years, the evolution of simulation programs using the Finite Element Method (FEM) like ANSYS and ABAQUS made possible the modeling and the analysis of composite structures of almost any geometry and mechanical properties, under various loads.

The current study deals with the mechanical behavior of composite shafts under torsion. The main aims are the understanding of the shaft's response to the applied torque and its failure mode. Emphasis is given in the development of a finite element model that will accurately simulate the mechanical response of the composite shaft. The calibration and validation of the finite element model is achieved through the comparison with experimental data acquired from the industry and by a torsion test conducted for the needs of this thesis.

1.2 Composite shaft applications, manufacturing process and Rules specifications

1.2.1 Composite shaft applications

Composite torque transmission shafting is now being used in many different applications. The driving force pushing its use originates in three basic physical characteristics that have already been mentioned: vibration damping, reduced weight/lower inertia and harmonic frequency.

As shown in Figure 1.7, some of the current applications include commercial/industrial use in vertical pumps and cooling towers, where high corrosivity problems exist, military vehicles drive systems, manned and unmanned air vehicles, wind turbines, automobiles including racing cars and marine propulsion shafting systems (Peters, 2011).
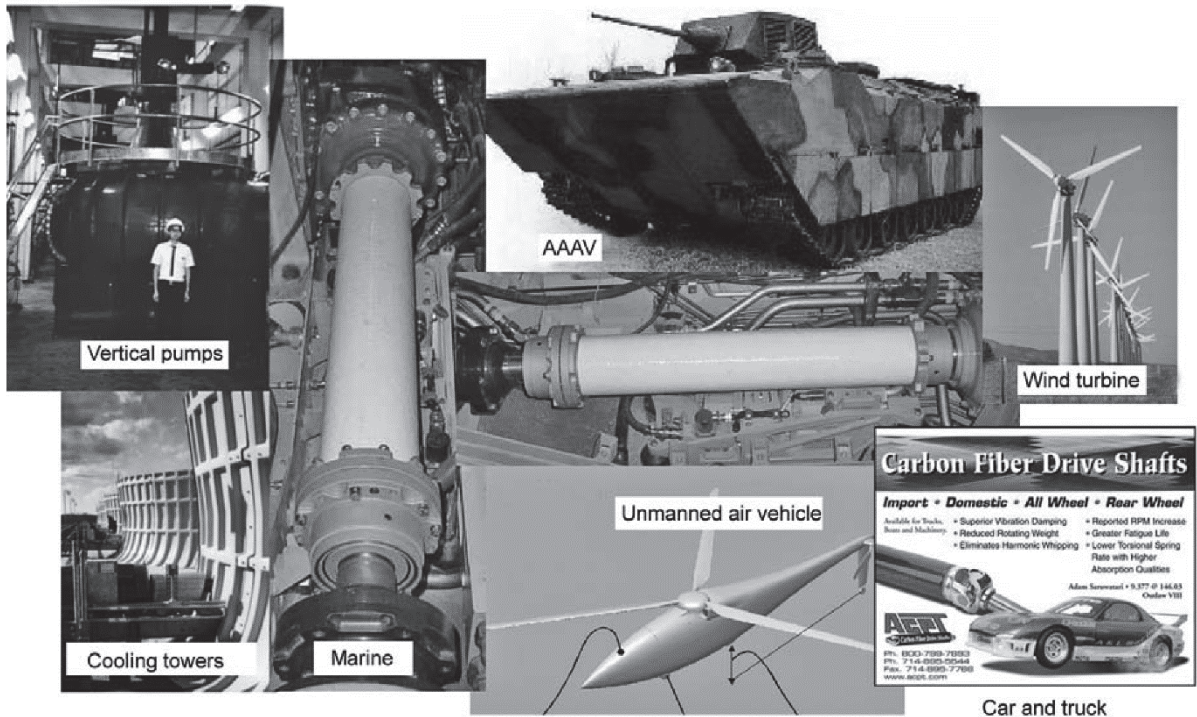
Fig. 1.7. Composite drive shaft applications. (AAAV, advanced amphibious assault vehicle)

This study focuses in marine applications of composite shafts. There are several companies that have been manufacturing composite shafts for marine applications, mainly from Carbon Fiber Reinforced Polymers (CFRP), for more than a decade. Figure 1.8 presents the various shaft sections that constitute the propulsion shafting system of a ship and are to be manufactured from composite materials.
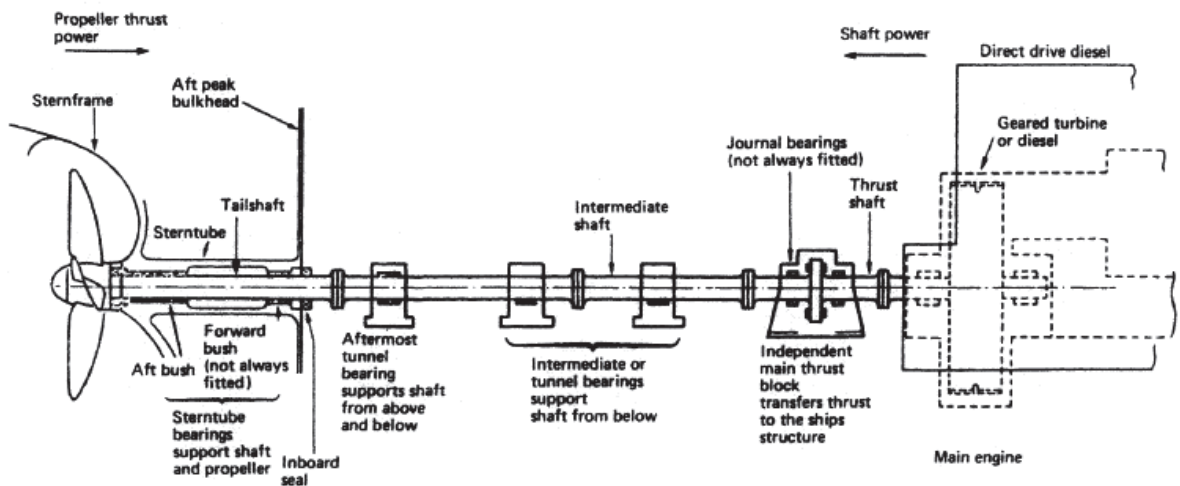
Fig. 1.8. Propulsion shafting system components

CENTA

CENTA (http://www.centa.info/) is a large producer of flexible couplings and shafts for industrial and marine applications, for power generation and rail applications.

According to CENTA's website, they have equipped more than 150 ships with 500 drive shafts. The company also boasts close cooperation with all involved partners such as shipyards, engine, gear, waterjet, shaft bearing, shaft seal manufacturers etc. and classification societies for the design and optimization of the manufactured products.

Additionally, for the secure connection of CFRP shafts with the metal hubs, CENTA has developed a new well proven and special patented method. The wide portfolio of power transmission elements consists of a series of torsionally flexible or torsionally stiff couplings, thus achieving optimum and reliable solutions with confidence for any combination.

CENTA CFRP shafts have successfully been applied in numerous fast ferries (monohull and catamaran), cruise vessels, naval ships, luxury yachts, tug boats, dredgers, research ships, drill ships, rescue boats, excursion boats, hydrofoils, double ended ferries and pilot boats. Some of these applications are presented in Figure 1.9.

Fig. 1.9. Some vessels using CENTA CFRP power transmission shafts.

According to CENTA, there are no theoretical limits for the dimensions and torques of CFRP shafts, but practical ones. Any length is possible (using several sections), but up to 12m per section is the practical limit. Concerning torque limits, to date, up to 1000kNm shafts have been delivered but up to 2200kNm have been designed and quoted. The rotational speed limit depends on the length of the shaft, the diameter and the wrapping angle. To date the maximum

speed is 3000 rpm. The maximum power transmitted to date is 23000 kW (gas turbine) per shaft, but projects for 50000 kW per shaft have been quoted.

Figure 1.10 presents two CENTA carbon fiber shaft applications.

Fig. 1.10. CENTA carbon fiber shafts in "Flying Cat" (left) and "Jumbo Cat"(right) catamarans

CENTA CFRP shafts have already been delivered with classifications of ABS, DNV, GL, LRS, RINA and in general can be supplied to any classification.

Beside the tailored applications, CENTA has developed two standard series. Series P for high specific torques and series S for high speeds and/or large spans.

A special reference is done to the CENTA flexible components used for shaft couplings.

CENTAFLEX series A, G, GZ or GB

Torsionally soft, economic flexible shafts that use the CENTAFLEX A series elements, which compensate for axial, radial and angular misalignment. Suitable for all kind of applications. Continuous angular deflection up to 2 degrees, per element, is possible. Torque range up to 14kNm.
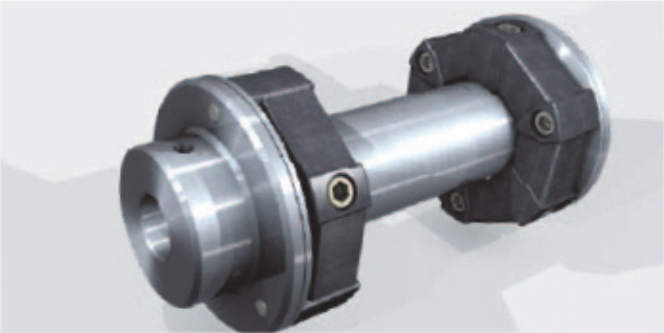
CENTALINK

Torsionally stiff but capable of compensating for substantial misalignments of all kinds while dampening transmitted noise. Proven of the years in many applications in shaft lines of up to 25m in length, e.g. windturbines, pump sets and ship propulsion. Torque range up to 540 kNm.
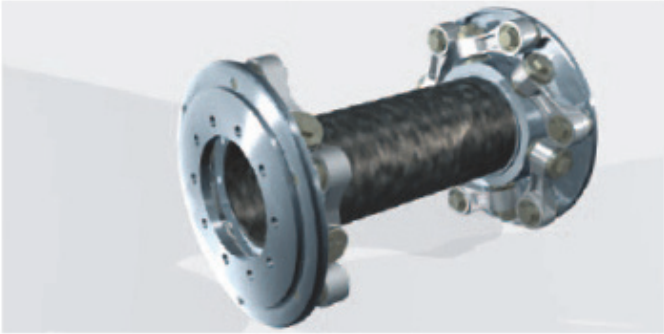
CENTADISC-M

Based on the proven and patented steel membrane design of the CENTAX series
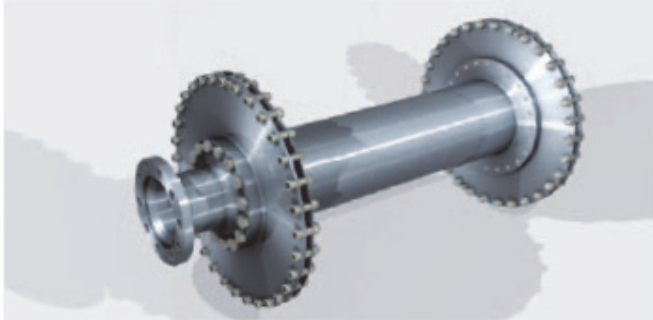
M coupling, and compensating for all kinds of misalignment and lengths up to 10m. Using intermediate bearings and additional membranes any length of shaft can be provided. Torque range up to 160 kNm

CENTADISC-C

Newly developed flexible shaft, comprising moulded membranes, made of highgrade GFRP composite, and hollow shafts made of GFRP or CFRP composite. Extreme low weight, free of maintenance and corrosion. Torque up to 20kNm
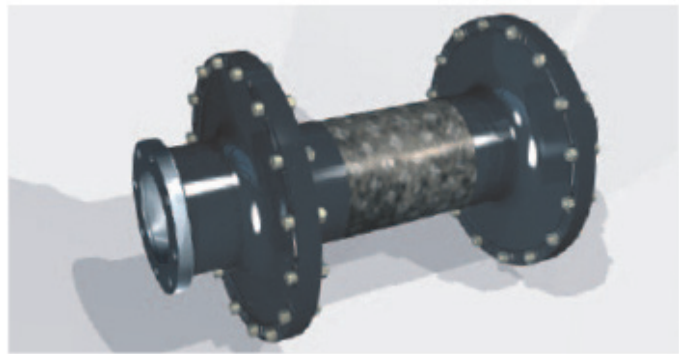
CENTABUSH

This series comprises the same proven rubberbushes as the CENTALINK, but without links. This way very high torques can be achieved on a rather small diameter. The ideal connection for confined space. Nevertheless it provides flexibility and noise damping. Torques up to 500 Nm.

JAURE
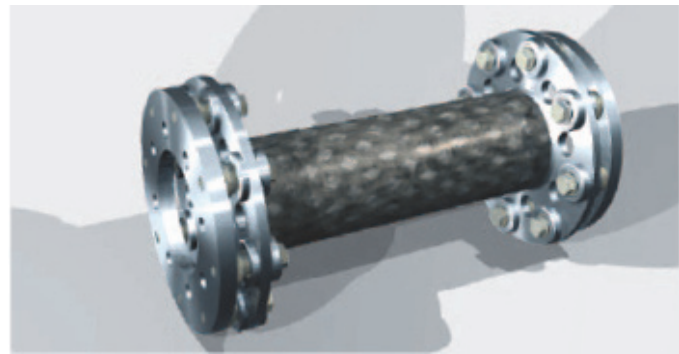
JAURE (http://www.regalpts.com/brands/jaure/Pages/jaure.aspx) is a big supplier of marine composite shafts and couplings for propulsion and maneuvering, covering the waterjet, propeller and thruster applications. JAURE carbon fiber shafts, in combination with JAURE couplings, were first introduced in fast ferries and are now making inroads on other types of vessels such as dredgers, supply vessels, commercial and cruise ships. Figure 1.11 presents several ships that are using JAURE carbon fiber shafts and couplings.

Fig. 1.11. Ships that are using JAURE carbon fiber shafts and couplings

JAURE Carbon Fibre shaftlines usually include flexible and rigid couplings, which offer a complete package to fit specific project requirements. The offered couplings are:

• LAMIDISC®: Non-lubricated and high torque capacity disc-pack couplings. Torsionally stiff.

• MT / HA: Compact design gear couplings valid for most marine applications, including underwater solutions.

• IXILFLEX®: Rubber joint link-type couplings. Bidirectional coupling for high misalignment.

• COMPOLINK®: Maintenance free composite link-type flexible couplings. Combination of high misalignment capability with excellent service life.

• JHC: Easy installation hydraulic rigid couplings for shaft connection.
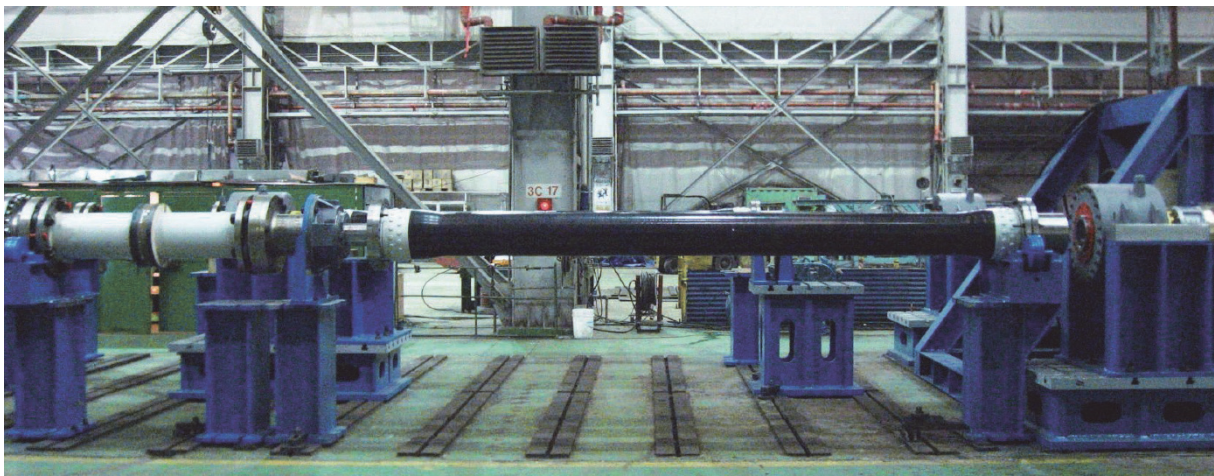
Fig. 1.12. JAURE carbon fiber shaft combined with LAMIDISC coupling

JAURE shaftlines are approved by most of the classification societies such as: ABS, BV, DNV, GL, KR, RINA etc.

Apart from customized products, JAURE offer two standardized series. L-series suitable for long distance between bearing and high speeds and T-series developed for high torques above 65 kNm. Although standardization covers up to 900kNm, there are no restrictions for higher rating. JAURE has supplied carbon fiber shaftlines for 112,2 kNm torque, which are powered by 8400 kW gas turbines. Speed limitations depend on the length and manufacturing process. JAURE composite shafts up to 6000rpm have been supplied for industrial purposes. Finally, concerning the length, 14m long tubes can be manufactured, however installation and logistic issued must be taken into consideration.

VULKAN

VULKAN (http://www.vulkan.com/en-us/holding) produces composite Shafts with steel end fittings, steel intermediate shafts to take the bearing, shaft bearings, bulkhead seals and appropriate VULKAN misalignment couplings (like METAFLEX, METADISC) or steel membranes. VULKAN Composite Shafts can also be combined with all types of VULKAN highly flexible couplings. VULKAN Composite Shafts are made from filament winding technique with Epoxy resins and carbon or glass fibers reinforcement. They are available in a torque range from 5 to 800 kNm, diameters from 170 to 670 mm and lengths up to 12 m. Depending on the operational shaft speed and the respective critical speed of the Composite

shaft, long bearing distances can be bridged. VULKAN composite shafts are available in high torque capacity (T) or in high bending stiffness (B) execution. Basically the manufacturing technique allows the production of VULKAN composite shafts with diameter up to 1500 mm and length up to 20 m. Thus VULKAN composite shafts with nominal torque up to 5000 kNm can be designed and offered for special projects. VULKAN composite shaft systems are supplied with certificates of all international classification societies.

There are more composite shafts manufacturers that supply the marine sector but the aforementioned three are among the major. Theirs products summarize most of the composite shaft marine applications.

1.2.2 Composite shaft manufacturing process: Filament Winding

The manufacturing process of composite shafts is filament winding. Most shapes generated through this process are surfaces of revolution, such as pipes, cylinders and spheres. In filament winding, continuous reinforcements, such as roving, are wound onto a mandrel until the surface is covered and the required thickness is achieved. The process uses raw materials, fiber and resin, in a fairly automated process with low labor, thus contributing to a low production cost. The preprogrammed rotation of the mandrel and horizontal movement of the delivery eye produce the helical pattern depicted in Figure 1.13, which is the simplest mode of operation of an helical winding machine.
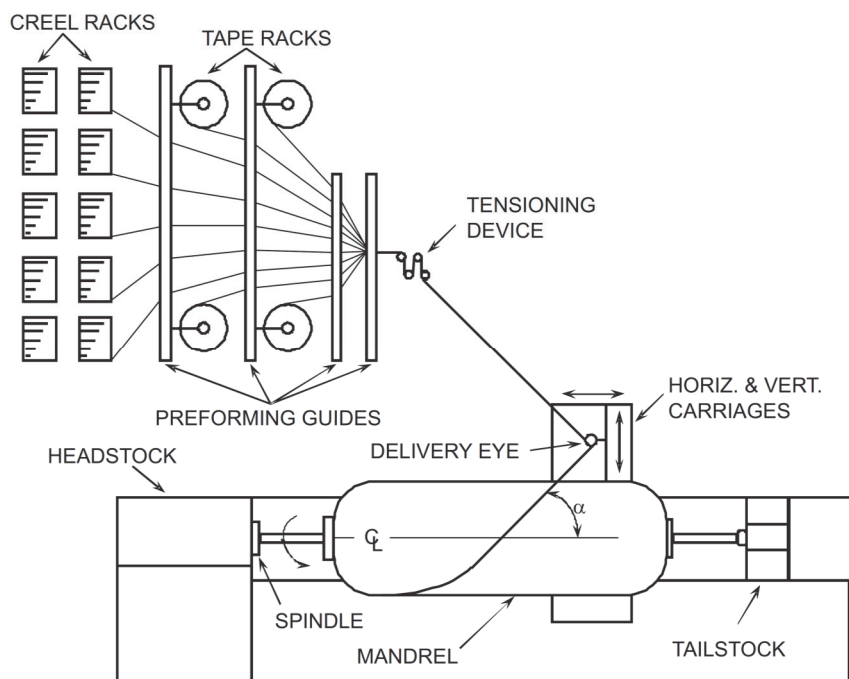
Figure 1.13. Filament Winding

There are two basic types of winding machines: helical and polar. The helical winding machine is similar to a lathe. The mandrel rotates continuously while the delivery eye moves back and forth. The rotational speed of the mandrel and the linear speed of the delivery eye can be adjusted to produce any fiber orientation between 5° and 90°, the latter called hoop winding. Several back-and-forth travels of the carriage are needed to complete a lamina covering the mandrel. Such a lamina is always a two-ply balanced laminate at ±θ. The fiber reinforcements

are delivered from creel and tape racks, and through a tensioning device or brake that can be adjusted to control the tension in the reinforcement. Next, the reinforcement goes through a resin bath where it picks up resin. Then, the wet reinforcement is delivered through the delivery eye that is mounted on a carriage. In addition to the spindle rotation, the carriage and delivery eye can move in a number of ways designed to help place the reinforcement along complicated contours. A helical winder with three possible movements, called *axes*, is depicted in Figure 1.13, but machines with up to six axes are available. A six axes machine independently controls its spindle rotation, horizontal carriage feed, radial carriage position, delivery eye angle and yaw, and vertical carriage feed. Winders employing fewer axes are used for simple parts such as golf shafts and larger number of axes are used for more complex components such as windmill blades.

A helical winder naturally produces a geodesic path, that is the path followed by a string under tension on the surface of the mandrel. An example of such a path used for winding a cylindrical vessel is shown in Figure 1.13. For more complex shapes, the winder can be programmed to deviate from the geodesic path. In this case, the roving tends to slip back into the geodesic path. The difference between the geodesic and the set path is the slip angle, which is limited by processing conditions. A string free to slip, stretched between two points on the convex side of any surface, follows a geodesic path. If the shape of the surface can be designed so that the geodesic path coincides with the resultant of the hoop and meridional forces, the shape is called a *geodesic dome*. The design of such a shape is used for the end domes of pressure vessels.

Polar winders are used to produce spherical vessels or cylindrical vessels with length/diameter ratio less than 2.0. A polar winder is mechanically simpler, thus less expensive, and faster than a helical winder. It consists of an arm that rotates around the mandrel delivering the roving into a planar path. The mandrel is stepped slowly so that the arm covers its surface. Except for the perfect sphere, the planar path always has a slip angle with respect to the geodesic path that limits the applicability of polar winding to nearly spherical shapes.

After winding the part is moved to a gas fired or electric oven, thus freeing the winder for winding another part. The need for continuous tension of the fiber around the mandrel virtually prevents the manufacturing of shapes with negative curvature, unless special fixtures are used. Small radii of curvature are also a problem because fiber breakage and sudden changes in curvature tend to create resin rich zones. The need for a mandrel and for its removal after the composite is cured also limits the shapes that can be wound. In general filament winding finds most of its applications in surfaces of revolution.

Several types of mandrels have been developed to facilitate removal. The easiest alternative used for some pressure vessels is to use a metallic liner as a mandrel and leave the liner as an integral part of the end product. This is sometimes required to prevent the leakage of gasses by diffusion through the composite wall. Collapsible mandrels are made of segments that can be disassembled after the part is cured. These are the most expensive mandrels, and thus they are used for large volume productions. A soluble sand mandrel is made of sand and polyvinyl alcohol. The mixture is cast in two or more parts, that when assembled, give the desired shape. Once the composite is cured, the mandrel is dissolved by injecting hot water. Plaster molds are used only for prototypes or low runs of large parts because they are labor intensive and damage to the part may result during removal.

Besides using wet reinforcements, it is possible to use prepreg or wet rerolled material, but these options invariably add more operations and cost to the product. Using wet reinforcements, fiber placement, impregnation, and consolidation are achieved simultaneously. The wet reinforcement is placed on the mandrel under tension, thus compacting the material previously wound. The maximum tension that can be used is a function of the fiber strength and the feed rate being used. The consolidation is not as good as that obtained with an autoclave resulting in higher void content and somewhat lower mechanical properties. However, not needing an autoclave is advantageous because it reduces the cost through lower capital expense and lower processing time. Furthermore, large parts that would not fit in any available autoclave can be fabricated by filament winding.

The maximum thickness that can be wound is limited by fiber slippage and wrinkling under the pressure of new laminae on top. When the thickness is large, it may be necessary to stop winding and let the part cure partially, until the resin gels, before adding more laminae. This slows the process resulting in additional cost. Therefore, as with virtually all processes, relatively thin laminates are preferred from a production point of view.

The major limitations of filament winding are size restrictions, geometric possibilities, the orientation of the fibers, and the surface finish of the final product. Void content may be high since no vacuum or autoclave is used and the resin cures at low temperature.

Production rates for filament winding processes vary greatly because the size of the part and the mandrel type dictate the amount of time needed to setup and remove a part from the winding machine. If setup and removal time are not considered, production rate is dictated by the feed rate at which fibers are wound onto the mandrel. Feed rates vary according to the strength of the fiber used, typically 0.6‑1.2 m/s for production using a wet fiber setup (Barbero, 2010).

1.2.3 Rules specifications

As composite propulsion shafts are gaining ground over steel shafts, some shipping registers are starting to answer to the need for rules and regulations for the use of composites shafts on ships. Most major shipping registers with activity in Greece (Lloyd's, DNV-GL, ABS, BV, RINA) were contacted for information. Only Lloyd's and DNV-GL provided us with some technical papers with rules concerning propulsion shafting and composite materials. A search on the internet was also conducted but no further regulations from the other classes were found with free access.

i) Lloyd's Register
Lloyd's does not offer rules dedicated to composite shafts, however it offers some general rules for shafting systems as well as rules for the manufacture, testing and certification of composite materials.

In the "Rules and Regulations for the Classification of ships, January 2016" document in the section that refers to materials for shafts (part 5, chapter 6, section 2) there is no reference to composite materials as it can be seen in the following lines which are directly extracted from the document.

In the next sections of the rules' chapter, the design parameters, like the diameter, of the various shaft types are listed and described.

Later in the same rules document, in chapter 16 which refers to water jet systems, it is noted that *"where it is proposed to use composite shafts, details of the connection at flanges, materials, resin, lay-up procedures, quality control procedures and documentary evidence of endurance strength is to be provided"* indicating that the use of composite shafts in water jet systems is approved.

In the "Rules and Regulations for the Classification of Special Service Craft, January 2016" document in the Shafting systems chapter (part 11, chapter 2) in the materials section it is noted *"where shafts are manufactured from composite materials the process is to be approved"*, as it can be seen in the following lines that are extracted from the document.

■ *Section 3*
Materials

3.1 Materials for shafts

3.1.1 Components are to be manufactured and tested in accordance with the requirements of the *Rules for the Manufacture, Testing and Certification of Materials, July 2015* (hereinafter referred to as the Rules for Materials).

3.1.2 The specified minimum tensile strength of forgings for shafts is to be selected within the following general limits:

(a) Carbon and carbon-manganese steel – 400 to 760 N/mm^2. *See also Pt 11, Ch 2, 4.4 Screwshafts and tube shafts 4.4.3.*

(b) Alloy steel main propulsion shafting:

    (i) not exposed to seawater – not exceeding 800 N/mm^2,

    (ii) for other forgings - not exceeding 1100 N/mm^2.

3.1.3 Where it is proposed to use alloy steel forgings, particulars of the chemical composition, mechanical properties and heat treatment are to be submitted for approval.

3.1.4 Where shafts may experience vibratory stresses close to the permissible stresses for transient operation, the materials are to have a specified minimum tensile strength of 500 N/mm^2.

3.1.5 Where materials with greater specified or actual tensile strengths than the limitations given above are used, reduced shaft dimensions or higher permissible vibration stresses are not acceptable when derived from the formulae used in sub-Sections *Pt 11, Ch 2, 4.2 Intermediate shafts*, *Pt 11, Ch 2, 4.4 Screwshafts and tube shafts*, *Pt 11, Ch 2, 4.5 Hollow shafts* and *Pt 13, Ch 1, 3.2 Limiting stress in propulsion shafting*.

3.1.6 Unprotected screwshafts and tubeshafts exposed to sea-water are in general to be manufactured from materials that show improved corrosion resistance in seawater when compared to carbon steel and alloy steels, referred to in *Pt 11, Ch 2, 3.1 Materials for shafts 3.1.1* and *Pt 11, Ch 2, 3.1 Materials for shafts 3.1.3*; examples of some such alloys are indicated in *Table 2.4.1 'A' Value for use in unprotected screwshaft formula* . However, the selection of these alloys should carefully consider the level of corrosion resistance in relation to all the environmental service conditions and operational requirements applicable to the individual vessel.

3.1.7 In the selection of materials for shafts, keys, locking nuts etc. consideration is to be given to their compatibility with the proposed propeller material.

3.1.8 Where shafts are manufactured from composite material the process is to be approved.

Concerning the design and construction of the shaft, Lloyd's Register states that as an alternative to the typical requirements that are presented in section 4.2 of the rules' chapter, a fatigue strength analysis of components can be submitted indicating a factor of safety of 1.5 at the design loads, based on a suitable fatigue failure criteria. The effects of stress concentrations, material properties and operating environment are to be taken into account. The typical requirements of chapter 4 for special service crafts are presented in the following lines, extracted from the document, and are almost identical to the ship's requirements. It must be reminded that composite shafts are hollow.

4.2 Intermediate shafts

4.2.1 The diameter, d, of the intermediate shaft is to be not less than:

$$d = Fk\sqrt[3]{\frac{P}{R}\left(\frac{560}{\sigma_u + 160}\right)} \text{ mm}$$

where

k = 1,0 for shafts with integral coupling flanges complying with *Pt 11, Ch 2, 4.8 Couplings and transitions of diameters* or shrink fit couplings

= 1,10 for shafts with keyways, tapered or cylindrical connections, where the fillet radii in the transverse section of the bottom of the keyway are not less than $0,0125d$

= 1,10 for shafts with transverse or radial holes (d_h) where the diameter of the hole does not exceed $0,3d$

= 1,20 for shafts with longitudinal slots, *see Pt 11, Ch 2, 4.2 Intermediate shafts 4.2.7*

F = 95 for turbine installations, electric propulsion installations and diesel engine installations with slip type couplings

= 100 for other diesel engine installations

= P and R are as defined in *Pt 9 General Requirements for Machinery* (losses in gearboxes and bearings are to be disregarded)

σ_u = specified minimum tensile strength of the shaft material, in N/mm^2.

4.2.2 Beyond a length of $0,2d$ from the end of a keyway, transverse hole or radial hole and $0,3d$ from the end of a longitudinal slot, the diameter of the shaft may be gradually reduced to that determined with k = 1,0.

4.2.3 For shafts with design features other than stated as above, the value of k will be specially considered.

4.2.4 The Rule diameter of the intermediate shaft for diesel engines, turbines and electric propelling motors may be reduced by 3,5 per cent for craft classed G1 (Service Group 1), *see Pt 1, Ch 2, 3.5 Service area restriction notations*.

4.2.5 For shrink fit couplings, k refers to the plain shaft section only. Where shafts may experience vibratory stresses close to the permissible stresses for continuous operation, an increase in diameter to the shrink fit diameter is to be provided, e.g. a diameter increase of 1 to 2 per cent and a blending radius as described in *Pt 11, Ch 2, 4.8 Couplings and transitions of diameters*.

4.2.6 Keyways are in general not to be used in installations with a barred speed range.

4.2.7 The application of k = 1,20 is limited to shafts with longitudinal slots having a length of less than $0,8d_o$ and a width greater than $0,15d_o$ and a diameter of central hole d_i of less than $0,7d_o$, *see Pt 11, Ch 2, 4.5 Hollow shafts*. The end rounding of the slot is not to be less than half the width. An edge rounding should preferably be avoided as this increases the stress concentration slightly. The values of C_K, *see Table 1.3.1 C k factors* in *Pt 13, Ch 1 Torsional Vibration*, are valid for 1, 2 and 3 slots, i.e. with slots at 360, 180 and 120 degrees apart respectively.

4.2.8 Where the intermediate shaft is constructed of the same material as the screwshaft and of a material listed in *Table 2.4.1 'A' Value for use in unprotected screwshaft formula* , the diameter of the intermediate shaft is not required to be greater than that of the screwshaft.

4.5 Hollow shafts

4.5.1 Where the thrust, intermediate, tube shafts and screwshafts have central holes having a diameter greater than 0,4 times the outside diameter, the equivalent diameter, d_e, of a solid shaft is not to be less than the Rule size, d, (of a solid shaft), where d_e is given by:

$$d_e = d_o\sqrt[3]{1 - \left(\frac{d_i}{d_o}\right)^4}$$

where

d_o = proposed outside diameter, in mm

d_i = diameter of central hole, in mm

4.5.2 Where the diameter of the central hole does not exceed 0,4 times the outside diameter, the diameter is to be calculated in accordance with the appropriate requirements for a solid shaft.

In the "Rules for the manufacture, testing and certification of materials, January 2016" document in chapter 14 that refers to plastics materials and other non-metallic materials, there is extensive information about the requirements for the classification and certification of such materials. This information covers all steps from the base material certification and the manufacturing process until the testing of the material.

The materials to be classified according to the aforementioned document are the following:

(a) Thermoplastic polymers.
(b) Thermosetting resins.
(c) Reinforcements.
(d) Reinforced thermoplastic polymers.
(e) Reinforced thermosetting resins.
(f) Core materials.
   (i) End-grain balsa.
   (ii) Rigid foams.
  (iii) Synthetic felt type materials.
(g) Machinery chocking compounds.
(h) Rudder and pintle bearings.
(i) Stern tube bearings.
(j) Plywoods.
(k) Adhesive and sealant materials.
(l) Repair compounds.

Composite shafts are manufactured using mainly thermosetting resins and carbon or glass reinforcing fiber. Consequently, the requirements for these materials will be presented in the following lines which are extracted directly from the document.

2.3   Thermosetting resins

2.3.1   The data listed in *Table 14.2.1 Data requirements for thermosetting resins* is to be provided by the manufacturer for each thermosetting resin.

Table 14.2.1 Data requirements for thermosetting resins

Data	Type of resin		
	Polyester (*See* Note 3 for vinylester)	Epoxide	Phenolic
Specific gravity of liquid resin	required	required	required
Viscosity	required	required	required
Gel time	required	required	not applicable
Appearance	required	required	required
Mineral content	required	required	not applicable
(*see* Note 1)			(*see* Note 2)
Volatile content	required	not applicable	not applicable
Acid value	required	not applicable	not applicable
Epoxide content	not applicable	required	not applicable

Free phenol	not applicable	not applicable	required
Free formaldehyde	not applicable	not applicable	required

Note 1. This is to be the total filler in the system, including thixotrope, filler, pigments, etc. and is to be expressed in parts by weight per hundred parts of pure resin.

Note 2. If the resin is pre-filled, the mineral content is required.

Note 3. Vinylesters are to be treated as equivalent to polyesters.

2.3.2   Cast samples are to be prepared in accordance with the manufacturer's recommendations and are to be cured and post-cured in a manner consistent with the intended use. The curing system used and the ratio of curing agent (or catalyst) to resin are to be recorded. Where post-cure conditions equivalent to ambient-cure conditions apply, *see Ch 14, 3.2 Preparation of test samples 3.2.2* and *Ch 14, 3.2 Preparation of test samples 3.2.3*.

2.3.3   The following are to be determined using these samples:

(a)   Tensile strength (stress at maximum load) and stress at break.
(b)   Tensile strain at maximum load.
(c)   Tensile secant modulus at 0,5 per cent and 0,25 per cent strain respectively.
(d)   Temperature of deflection under load.
(e)   Barcol hardness.
(f)   Determination of water absorption.
(g)   Volume shrinkage after cure.
(h)   Specific gravity of cast resin.

2.3.4   In addition, for gel coat resins the stress at break and modulus of elasticity in flexure are to be determined.

2.3.5   Where resins which have been modified by the addition of waxes or polymers, for example 'low styrene emission or air inhibited' materials, it is to be confirmed that the use of such resins will not result in poor interlaminar adhesion when interruptions to the laminating process occur. The test procedure is to be as follows:

(a)   A conventional room temperature curing catalyst/ accelerator system is to be used with the resin for laminate preparation.
(b)   A laminate of 25 to 35 per cent glass content in mass is to be prepared using two plies of 450 g/m^2 chopped strand mat. The laminate is to be prepared at ambient temperature (18° to 21°C). The laminate is to be allowed to stand for a minimum of four days but no longer than 6 days at ambient temperature.
(c)   A further two plies of 450 g/m^2 chopped strand mat are to be laminated onto the exposed surface and cured at ambient temperature for 24 hours. The finished laminate is then to be post-cured at 40°C for 16 hours. The finished laminate is to have a glass content of 25 to 35 per cent.
(d)   After cooling, the apparent interlaminar shear strength of the laminate is to be determined in accordance with ISO 14130; the minimum value is given in *Ch 14, 5.11 Minimum tested requirements for material approval 5.11.4*. Before testing the samples shall be conditioned at 23°C and relative humidity of 50 per cent for a period of 88 hours before testing.
(e)   If the tests are undertaken at the resin manufacturer's own laboratory, the individual test values are to be reported and the broken test specimens retained for examination by LR.

Alternative test procedures will be considered with prior agreement.

2.4   Reinforcements

2.4.1   The following data is to be provided, where applicable, for each type of reinforcement:

(a)   Reinforcement type.
(b)   Fibre type for each direction.
(c)   Fibre tex value.
(d)   Fibre finish and/or treatment.
(e)   Yarn count in each direction.
(f)   Width of manufactured reinforcement.
(g)   Weight per unit area of manufactured reinforcement.
(h)   Weight per linear metre of manufactured reinforcement.
(i)   Compatibility (e.g. suitable for polyesters, epoxides, etc.).

(j)   Constructional stitching – details of yarn, specific gravity, type, frequency and direction.

(k)   Weave type.

(l)   Binder type and content.

(m)   Density of the fibre material.

2.4.2   Tests of the mechanical properties are to be made on laminate samples containing the reinforcement and prepared as follows:

(a)   an approved resin of suitable type is to be used;

(b)   a minimum of three layers of the reinforcement is to be laid with parallel ply to give a laminate not less than 4 mm thick;

(c)   the weights of resin and reinforcement used are to be recorded together with the measured thickness of the laminate, including the measured weight per unit area of the reinforcement used;

(d)   for glass reinforcements, the glass/resin ratios, by weight, as shown in *Table 14.2.2 Glass fraction by weight for different reinforcement types* are to be used;

(e)   for reinforcement type other than glass, a fibre volume fraction, as shown in *Table 14.2.3 Content by volume for different reinforcement types*, is to be used.

Table 14.2.2 Glass fraction by weight for different reinforcement types

Reinforcement type	Glass fraction nominal values
Unidirectional	0,60
Chopped strand mat	0,30
Woven roving	0,50
Woven cloth	0,50
Composite roving (*see* Note)	0,45
Gun rovings	0,33
±45° stitched parallel plied roving	0,50
Triaxial parallel plied roving	0,50
Quadriaxial parallel plied roving	0,50
Note Continuous fibre reinforcement with attached chopped strand mat.	

2.4.3   Rovings intended for filament winding are to be tested as unidirectional rovings.

Table 14.2.3 Content by volume for different reinforcement types

Reinforcement type	Content by volume nominal values
Unidirectional	0,41
Chopped strand mat	0,17
Woven roving	0,32
Woven cloth	0,32
Composite roving (*see* Note)	0,28
Gun rovings	0,19
±45° stitched parallel plied roving	0,32
Triaxial parallel plied roving	0,32

33

Quadriaxial parallel plied roving	0,32

Note The volume content may be converted to weight fractions by use of the formula: $W_F = V_F D_F/(D_F V_F + D_R V_R)$ where W_F = fibre fraction by weight D_F = density of fibre D_R = density of cured resin V_F = fibre fraction by volume V_R = resin fraction by volume

2.4.4   The following tests as defined in *Ch 14, 3 Testing procedures* are to be made on the samples:

(a)   Tensile strength (stress at maximum load).

(b)   Tensile strain at break.

(c)   Tensile secant modulus at 0,5 per cent and 0,25 per cent strain respectively.

(d)   Compressive strength (stress at maximum load).

(e)   Compressive modulus.

(f)   Flexural strength (stress at maximum load).

(g)   Modulus of elasticity in flexure.

(h)   Apparent interlaminar shear.

(i)   Fibre content.

(j)   Determination of water absorption.

2.4.5   The laminate is to be tested in air in the directions indicated by *Table 14.2.4 Fibre orientations in reinforced test specimens*.

Table 14.2.4 Fibre orientations in reinforced test specimens

Type of reinforcement	Test orientations
Unidirectional	0°
Chopped strand mat Gun roving	any direction
Woven roving Woven cloth Composite roving	0° and 90°
± 45° parallel plied roving Triaxial plied roving Quadriaxial plied roving	0°, 45°, 90° and -45°

2.4.6   Additionally, tests in *Ch 14, 2.4 Reinforcements 2.4.4* are to be repeated, in one direction only, after immersion in fresh water at 35°C for 28 days with the exception of *Ch 14, 2.4 Reinforcements 2.4.4*.

2.5   Reinforced thermoplastic polymers

2.5.1   Thermoplastic polymers intended for use with reinforcements are to be tested in accordance with *Ch 14, 2.2 Thermoplastic polymers 2.2.1*.

2.5.2   A laminate is to be prepared using the polymer and an approved reinforcement in accordance with a manufacturing specification. The laminate is to be tested in accordance with the appropriate requirements of *Ch 14, 2.4 Reinforcements 2.4.4*. Testing may be confined to one direction only.

2.6   Reinforced thermosetting resins

2.6.1   Thermosetting resins intended for use with reinforcements are to be tested in accordance with *Ch 14, 2.3 Thermosetting resins 2.3.1*.

2.6.2   No further tests are required for gel coat resins.

2.6.3   For laminating resins, a laminate is to be prepared using the resin and an approved reinforcement as follows:

(a)   For polyester resins, chopped strand mat.

(b)   For epoxide resins, a balanced woven roving.

(c)   For phenolic resins, a balanced woven material.

2.6.4   The laminate is to be tested in accordance with procedures outlined in MQPS Book K procedure 14-1 and *Ch 14, 2.4 Reinforcements 2.4.4* in one fibre direction only.

In the next section of the Lloyd's document, the testing procedures for the aforementioned materials are presented.

■ *Section 3*
Testing procedures

3.1 General

3.1.1   This Section gives details of the test methods to be used for base materials and on finished plastics products such as fibre reinforced plastics (FRP) piping and any testing required in the construction of composite vessels.

3.1.2   In general, testing is to be carried out by a competent independent test house which, at the discretion of LR, may or may not require witnessing by the Surveyor.

3.1.3   Alternatively, testing may be carried out by the manufacturer subject to these tests being witnessed by the Surveyor.

3.1.4   All testing is to be carried out by competent personnel.

3.1.5   Unless specified otherwise, testing is to be carried out in accordance with a recognised ISO standard, where one exists, and all test programmes are to have written procedures.

3.1.6   Alternatively, testing may be carried out in accordance with a National Standard provided that it conforms closely to an appropriate ISO standard and subject to prior agreement with the Surveyor.

3.1.7   Mechanical properties are to be established using suitable testing machines of approved types. The machines and other test equipment are to be maintained in a satisfactory and accurate condition and are to be recalibrated at approximately annual intervals. Calibration is to be undertaken by a nationally recognised authority or other organisation of standing and is to be to the satisfaction of the Surveyor. A record of all calibrations is to be kept available in the test house. The accuracy of test machines is to be within ± one per cent.

3.2 Preparation of test samples

3.2.1   Thermoplastic samples are to be prepared in accordance with the manufacturer's recommendations for moulding. For finished products, samples are to be taken from the product during production in accordance with the manufacturer's quality plan, but where this is impractical, separate test samples are to be prepared in a manner identical with that of the product.

3.2.2   Samples of thermosetting resins are to be prepared using the curing system recommended by the manufacturer and identical with that used for the finished product.

3.2.3   The post curing conditions for samples of thermosetting resins are to be as recommended by the manufacturer and identical with those used for the finished product. Where the samples are made for the general approval of a resin, the post curing conditions are to be those in which the resin is intended to be used.

3.2.4   Where curing of the product is intended to take place at room temperature, the sample is to be allowed to cure at room temperature (18 to 21°C) for 24 hours followed by a post-cure at 40°C for 16 hours.

3.2.5   Where a reinforcement is to be used, the ratio of reinforcement to resin or polymer is to be nominally the same as that of the finished product or in accordance with *Table 14.2.2 Glass fraction by weight for different reinforcement types* or *Table 14.2.3 Content by volume for different reinforcement types*.

3.2.6   Where laminates are prepared specifically for approval test purposes, the reinforcement is to be laid parallel plied.

3.3　　Preparation of test specimens

3.3.1　　The test specimen is to be prepared in accordance with the appropriate ISO standard and the requirements of this Section.

3.3.2　　Precautions are to be taken during machining to ensure that the temperature rise in the specimen is kept to a minimum.

3.4　　Testing

3.4.1　　Strain measurement is to be made by the use of a suitable extensometer or strain gauge.

3.4.2　　The rate of strain is to be in accordance with the appropriate ISO standard.

3.4.3　　The number of test specimens from each sample to be tested is to be in accordance with the ISO standard. For mechanical testing this is five.

3.5　　Discarding of test specimens

3.5.1　　If a test specimen fails because of faulty preparation or incorrect operation of the testing machine, it is to be discarded and replaced by a new specimen.

3.5.2　　In addition, if the deviation of one result in a group of five exceeds the mean by more than two standard deviations, that result is to be discarded and one further specimen tested, *see Ch 14, 1.8 Re-test procedure 1.8.1* and *Ch 14, 1.8 Re-test procedure 1.8.2*.

3.6　　Reporting of results

3.6.1　　All load/displacement graphs and tabulated results are to be reported, including mean values and the calculated standard deviation.

3.6.2　　Additionally, full details of the sample and specimen preparation are to be provided including (where applicable):

(a)　　Catalyst/accelerator or curing agent types and mix ratio.
(b)　　Weights of resins, and/or reinforcements used.
(c)　　Casting/laminate dimensions.
(d)　　Number of layers of reinforcement used.
(e)　　Curing/post-curing conditions.

3.7　　Tests for specific materials

3.7.1　　The data requirements in *Ch 14, 2.2 Thermoplastic polymers* and *Ch 14, 2.3 Thermosetting resins* for thermoplastic or thermosetting resins or polymers are to be determined in accordance with suitable National or International Standards.

3.7.2　　Recognised Standards to which specimens of unreinforced thermoplastic resins are to be tested are listed in *Table 14.3.1 Tests for unreinforced thermoplastic resins*.

Table 14.3.1 Tests for unreinforced thermoplastic resins

Test	Standard	
Tensile properties	ISO 527-2:1993	Test speed = 5 mm/min Specimen 1A or 1B
Flexural properties	ISO 178:2001	Test speed = $\frac{Thickness}{2}$ mm/min
Water absorption	ISO 62:2008	Method 1
Temperature of deflection under load	ISO 75-2:2004	Method A
Compressive properties	ISO 604:2002	Test speed - as for ductile materials
Note 1. Water absorption - result to be expressed as milligrams.		
Note 2. Tensile modulus values are to be determined using an extensometer which may be removed for strain to failure.		

3.7.3　　Test standards for unreinforced cast thermosetting resins are given in *Table 14.3.2 Tests on unreinforced cast thermoset resin specimens*.

Table 14.3.2 Tests on unreinforced cast thermoset resin specimens

Test	Standard	
Tensile properties	ISO 527-2:1993	Test speed = 5 mm/min Specimen 1A or 1B
Flexural properties	ISO 178:2001	Test speed = $\frac{Thickness}{2}$ mm/min
Water absorption	ISO 62:2008	Method 1
Temperature of deflection under load	ISO 75-2:2004	Method A
Compressive properties	ISO 604:2002	Test speed = 1 mm/min

Note 1. ISO 62:2008 - where resins are intended for use under ambient conditions to avoid additional post-curing, the requirement in ISO 62:2008 for pre-drying the test specimen at 50°C is to be omitted. The test result is to be expressed as mg of water.

Note 2. ISO 527-2:1993 - tensile properties are to be measured using extensometry.

3.7.4   The Standards to which laminate specimens of any type are to be tested are listed in *Table 14.3.3 Tests on laminate specimens*.

Table 14.3.3 Tests on laminate specimens

Test	Standard	
Tensile properties	ISO 527-4:1997	Test speed = 2 mm/min Specimen types II or III
Flexural properties	ISO 14125:1998	Test speed = $\frac{Thickness}{2}$ mm/min Method A
Compressive properties	ISO 604:2002	Test speed = 1 mm/min
Interlaminar shear	ISO 14130:1997	
Water absorption	ISO 62:2008	Method 1
Glass content	ISO 1172:1996	

Note 1. ISO 62:2008 - where resins are intended for use under ambient conditions to avoid additional post-curing, the requirement in ISO 62:2008 for pre-drying the test specimen at 50°C is to be omitted. The test result is to be expressed as mg of water.

Note 2. ISO 527-4:1997 - tensile properties are to be measured using extensometry.

Note 3. Tensile modulus values are to be determined using an extensometer which may be removed for strain to failure.

In the next section of the document, the control of material quality for composite construction is discussed. All materials used for the construction need to be approved and several tests are to be done during the construction of the structure. However, this section refers mainly to the construction of batches or the craft's structure so no further reference is useful for this study.

ii) DNV GL

DNV-GL offers general rules for the classification of propulsion shafts made of steel and for the classification of composite materials. Additionally, it offers a class programme type approval for "Composite drive shafts and flexible couplings – Non-metallic materials". The objective of this class programme (CP) is to give a description of the procedures and requirements related to documentation, design and type testing applicable for type approval (TA) of composite drive shafts and flexible couplings. The type approval is based on compliance with design requirements given in the Society's rules and/or other regulations and standards. According to this fact, the rules for the classification of propulsion shafts made of steel and for the classification of composite materials won't be presented as it was done for Lloyd's Register. It must be noted however, that there are similarities between the rules of the two registers, especially for the classification of composite materials.

Section 1 General

The "Composite drive shafts and flexible couplings – Non-metallic materials" class programme covers drive shafts and flexible couplings consisting of a central section(s) fabricated from a fiber-reinforced thermoset plastic (FRP) which is joined at each end to a metallic flange (CMn-steel, corrosion resistant steel, titanium etc.) for connection and for load transfer to other driveline components. The central FRP section may be divided in more than one piece, the pieces being joined with or without the aid of metallic flanges. Joints may consist of adhesive bonds or mechanical connections (e.g. pinned or bolted connections) or combinations thereof.

A type approval covers the central FRP section(s) and the bonds between this section(s) and the flanges. (Metal flanges and other metallic components shall comply with the rules requirements for shafting.)

A type approval can be given for a range of shaft designs. An approved range can include:
— a range of nominal torques for shafts/couplings of similar geometrical configuration and where the variation of the capacity of the shaft/coupling is achieved by scaling the design
— minor changes or variations in design details, e.g. limited variations of the number of pins, the pin diameter, pin configuration and/or laminate thickness for pinned connections, limited changes in bonded joint configurations etc.

A type approval will be given for one specified set of raw materials, one specified method of fabrication of the central section and for one specified method of bonding between central section and the flanges including choice of materials (e.g. adhesive, type of material, steel grade etc. in the flange etc.).

Type tests shall be carried out and verified in one of the following ways:
— at a DNV GL laboratory
— at a recognized and independent laboratory or a laboratory accepted by the Society
— at the manufacturer's premises in the presence of the Society's surveyor.

Documentation

The required documentation for type approval:
1) type designation, i.e. product name (grade) with list of variants to be included in and stated on the type approval certificate
2) name and address of the manufacturer, to be listed on type approval certificate. The following shall be specified:
— details for all relevant production places
— manufacturer's name
— mailing address
— contact person
— phone and fax number
— e-mail and web address (if applicable).
3) basis for approval. A reference of applicable rules and standards which the product shall comply with

4) product specification/description including design, laminate lay-up, material specifications etc.

5) field of application and operational limitations of the product

6) description of production processes, including standard operating procedures

7) description of quality assurance system or copy of ISO 9001 certificate

8) quality plan for drive shafts/flexible couplings intended to be installed on board ships

9) test results (from tests already carried out) with references to standards, methods etc.

10) information regarding marking of the product or packaging

11) in-service experience, if available

12) witnessed type test results and initial assessment report by DNV GL local office shall be submitted when completed

13) list of test and measuring equipment, including calibration certificates.

The type approval of the drive shafts/flexible couplings will be based on:

— design analyses (calculations of stress and strain) of the central section(s) and the joints according to recognized engineering practice for one or more selected sizes of the sizes included in the type approval. The number of documented designs shall be agreed with the Society

— small-scale materials testing for characterization of laminate properties and the bond between central section(s) and flanges. The extent of materials testing shall be agreed with the Society.

— full scale testing of one or more of the sizes included in the type approval, as specified in this document

— a specification of materials used

— a specification of the method of fabrication of the central section(s) and of the bonds.

Section 2 Design input

1 Design requirements

The composite drive shafts and flexible couplings shall comply with the relevant requirements of the Society's rules and standards.

2 Functional requirements

Concerning design input, the the type approval will be given based on the following functional requirements:

— torsional static strength – transfer of engine torque

— torsional fatigue strength – sustain normal operational load cycles and induced vibrations

— bending fatigue strength – sustain permanent and variable shaft misalignments

— angular misalignment – accommodate shaft misalignments under given maximum bending moments

(applies to flexible couplings)

— axial offset – accommodate axial offset of shaft under given maximum reactions forces (applies to flexible

couplings)

— radial offset – accommodate radial offset of shaft under given maximum reaction forces (applies to flexible

couplings).

Reliable documentation of the following shall be provided:
— torsional stiffness – for torsional vibration analysis
— bending stiffness – for calculation of critical revolutions pr. minute.
In addition the following item may be evaluated in a type approval:
— resistance to impact damages due to e.g. handling, dropped objects etc.

Other functional requirements may be included depending on the type of installation for which the component is intended. In such a case the drive shaft/flexible coupling design and fabrication method will be subject to special consideration.

3 Load conditions

The shaft shall as a minimum be analysed for the following load conditions:
— start-stop cycles: start – max. load – reversing (if relevant) – stop. Dynamic effects shall be included.
— rare peak torques, e.g. due to synchronization problems with a generator or other rare disturbances of normal operation
— transient operation, e.g. passing through a speed range barred from normal operation, ice shock loads etc.
— steady state torsional vibrations
— bending induced by shaft misalignment
— angular misalignment (for flexible couplings)
— radial offset (for flexible couplings)
— axial offset (for flexible couplings).

The different parameters are described in Figure 1.14.
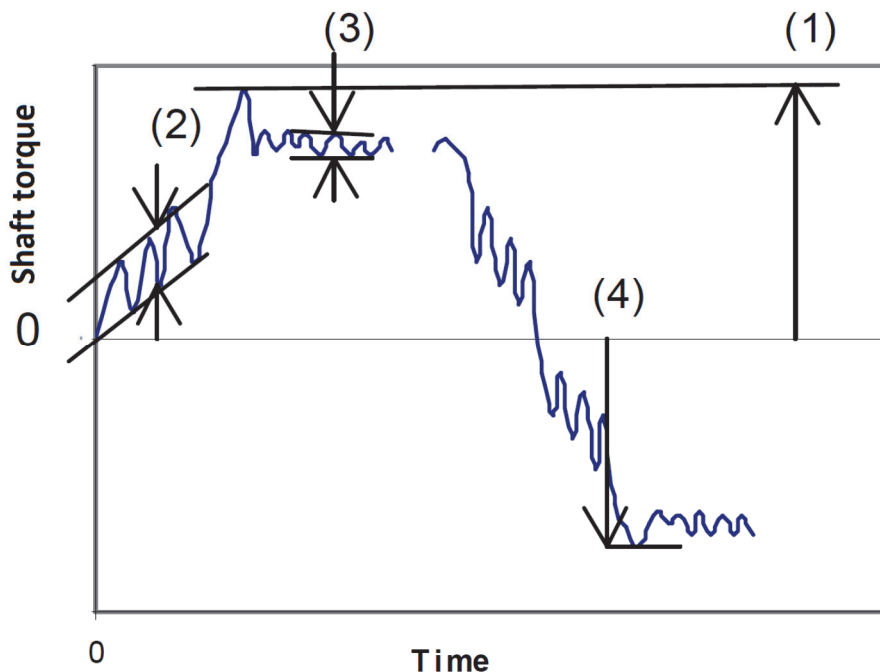

Fig. 1.14 Graph indicating parameters listed below

(1) peak torque: start - max. load - stop-cycle, rare peak torques
(2) $2 \times T_v$(transient): transient operation vibrations
(3) $2 \times T_v$(continuous): steady state torsional vibrations
(4) peak torque: reversing.

The loads and the associated number of load cycles shall be calculated according to the relevant rule requirements for shafting for a particular application. These load conditions shall be specified in the form of a table of maximum and minimum torque in each load cycle and the corresponding number of load cycles. Alternatively manufacturer shall specify the peak torque and a fatigue load envelope in this form within which the shaft satisfy the requirements to fatigue strength.

The load conditions for bending, axial offset, radial offset and angular misalignment shall be documented in the same way when relevant. For these modes of loading other load conditions than used for the torsional load may be relevant.

If other functional requirements than listed above are identified other load conditions may apply.

In the Type Approval Certificate will be stated a maximum design envelope of load conditions based on the manufacturer's specification and verified through the type approval process. Similar tables for bending, axial offset, radial offset and angular misalignment will be included as required.

4 Environmental conditions

If not specified otherwise the type approval will be given for operation under the following conditions:
— a temperature within the range +5 to + 55°C
— a relative humidity within the range 0 to 96%
— no exposure to liquids or gases with a possible detrimental effect on the properties of the shaft.

If other operational conditions shall apply this shall be specified by the manufacturer and they shall be reflected in the design analysis and, if necessary, during materials testing and type testing. In such a case as a minimum the following conditions shall be defined:
— maximum and minimum operating temperature
— maximum relative humidity
— possible exposure to detrimental liquids or gases.

The environmental conditions will be stated on the type approval certificate.

Section 3 Materials

The following types of fibres are accepted:
— glass-fibre
— carbon-fibre.
Other types of fibres may be accepted based on special consideration.
The following typeof resins is accepted:
— epoxy.
Other resin types may be accepted based on special consideration.
Only type approved fibres, resins and adhesives will be accepted. In case of the adhesive the type approval shall cover the particular combination of adherents, surface preparation of the adherents and the specified environmental conditions.

Fibres, resins and adhesives not covered by a type approval may be accepted after special consideration.

The temperature of deflection of the laminate(s) measured according to ISO 75, method A shall exceed the maximum operation temperature by at least 20°C.

The stacking sequence in laminates shall be such that the risk for delamination between plies is minimised:
— it shall be avoided to stack parallel plies of unidirectional reinforcement on top of each other
— the angle between the principal directions of two adjacent plies shall preferably exceed 30°
— for components not fabricated by filament winding one shall aim at having fibres oriented in at least three different angles in the laminate, observing the requirement above.

Adhesives shall be selected with due regard to the operating conditions. As a minimum the adhesive shall be suitable for the environmental conditions specified in Sec.2 [4]. The adhesive shall combine adequate properties at high and low temperatures. The minimum glass transition temperature of the adhesive shall exceed the maximum operation temperature by at least 15°C. The peeling strength of the adhesive at low temperatures shall be addressed especially.

The risk for corrosion, e.g. in connection with use of carbon fibre reinforcements together with steel, shall be considered and eliminated when necessary depending on the type of installation.

Section 4 Failure mechanisms and criteria

1 Failure mechanisms

The FRP section(s) shall as a minimum be analysed for the following failure mechanisms:
— fibre failure
— matrix cracking
— delamination
— buckling
— fatigue failure.

The bonds between the FRP section(s) and flanges shall as a minimum be analysed for the following failure mechanisms, as relevant:
— fibre failure
— matrix cracking
— delamination
— shear failure of the bond line (the possible effect of peeling stresses shall be carefully considered)
— bearing pressure (e.g. hole edge bearing pressure in pinned connections)
— fatigue failure.

Other failure mechanisms shall be analysed if relevant for the drive shaft/flexible coupling design. This will for example apply to novel designs or novel technical solutions. Such cases will be subject to special consideration.

The design analysis shall include a careful analysis of stresses due to cure cycles of the central section(s) and of the adhesives, including residual stresses.

2 Failure criteria

For the FRP section(s) a maximum stress failure criterion shall be used. The mechanical strength values and load effects shall be expressed as stress in the laminate and/or in the

individual plies. Other failure criteria may be used if conservative w.r.t. the maximum stress criteria.

For bearing pressure a criterion based on maximum stress shall be used.

For buckling of the FRP section(s), criteria based on maximum shear stress and maximum bending stress shall be used.

For adhesive bonds a failure criteria based on shear line-load in the adherents (laminate and flange) or similar shall be used. A criteria based on nominal bondline shear stress shall not be used.

Section 5 Material Properties

1 Mechanical properties – static strength

The characteristic values of mechanical strength used in the calculation of the capacity shall represent the 2.5% fractile, i.e. the probability that the mechanical strength is larger than the characteristic value shall be 97.5%.

The modulus of the laminate can be measured in relevant tests or estimated based on generally accepted micromechanic models and laminate theory. (The torsional stiffness of the shaft subjected to the type tests shall be verified during the tests, see Sec.7.) The variability in modulus of the laminate as manufactured shall be estimated based on generally accepted methods and/or experience.

The change in mechanical properties during the service life of the shaft shall be determined and reflected in the design analysis. As a minimum the following effects shall be considered:

— effect from the surrounding environment: temperature, humidity, exposure (see Section 2)
— fatigue loading, which may have an effect on the shaft stiffness and mechanical strength of the FRP section and the bonds.

2 Fatigue strength

Fatigue strength data shall be generated based on recognised methods to the satisfaction of the Society. Fatigue strength data of filament wound laminates and laminates based on unidirectional pre-pregs can be based on fatigue testing of 0°/90° laminates with a stacking sequence representative for the end product and loaded in the most relevant direction. The fatigue tests may be carried out as pulsating tensile tests. The R-value shall be as close to zero as possible and not larger than 0.05. Fatigue strength data for adhesive bonds may be derived from pulsating fatigue testing of double-lap-shear joint specimens as long as the results can be considered conservative with respect to the finished product.

The specimens shall have substrates, surface preparation, adhesive and cure cycle representative for the finished product.

Fatigue strength data used in calculations shall be presented and analysed on a double logarithmic scale.

Section 6 Design Analyses

1 Static Strength

The mechanical strength of the drive shaft/flexible coupling shall be determined for each of the specified failure mechanisms by use of standard analytical methods recognised by the industry, such as adequate stress analyses, conventional laminate theory, micromechanics, analysis of

the distribution of bond-line shear stress etc. Careful attention shall be given to stress concentrations. Other methods may be accepted based on special consideration. The analytical methods shall be substantiated by adequate small scale and large scale tests. Full scale test(s) as specified in Section 7 shall be carried out.

The capacity of the shaft shall be determined with respect to each of the specified failure mechanisms (except fatigue) for the peak torque and peak bending moment. In the analysis the peak torque and the peak bending moment shall be combined in a conservative manner. This load combination is designated the "Design Load".

Similarly the Design Load for a coupling shall be the worst case combination of the peak torque and allowable axial and radial offsets and angular misalignment.

Local stress- and strain-levels shall be calculated at ply-level at all relevant locations such that a representative picture of the stress-/strain-distribution in the shaft including the joints is achieved. All strain concentrations, e.g. due to geometrical effects, shall be included in the analysis.

The variability in the modulus of the material shall be included in a conservative way in the analysis.

The ratio "SF" of characteristic strength to the local stress or strain corresponding to the design load shall be:

Table 1.1 Safety factors

Part	Failure Mechanism	SF
Central section joint	Fibre failure	3.0-4.0[1]
Central section joint	Matrix cracking	1.5
Central section joint	Delamination – Shear Delamination – through-thickness stress	4.0[2]
Central section joint	Buckling	3.0
Joint: adhesive bond	Shear of adhesive bond-line	6.0[3]
Joint: pin/bolt connection	Contact pressure	5.0[3]
1) for designs with SF ≥4.0 design against fatigue due to torsion will normally not be required. For designs with 3.0 ≤ SF < 4.0 documentation of the slope "m" of the fatigue curve of the material will be required for design against torsion fatigue. For fatigue wrt other load conditions (e.g. deformations in flexible couplings) other requirements apply. 2) to ensure an adequate safety against delamination the through thickness shear stress in the laminate including residual stresses shall not exceed 5 MPa at any location 3) the capacity of the joint will be based on static tests in addition to the design analyses, see Sec.7. The manufacturer shall provide a calculation procedure for applying the test results to other shaft designs included in the type approval to the satisfaction of the Society		

The shaft's/coupling's strength with respect to buckling shall be determined by FEM calculations supported by the type tests, see Sec.7. The FEM analysis and/or tests shall be carried out in such a way that conservative predictions of the buckling strength are obtained. The safety factor SF shall apply to this conservative prediction. If the buckling strength of the

component is based on realistic tests in full scale taking into account all relevant imperfections (e.g. geometrical) a SF lower than stated in Table 1 may be accepted.

For long cylindrical cross sections the critical buckling stress in torsion can be calculated according to the following equation as an alternative to FEM-analyses or tests:

$$\tau_{crit} = \frac{E}{1-\nu^2} \cdot \left(\frac{t}{l}\right)^2 \cdot (-2.39 + \sqrt{96.9 + 0.605H^{1.5}})$$

$$H = \sqrt{1-\nu^2}\,\frac{l^2}{r \cdot t}$$

For long cylindrical cross sections the critical buckling stress in bending can be calculated according to the following equation as an alternative to FEM-analyses or tests:

$$\sigma_{crit} = \frac{E}{\pi(1-\nu^2)} \cdot \frac{t}{r}$$

τ_{crit} = critical shear stress due to torsion

σ_{crit} = critical bending stress

r = inner radius of cylindrical section

t = minimum thickness of laminate in central section

l = length of central section between flanges

E = the lowest of the engineering moduli in longitudinal and circumferential direction of the central section

ν = the lowest of the Poison ratios of the central section.

The equations are valid for r/t > 10.

Combined loading shall be checked according to the following formula:

$$\tau_{crit}/\tau + \sigma_{crit}/\sigma \geq SF$$

where σ and τ refers to the extreme bending stress and extreme torsional stress in the central section.

2 Calculation of stiffness

The torsional and bending stiffnesses of a shaft and the relevant stiffness parameters of a coupling shall be calculated by the same analytical approach as specified in [1]. The variability in the modulus of the material shall be included in a conservative way in the analysis.

3 Fatigue strength

Torsion:

The fatigue strength of the drive shaft(s)/flexible coupling(s) w.r.t. to torsion shall be demonstrated based on the chosen safety factors (SF) in the design as specified in [1]. Procedures for calculation of the fatigue strength of the drive shaft/ flexible coupling design(s) included in the type approval certificate shall be based on generally accepted principles and they shall be submitted as part of the type approval documentation.

SF ≥ 4.0; for designs w.r.t. fibre failure, design against torsion fatigue will normally not be required.

3.0 ≤ SF < 4.0; for designs w.r.t. fibre failure , documentation of the torsion fatigue properties (for torsion in any part of the drive shaft/flexible coupling) including the slope "m" of the fatigue curve of the material will be required. "m" shall exceed 12.

For fatigue w.r.t. other load conditions (e.g. deformations in flexible couplings) other requirements apply, see *Other load conditions*.

Requirements to fatigue testing (other than full scale test) are given in Sec.5 [2].

It shall be documented that the slope m of the fatigue curve of the adhesive bond is larger than or equal to m ≥ 7.0.

As an alternative the fatigue strength can be demonstrated by full scale testing according to the procedure specified in Sec.7 [3].

Other load conditions

The fatigue strength w.r.t. other load conditions shall be demonstrated by similar methods as for torsion, except that the provisions based on the level of SF do not apply. For flexible couplings a full fatigue analyses w.r.t. to the relevant allowable misalignments will normally be required. Full scale testing may be required for complicated designs and for designs with a high degree of utilisation. All relevant conditions shall be considered in the analyses, i.e. as a minimum torsion, bending, axial and radial offset and angular misalignment as relevant.

All requirements to fatigue strength is based on the assumption that the residual strength of the drive shaft/flexible coupling will never be lower than 90% of the original value during the drive shaft's/flexible coupling's service life. If the reduction is larger the drive shaft/flexible coupling will be subject to special consideration.

Section 7 Type Testing

1 General

At least one drive shaft/flexible coupling design shall be tested with respect to properties under static torsional load. Fatigue testing shall be carried out as required in the preceding sections. If the bending moment in the shaft is significant testing with bending moments may also be required.

2 Test specimens

At least one test specimen shall be prepared for testing of the static strength. Specimens for fatigue testing shall be prepared as agreed with the Society. The test specimens shall be representative for the normal production. The same materials and fabrication methods as applied in the normal production shall be used when fabricating the specimens. The nominal torque of the specimen(s) for testing shall be at least equal to 30% of the maximum nominal torque included in the range for which the type approval shall apply.

For shafts the length of the central section between the innermost edges of the end flanges shall be at least equal to 3 times the outside diameter of the central section. For particular designs where the length of the component is less than 3 times the diameter the requirement to the length of the specimen may be waived.

The interface between the central section and the end flanges shall be identical in design to normal production shafts. Modifications to the metallic flanges for testing purposes, not affecting the performance of the joint are acceptable.

3 Test under static load

The purpose of the test is to verify that the calculated torsional strength and stiffness of the shaft will be reached in actual production with a certain level of confidence. As a minimum one test shall be carried out.

Instrumentation:

The following instrumentation shall be included:

— equipment for continuously measuring the torque with an uncertainty < 4%

— equipment for continuously measuring the twist between the end flanges with an uncertainty to be agreed in each case

— equipment for continuous (or equivalent) logging of torque and twist.

It is recommended that additional equipment such as e.g. strain gauges are included to gain further information regarding the performance of the shaft and to verify the design calculations.

Test environment:

The test shall be carried out in a temperature within the range $22 \pm 5°C$ and with a relative humidity within the range 35 – 90% unless otherwise agreed.

Test procedure:

The specimen shall be loaded in pure torsion. Four load sequences shall be carried out:

Seq. 1-3: the shaft shall be loaded to peak torque and back to zero torque three times

Seq. 4: the torque shall be increased to failure of the shaft.

In all sequences the torque shall be increased/decreased with a rate not exceeding the nominal torque/60 pr. second.

When the torque exceeds three times the nominal torque sensitive measuring equipment, except the equipment measuring and logging the torque, may be disconnected.

After the test has been completed a graph or graphs over torque vs. twist until failure with adequate resolution and covering all sequences shall be submitted to the Society together with documentation of the location of the failure and the mechanism of the failure.

Acceptance criteria:

The maximum torque recorded during the test, T_{fail}, shall satisfy the following requirement:

$$T_{fail} \geq 1.16 \cdot SF_{max} \cdot \text{Peak torque}$$

Where SF_{max} is equal to the maximum of the safety factors SF specified in Section 6 Table 1.1

If the test result fails to meet the requirement above an additional specimen shall be tested. The mean value of the maximum torques recorded in the two tests shall exceed:

$$1.16 \cdot SF_{max} \cdot \text{Peak torque}$$

No result shall be lower than $SF_{max} \cdot \text{Peak torque}$.

4 Full scale fatigue testing

Full scale fatigue testing shall be carried out when required as specified in Sec.7 [3].

Purpose:

The purpose of the test(s) is to verify the fatigue strength of the shaft and that it will be reached in actual production with a certain level of confidence.

Fatigue test load condition:

The test condition during the fatigue test(s) shall be based on the fatigue load conditions as specified in Sec.2 [3]. A table as shown below shall be established:

Condition	Mean	Amplitude	Range	Cycles
1	M_1	A_1	ΔT_1	N_1
2	M_2	A_2	ΔT_2	N_2
3	M_3	A_3	ΔT_3	N_3
Etc.	Etc.			

where:
M_i = mean torque for condition "i"
A_i = torque amplitude for condition "i"
ΔT_i = equivalent torque range for condition "i"
N_i = number of load cycles for condition "i".

The equivalent torque range is defined for R=0. ΔT_i is calculated according to the following equation:

$$\Delta T_i = 2 \cdot A_i / (1 - M_i/UT + A_i/UT)$$

UT = ultimate torsional strength of the central section as measured in the static test.

Definition of safety margin:
The safety margin applied in the fatigue test is composed of two elements:
1) to account for possible sequence effects from the service fatigue load history
2) to ensure an adequate reliability of the shaft with respect to fatigue failure.

To account for the first requirement the factor F_1 is set to $F_1 = 5$.
To account for the second requirement the factor F_2 is set to $F_2 = 10^{2 \cdot \log(\sigma)}$ where $\log(\sigma)$ is equal to the standard deviation of the logarithm of the fatigue life. In lack of more precise information $\log(\sigma)$ can be set equal to 0.4.
$F1 \cdot F2$ shall not be taken smaller than 32.

Definition of minimum required fatigue curves:
For each condition "i" calculate m_i and C_i according to the following equation:

$$m_i = [\log(N_i)+\log(F_1)+\log(F_2)]/[\log(UT)-\log(\Delta T_i)]$$
$$C_i = UT^{m_i}$$

It is assumed that the fatigue strength of the component can be represented by the following expression (i.e. a linear representation in a log-log-diagram): $N = C \cdot \Delta T^{-m}$.

Determine the required fatigue curve:

$$m = \max_i (m_i)$$
$$C = \max_i (C_i)$$

Fatigue damages:
Calculate the fatigue damage for each condition "i":
$D_i = N_i/C \cdot \Delta T_i^{-m}$
Calculate the total fatigue damage and relative fatigue damages:
Dtotal = $\Sigma_i D_i$ total fatigue damage
$d_i = D_i/D_{total}$ relative fatigue damage for condition "i"

Fatigue test condition:
Determine the fatigue test condition $\Delta T test$ and Ntest such that the following two conditions are satisfied:

$$N_{test} = C \cdot \Delta T_{test}^{-m}/\max_i(\delta_i)$$

$2 \cdot \min_i(A_i) \leq \Delta T_{test} \leq$ torque at onset of matrix cracking

Instrumentation:
The following instrumentation shall be included:
— equipment for continuously measuring the torque with an uncertainty < 5%

— equipment for continuously measuring the twist between the end flanges with an uncertainty to be agreed in each case
— equipment for continuous (or equivalent) logging of torque and twist.
It is recommended that additional equipment such as e.g. strain gauges are included to gain furtherinformation regarding the performance of the shaft and to verify the design calculations.

Test environment
The test shall be carried out in a temperature within the range $22 \pm 5°C$ and with a relative humidity within the range $35 - 90\%$ unless otherwise agreed.

Test procedure
The specimen shall be loaded in pure torsion.
The following sequence shall be followed:
1) the shaft shall be loaded to extreme torque and the load released three times. The torque shall be increased/decreased monotonously with a rate not exceeding the nominal torque/60 pr second
2) the torsional stiffness is measured
3) fatigue test at the following conditions:
range of torque: ΔT_{test}
R-ratio: ≤ 0.05
number of load cycles: the larger of N_{test} or $5 \cdot 10^6$ load cycles, or to failure.
4) the torsional stiffness shall be measured at N_{test}.
During sequence 3 the equipment for measurement of twist may be disconnected.

Acceptance criteria:
In case the number of load cycles to failure $N_{fail} > N_{test}$ the test result is acceptable.
In case the shaft fails at $N_{fail} < N_{test}$ an additional fatigue test shall be carried out. The mean value of the $\log(N_{fail})$ for the two tests shall be larger than $\log(N_{test})$.
In case the shaft fails at a number of load cycles $N_{fail} < N_{test}/10^{2 \cdot \log(\sigma)}$ the test result is unacceptable.

No failure signifies that no failures or damages of any kind are observed on the FRP central section or in the bonds between central sections and end flanges after completion of the test. After completion of the test the bonds on the shaft shall be inspected carefully such that it can be ascertained that no damages to the bonds have occurred. Normally this will mean that the bond have to be cut through the thickness at least 4 locations around the circumference of the bond such that the bond line is exposed for inspection.

Section 8 Documentation required for each delivery

1 Proof testing

All shafts and couplings shall be torque tested to 1.5 times the peak torque before delivery. If adequate QA and QC procedures are available and implemented the requirement to proof testing of some or all of the delivered items may be waived. Such QA and QC procedures and their implementation shall be accepted by the Society prior to start of manufacture.

2 Design documentation

Design analysis as specified in this class programme shall be documented and filed for each design and shall be made available to the Society on request.

3 Requirements to production and quality control arrangement

The manufacturer should have a quality system that meets ISO 9001 standards, or equivalent. If this quality standard is not fulfilled, the extent of type testing and assessments will be specially considered.
The quality control arrangement shall include all activities and parameters relevant for the quality of the end product. As a minimum the following items shall be considered:
— design and calculation procedures and methods
— documentation of design
— control of incoming materials
— test equipment, test methods, test samples and reference to standards used
— fabrication procedures
— cure cycles
— traceability and marking systems
— production logs and test reports.

Section 9 Requirements for marking of product

1 General

The pipes and fittings shall be marked. The marking shall at least include the following information:
— manufacturer's name and/or logo
— type designation
— materials
— size/dimensions
— date of fabrication and/or serial number.
The marking shall be carried out in such a way that it is visible, legible and indelible. The marking of product shall enable traceability to the Society's type approval certificate.

Extrait from DNV-GL Rules

---

iii) Conclusion

The Lloyd's Register's rules and regulations of the shipping registers about the classification of propulsion shafts give valuable information concerning their design and manufacturing. Combined with the rules for the manufacturing, testing and classification of composite materials can become the basic guidelines for the design and manufacturing of composite shafts. On the other hand, the DNV GL class programme for the type approval of "Composite drive shafts and flexible couplings – Non-metallic materials" offers dedicated guidelines for the design, manufacturing and testing of composite shafts.

1.3 Introduction to finite element analysis of composite shafts

In recent years, the development of strong computational packages has opened the road for the simulation of the mechanical behavior of composite materials. The analytical methods available are insufficient in dealing with problems with complex geometries, while the complexity resulting from the interlaced form of the equations causes more problems that have not been solved yet. Additionally, no equations have been devised, that could express all the phenomena taking place in the mechanical behavior of a composite material.

The Finite Element Method (FEM) comes to fill the gap that the insufficiencies of the analytical methods have created. The main difference between the two methods relies on the way that they deal with the structure and the solution procedure that they follow. The classical analytical method considers the structure continuous and its mechanical behavior is described by sectional or continuous common equations. On the other hand, the finite element method is a numerical method for the approach of the behavior of a structure. According to the finite element method, the structure is represented by a number of individual elements that are interconnected with continuity equations. By the solution of these equations, combined with the equilibrium equations of each element, the desired quantities at every point of the structure can be calculated. Consequently, during the solution of a problem with the finite element method, the whole structure is assessed and not a specific part, as the analytical methods do, thus allowing the solution of complex structures. Additionally, the accuracy of the finite element method is satisfactory and often comparable to experimental methods, and depends on the various parameters that are involved during its application. These parameters are defined depending on the desired solution accuracy and speed combination. In general terms, the finite element method combines speed and accuracy and as a result has become a valuable tool for a large number studies (Cook, 1995).

Many commercial programs exist with finite element analysis capabilities for different engineering disciplines. They help solve a variety of problems from simple linear static analysis to nonlinear transient analysis. A few of these codes, such as ANSYS and Abaqus, have special capabilities to analyze composite materials and they accept custom, user-programmed constitutive equations and element formulations. Since these software packages not only provide analysis tools, geometric modeling, and visualization of results, but also they can be integrated in the larger design, production, and product life-cycle process, they are often called complete analysis environments or computer aided engineering (CAE) systems (Barbero, 2013).

Modern finite element analysis (FEA) software are commonly organized into three blocks: the pre-processor, the processor, and the post-processor. In the preprocessor, the model is built defining the geometry, material properties, and element type. Also, loads and boundary conditions are entered in the pre-processor, but they may also be entered during the solution phase. With this information, the processor can compute the stiffness matrix and the force vector. Next, the algebraic equations are solved and the solution is obtained in the form of displacement values. In the last block- the post-processor-derived results, such as stress, strain, and failure ratios, are computed. The solution can be reviewed using graphic tools.

The first requirement of the model is the geometry. Then, material properties are given for the various parts that make up the geometry. Next, loads and boundary conditions are applied on the geometry. Next, the geometry is discretized into elements, which are defined in terms of the

51

nodes and element connectivity. The element type is chosen to represent the type of problem to be solved. Next, the model is solved. Finally, derived results are computed and visualized.

All the aforementioned steps are extensively discussed in the modelling of the GFRP shaft in the following chapter. At this point only the ANSYS Element Types used will be presented.

For thin cylidrical structures, with thickness to diameter ratios under 5%, Shell Elements give quite good results and effectively reduce computing cost in comparison to Solid Elements. In this study SHELL281and SOLID186 Elements were used, both of which support layered modelling, which is essential in modelling composite shafts and layered composite materials in general.

SHELL281 is an 8-Node Structural Shell Element which is suitable for analyzing thin to moderately-thick shell structures. It is well-suited for linear, large rotation, and/or large strain nonlinear applications. SHELL281 may be used for layered applications for modeling composite shells or sandwich construction. The accuracy in modeling composite shells is governed by the first-order shear-deformation theory (usually referred to as Mindlin-Reissner shell theory). The element formulation is based on logarithmic strain and true stress measures. The element kinematics allow for finite membrane strains (stretching). However, the curvature changes within a time increment are assumed to be small.
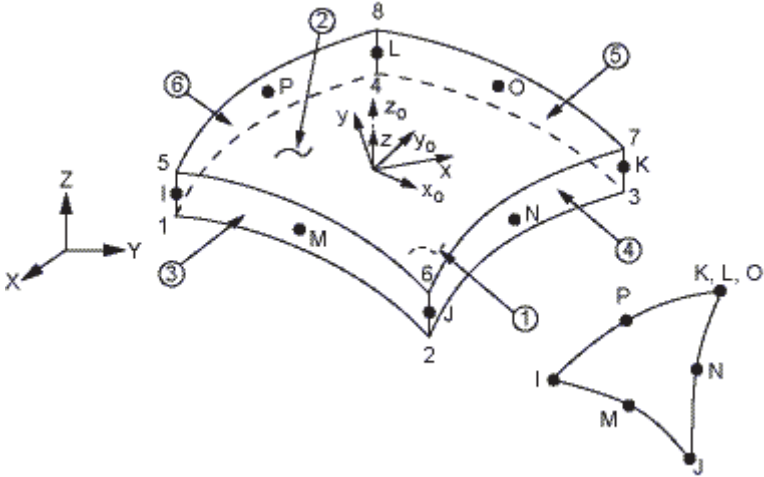
x_o = Element x-axis if element orientation is not provided.
x = Element x-axis if element orientation is provided.

Figure 1.15: SHELL281 Geometry

SOLID186 is a higher order 3-D 20-node solid element that exhibits quadratic displacement behavior. The element is defined by 20 nodes having three degrees of freedom per node: translations in the nodal x, y, and z directions. The element supports plasticity, hyperelasticity, creep, stress stiffening, large deflection, and large strain capabilities. SOLID186 Layered Structural Solid is used to model layered thick shells or solids. The layered section definition is given by ANSYS section (SEC*xxx*) commands. A prism degeneration option is also available.
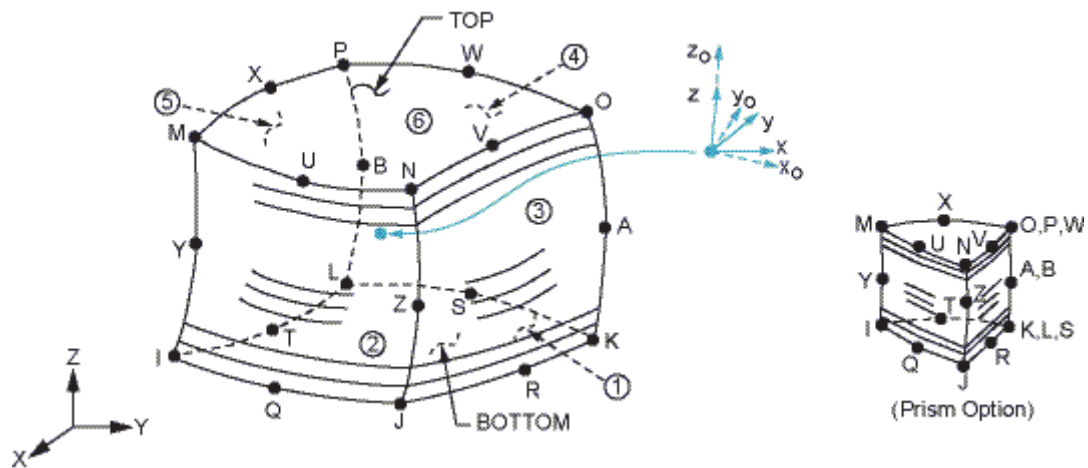
x_o = Element x-axis if ESYS is not supplied.
x = Element x-axis if ESYS is supplied.

Figure 1.16: SOLID186 Layered Structural Solid Geometry

Depending on the shell or solid modeling decision, the geometry of the shaft is created by defining either cylindrical areas or volumes. After the creation of the geometry, the mesh is defined, which in turn defines the size, the shape and the orientation of the elements. The orientation of the elements, the element coordinate system as it is also referred, is very critical in the modelling of layered elements as they use the x-axis of the element coordinate system as the basic axis from which to rotate each layer to the layer coordinate system. The layers are rotated by the angles input on the **SECDATA** or **RMORE** commands. Material properties, stresses, and strains for layered elements are based on the layer coordinate system, not the element coordinate system.

1.4 Objectives of the diploma thesis

The purpose of this diploma thesis is the study of the mechanical behavior of composite shafts utilizing Finite Element Analysis.

As composite shafts are gaining ground over steel shafts in various fields such as the transportation and the marine industries, the knowledge of their mechanical behavior becomes of a greater importance. High strength, light weight, flexibility, fatigue and corrosion resistance are the main advantages that are promoting composite shafts in the marine sector.

However, the efficient design of composite shafts remains an issue, which finds its roots in the general problem of understanding composite material mechanical behavior and their failure modes and mechanisms, due to their anisotropic nature. Consequently, the failure mode of shafts is hard to determine. Designing a composite shaft, requires not only the design of the geometry but also the design of the material itself, considering that there are numerous matrix-fiber-layup combinations, each one of which leads to a different structural response of the shaft.

The evolution of simulation programs using the Finite Element Method (FEM) like ANSYS, made possible the modeling and the analysis of composite shafts. Today, shipping registers like DNV-GL require finite element analysis of composite shafts in order to provide classification.

In order to provide a solution to the aforementioned needs, finite element models are developed for the simulation of the mechanical response of composite shafts. Additionally, the most dominant failure mode is determined, giving valuable information about the needed reinforcement of the structure. The parameters affecting the structural response are also investigated allowing the future design-cost optimization. Various modelling methods (shell, solid, homogeneous) are applied in order to determine the most appropriate for the modelling of composite shafts. The calibration and validation of the finite element models is pursued through the comparison with experimental data acquired from the industry and by a torsion test conducted for the needs of this thesis by the Shipbuilding Technology Laboratory (STL - NTUA) in cooperation with B&T Composites.

Shipbuilding Technology Laboratory's main motivation is to deal with composite shaft applications and obtain significant knowledge on a topic in which there is no prior experience, improving at the same time the already existing knowledge in composite material testing and composites numerical modelling.

CHAPTER 2
FINITE ELEMENT ANALYSIS OF THE GFRP SHAFT

2.1 Introduction

2.1.1 GFRP shaft specifications

The Glass Fiber Reinforced Polymer (GFRP) shaft is a wind turbine power shaft that was manufactured by the composite manufacturing company B&T Composites in Florina, Greece (http://www.btcomposites.gr/). The manufacturing method was filament winding, its main dimensions are presented in Table 2.1 and its design in Figures 2.1 and 2.2:

Table 2.1. Dimensions of the Shaft

Length (m)	Internal diameter (m)	External Diameter (m)	Thickness (m)	Winding Pattern
0.862	0.250	0.260	0.005	$[\pm45]_{12}$

The shaft was designed to transfer torque up to 120kNm but during a torsion test carried out by CENTA (http://www.centa.info/), it failed at a torque of 61.12kNm. More information about the test are given in section 2.1.2.

The aim of this work is to develop a Finite Element Model of the shaft using ANSYS that will predict its mechanical behavior. Three different models were created. A layered shell model, a homogeneous shell model and a layered solid model.
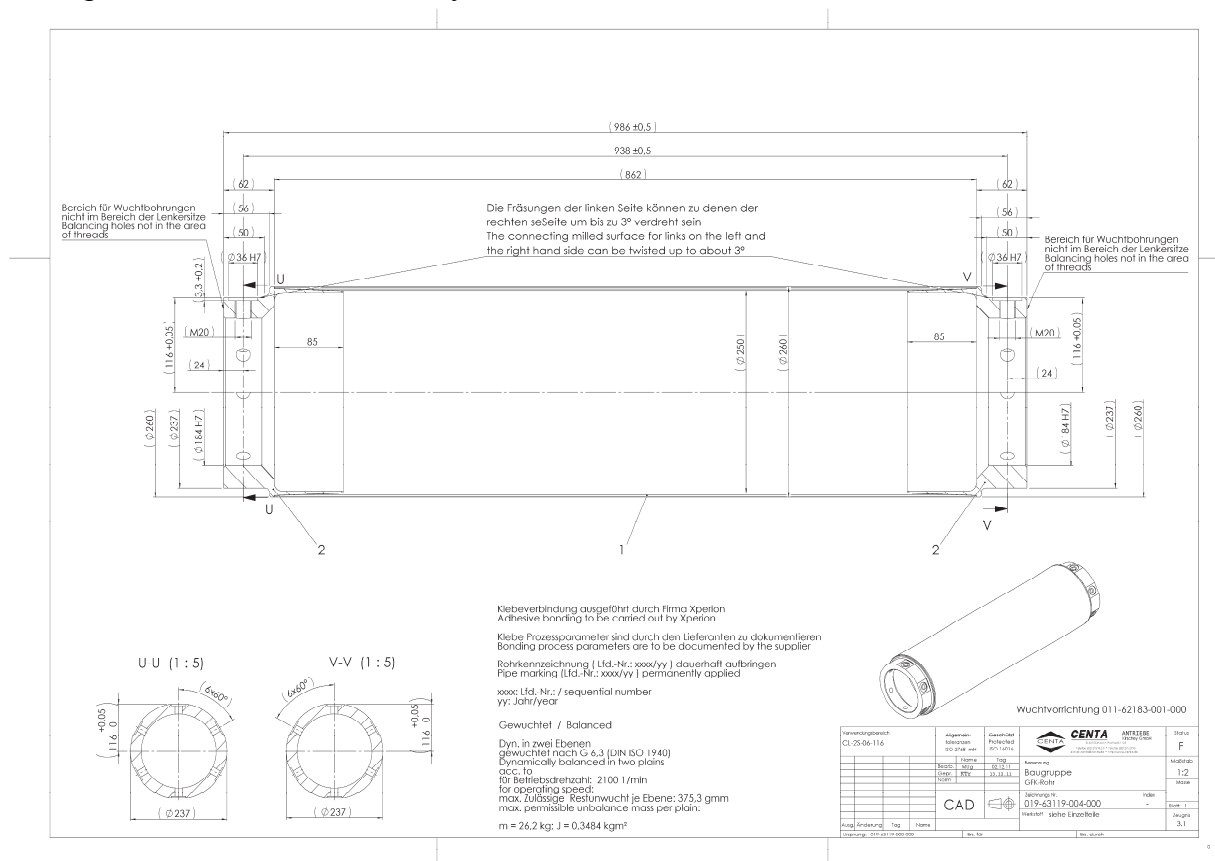

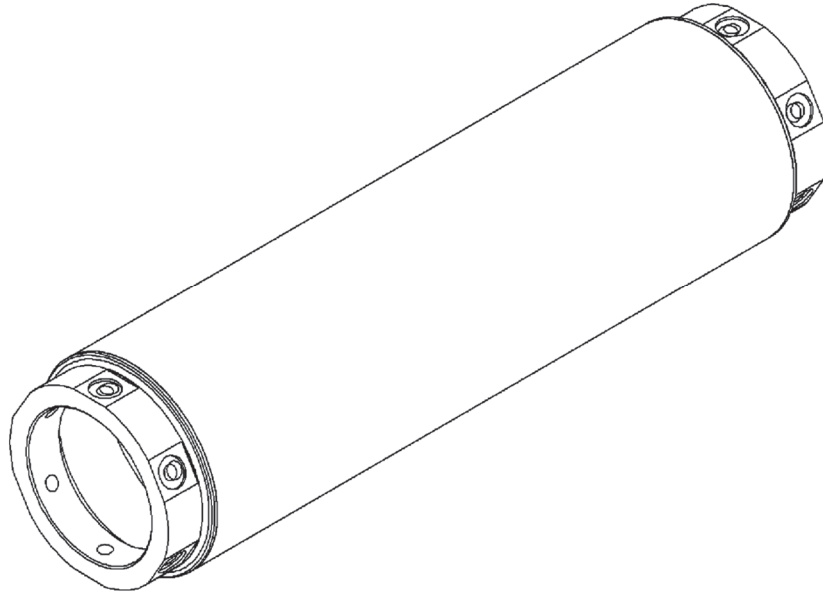Fig. 2.1. Construction plan of the shaft

Fig. 2.2. Isometric view of the shaft

According to the manufacturer, the fiber system is the 1062 Multi-End Roving from PPG Fiber Glass (www.ppgfiberglass.com) and the epoxy matrix system is the Araldite LY 556 epoxy resin combined with Aradur 917 anhydride hardener and imidazole Accelerator DY 070 from Huntsman Advanced Materials (www.huntsman.com/advanced_materials). The shaft was manufactured under constant temperature and humidity (18°C/48% humidity) and was polymerized in a polymerization oven for 1 hour at 90°C and 2 hours at 150°C. Additionally, the couplings were bonded to the shaft according to their manufacturer's specifications.

The mechanical properties of the composite material were provided by B&T Composites, based on literature information, and are the following:

$$E_1 = \quad 37.04 \quad \text{GPa}$$
$$E_2 = \quad 15.04 \quad \text{GPa}$$
$$G_{12} = \quad 5.5 \quad \quad \text{GPa}$$
$$v_{12} = \quad 0.28$$

The rest mechanical properties required for the modelling were assumed based on literature information (Christensen, 1979) and (Jones, 1975) and the experimental data of the Shipbuilding Technology Laboratory(NTUA).

$$E_3 = E_2 = 15.04 \text{ GPa} \tag{2.1a}$$

$$G_{13} = G_{12} = 5.5 \text{ GPa} \tag{2.1b}$$

$$G_{23} = 0.5 G_{12} = 2.75 \text{ GPa} \tag{2.1c}$$

$$v_{21} = v_{12} \frac{E_2}{E_1} = 0.113 \tag{2.1d}$$

$$v_{23} = v_{12} \frac{1 - v_{21}}{1 - v_{12}} = 0.3447 \tag{2.1e}$$

$$v_{13} = v_{12} = 0.28 \tag{2.1f}$$

All the mechanical properties are summed in table 2.2.

Table 2.2. Mechanical Properties of the GFRP

E_1 (GPa)	37.04
E_2 (GPa)	15.04
E_3 (GPa)	15.04
G_{12} (GPa)	5.5
G_{23} (GPa)	2.75
G_{13} (GPa)	5.5
ν_{12}	0.28
ν_{23}	0.3447
ν_{13}	0.28

2.1.2 Torsion test of the GFRP shaft

The experimental data that were given by Centa are the Moment vs Rotation diagram from the test of the shaft, presented in Figure 2.3, as well as the minimum and maximum values of Torque and Angle that are presented in table 2.3. Angle represents the angle of rotation of the rotating end of the shaft with respect to the other, fixed end. The duration of the test was 1min and 29seconds as indicated in the test report.
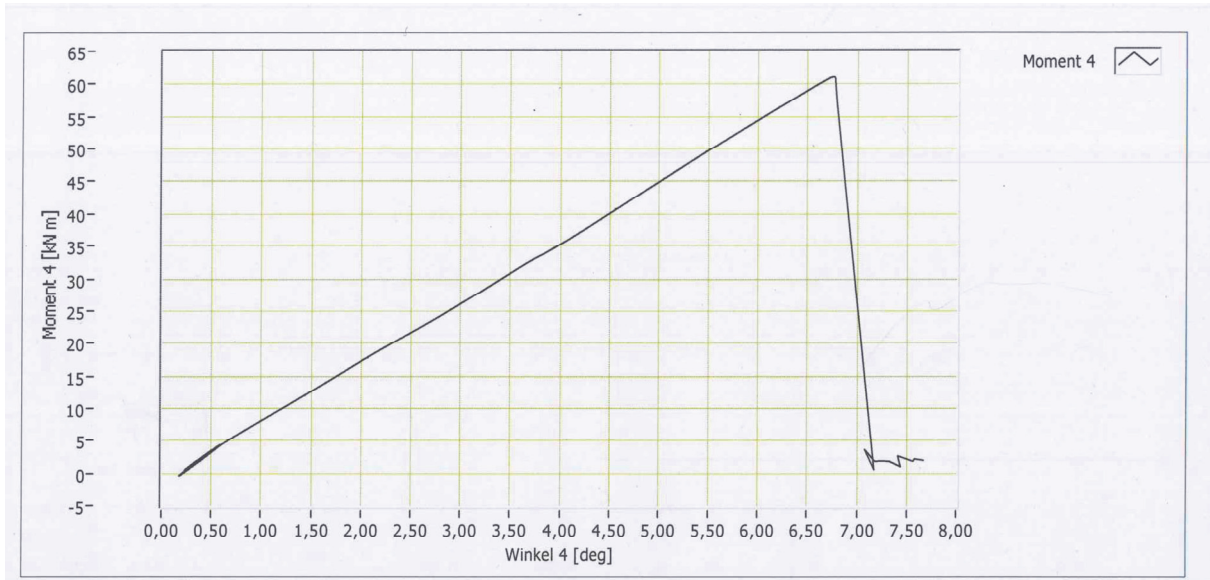
Fig. 2.3. Torque (Moment) to Rotation diagram from the test of the shaft.

Table 2.3. Experimental Results

Starting Angle (deg)	Maximum Angle (deg)	Failure Angle (deg)	Starting Torque (kNm)	Maximum Torque (kNm)
0.22	7.67	6.8	0	61.12

It must be noted that only the failure angle was extracted from the diagram, whereas the rest of the remaining values were given by the experimental report.

2.2 Layered Shell Modelling of the GFRP Shaft

The first Finite Element Modeling approach is a layered shell model of the shaft. Layered shell elements were used because the shaft is relatively thin, as its thickness to diameter ratio is 2%. The element type used is the 8-node structural shell element, SHELL281.

The developed ANSYS model implements both eigenvalue buckling analysis and nonlinear buckling analysis. There is a connection between the two, as the modeshapes of the eigenvalue buckling analysis are used as a pattern for the initial imperfections that are necessary for triggering nonlinear buckling at the latter. That is the reason for describing the model as a whole in the following sections 2.2.1 and 2.2.2. The APDL code of the model is available in appendix A. In the next sections, the results of both analyses are discussed and factors affecting these results, like for example material properties etc., are investigated.

2.2.1 Preprocessing

Before beginning preprocessing, the working directory, the naming of the files created by ANSYS and the title of the analysis were defined. ANSYS graphics were set to full in order to include all element results values (interior and surface), but this affects post-processing.

```
/CWD,'C:\Users\ibil\Desktop\Shaft\bntglass\shell1'
/FILNAME,bntglassnlshell281,1
/TITLE, bntglassnlshell281
/graphics,full    !powergraphics off
```

The next step was the creation of the geometry of the Shaft. In the first lines of the code all necessary parameters were defined. The decision was taken to model the part of the shaft between its metal couplings, in order to avoid modelling the interaction between Steel and GFRP, without altering the problem.

```
/prep7            ! Enter the preprocessor
!* --------
!* GEOMETRY
!* --------
/units,si         ! Unit System SI
*SET,L,0.692      ! Length in m
*SET,Di,0.250     ! Internal diameter in m
*SET,t,0.005      ! Thickness in m
*SET,R,Di/2       ! Internal radius
*SET,Do,Di+(2*t)  ! External diameter
*SET,pi,acos(-1)  ! Set the Value of pi
```

Then, the geometry was defined by creating 2 circles and connecting them with four lines, one for each quadrant, as it can be seen in Figure 2.4, and finally the cylindrical surface/area was created between the created lines, as it is displayed in fig 2.5.

```
!*---------------
!*DEFINE GEOMETRY
!*---------------
k,1,0,0,0              ! define keypoints
k,2,0,R,0
k,3,L,0,0,0
k,4,L,R,0,0
```

```
circle,1,R,3,2,360,4 ! create cicrles
circle,3,R,1,4,360,4

l,6,12                 ! create lines
l,7,11
l,8,10
l,5,9

csys,6                 ! activate a cylindrical coordinate system along the
                       ! main x-axis

al,9,1,12,8            ! create area from lines
al,10,2,9,7
al,11,3,10,6
al,12,4,11,5
```

It is necessary to underline that the line sequence, used in the aforementioned `al,,,,` commands, defines the orientation of the element coordinate system, following the right hand rule. The chosen sequence gives the desired element coordinate system orientation, with the z-axis directed from the inner to the outer surface of the shaft.
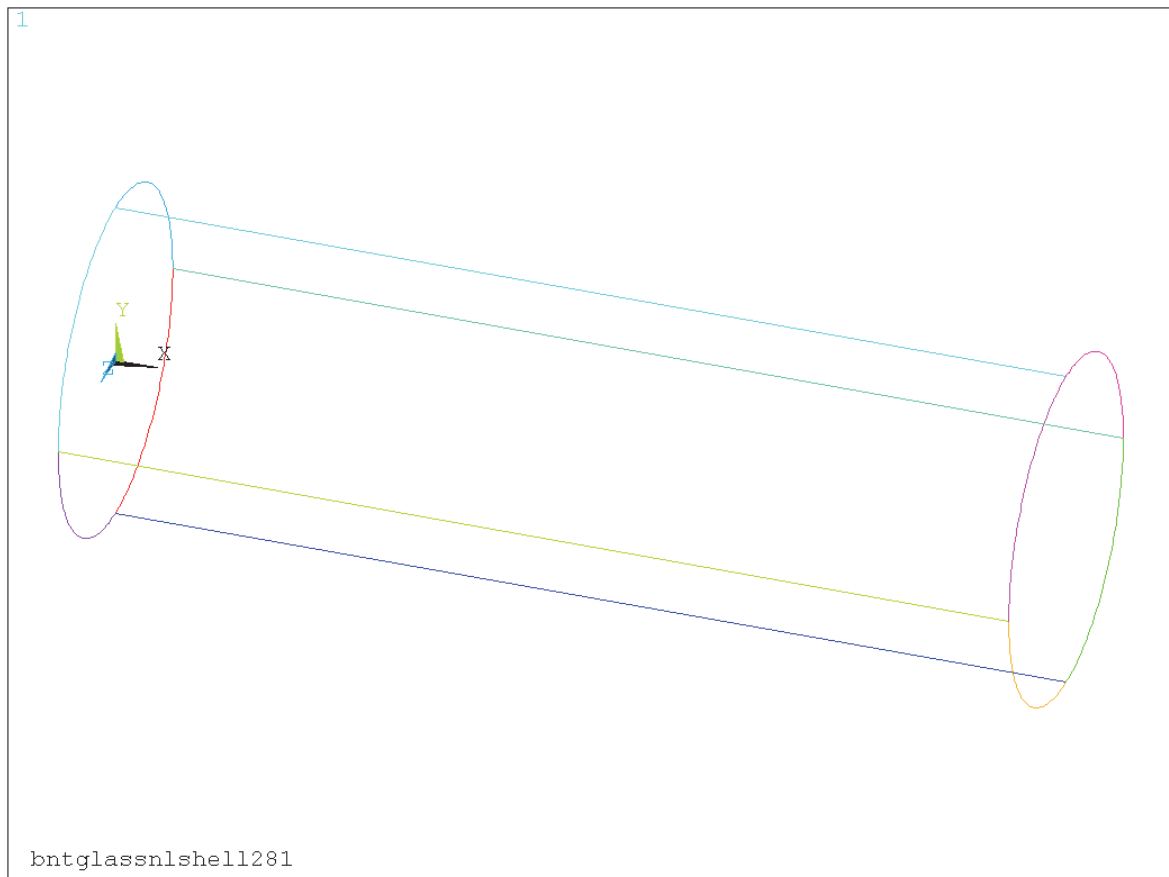
Fig. 2.4. Plot of the lines that were used to create the areas.
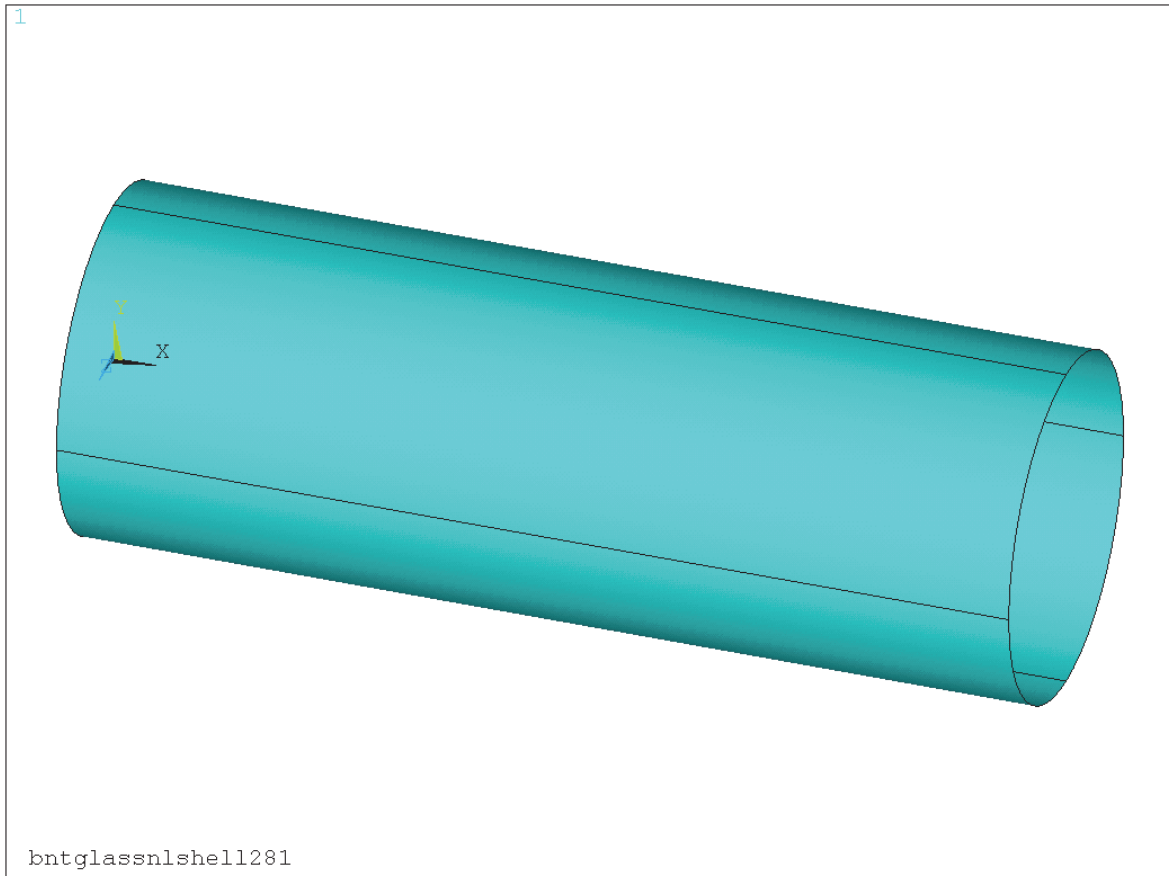
Fig. 2.5. Plot of the final geometry.

After the creation of the geometry, the element type and its key-options were defined, as well as the material properties. As it is mentioned earlier, the chosen element type is SHELL281 and the material properties are all listed in table 2.2.

```
!* --------
!* ELEMENTS
!* --------
ET,1,SHELL281 !Define element type
ESYS,0        !Set the element coordinate system to global cartesian
!*
KEYOPT,1,1,0  !Element has both bending and membrane stiffness (default)
KEYOPT,1,8,2  !Store data for TOP, BOTTOM, and MID for all layers
KEYOPT,1,9,0  !No user subroutine to provide initial thickness (default)


!*--------------------
!* MATERIAL PROPERTIES
!*--------------------
MP,EX,1,37.04*1e9
MP,EY,1,15.04*1e9
MP,EZ,1,15.04*1e9
MP,PRXY,1,0.28
MP,PRYZ,1,0.3447
MP,PRXZ,1,0.28
MP,GXY,1,5.5*1e9
MP,GYZ,1,2.75*1e9
MP,GXZ,1,5.5*1e9
```

60

In order to define multilayer SHELL281 elements the shell section commands were used. As it is already mentioned in section 1.3, there are options available for specifying the thickness, material, orientation, and number of integration points through the thickness of the layers and are defined in this order by the SECDATA command. The command SECTYPE, that defines the type of the section, and SECOFFSET, that defines the starting point of the section were also used. Figure 2.6 shows the defined stacking sequence.

```
!* --------
!* SECTIONS
!* --------
*SET,NL , 12       !* Number of layers
*SET,tl , t/NL     !* Thickness of the layer
*SET,wangle , 45   !* Winding Angle
sectype,1,shell    !Defines the type of the section as shell
secoffset,bot      !Starts the layup from the bottom of the section

!Stacking Sequence
![+-45]12
*do,Layer,1,NL,1
   secdata,tl,1, wangle,3 !Defines the data describing the geometry of a
   wangle=-wangle         !section.
*enddo
```
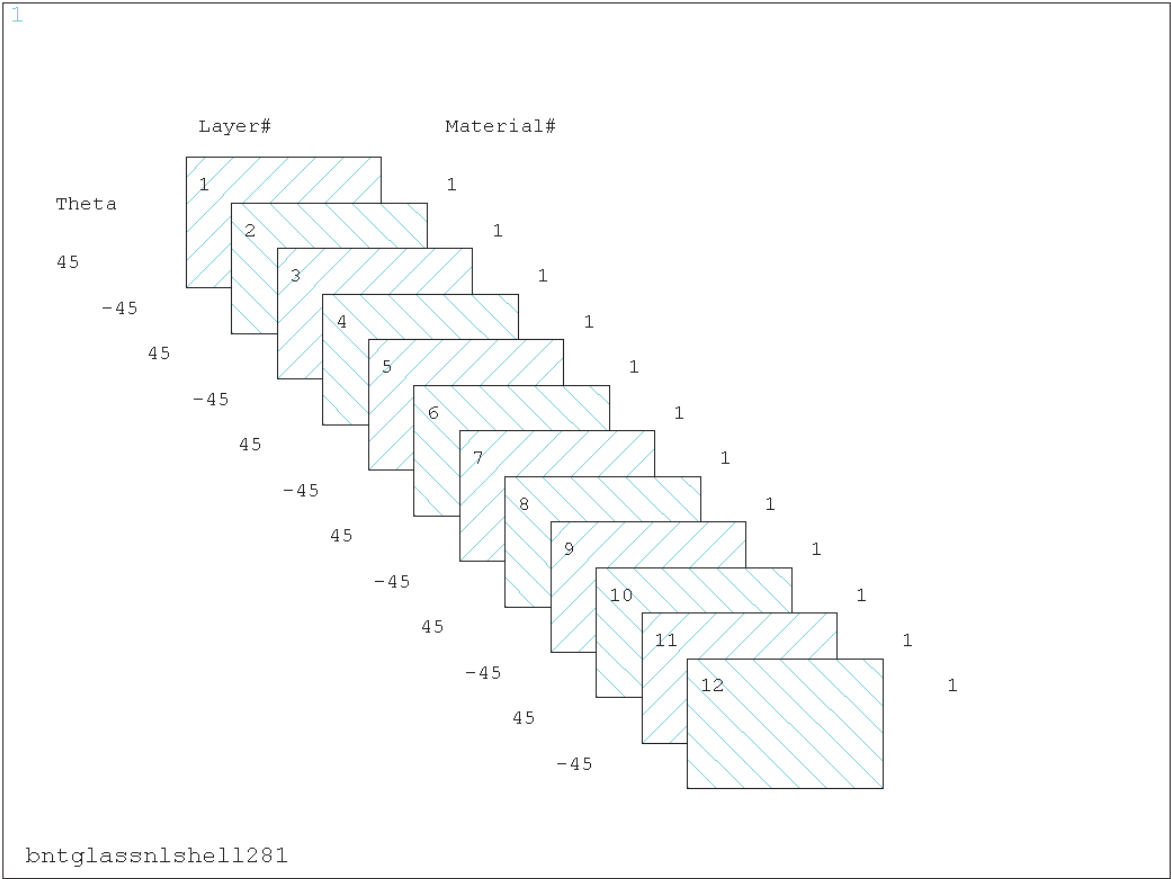

Fig. 2.6 Stacking Sequence of the Composite Material

The next task is the definition and creation of the mesh. Two parameters A and C are introduced defining the desired mesh density. The length of the shaft is divided by A and each quadrant of the circular edge by C. The aim is to create square or almost square elements. In order to achieve

61

this, the ratios *Le=length/A* and *Ce=perimeter/(4·C)*, that correspond to the element length and width, must be almost equal. For the construction of the element mesh, an initial convergence analysis was carried out, resulting in selecting 60 equal length elements along the cylinder longitudinal axis and 64 along the circumference of the cylinder. This results in a mesh of 3840 Elements, with 0.0115m side length. Further comment on convergence analysis is done later in this study, in section 2.2.4. Figure 2.7 represents the meshed geometry.

```
!* ---------------
!* MESH DEFINITION
!* ---------------
*SET,A , 60          ! Axial line mesh
*SET,C , 16          ! Circumferential Quadrant mesh

!Longitudinal Lines
lesize,9 ,,,A,,,,,1 !Specifies the divisions and spacing ratio on unmeshed
lesize,10,,,A,,,,,1 !lines.
lesize,12,,,A,,,,,1
lesize,11,,,A,,,,,1
!Circumferential Lines
lesize,1,,,C,,,,,1
lesize,2,,,C,,,,,1
lesize,3,,,C,,,,,1
lesize,4,,,C,,,,,1
lesize,5,,,C,,,,,1
lesize,6,,,C,,,,,1
lesize,7,,,C,,,,,1
lesize,8,,,C,,,,,1
amesh,1,4,1 !area mesh
```
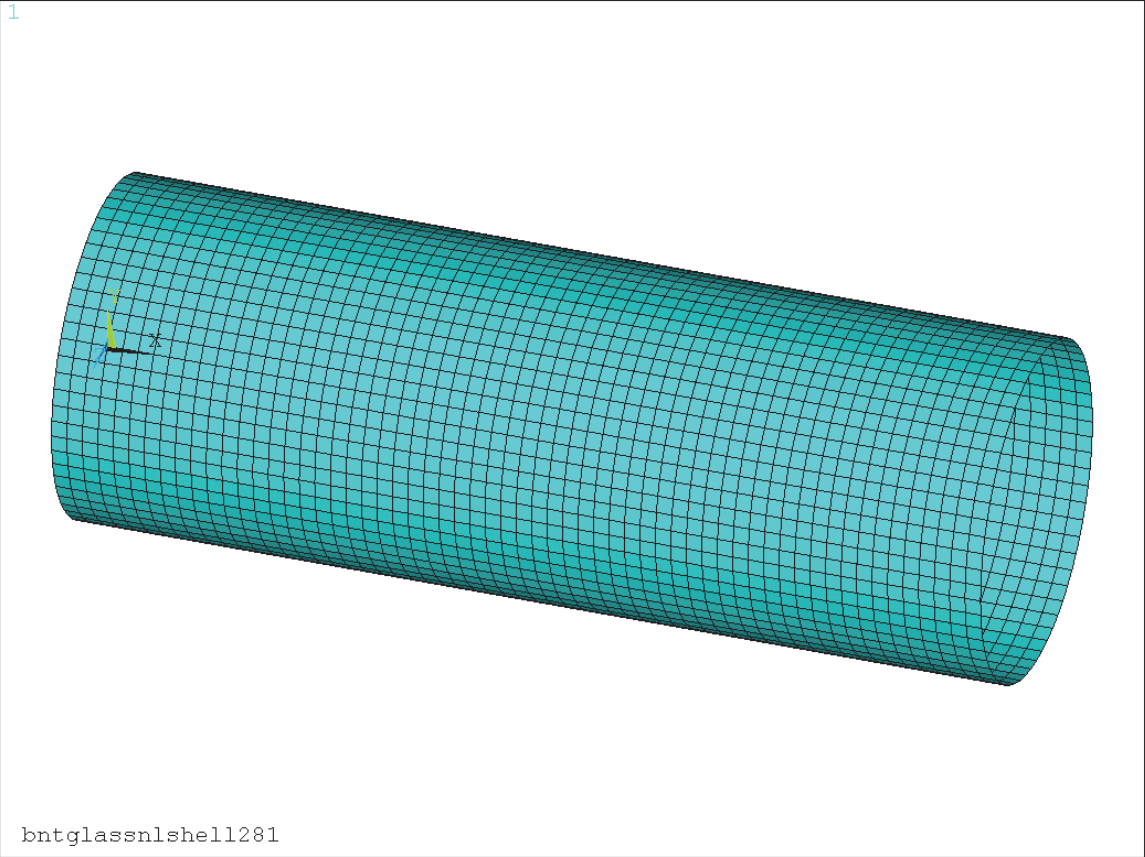

Fig. 2.7. Plot of the meshed geometry.

For the application of the torque to the shaft, Multipoint Constraint elements were used. They were set to behave like rigid beams and they connected all nodes at the circumference of the one end with a master node at the center of the circular end, as shown in Fig. 2.8. This resulted in the creation of 128 MPC Elements and now the total Elements number is 3968.

```
!*-------------------------------------------
!*Creation of master node and mpc184 elements
!*-------------------------------------------
et,2,184      !Defines Element Type mpc184
keyopt,2,1,1 !Element Behaviour, K1=1 Rigid Beam, K2=1 Lagrange Multiplier
             !Method
nsel,all
csys,6
*get,nmpc,node,0,num,max  !Get the maximum node number and store it in nmpc
                          !parameter
*set,nmpc,nmpc+1          !Set parameter nmpc=nmpc+1
n,nmpc,0,0,L+0.02         !Create the master node
type,2                    !Set the Element Type to mpc184
nsel,s,loc,z,L            !Select all the nodes at the end of the shaft
*get,nnum,node,0,count    !Count the number of the nodes at the end
*get,ND,node,0,num,min    !Get the minimum node number at the end and store
                          !it in ND parameter

*do,i,1,nnum              !Loop for the creation of the MPC184
E,nmpc,ND                 !Create the element from nodes nmpc and ND
*SET,ND,NDNEXT(ND)        !Set ND to the next node number
*enddo
```
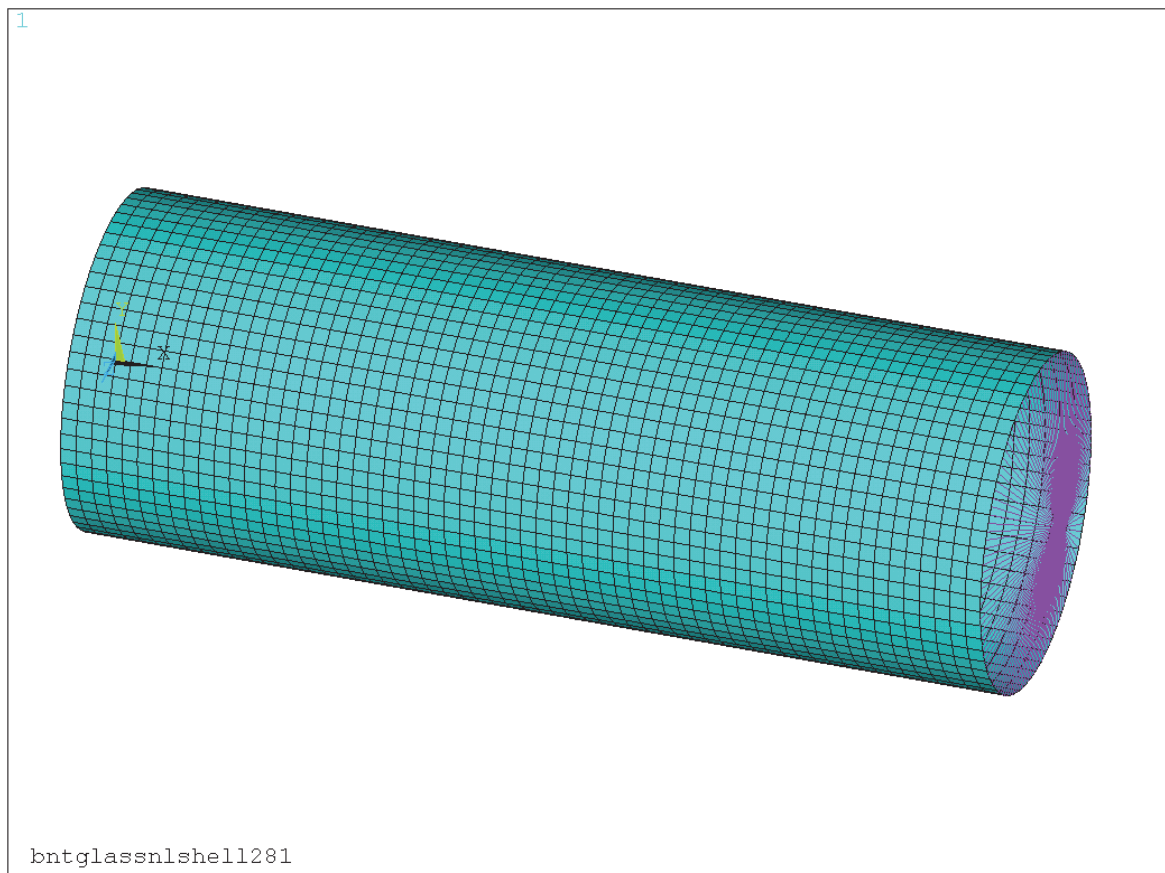

Fig. 2.8. Plot showing the MPC184 Elements.

63

The torque was applied to the master node and transferred through the MPC184 elements to the rest of the shaft. The master node was also constrained and allowed only to rotate around the x-axis. The other end of the shaft was considered fully fixed, by constraining all degrees of freedom (DOFs) of all its nodes. All loads and constraints are shown in Figure. 2.9

```
!* -------------------
!* LOADS & CONSTRAINTS
!* -------------------
!Constraints on the fixed edge
Allsel            !Select everything
csys,0            !Set the active coordinate system to Global Cartesian
nsel,s,loc,x,0    !Select all nodes of the left end
d,all,all,0       !Constrain all degrees of freedom
nsel,all          !Select all Nodes
!* --------
!* LOADS
!* --------
*SET,P , 120000   !Set the Torque to 120 kNm, which is equal to the required
                  !strength of the shaft
!Torque
F,nmpc,MX,-P      !Apply the torque on the Master node
!Constraints on the master node
csys,0
D,nmpc,ux,0
D,nmpc,uy,0
D,nmpc,uz,0
D,nmpc,roty,0
D,nmpc,rotz,0
FINISH
```
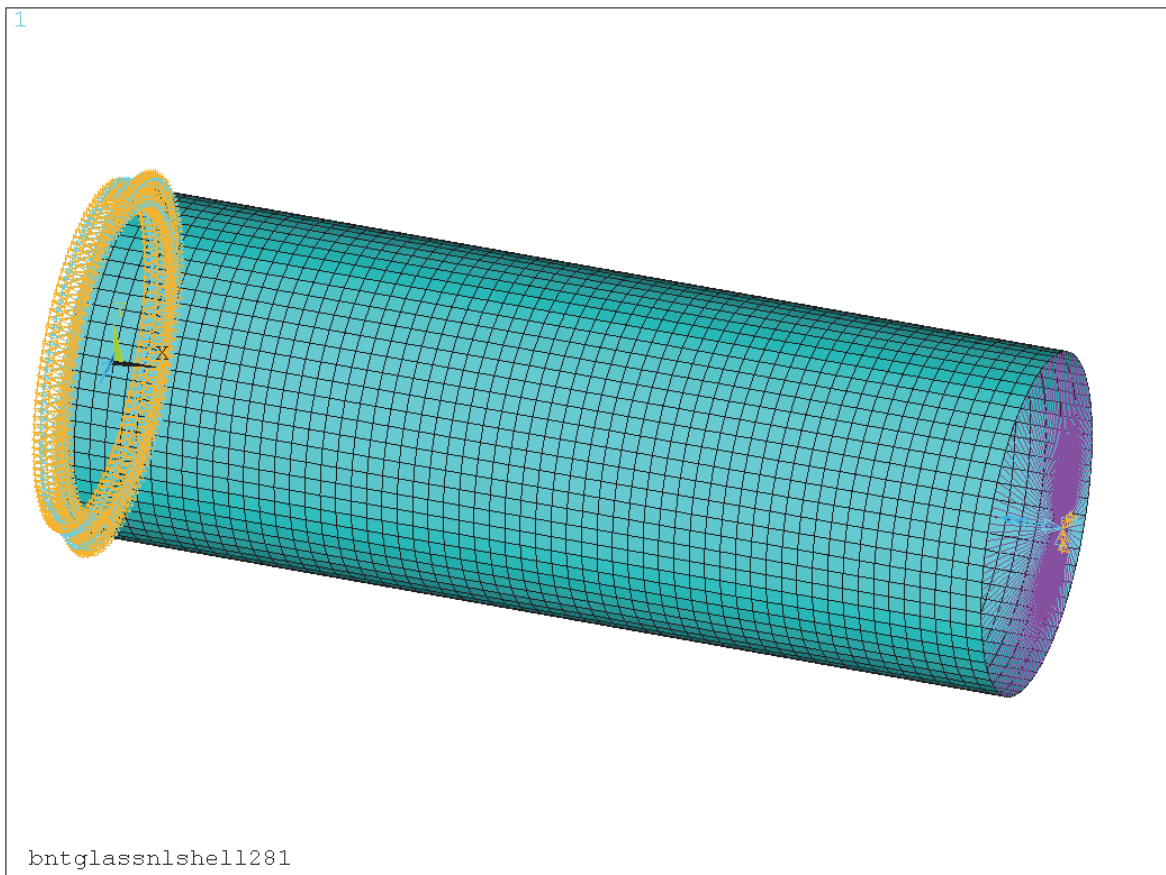

Fig. 2.9. Plot of the shaft with its boundary conditions and the torque applied on the master node.

2.2.2 Solution

The expected failure mode of the shaft is rotational buckling. ANSYS offers the solution of Eigenvalue Buckling Analysis which predicts the theoretical buckling strength of an ideal linear elastic structure. A more accurate solution for the current application is the nonlinear buckling analysis because it employs non-linear, large-deflection, static analysis to predict buckling loads. Its mode of operation is very simple: it gradually increases the applied load until a load level is found whereby the structure becomes unstable (ie. suddenly a very small increase in the load will cause very large deflections). The true non-linear nature of this analysis thus permits the modeling of geometric imperfections and material nonlinearities. For this type of analysis, note that geometric imperfections are necessary to initiate the desired buckling mode. (ANSYS Documentation, Chapter 7.1. Types of Buckling Analyses)

Eigenvalue Buckling Analysis

Concerning eigenvalue buckling analysis, a random value of torque needs to be applied for the calculation of the eigenvalue buckling load. In the current analysis the applied torque is 120kNm, as it was mentioned in the previous section, and the buckling loads of the first 10 modeshapes are calculated. The lowest of the calculated buckling loads and the corresponding modeshape are the critical. A linear static solution is necessary prior to the eigenvalue buckling analysis.

```
!*--------
!*SOLUTION
!*--------

!FIRST STEP

!Linear Static Solution
/SOL
ANTYPE,STATIC          !Analysis Type: Static Analysis
NLGEOM,OFF             !Large deflection effects OFF

allsell
OUTRES,ERASE           !Resets OUTRES specifications to their default
                       !values.
OUTRES,ALL,ALL         !Writes all solution items for every substep.
SOLVE
FINISH

!Eigenvalue Buckling Analysis
/SOLU
OUTRES,ALL,ALL
ANTYPE,1                    !Analysis type: Eigenvalue Buckling Analysis.
BUCOPT,LANB,10,0,1,CENTER !Specifies buckling analysis options.
                           !10 Mode Shapes Extracted
SOLVE
FINISH

!Expansion Pass
/SOLU
!*
EXPASS,1
MXPAND,10,0,0,1,,          !Expand the 10 modes of the Buckling Analysis
SOLVE
FINISH
```

After the eigenvalue buckling analysis, the general post-processing menu is entered in order to review and assess how realistic the buckling mode shapes of the shaft and the buckling loads are. The magnitude of the displacements is also taken into account, in order to calculate the factor that will produce the desired initial geometric imperfections necessary for the nonlinear buckling analysis.

The results of the eigenvalue buckling analysis are listed in table 2.4. The buckling loads are the product of the applied torque (120kNm) multiplied by the eigenvalue buckling factor. All eigenvalue buckling factors are double which implies that the structure can buckle at the same load with a similar mode shape. After reviewing the double mode shapes, it is obvious that they are exactly the same in terms of magnitude of displacement and pattern but they differ in the angular position of their crests and troughs. In simple terms, they look like the same mode shape rotated around the x-axis. All mode shapes depict only one crest along the longitudinal direction. However, along the circumference of the shaft the number of crests varies

The critical (minimum) eigenvalue buckling load, as calculated by this analysis, is **65.4kNm**. It is 7% higher than the experimental failure load of the shaft. These results are listed in table 2.4 in bold. The results of the eigenvalue buckling analysis also indicate that at the critical load the shaft buckles in mode-shape 4 deformation of the structure, meaning that 4 crests are formed around the circumference of the shaft. Along the axial direction of the shaft there is only one crest, as it can be seen in Figure 2.10.

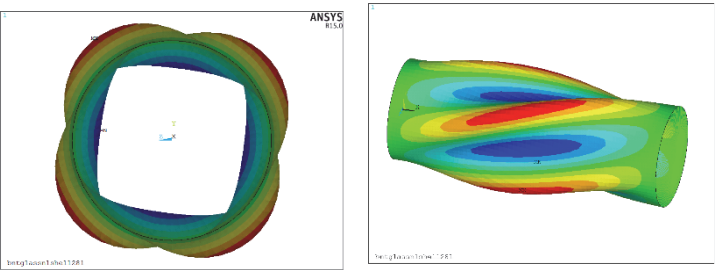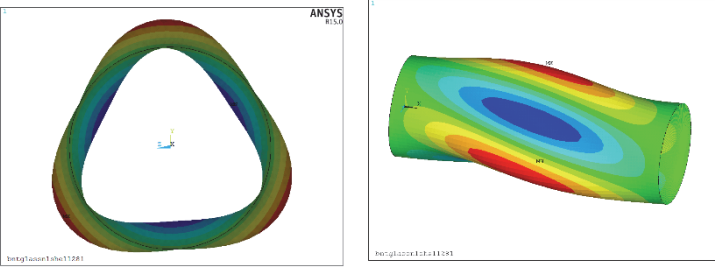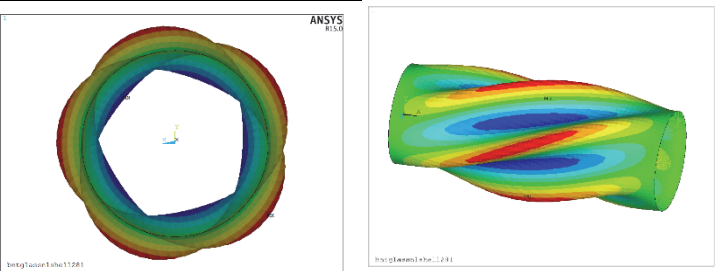Table 2.4. Results of the eigenvalue buckling analysis

Buckling load (kNm)		Buckling modeshape	
65.4	**mode 4**		
65.4	mode 4		
-66.2	mode 4		
-66.2	mode 4		
72.2	mode 3		
72.2	mode 3		
-73.1	mode 3		
-73.1	mode 3		
80.3	mode 5		
80.3	mode 5		

Figure 2.10 represents the buckled shaft with its radial displacements at the critical buckling load. The coloring represents the magnitude of the nodal radial displacement, with red representing the maximum(outwards) and blue representing the minimum(inwards) displacements.
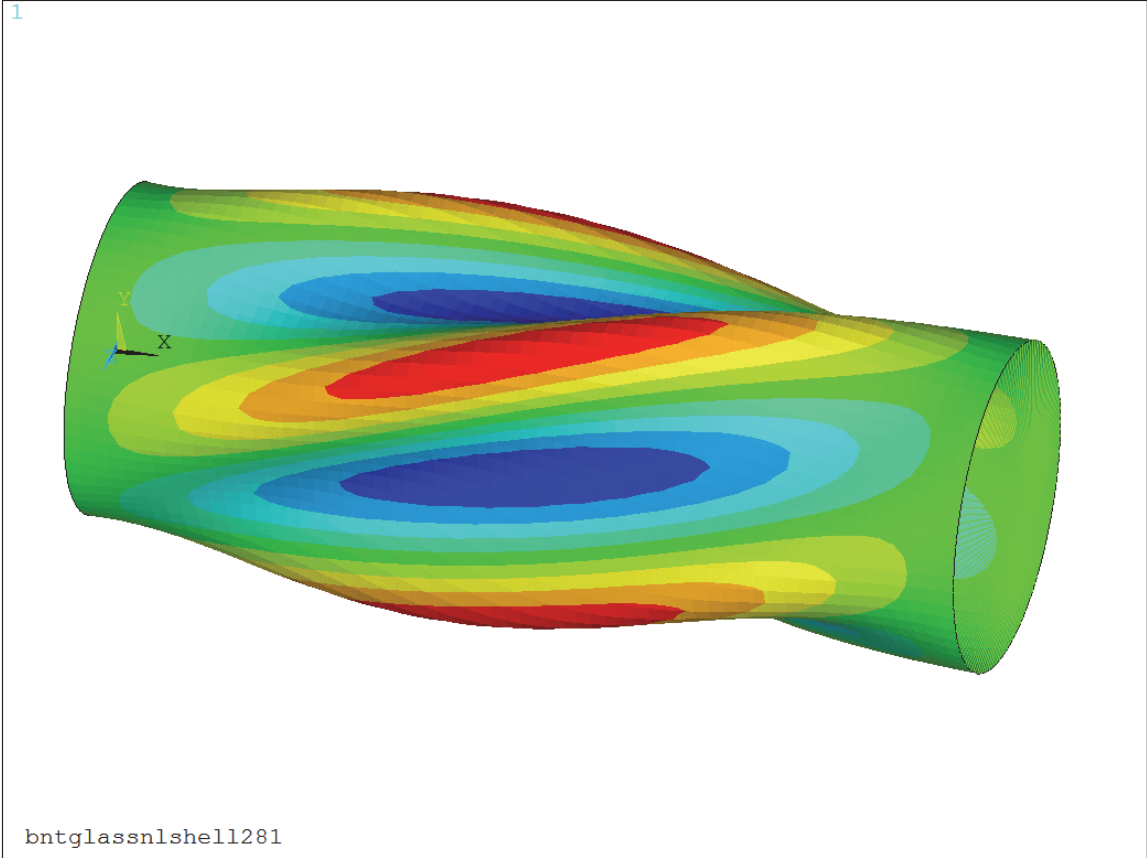

Fig. 2.10. Contour plot of the radial displacements of the buckled shaft.

Nonlinear Buckling Analysis

Nonlinear buckling analysis consists of two steps. The first is the generation of the geometric imperfections and the second is the nonlinear run. In order to generate the initial imperfections, an eigenvalue buckling analysis is run. Then, the eigenvalue buckling analysis modeshapes are expanded and output to the results file. The deformed shape of the buckled shaft that corresponds to the minimum eigenvalue buckling load, scaled by a specific magnitude, is then used as the shaft with the initial geometric imperfections, safely assuming that the shaft is going to buckle following this predicted mode shape (Papadakis & Tsouvalis, 2016). This is performed by the UPGEOM command which adds the displacements from the buckling analysis and updates the geometry of the finite element model to the deformed configuration. It is also possible to combine the deformed shapes (eigenmodes) of several eigenvalues to generate the initial imperfections pattern. The size of the geometric imperfections depends on the application and is expressed in this study as a ratio to the shaft's diameter. The effect of the size of the initial imperfections has been investigated and is discussed in section 2.6.3. In the

67

following lines of the APDL code, the chosen size of the maximum imperfection is 0.1% of the internal diameter of the shaft.

The second step is the nonlinear static analysis run.

In order to generate the geometric imperfections, that are necessary for nonlinear buckling analysis, with the desired maximum magnitude equal to **0.1% of Di**, parameter **mag** is defined. Mag is equal to the desired maximum radial initial imperfection uxmax'=0.00025m (0.1% of Di) divided by the maximum absolute radial displacement uxmax.

$$mag = \frac{ux\,max'}{ux\,max}$$

(2.2)

As a result of the aforementioned values of uxmax and uxmax', **mag=0.0072**.

The preprocessor is reentered and the UPGEOM command is applied. All displacements of the critical mode-shape of the eigenvalue buckling analysis are multiplied by the parameter mag, generating this way the desired geometric imperfections. The term critical means the mode shape that corresponds to the critical (minimum) buckling load.

```
!Generate Geometric Imperfections
/prep7
*SET,mag,0.0072              !This value of the parameter "mag" results in
                            !geometric imperfections with the maximum
                            !displacement being equal to 0.1% of Di
UPGEOM,mag,1,5,bntglassnlshell281,rst,
FINISH
```

After the generation of the geometric imperfections, the nonlinear static analysis is run. The final Time is set equal to 1 so that every time step is a percentage of 1 and the torque applied at this time step is the same percentage of the maximum applied torque (120kNm). Automatic time stepping is used because it increases the number of time steps near the critical load and thus increases the accuracy of the results. The convergence criteria were set to default, after checking that changing them had insignificant effect in the solution of the problem.

```
!SECOND STEP

!Nonlinear Static Analysis
/SOLU
ANTYPE,STATIC
NLGEOM,ON                   !Large Displacements ON
PRED,OFF                    !No prediction occurs
TIME,1
*SET,timev,0.01             !Time step value
*SET,timn,0.001             !Minimum time step
*SET,timx,0.1               !Maximum time step
DELTIM,timev,timn,timx,     !Time step values (value, minimum, maximum)
AUTOTS,ON                   !Automatic time step on
OUTRES,all,all
SOLVE
FINISH
```

After 14 substeps the following error message appeared:
```
*** ERROR ***                        CP =     2583.579   TIME= 13:02:54
Solution not converged at time 0.5088125 (load step 1 substep 14).
 Run terminated.
```

This was expected and it identifies that the structure had become unstable, in other words that the shaft buckled. The load at this substep is equal to time·(full load) = 0.5088125·120 = 61.06 kNm.

2.2.3 Post-processing

At this section the results of the nonlinear buckling analysis are discussed.

Rotational Stiffness and Buckling Load

The results of the nonlinear buckling analysis concerning the rotation of shaft and the buckling load are the first discussed. The node that expresses the total rotation of the shaft is the master node and its angle of rotation is presented in the table 2.5 and Figure 2.11. The comparison between the experimental results, listed in table 2.3 and plotted in fig 2.3, and the results of the nonlinear buckling analysis indicate that our model predicts relatively well the buckling load. Buckling can be identified in Figure 2.11, at the point where the FEM curve starts to bend. The diagram shows that the shaft buckled somewhere between 55kNm and 58kNm, before the last converged substep. Figure 2.11 also indicates that the FE model predicts a much higher rotational stiffness of the shaft than the experimental as it can be seen by the gradient of the FEM curve in comparison to the experimental one.

Table 2.5. Results of the nonlinear buckling analysis

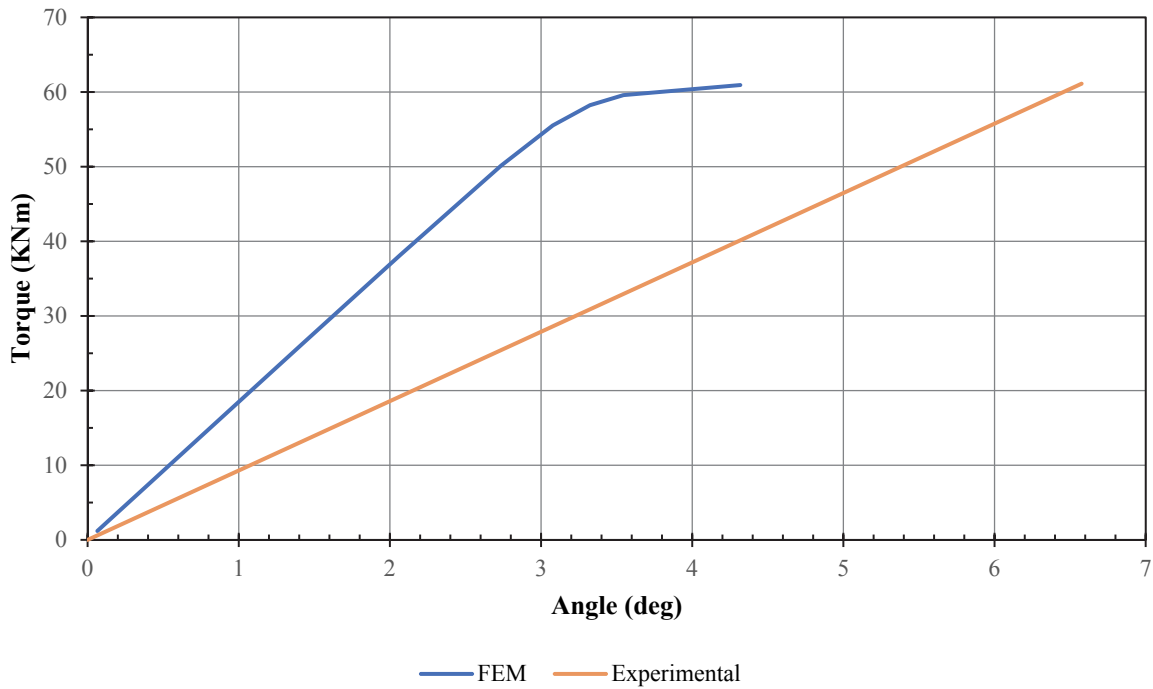| Torque (kNm)	Angle of rotation of the master node (deg)
1.2000	0.0648
2.4000	0.1297
4.2000	0.2270
6.9000	0.3729
10.9500	0.5919
17.0256	0.9204
26.1372	1.4138
38.1372	2.0664
50.1372	2.7355
55.5372	3.0780
58.2372	3.3234
59.5872	3.5442
60.9372	4.3180

Torque vs Rotation

Fig. 2.11. Comparison between FEM Results and Experimental Curve.

Stresses

Additionally, the calculated stresses are examined. The maximum tensile and compressive stresses at the external surface of the shaft in the direction of the fibers and in the direction normal to the fibers are presented in Figure 2.12. The fiber orientation of the external ply of the shaft is -45°. The node with the maximum tensile stresses in both directions is situated at mid-length on a crest and the node with the maximum compressive stresses is situated at mid-length on a trough of the buckled modeshape, as it was expected. σ_1 is the stress in the direction of the fibers and σ_2 is in the direction normal to the fibers.
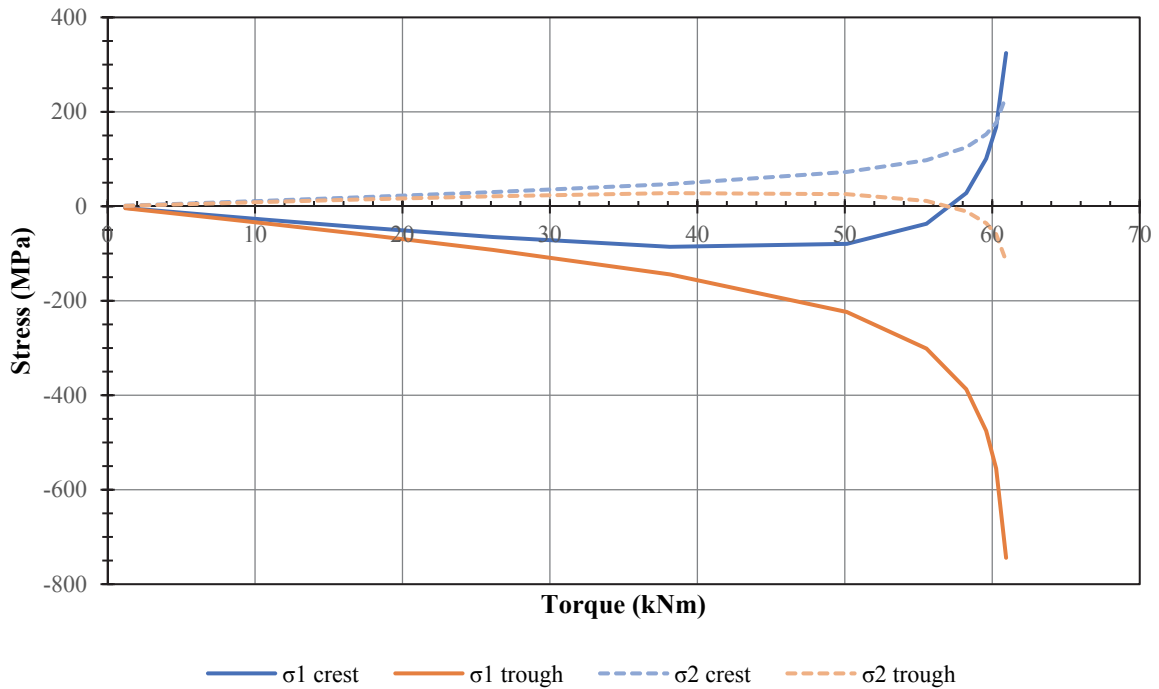
Torque vs Stress

Fig. 2.12. Torque vs Stress diagram of σ_1 and σ_2 at a crest and a trough on the external surface

Figure 2.12 shows the pattern that stresses follow in buckling. The maximum stresses, in terms of magnitude, in the direction of the fibers are compressive and when buckling initiates one of them becomes tensile. The stresses in the direction normal to the fibers follow the opposite pattern. Additionally, all stress curves show a rapid increase after 50 kNm where buckling initiates.

Figure 2.13 represents the stresses of the same nodes in the internal surface of the shaft in the direction of the fibers and in the direction normal to the fibers. The fiber orientation of the internal ply of the shaft is 45°.

Torque vs Stress
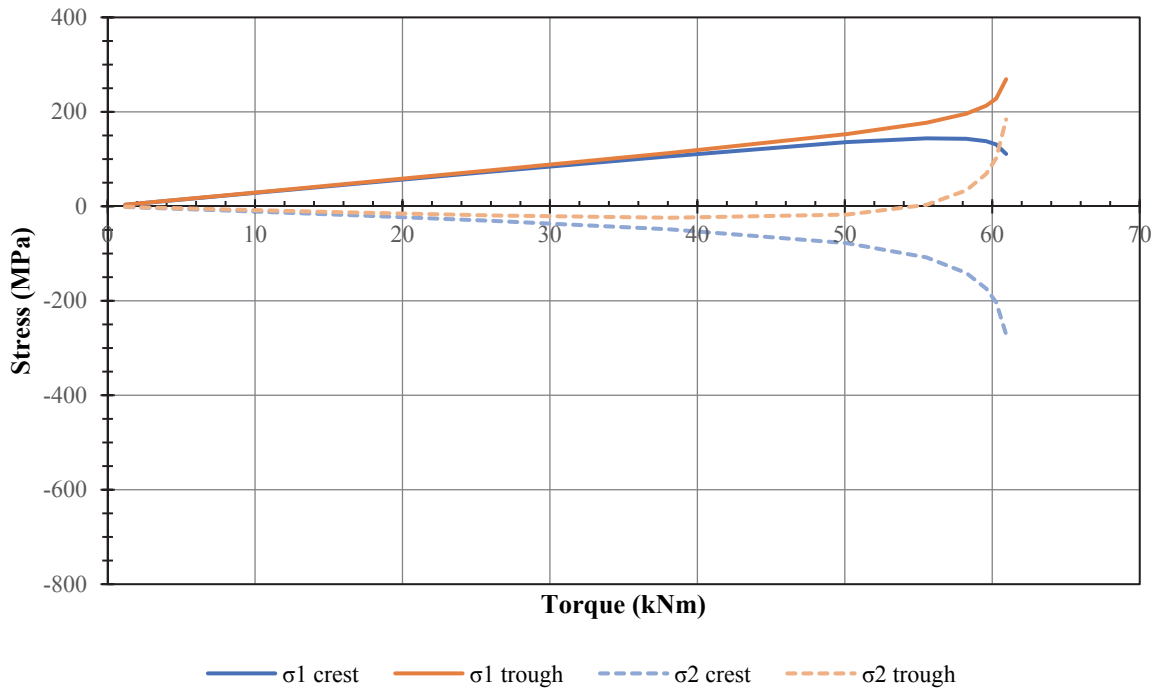
Fig. 2.13. Torque vs Stress diagram of σ_1 and σ_2 at a crest and a trough on the internal surface

Figure 2.13 shows that on the internal surface, the maximum stresses, in terms of magnitude, in the direction of the fibers are tensile, in contrast to the corresponding stresses on the external surface which are compressive. When buckling initiates the stress measured on a crest reduces its magnitude as it was expected, due to the compression of the internal surface of the shaft at the position of the crest. The stresses in the direction normal to the fibers follow the opposite pattern. Additionally, the magnitudes of these stresses are lower than the ones at the external surface.

Figure 2.14 represents the stresses of the same nodes on the external surface of the shaft in the direction of the axis of the shaft and in the direction of the circumference of the shaft.
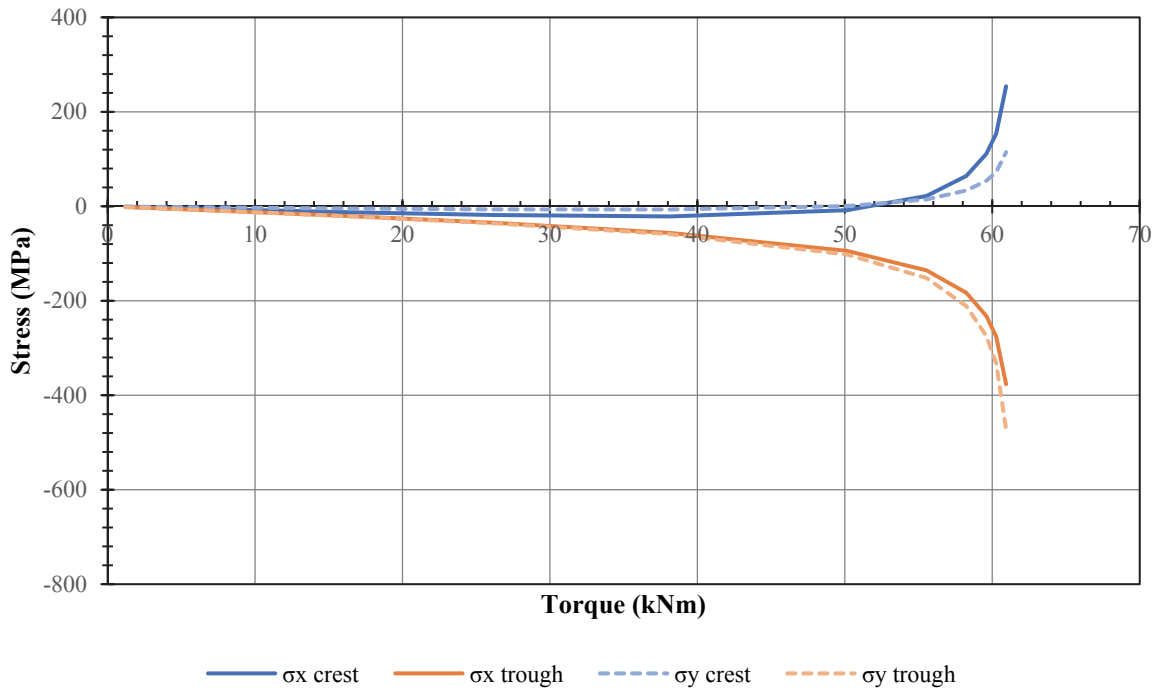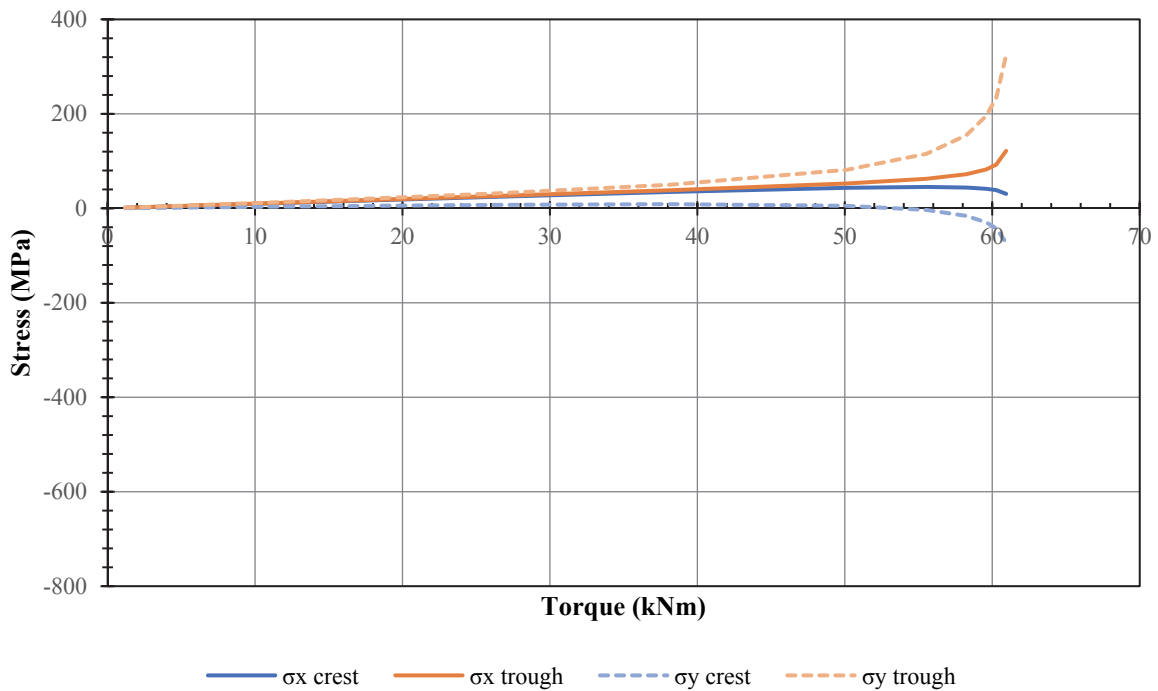
Torque vs Stress

Fig. 2.14. Torque vs Stress diagram of σ_x and σ_y at a crest and a trough on the external surface

Figure 2.14 also shows the pattern that stresses follow in buckling. The maximum compressive stresses, in terms of magnitude, are in the circumferential direction whereas the maximum tensile stresses are in the axial direction. Additionally, all stress curves show a rapid increase after 50 kNm where buckling initiates.

Figure 2.15 represents the stresses of the same nodes on the internal surface of the shaft in the direction of the axis of the shaft and in the direction of the circumference of the shaft.

Torque vs Stress

Fig. 2.15. Torque vs Stress diagram of σ_x and σ_y at a crest and a trough on the internal surface

Figure 2.15 shows that on the internal surface, all stresses are tensile, in contrast to the corresponding stresses on the external surface which are compressive. Only the circumferential stress on a crest becomes compressive when buckling initiates. The stresses measured on a trough increase their magnitude, when buckling initiates, whereas the stresses measured on a crest reduce their magnitude, when buckling initiates, as it was expected.

Failure Criteria

Failure Criteria were also introduced in order to check the strength of the shaft. Since there was no information about the ultimate strengths of the material given by the manufactured, some typical values were used, drawn from the database of the Shipbuilding Technology Laboratory (NTUA). These values are listed in the following table.

Table 2.6. Strengths of the material

X_t (MPa)	500
Y_t (MPa)	20
Z_t (MPa)	20
XY (MPa)	200
YZ (MPa)	200
XZ (MPa)	200

The strengths were input to ANSYS by the following set of commands:

```
/post1
FC,1,S,XTEN,   500e6
FC,1,S,YTEN,    20e6
FC,1,S,ZTEN,    20e6
FC,1,S,XY  ,   200e6
FC,1,S,YZ  ,   200e6
```

74

```
FC,1,S,XZ  ,  200e6
finish
```

The failure criterion used was Tsai-Wu strength index. According to this criterion and the given material strengths, the first ply failure occurs at 17 kNm which is very low compared to the moment of 55 kNm where significant stiffness decrease is noticed. A sensitivity analysis was conducted and it revealed that the strength in the direction normal to the fibers, Y_t, had the most significant effect. By increasing Y_t by 50%, the first ply failure load became 30 kNm. By setting Y_t equal to X_t the failure load almost reached the buckling load near 60 kNm. This indicates the limited ability of the Tsai-Wu failure criterion to correctly predict failure in filament wound shell structures.

Conclusions and further investigation

It is obvious from Figure 2.11 that, despite the relatively good prediction of the model concerning the buckling load, it predicts a much higher rotational stiffness of the shaft. The experimental rotational Stiffness is 9.6 kNm/deg whereas the FE rotational stiffness is 18.03 kNm/deg, 87.8% higher than the experimental.

There are various factors affecting this result that will be investigated in the next sections. The first is the effect of the Layered Modelling Method that was used and will be investigated by creating a Homogeneous Model using the Mechanics of Composite Materials and comparing them. A layered solid model is also created. Additionally, the effect of material properties, shaft thickness and geometric imperfections will be investigated in an attempt to explain the above disagreement.

Concerning stresses, their evolution and their values are reasonable until buckling initiation. Then their values become too high confirming that the shaft buckled. Tsai-Wu failure criterion with the initial material strengths predicted a very early first ply failure and the sensitivity analysis showed that the strength in the direction normal to the fibers had the most significant effect.

Before any of the aforementioned comparisons are attempted, a Steel Shaft of the same geometry will be modelled and the results of the FEM analysis will be compared with the analytical based on the book Roark's Formulas for Stress and Strain (Young & Budynas, 2002), in order to check the validity of our model.

In the next section, the mesh convergence analysis that was mentioned earlier in section 2.2.1 is discussed.

2.2.4 Mesh Convergence Analysis

At this point that the full overview of the solution has been presented, mesh convergence can be discussed. Four different meshes were checked and the resulting eigenvalue critical buckling factors, the nonlinear ultimate load at the last converged substep, which is time-step dependent, and the rotation of the master node at the ultimate load were compared. The first mesh consisted of 1080 square elements, 30 elements longitudinally and 36 elements circumferentially, with side length 0.023m and 3 integration points through the thickness of each layer. The second mesh consisted of 3840 square elements, 60 elements longitudinally and 64 circumferentially, with side length 0.0115m and 3 integration points through the thickness of each layer. The third

mesh consisted of 3840 elements, 60 elements longitudinally and 64 circumferentially, and 9 integration points through the thickness of each layer. The fourth mesh consisted of 16320 square elements, 120 longitudinally and 136 circumferentially with side length 0.0057m and 3 integration points through the thickness of each layer. The results are listed in table 2.7.

Table 2.7 Mesh Convergence Comparison

Mesh	Eigenvalue Buckling Load	Nonlinear Ultimate Load	Rotation of the Master Node at the Ultimate Load	Solution Duration
30x36 Elements, 3 integration points	65.49 kNm	61.05 kNm	4.57 deg	2 min
60x64 Elements, 3 integration points	65.44 kNm	60.94 kNm	4.34 deg	9 min
60x64 Elements, 9 integration points	65.44 kNm	60.94 kNm	4.34 deg	14 min
120x136 Elements, 3 integration points	65.55 kNm	61.05 kNm	4.40 deg	30 min

The difference between the coarser and the finer mesh is 0.09% concerning the critical eigenvalue buckling load, negligible concerning the nonlinear ultimate calculated load and 3.7% concerning the maximum rotation of the master node. More integration points through the thickness of the layer offer no benefits in this particular analysis. Considering the results and the duration of the solution the mesh of 3840 Elements and 3 integration points through the thickness of each layer is chosen. Finally, concerning the duration of the solution, it is noted that the solution was run on a personal computer with an AMD Quad Core Processor at 3.40 GHz and 8 GB RAM.

After the discussion about mesh convergence, the modelling of the steel shaft will be discussed in the next chapter, in order to check the validity of the model.

2.3 Modelling of the Steel Shaft

2.3.1 FE modeling of the steel shaft.

As it has been already mentioned the geometry of the steel shaft is identical to the GFRP shaft. The mechanical properties of steel that were used for the modeling are listed in table 2.8. The material model used for steel is linear isotropic.

Table 2.8. Mechanical Properties of Steel

E (GPa)	207
ν	0.33

The APDL code is exactly the same, apart from the commands that define the material properties and the sections. These sets of commands are listed below.

```
!*--------------------
!* MATERIAL PROPERTIES
!*--------------------
MP,EX,1,207*1e9
MP,PRXY,1,0.33
```

```
!* --------
!* SECTIONS
!* --------
secnum,1
sectype,1,shell
secoffset,bot
secdata,t,1,0,3
```

There is only one layer with the full thickness of the shaft.

The critical buckling load of the eigenvalue buckling analysis is 657kNm. The results of the eigenvalue buckling analysis is considered unnecessary to be further discussed. The results of the nonlinear analysis, the angle of rotation of the master node and the maximum shear stress of the section are listed in table 2.9 and presented in Figures 2.18 and 2.19 respectively. It is noted that the maximum shear stress was calculated at mid-length as it was expected.

Table 2.9. Results of the FEM analysis

Torque (kNm)	Angle of rotation of the master node (rad)	Maximum Shear Stress (MPa)
1.2000	0.0002	2.42
2.4000	0.0003	4.84
4.2000	0.0006	8.47
6.9000	0.0009	13.92
10.9500	0.0015	22.08
17.0256	0.0023	34.33
26.1372	0.0036	52.70
38.1372	0.0052	76.88
50.1372	0.0068	101.05
62.1372	0.0085	125.22
74.1372	0.0101	149.37
86.1372	0.0118	173.52
98.1372	0.0134	197.67
110.1372	0.0150	221.80
120.0000	0.0164	241.64

2.3.2 Roark's formulas analytical results and comparison with the FEM results

Young & Budynas, (2002) offer formulas for the calculation of the buckling torque of a thin-walled circular tube under a twisting moment T that produces a uniform circumferential shear stress:

$$\tau = \frac{T}{2\pi r^2 t}$$

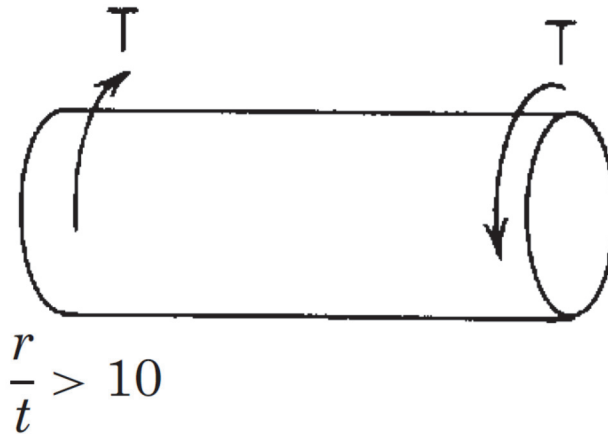where l=length of tube; r=radius of tube, t=wall thickness

Fig. 2.16 Thin-walled circular tube under twisting moment T

The buckling stress is: $\tau' = \dfrac{E}{1-v^2}\left(\dfrac{t}{l}\right)^2 \left(-2.39 + \sqrt{96.9 + 0.605H^{1.5}}\right)$

where $H = \sqrt{1-v^2}\,\dfrac{l^2}{tr}$, E=modulus of elasticity, v=poisson ratio

The buckling torque is $T' = \tau' 2\pi r^2 t = 634\text{kNm}$, 3.5% lower than the buckling torque of the eigenvalue buckling analysis.

Young & Budynas, (2002) also offer formulas for the angle of twist (rotation) θ and the maximum shear stress τ_{max}. The formulas for a hollow concentric circular section, like the shaft are given in table 2.10. Additionally, since the shaft is made of steel which is a homogeneous and isotropic material, the calculated maximum shear stress is the same everywhere along the outer surface of the shaft.

Table 2.10. Formulas for torsional deformation and stress

Formula for K in $\theta = \dfrac{TL}{KG}$	Formula for shear stress
$K = \dfrac{1}{2}\pi(r_o^4 - r_i^4)$	$\tau_{max} = \dfrac{2Tr_o}{\pi(r_o^4 - r_i^4)}$ at outer boundary

where θ = angle of twist (radians); T = twisting moment (force·length); L=length, τ = unit shear stress (force per unit area); G = modulus of rigidity (force per unit area); K (length to the fourth) is function of the cross section.
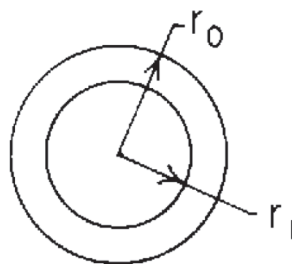
Fig. 2.17 Hollow concentric circular section

The graphical comparison between FEM and analytical results, concerning the angle of rotation of the rotating end of the shaft and the maximum shear stress at the outer surface of the shaft is displayed in the following Figures 2.18 and 2.19.
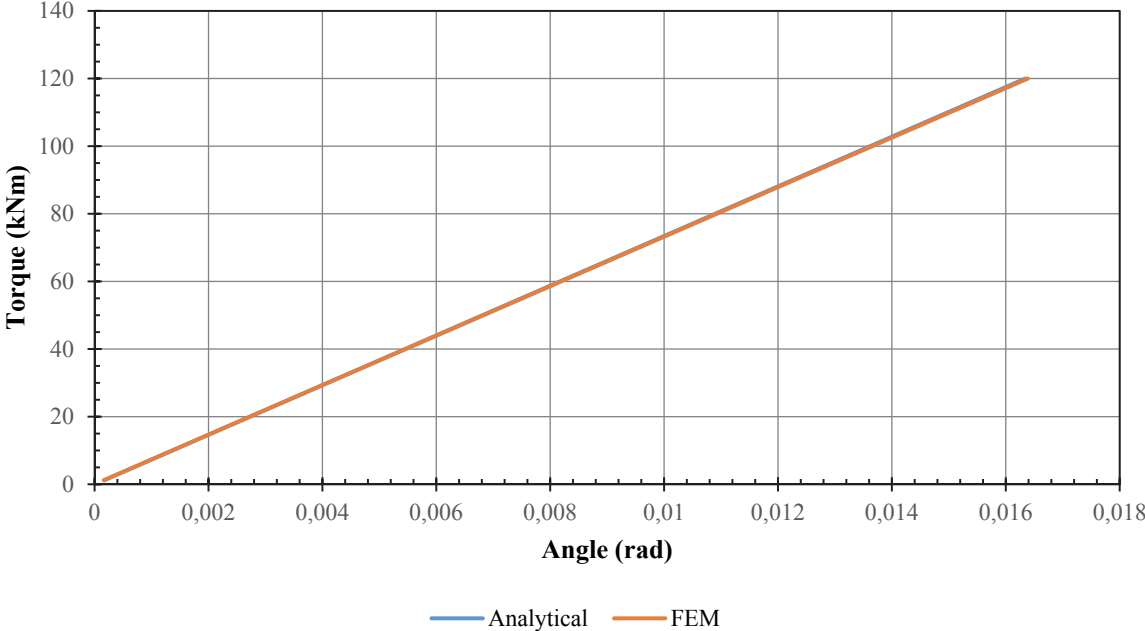
Torque vs Rotation

Fig. 2.18. Comparison between analytical and FEM results for Rotation.
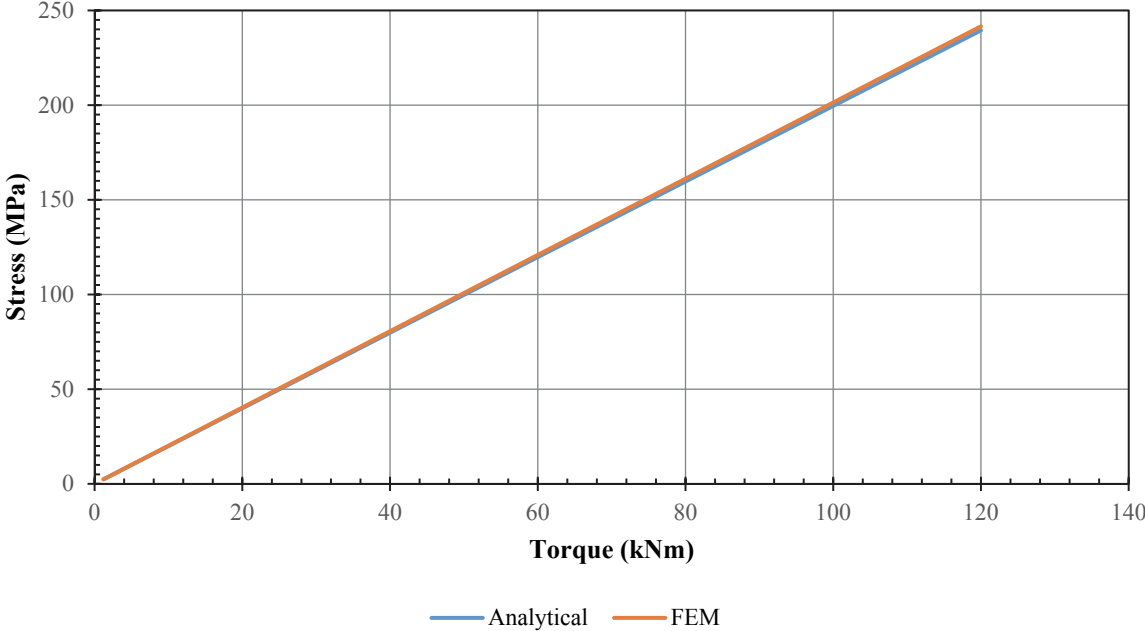
Torque vs Stress

Fig. 2.19. Comparison between analytical and FEM results for maximum shear stress.

The comparison indicates that the Finite Element Model gives very good results for the steel shaft so there is need for further investigation in the modelling of the GFRP shaft. The next attempt is the creation of a Homogeneous Model using Mechanics of Composite Materials.

2.4 Homogeneous Modelling of the GFRP Shaft

The idea of homogeneous modelling is to model the shaft as single-layered, with the single layer having the equivalent mechanical properties of the multilayered composite. This is attempted because Filament Winding, the manufacturing method of the shaft, does not produce discrete layers as for example hand layup does. So it is necessary to check if homogeneous modelling of the shaft would reproduce the real shaft better. The calculation of the equivalent mechanical properties is based on the Mechanics of Composite Materials as it is described by (Tsouvalis, 1998).

2.4.1 Calculation of the mechanical properties of homogeneous material

Theory refers to composite plates but it can be safely assumed that the calculated mechanical properties can also be used in the problem of the shaft.

The approach used transforms a specially orthotropic multilayered plate to an equivalent homogeneous orthotropic plate. Due to its layup, $[\pm 45]_{12}$, the shaft can be considered as specially orthotropic. The equations for the calculation of the equivalent mechanical properties are the following:

$$E_1 = \frac{A_{11}(1 - \nu_{12}\nu_{21})}{t} \tag{2.3a}$$

$$E_2 = \frac{A_{22}(1 - \nu_{12}\nu_{21})}{t} \tag{2.3b}$$

$$\nu_{12} = \frac{A_{12}}{A_{22}} \tag{2.3c}$$

$$\nu_{21} = \frac{A_{12}}{A_{11}} \tag{2.3d}$$

$$G_{12} = \frac{A_{66}}{t} \tag{2.3e}$$

where t is the total thickness of the plate and A_{11}, A_{12}, A_{22}, and A_{66} are the extensional rigidities of the multilayered plate that are calculated by the equation:

$$A_{ij} = \sum_{k=1}^{N} (\overline{Q}_{ij})_k (t_k) \tag{2.4}$$

where t_k is the thickness of each layer and $\overline{Q}_{ij}$ are the transformed reduced stiffnesses of a layer and are calculated by the equations:

$$\overline{Q}_{11} = Q_{11} m^4 + 2(Q_{12} + 2Q_{66})m^2 n^2 + Q_{22} n^4 \tag{2.5a}$$

$$\overline{Q}_{12} = (Q_{11} + Q_{22} - 4Q_{66})m^2 n^2 + Q_{12}(m^4 + n^4) \tag{2.5b}$$

$$\overline{Q}_{16} = -mn^3 Q_{22} + m^3 nQ_{11} - mn(m^2 - n^2)(Q_{12} + 2Q_{66}) \tag{2.5c}$$

80

$$\bar{Q}_{22} = Q_{11}\, n^4 + 2(Q_{12} + 2Q_{66})m^2 n^2 + Q_{22}\, m^4 \tag{2.5d}$$

$$\bar{Q}_{26} = -m^3 n Q_{22} + m n^3 Q_{11} + mn(m^2 - n^2)(Q_{12} + 2Q_{66}) \tag{2.5e}$$

$$\bar{Q}_{66} = (Q_{11} + Q_{22} - 2Q_{12})m^2 n^2 + Q_{66}(m^2 - n^2)^2 \tag{2.5f}$$

m=cosθ, n=sinθ, θ is the fiber orientation angle and

$$Q_{11} = \frac{E_1}{1 - \nu_{12}\nu_{21}} \tag{2.6a}$$

$$Q_{12} = \frac{\nu_{12} E_1}{1 - \nu_{12}\nu_{21}} \tag{2.6b}$$

$$Q_{22} = \frac{E_2}{1 - \nu_{12}\nu_{21}} \tag{2.6c}$$

$$Q_{66} = G_{12} \tag{2.6d}$$

The combination of the aforementioned equations gives the equivalent mechanical properties of the layered plate that are listed in Table 2.13. It must be mentioned that the calculated properties are in L, C and T directions, i.e. in the longitudinal, in the circumferential and in the through-thickness directions respectively.

Table 2.13. Equivalent Mechanical Properties of the GFRP

E_L (GPa)	16.27
E_C (GPa)	16.27
E_T (GPa)	16.27
G_{LC} (GPa)	11.27
G_{CT} (GPa)	5.636
G_{LT} (GPa)	11.27
ν_{LC}	0.479
ν_{CT}	0.479
ν_{LT}	0.479

2.4.2 Finite element analysis of the homogeneous model

The calculated material properties are implemented in the APDL code and a run is conducted. The results are discussed in the following lines.

a) Eigenvalue Buckling Analysis

The results of the eigenvalue buckling analysis of this approach are listed in table 2.14. The calculated critical buckling load is 66.3 kNm, 8.5% higher than the experimental failure load and 1.4% higher than the layered shell model. The pattern of the buckling modeshapes is the same between the two approaches.

Table 2.14. Results of the eigenvalue buckling analysis

Buckling load	Buckling modeshape
66.3	**mode 4**
66.3	mode 4
-66.3	mode 4
-66.3	mode 4
72.7	mode 3
72.7	mode 3
-72.7	mode 3
-72.7	mode 3
82.0	mode 5
82.0	mode 5

b) Nonlinear Buckling Analysis

Rotational Stiffness and Buckling Load

The results of the nonlinear buckling analysis concerning the rotation of the master node are listed in table 2.15.

Table 2.15. Results of the nonlinear buckling analysis

Torque (kNm)	Angle of rotation of the master node (deg)
1.2000	0.0649
2.4000	0.1297
4.2000	0.2270
6.9000	0.3730
10.9500	0.5920
17.0256	0.9206
26.1372	1.4141
38.1372	2.0665
50.1372	2.7337
55.5372	3.0675
60.9372	3.7883
61.3068	3.9963
61.4916	4.1782
61.6116	4.3903

Figure 2.20 represents the torque vs rotation diagram. The blue curve represents the FEM results and the orange curve represents the experimental results. It is obvious that the current approach did not reduce the rotational stiffness, which now equals to 18.096 kNm/deg, 0.35% higher than the layered model. It can also be seen that the predicted buckling load is around 55 kNm but the transition from the stable to the buckled condition is sharper than the layered shell model. The comparison between the layered and the homogeneous model can also be seen in Figure 2.20.

Torque vs Rotation
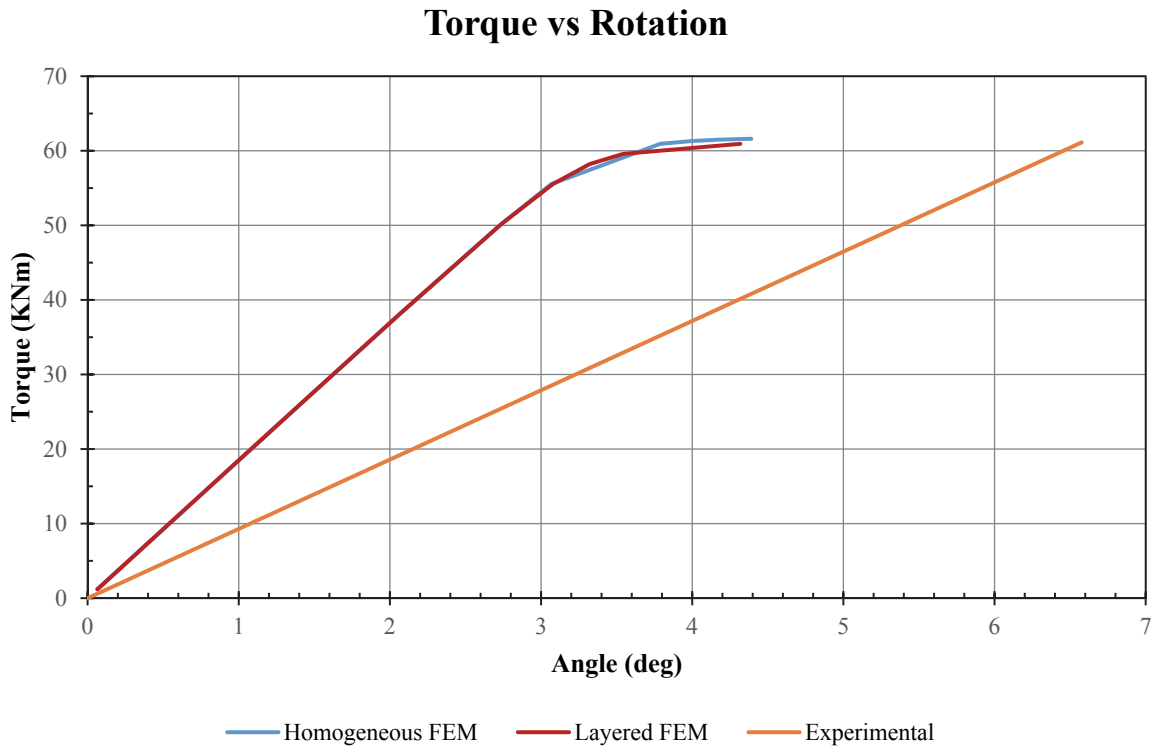
Fig. 2.20. Comparison between the homogeneous, layered and experimental results.

Stresses

Figure 2.21 represents the torque vs stress diagram of the maximum tensile and compressive stress in the two main directions of the homogeneous GFRP material. The first direction is in the direction of the axis of the shaft and the second is along the circumference of the shaft. This differs from the layered shell model, where each layer had the orientation of the reinforcing fibers and thus the stress in the direction of the fibers and in the direction normal to the fibers could be calculated. These stresses were calculated at mid-length at the position of a crest and a trough respectively on the external surface of the shaft. Due to the different modelling, the pattern as well as the range of the stresses differs. Figure 2.21 represents the comparison of the stresses of the layered and the homogeneous model in the direction of the axis of the shaft(longitudinal direction) and in the direction of the circumference of the shaft. A main difference is that all stresses of the layered model start as compressive whereas this is not true for the homogeneous model. Additionally, there is a symmetry between the magnitudes of the compressive and the tensile stresses of the homogeneous model, as it was expected. This symmetry does not exist in the layered model due to the orientation of the layers.

Torque vs Stress
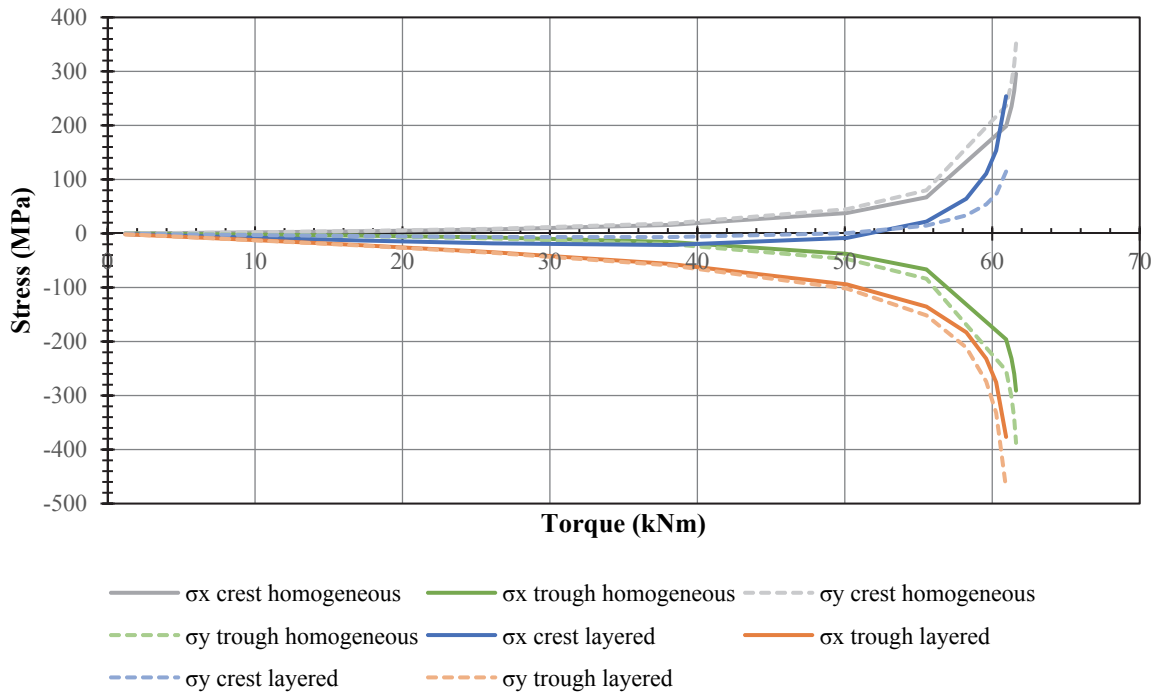
Fig. 2.21. Comparison of the stresses of the layered and the homogeneous model

Conclusion

Homogeneous modelling and layered shell modelling give almost the same results, concerning the rotational stiffness of the shaft. Concerning stresses, the homogeneous model can give results only in the longitudinal and the circumferential direction of the shaft. It also predicts tensile and compressive stresses of almost the same magnitude that are symmetrically developed about the x-axis, but the compressive stresses are slightly greater. The existence of this symmetry is an indication that the homogeneous material modelling represents more accurately the real filament wound shaft. The comparison of the stresses between the homogeneous and the layered shell model revealed some differences. A main difference is that the stresses of the layered shell model start all as compressive and the ones that remain compressive reach higher magnitudes than the ones that turn tensile. Additionally, the compressive stresses of the layered shell model are about 50 MPa greater than both compressive and tensile stresses of the homogeneous model until 50 kNm torque and then they become even greater. This occurs due to the orientation of the layers as we have already mentioned. The small differences in the eigenvalue buckling loads and in the stress range, i.e. the difference between the maximum and minimum stress values, between the two models reveal also that their difference is small, owing to the fact that the large number of layers of the ±45° lay-up considered in the first case is very close to the behavior of a homogeneous material. Finally, a weakness of the homogeneous model is the lack of available strengths for the homogeneous material, so no failure criteria could be introduced.

2.5 Layered Solid Modelling of the GFRP Shaft

A layered solid model was also created. The element type used was the 20-node structural solid element, SOLID186. The APDL code will not be extensively discussed since it is based on the code of the shell model, but the differences will be pointed out in the next section.

2.5.1 Preprocessing

A key difference between Solid and Shell modelling is the definition of the geometry. In shell modelling the geometry to be meshed is an area, whereas in solid modelling a volume must be defined. ANSYS offers the ability to directly create a solid cylinder with the use of the CYL4 command. The command requires the coordinates of the starting point of the cylinder, its internal and external diameter and its length. The set of commands for the creation of the cylinder is the following.

```
!*---------------
!*DEFINE GEOMETRY
!*---------------
csys,0
wprota,,,90 !Workplane Rotation so that the Axis of the Cylinder
            !coincides with the X-Axis
CYL4,0,0,Di/2, ,Do/2, ,L
wprota,,,-90
```

The set of commands for the definition of the element is listed below. It is necessary to note that a local cylindrical coordinate system around the global Cartesian x-axis is defined and used as the element coordinate system.

```
!* --------
!* ELEMENTS
!* --------

ET,1,SOLID186 !Define the element type

KEYOPT,1,2,0  !Uniform reduced integration (default)
KEYOPT,1,3,1  !Layered Structural Solid
KEYOPT,1,6,0  !0-Use pure displacement formulation (default)
KEYOPT,1,8,1  !Store top and bottom data for all layers.

CSYS,6
Clocal,11,1
ESYS,11      !Sets the element coordinate system attribute pointer.
```

All the rest commands until the mesh exhibit no difference. The command for meshing a cylindrical volume is VSWEEP and the command EORIENT is used to rotate the element coordinate system in the wanted direction.

```
vsweep,all      !Volume sweep
EORIENT,1,NEGX, !Sets the element x-axis parallel to the shaft's
                !axis
```

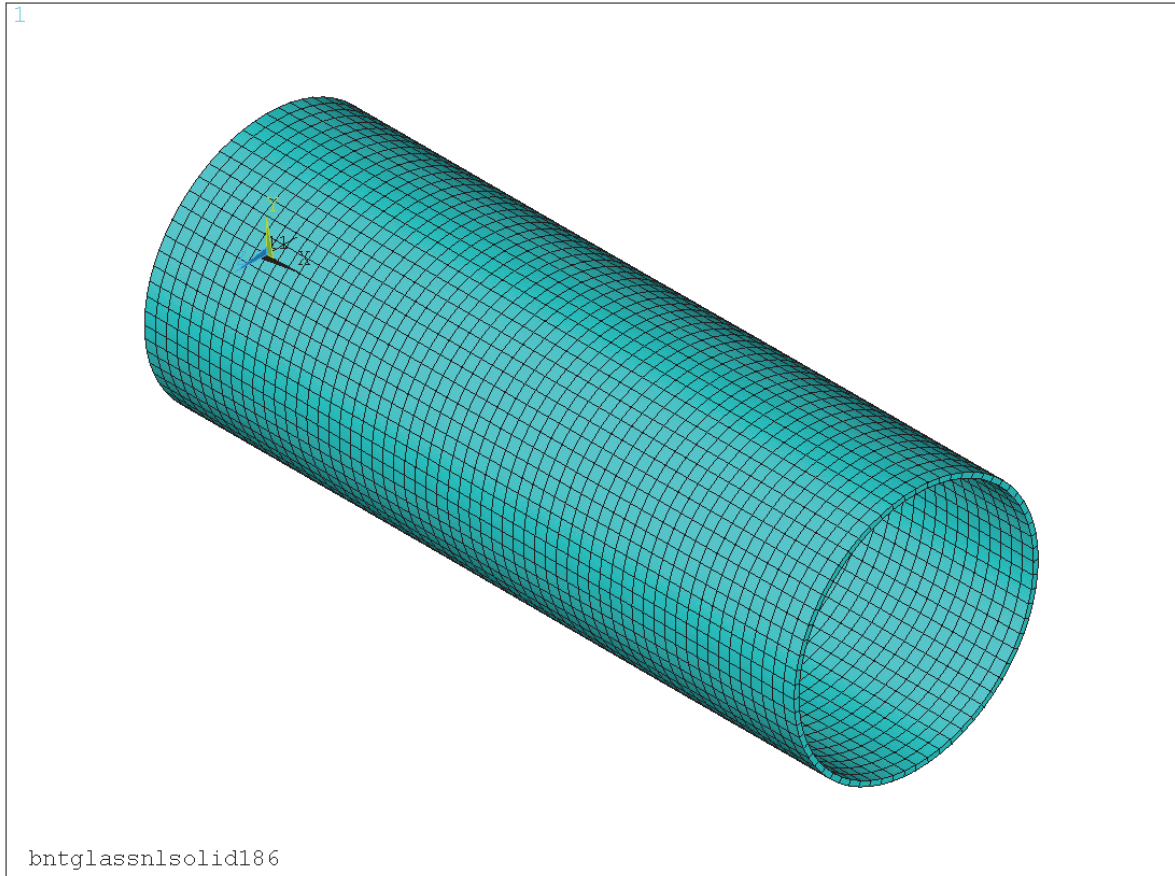Figure 2.22 represents the meshed geometry of the solid shaft.

Figure 2.22. Plot of the meshed geometry

2.5.2 Solution

The solution follows exactly the same procedure as in the shell model so it won't be discussed further. The results of the solution will be discussed in the next section.
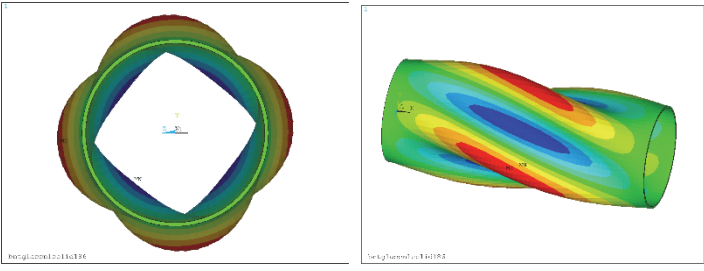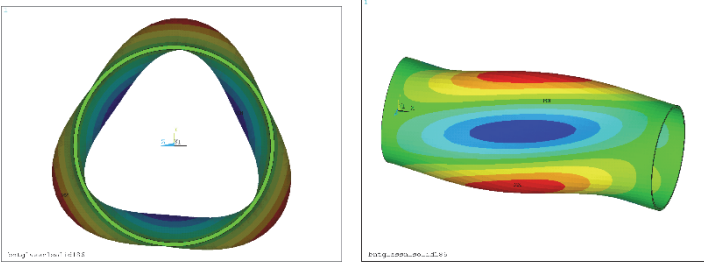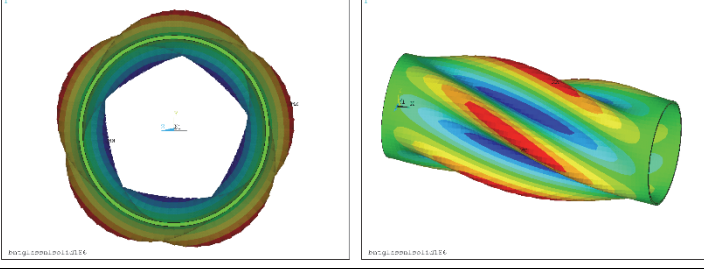
2.5.3 Post-processing

At this section the results of the analysis of the solid model are discussed, starting from the results of the eigenvalue buckling analysis and moving on to the results of the nonlinear buckling analysis.

a) Eigenvalue Buckling Analysis

The results of the eigenvalue buckling analysis are listed in table 2.16. The buckling loads are the product of the applied torque (120 kNm) multiplied by the buckling factor. All eigenvalue buckling factors are again double. The form of the buckled shaft at the critical buckling load is the same as the shell model and it has already been displayed in Figure 2.10. All mode shapes depict only one crest along the longitudinal direction. However, along the circumference of the shaft the number of crests varies

The critical (minimum) eigenvalue buckling load, as calculated by this analysis, is **63.6 kNm**. It is 4% greater than the experimental failure load of the shaft and 2.3% smaller than shell model. These results are listed in table 2.16 in bold. The pattern of the buckling modeshapes is also the same as the layered shell model.

Table 2.16. Results of the eigenvalue buckling analysis

Buckling load		Buckling modeshape
63.6	**mode 4**	
63.6	mode 4	
-64.3	mode 4	
-64.3	mode 4	
71.4	mode 3	
71.4	mode 3	
-72.1	mode 3	
-72.1	mode 3	
77.7	mode 5	
77.7	mode 5	

b) Nonlinear Buckling Analysis

The results of the nonlinear buckling analysis concerning the rotation of shaft and the buckling load are first discussed. The node that expresses the total rotation of the shaft is the master node and its angle of rotation is presented in table 2.17 and Figure 2.23. The comparison between the experimental results, listed in table 2.3 and plotted in fig 2.3, and the results of the nonlinear buckling analysis indicate that solid modelling also predicts relatively well the buckling load. Buckling can be identified in Figure 2.23 at the point where the FEM curve starts to bend. The diagram shows that the shaft buckled somewhere between 55 kNm and 58 kNm, before the last converged substep. The comparison between the FE Analysis' Torque to Rotation diagram with the experimental is shown in Figure 2.20. The comparison between the layered shell and the layered solid model can be seen in Figure 2.21.

Table 2.17. Results of the nonlinear buckling analysis

Torque (kNm)	Angle of rotation of the master node (deg)
1.2000	0.0648
2.4000	0.1297
4.2000	0.2270
6.9000	0.3729
10.9500	0.5918
17.0256	0.9203
26.1372	1.4136
38.1372	2.0660
50.1372	2.7358
55.5372	3.0849
57.9672	3.3211
60.3972	4.3135
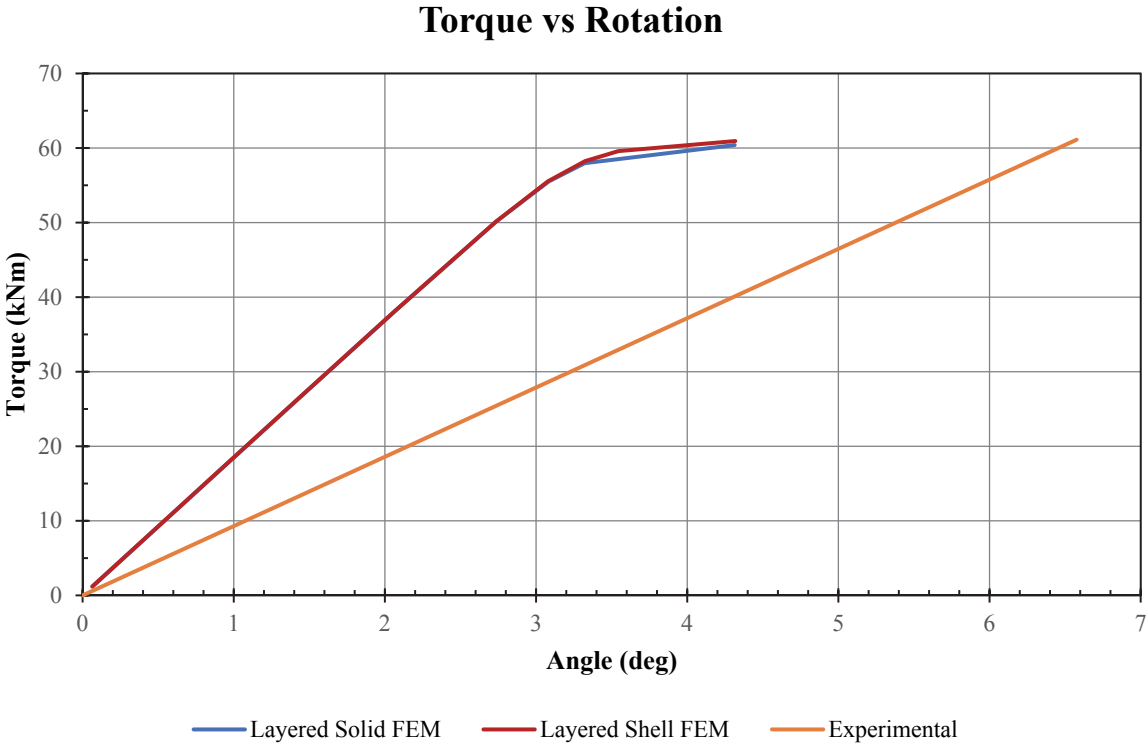
Fig. 2.23. Comparison between the layered solid, layered shell and experimental results.

Fig. 2.23 indicates that the layered shell and the layered solid models give almost identical results concerning the rotational stiffness of the shaft. The two diagrams differ insignificantly in the final steps of the analysis due to different time-stepping that was done automatically by ANSYS.

Stresses

The calculated stresses are also examined. The maximum tensile and compressive stresses in the direction of the fibers and in the direction normal to the fibers are presented in Figure 2.24. The node with the maximum tensile stresses in both directions is situated on a crest and the

node with the maximum compressive stresses is situated on a trough at mid-length of the buckled modeshape as it was expected. σ_1 is the stress in the direction of the fibers and σ_2 is in the direction normal to the fibers.

Figure 2.24 shows the pattern that stresses follow in buckling. The maximum stresses, in terms of magnitude, in the direction of the fibers are compressive and when buckling initiates one of them becomes tensile. The stresses in the direction normal to the fibers follow the opposite pattern. Additionally, all stress curves show a rapid increase after 50 kNm where buckling initiates, as it was expected.
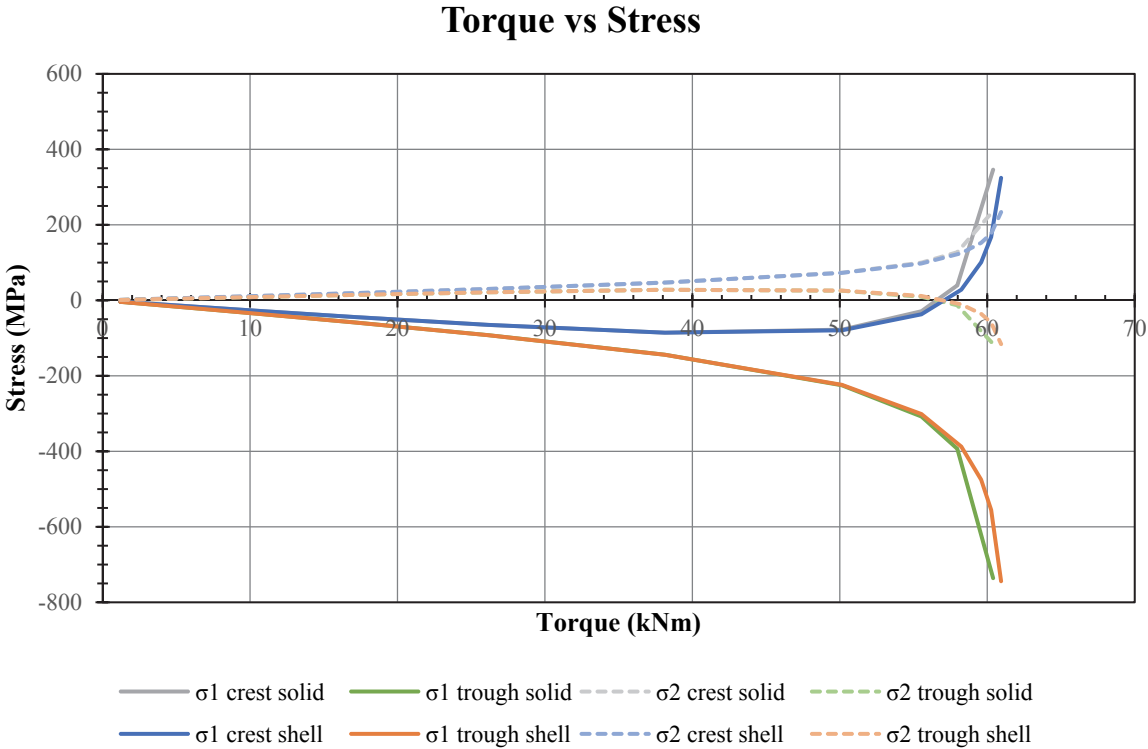
Fig. 2.24. Comparison between the stresses of the layered shell and the layered solid model

Figure 2.24 also represents the comparison of the stresses of the layered solid and layered shell model in the direction of the fibers and in the direction normal to the fibers. The stresses are identical up to the penultimate substep. The different stresses of the last substep are a result of different time-stepping that was done automatically by ANSYS but the difference is insignificant.

Figure 2.25 represents the stresses of the same nodes in the direction of the axis of the shaft and in the direction of the circumference of the shaft. Figure 2.25 represents the comparison between the stresses of the layered shell and layered solid model. The comparison gives the same conclusions as the comparison of the stresses in the direction of the fibers and normal to the fibers.
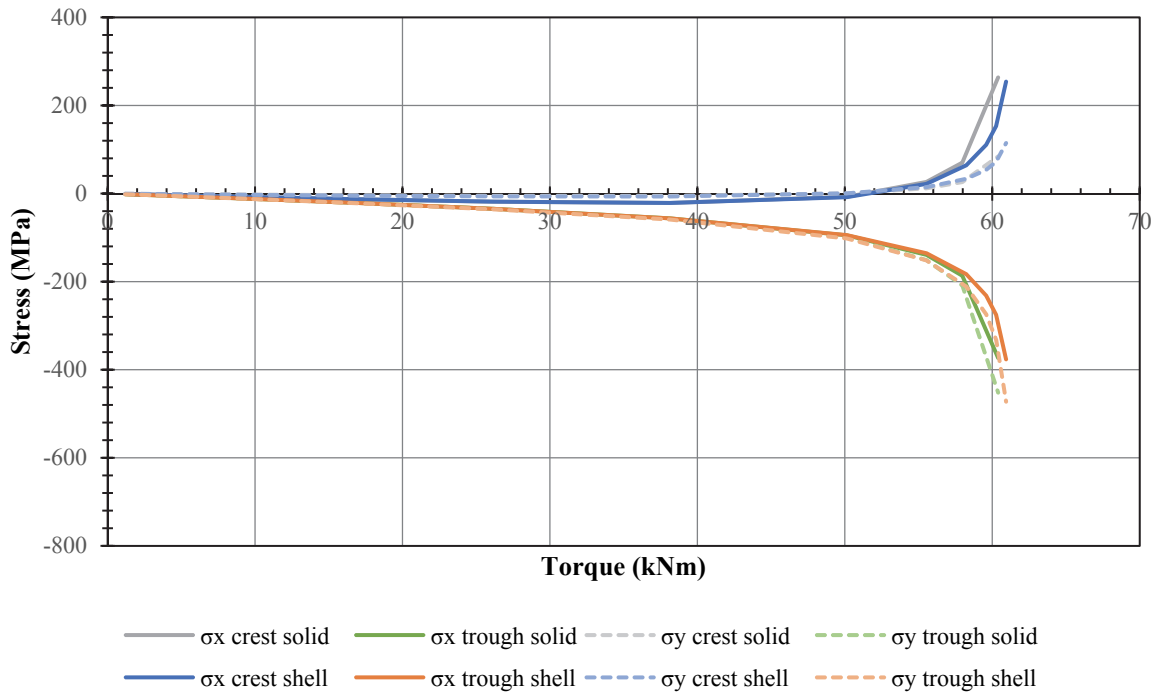
Torque vs Stress

Fig. 2.25. Comparison between the stresses of the layered shell and the layered solid model

Failure Criteria

Failure Criteria were also introduced in order to check the strength of the shaft. The same strengths as in the layered shell model were used and are listed in the following table.

Table 2.18. Strengths of the material

X_t (MPa)	500
Y_t (MPa)	20
Z_t (MPa)	20
XY (MPa)	200
YZ (MPa)	200
XZ (MPa)	200

The failure criteria used, was Tsai-Wu strength index. According to this criterion and the given material strengths, the first ply failure occurs at 17 kNm like the layered shell model. A sensitivity analysis was conducted and it revealed that the strength in the direction normal to the fibers, Y_t, had the most significant effect. By increasing Y_t by 50%, the first ply failure load became 30 kNm . By setting Y_t equal to X_t the failure load almost reached the buckling load near 55 kNm. This indicates that the Tsai-Wu failure criterion predicts the failure load very conservatively in layered shell structures. It also indicates the probable inaccuracy of the selected material strengths.

Conclusion

The comparison between the layered shell and the layered solid model shows that both models yield almost identical results. So for thin-walled layered composite shaft applications the extra

90

computing cost of layered solid modelling offers no benefits. For the further investigation of the mechanical behavior of the shaft, layered shell modelling will be used.

2.6 Sensitivity Analysis

In this section, the effect of material properties, shaft thickness and geometric imperfections will be investigated in an attempt to match the experimental rotational stiffness, which is the only experimental data available.

2.6.1 Material properties

Elastic modulus in fiber direction, E1

A drastic reduction of E1 by 50% is the first attempt.

Torque vs Rotation
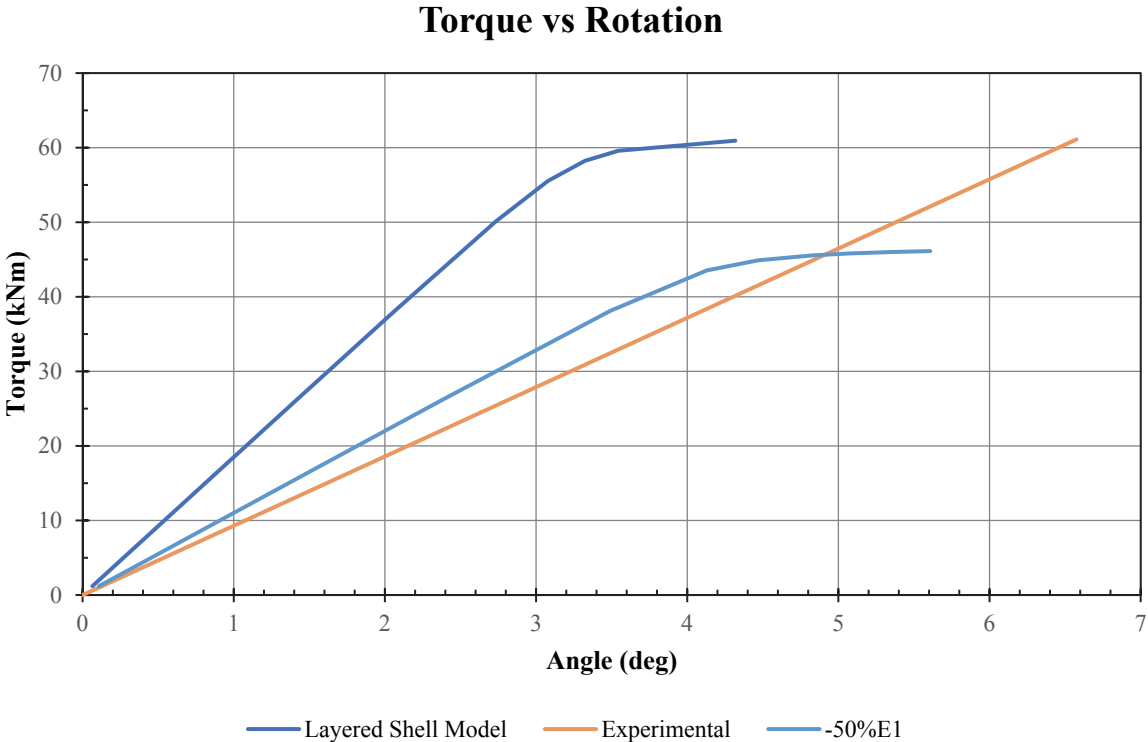
Fig. 2.26. Comparison between the layered shell model, the downgraded model and experimental results.

Figure 2.26 shows the effect that the reduction of E1 by 50% had to the rotational stiffness of the shaft. The shaft buckles at around 45 kNm but is still stiffer than the experiment.

A further decrease by 10% more is attempted. This decrease, led to a negative minimum eigenvalue, which means that the minimum torque required to buckle the shaft is in the opposite direction of the applied torque. It also means that the form of the modeshape of this eigenvalue is also in the opposite direction of the applied torque (the shaft turned in the opposite direction of the applied torque) as it can be seen in fig 2.27. The nonlinear analysis was run for both directions of the applied torque. Figure 2.28 shows the results of both analyses.
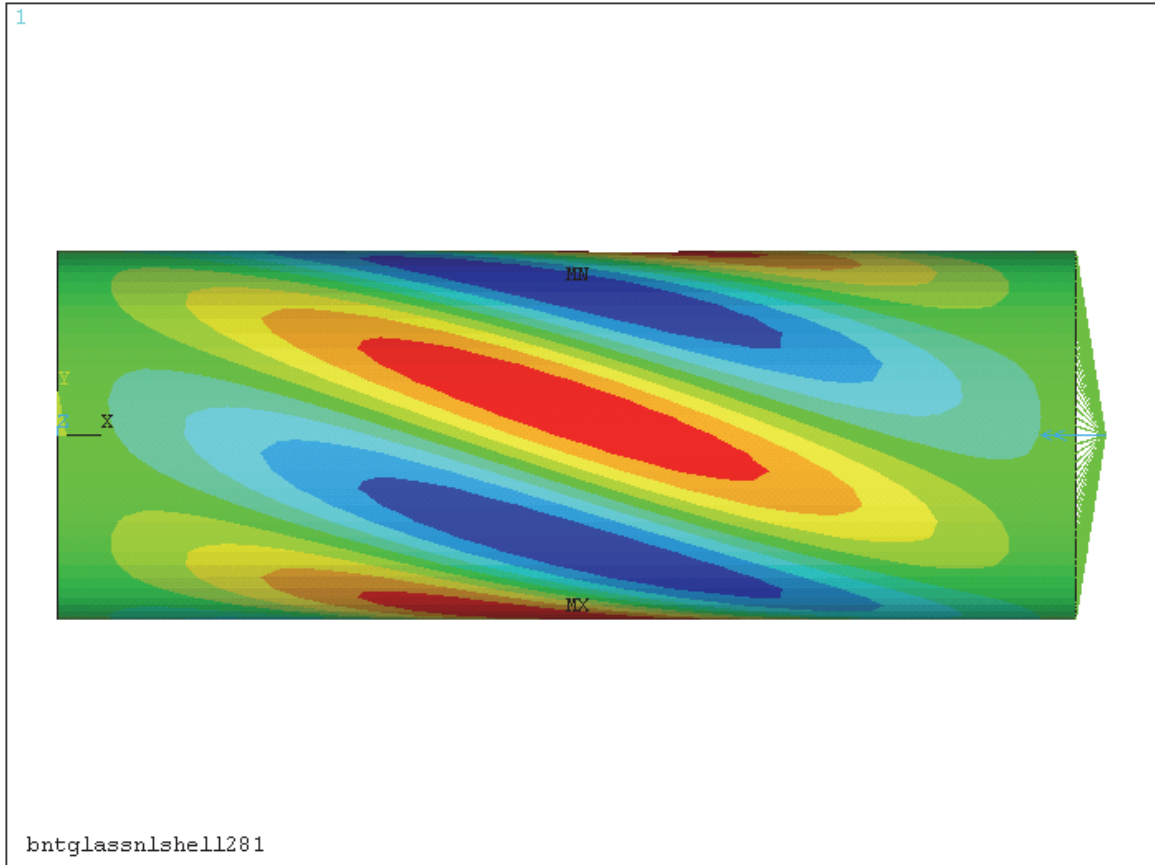
Fig 2.27. Image of the shaft indicating the opposing directions of the modeshape and the applied torque

Torque vs Rotation

Legend:
- Layered Shell Model
- Experimental
- -60% E1, torque in the direction of the eigenvalue
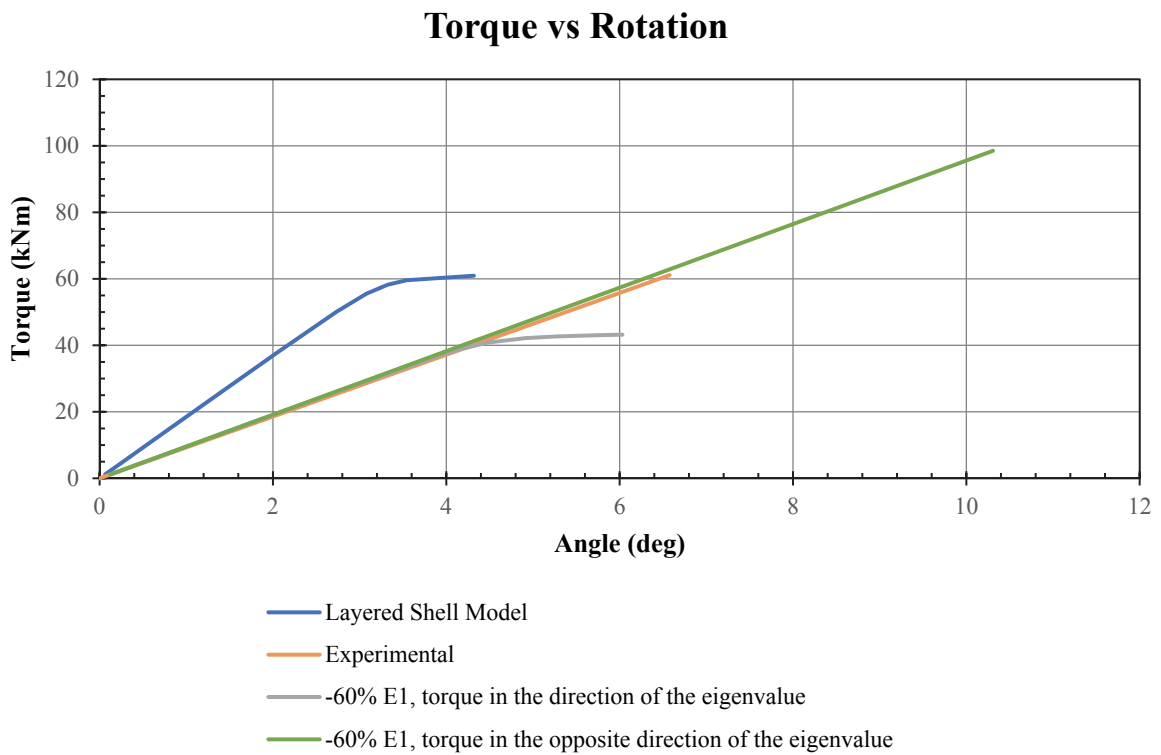- -60% E1, torque in the opposite direction of the eigenvalue

Fig. 2.27. Comparison between the layered shell model, the downgraded model and experimental results.

First and foremost, the green curve, which corresponds to the case that the applied torque is in the opposite direction of the eigenvalue and the corresponding modeshape, reaches almost 100kNm before buckling. This is reasonable, since the initial imperfection, based on the eigenvalue modeshape, opposed the direction of the applied torque as we have already mentioned. Additionally, the rotational stiffness of this case is a little higher than the experimental and a little higher than the second case. Concerning the grey curve of the second case, it shows that the shaft buckles around torque 40kNm. The rotational stiffness matches the experimental.

Elastic moduli in fiber direction and normal to the fiber direction, E1 and E2

The second attempt is the reduction of both E1 and E2 by 50%.
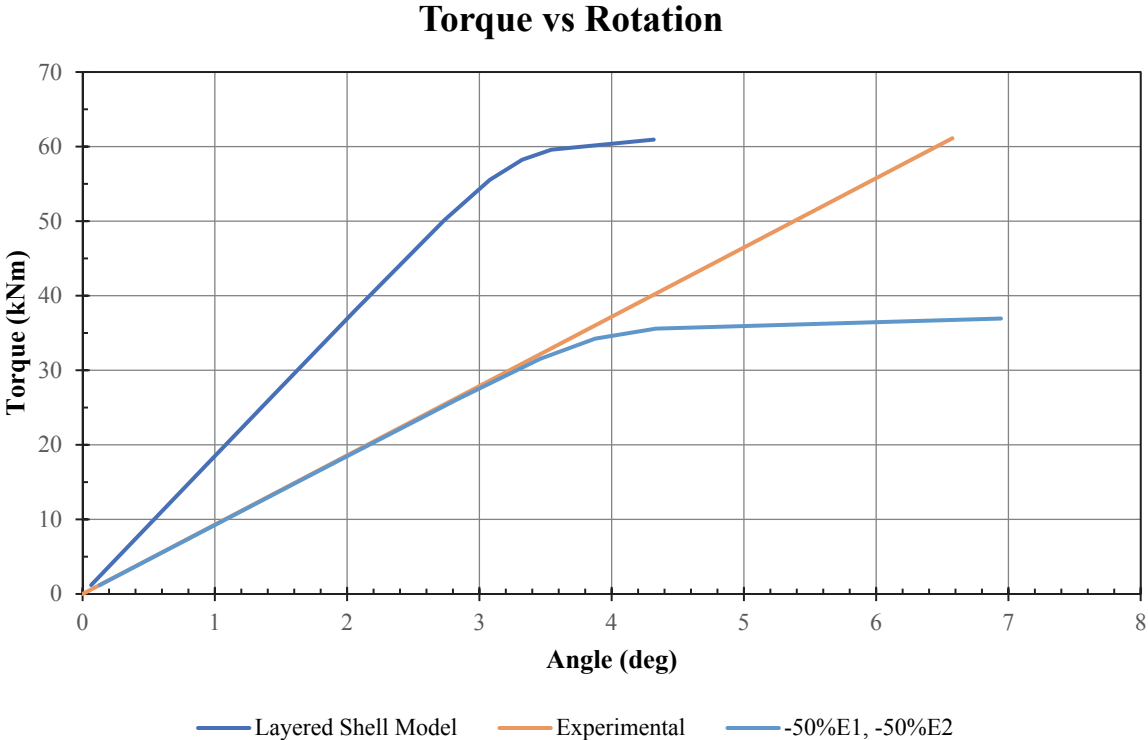
Fig. 2.28. Comparison between the layered shell model, the downgraded model and the experimental results.

Fig.2.28 shows that the reduction of E1 and E2 by 50% results in matching the experimental rotational stiffness of the shaft. In addition, the shaft buckles around 35 kNm. The effect of the reduction of E2 can be better understood by the comparison with the first case that had only E1 reduced by 50%. This comparison is shown in Figure 2.29.
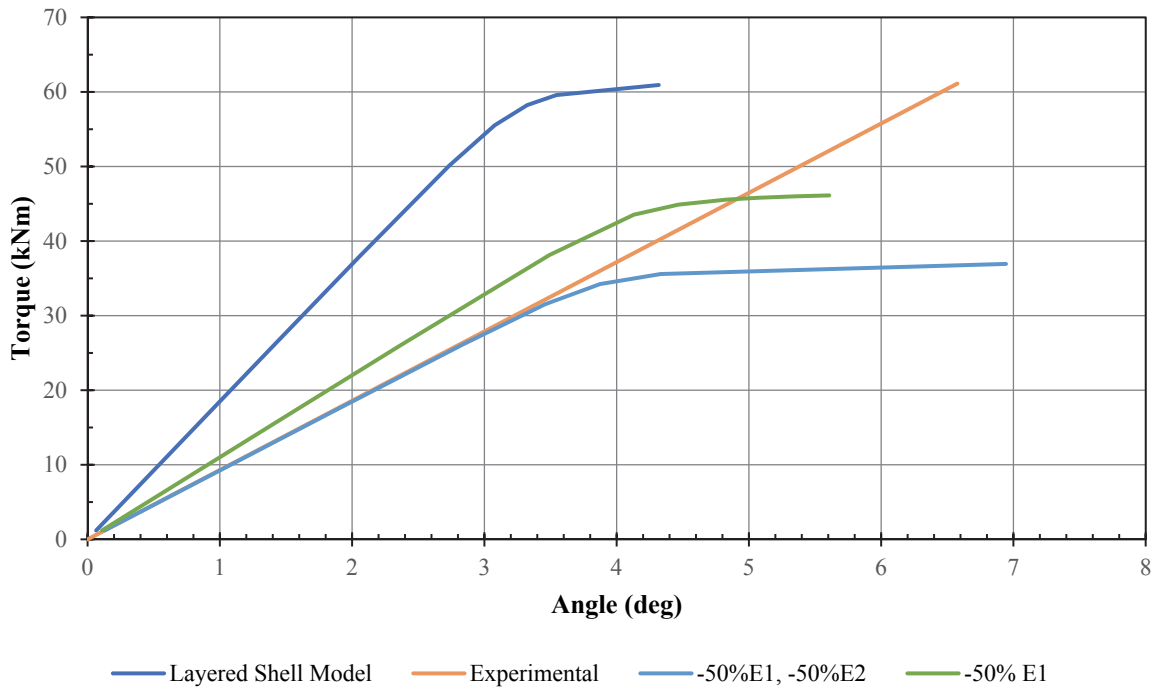
93

Torque vs Rotation

Fig. 2.29. Comparison between the downgraded E1 model and the downgraded E1 and E2 model

Shear moduli, G

The third attempt is the reduction of all shear moduli G12, G23 and G13 by 50% and 90%.
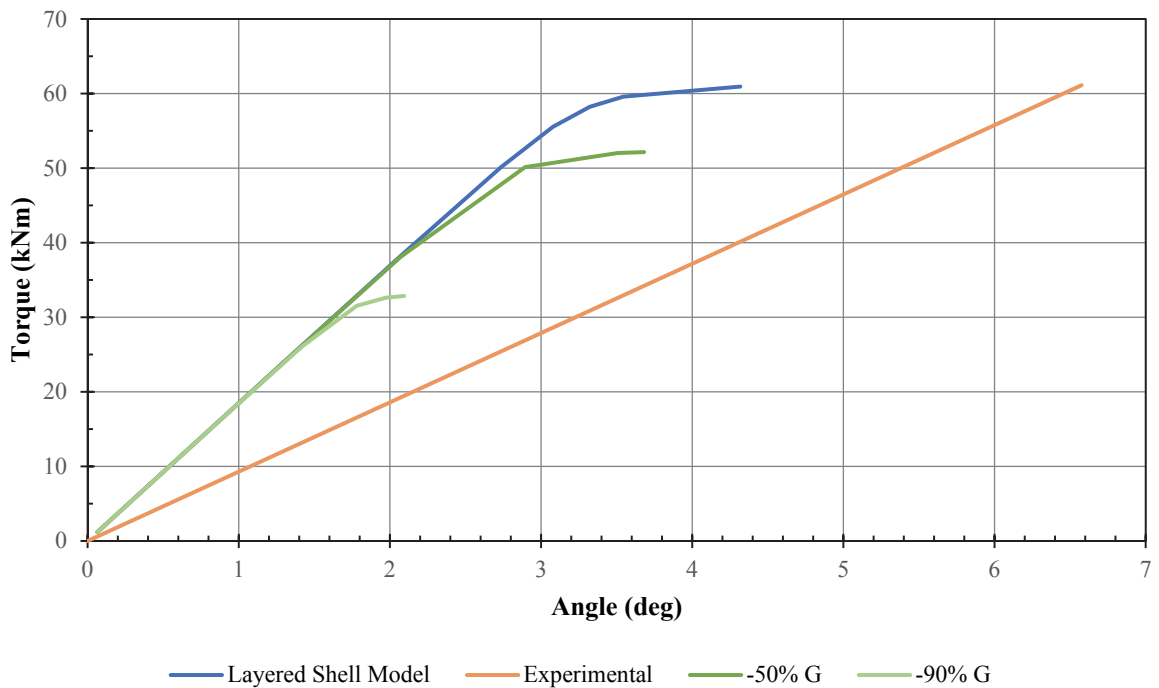
Torque vs Rotation

Fig. 2.30. Comparison between the layered shell model, the downgraded model and the experimental results

Figure 2.30 shows that the reduction of the shear moduli even by 90% has no effect on the rotational stiffness of the shaft. The reduction by 50% results in a buckling load of about 50kNm and the reduction by 90% results in a buckling load of about 32 kNm.

2.6.2 Thickness

The thickness was also reduced in order to match the experimental rotational stiffness. The necessary reduction was 50%.
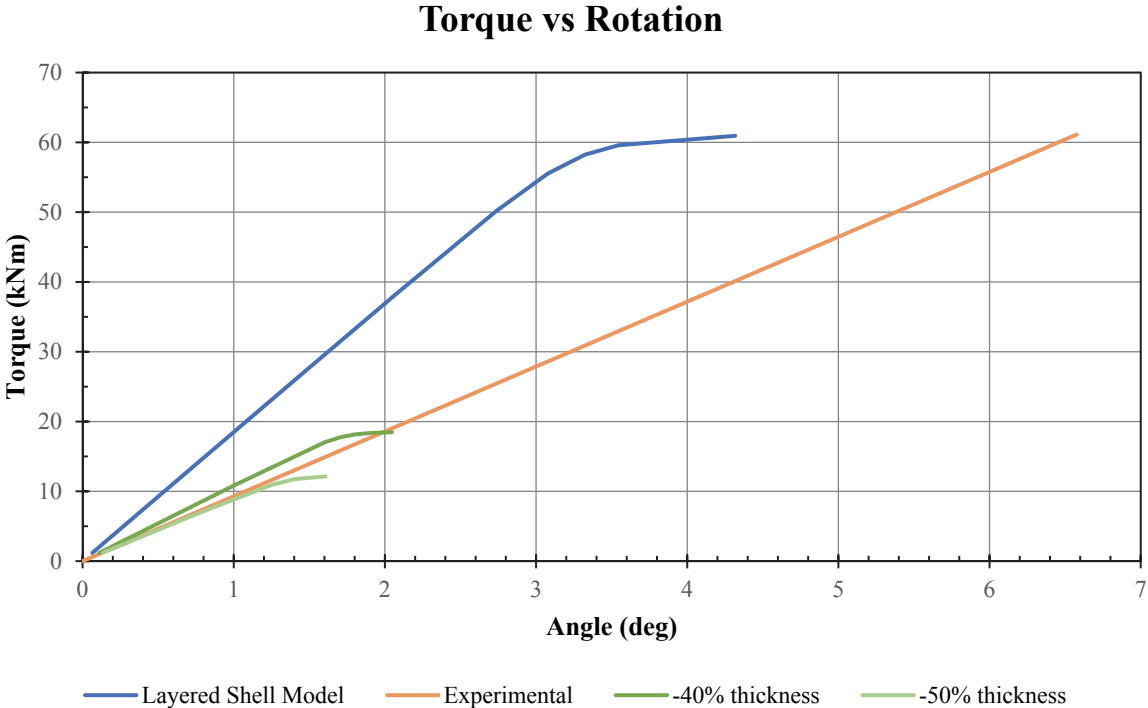
Torque vs Rotation

Fig. 2.31. Comparison between the layered shell model, the thinner model and the experimental results

Figure 2.31 shows that the reduction of the thickness of the shaft has drastic effect in the buckling load, which in the case of the reduction of the thickness by 50%, is a little higher than 10kNm. 40% reduction of the thickness of the shaft results in higher rotational stiffness than the experimental and the buckling load is around 18kNm.

2.6.3 Initial Imperfections

The effect of the size and the pattern of initial imperfections will also be investigated. As it has already been mentioned in section 2.2.2, the chosen size of the maximum initial imperfection that was used so far was 0.1% of the internal diameter of the shaft. The pattern used to generate the initial imperfections was the modeshape of the minimum eigenvalue. The analysis was run for 3 more different initial imperfections. The first two used the same pattern but with sizes of the initial imperfection equal to 0.01% and 1% of the internal diameter respectively. The third used all 10 modeshapes of the eigenvalue buckling analysis in order to generate the initial imperfection. The size of the maximum initial imperfection was 1% of Di. Figure 2.32 shows the results of these analyses.
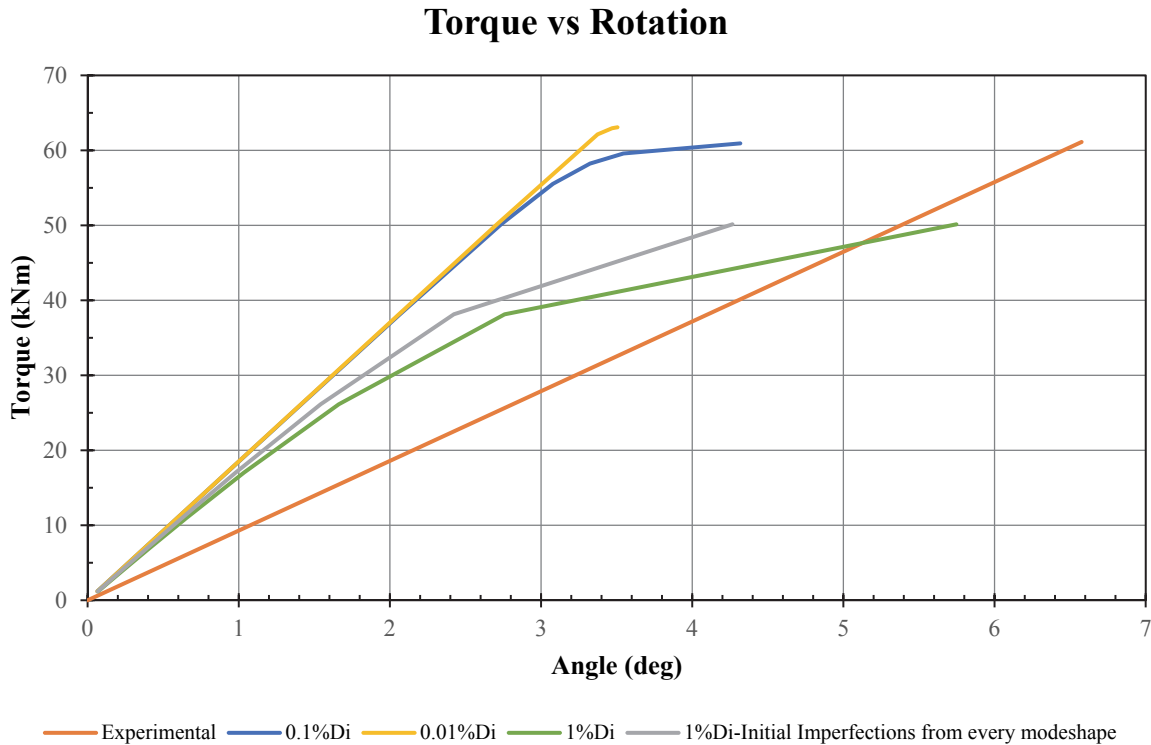
Torque vs Rotation

Fig. 2.32. Comparison between the models with the different initial imperfections.

From Figure 2.32., it can be seen that the two models with the smaller initial imperfections have almost the same rotational stiffness. The one with initial imperfection 0.01%Di buckles somewhere between 60 and 65 kNm, about 10 kNm higher than the one with 0.1%Di. Increase of the initial imperfection to 1%Di decreases a little the rotational stiffness and initiates buckling much earlier, somewhere between 30 and 35 kNm. The rotational stiffness remains significantly higher than the experimental. In the last case that all modeshapes were used for the generation of the initial imperfections, the rotational stiffness showed a slight decrease but was higher than the case with 1% of Di and lower than the other two cases with the critical modeshape imperfection pattern. Additionally, buckling started around 35kNm.

From this analysis, some conclusions can be reached. First of all, it showed that a within reasonable limits initial imperfection can't decrease the rotational stiffness enough to match the experimental rotational stiffness. It also showed that increasing the initial imperfection decreased the buckling load.

2.7 Conclusion and comments

Some interesting conclusions have been reached from the finite element analysis of the GFRP shaft. The layered shell model revealed its ability to quite accurately predict the buckling load of the shaft. The eigenvalue buckling analysis resulted in a buckling load 7% greater than the experimental one and the nonlinear buckling analysis resulted in a buckling load about 5% lower than the experimental one. The nonlinear analysis' buckling load highly depends on the chosen initial imperfection, as indicated by the sensitivity analysis. Both results can be considered as a reasonable estimation of the shaft's buckling load, with the latter being the more conservative and probably the more accurate of the two. However, the model predicted a much higher rotational stiffness of the shaft than the experimental one and this led to a thorough

investigation of the factors affecting this result. Additionally, the examined stresses showed a logical pattern and reasonable magnitudes until buckling initiation which led to their rapid increase. The Tsai-Wu failure criterion was also introduced and with the initial material strengths predicted a very low failure load. The sensitivity analysis showed that a very drastic increase of the strength in the direction normal to the fibers was necessary in order to predict a failure load near the experimental.

The modeling of the steel shaft and the comparison of its results with the analytical ones based on Young & Budynas, (2002), proved the validity of the model in the prediction of the mechanical behavior of a steel shaft.

The homogeneous model of the GFRP shaft yielded almost the same results with the layered shell model concerning the rotational stiffness. It also predicted tensile and compressive stresses of almost the same magnitude that are symmetrically developed about the x-axis. The existence of this symmetry is an indication that the homogeneous material modelling represents more accurately the real filament wound shaft. However, the homogeneous model lacked the ability to calculate stresses in the direction of the fibers as well as the ability of the direct application of failure criteria due to the lack of material strengths for the homogeneous material.

The layered solid model of the GFRP shaft yielded almost identical results with the layered shell model, leading to the conclusion that for thin-walled layered composite shaft applications the extra computing cost of layered solid modelling offers no benefits.

Finally, the sensitivity analysis showed that E1 had to be decreased by 60% in order to match the experimental rotational stiffness of the shaft and the buckling load dropped to about 40kNm. Reducing both E1 and E2 by 50% matched the experimental rotational stiffness and lowered the buckling load between 30 and 35 kNm. Reduction of the shear moduli had insignificant effect on the rotational stiffness. Reducing them by 50% lowered the buckling load between 45 to 50kNm and reducing them by 90% lowered the buckling load at around 30kNm. The reduction of the thickness by 50% matched the experimental rotational stiffness and dramatically lowered the buckling load at around 10kNm. The size of the initial imperfection basically affects buckling initiation. The smaller the initial imperfection the higher the buckling load. Using all modeshapes to generate the initial imperfection triggers buckling later than considering only a same magnitude critical modeshape initial imperfection.

By carefully assessing the results of the whole analysis and mainly the results of the sensitivity analysis, it seems quite unlikely that any specific material mechanical property could be so much lower than the one given by the manufacturer in order to match the experimental rotational stiffness. Additionally, it is quite unfamiliar that the failure-buckling load of the shaft is approximated quite accurately whereas the rotational stiffness is almost 90% higher than the experimental. Consequently, some doubts arise mainly about the correct interpretation of the experimental data and the accurate knowledge of the material properties-winding pattern-thickness distribution combination that unfortunately could not be answered during the elaboration of the diploma thesis.

CHAPTER 3
TORSION TEST AND FINITE ELEMENT ANALYSIS OF THE CFRP SHAFT

3.1 Introduction

3.1.1 CFRP shaft specifications

The B&T Composites Carbon Fiber Reinforced Polymer (CFRP) shaft is a power transmission shaft that was manufactured by the composite manufacturing company B&T Composites in Florina, Greece (http://www.btcomposites.gr/). Its manufacturing method is filament winding, its winding pattern is $[\pm12/+85/\mp12_2/-85/\pm12_2/+85/\mp12_2/-85/\pm12_2/+85/\mp12_2]$, its main dimensions are presented in Table 3.1 and a view of the shaft is displayed in Figure 3.1.

Table 3.1. Dimensions of the Shaft

Length (with couplings) (m)	Internal diameter (m)	External Diameter (m)	Thickness (m)
3	0.200	0.210	0.005

Fig. 3.1. A view of the shaft

According to the manufacturer, the fiber system is the Torayca T700S fiber (www.torayusa.com) and the epoxy matrix system is the Araldite LY 556 epoxy resin combined with Aradur 917 anhydride hardener and imidazole Accelerator DY 070 from Huntsman Advanced Materials (www.huntsman.com/advanced_materials). The shaft was manufactured under constant temperature and humidity conditions (18ºC/48% humidity) and was polymerized in a polymerization oven according to the material provider instructions. Additionally, the couplings were bonded and subsequently bolted to the shaft ends according to their manufacturer's specifications.

The mechanical properties of the composite material were provided by experimental data provided by the Shipbuilding Technology Laboratory of NTUA and are the following:

$$E_1 = \quad 143.7 \quad GPa$$
$$E_2 = \quad 9.2 \quad GPa$$
$$G_{12} = \quad 3.4 \quad GPa$$
$$v_{12} = \quad 0.32$$

Assumptions based on literature information were made for the determination of the rest of the mechanical properties required for modelling. Some of the information resources are: (Christensen, 1979), (Jones, 1975), and the experimental data of the Shipbuilding Technology Laboratory (NTUA). All the properties are summarized in table 3.2.

$$E_3 = E_2 = 9.2 \text{ GPa} \tag{3.1a}$$

$$G_{13} = G_{12} = 3.4 \text{ GPa} \tag{3.1b}$$

$$G_{23} = 0.5 G_{12} = 1.7 \text{ GPa} \tag{3.1c}$$

$$v_{21} = v_{12} \frac{E_2}{E_1} = 0.0205 \tag{3.1d}$$

$$v_{23} = v_{12} \frac{1 - v_{21}}{1 - v_{12}} = 0.46 \tag{3.1e}$$

$$v_{13} = v_{12} = 0.32 \tag{3.1f}$$

Table 3.2. Mechanical Properties of the GFRP

E_1 (GPa)	143.7
E_2 (GPa)	9.2
E_3 (GPa)	9.2
G_{12} (GPa)	3.4
G_{23} (GPa)	1.7
G_{13} (GPa)	3.4
v_{12}	0.32
v_{23}	0.46
v_{13}	0.32

3.2 Torsion test of the CFRP shaft

3.2.1. Experimental Set-up.

The torsion test of the CFRP shaft took place at the facilities of B&T Composites in Florina, Greece, in October 2015. The torque was applied to the shaft by a mechanical torsion in-house

manufactured fixture that is presented in Figure 3.2. The distance between the two blocks that are shown in the drawing is variable so that shafts of different lengths could be fitted and tested. Figure 3.3 shows the CFRP shaft fitted on the torsion fixture.
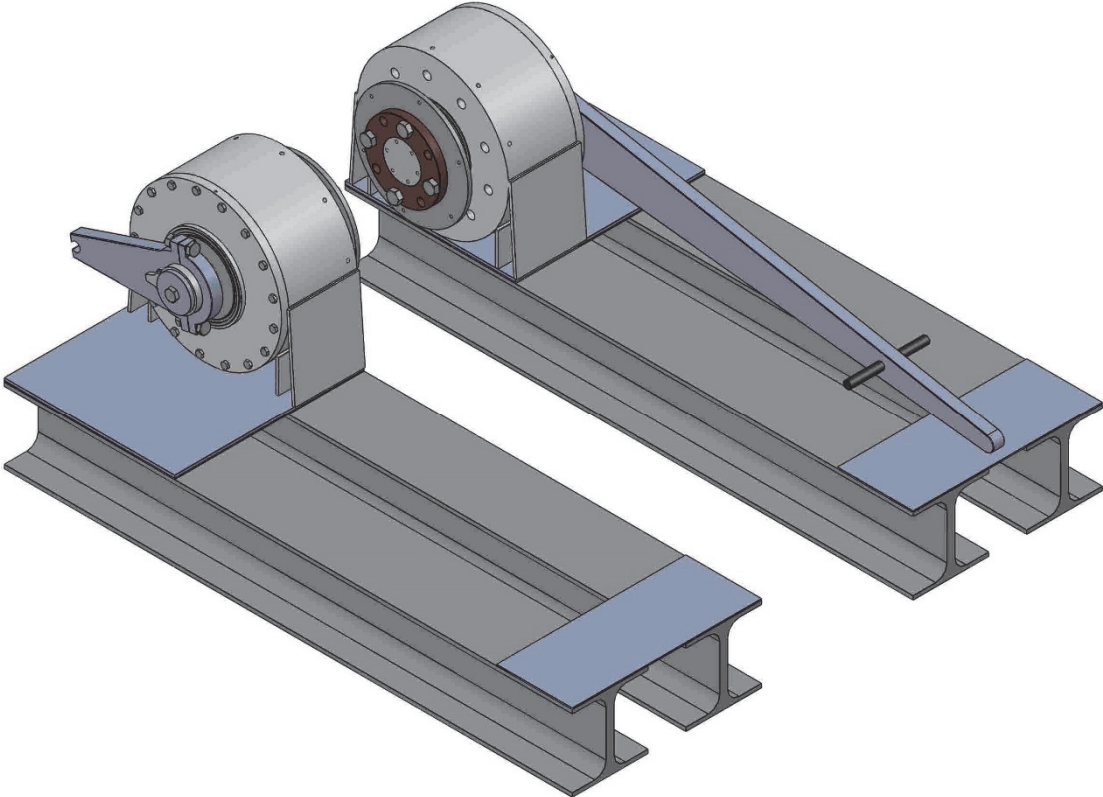

Fig. 3.2. Torsion test fixture

Fig. 3.3. The CFRP shaft fitted to the torsion fixture

One end of the shaft, the right one as shown in figure 3.3, was fixed and the other one was rotated by a lever that was lifted by a hydraulic piston. The distance between the center of the

100

shaft and the piston was 1 meter. Additionally, the force of the piston that lifted the lever was always vertical, so the normal to the lever component of the force which was responsible for the torque application had to be calculated, in order to correctly calculate the applied torque. The angle between the measured force, which is vertical and the component of the force normal to the lever was 15º (degrees) so $F_{normal}=F_{measured} \cdot \cos(\theta+15º)$, where θ is the angle of rotation of the shaft. The rotating part of the fixture can be better seen in Figure 3.4 that shows the side view of the torsion set-up.

Fig. 3.4. Side view of the torsion machine

The force of the piston that lifted the lever was measured via a digital force sensor with a sampling frequency of 1 Hz. The angle of rotation of the shaft was measured by a clinometer that was fixed at the center of the rotating end of the shaft. The sampling frequency of the clinometer was also 1 Hz. In addition, strain gages were installed in specific positions of the shaft's external surface, in order to measure both longitudinal and circumferential strains during the loading procedure and thus getting an idea of the global structural response of the shaft. The circumferential strain gages would provide information about the displacement of the cross section of the shaft, whereas the longitudinal strain gages would provide information about the longitudinal displacements of the shaft as well as the evolution of the buckling modeshape. A strain gages scheme, showing the positions and the type of each gage is presented in Figure 3.5. Figure 3.6 shows a picture of a biaxial rosette type strain gage that is used at the positions that strains in both directions are measured.
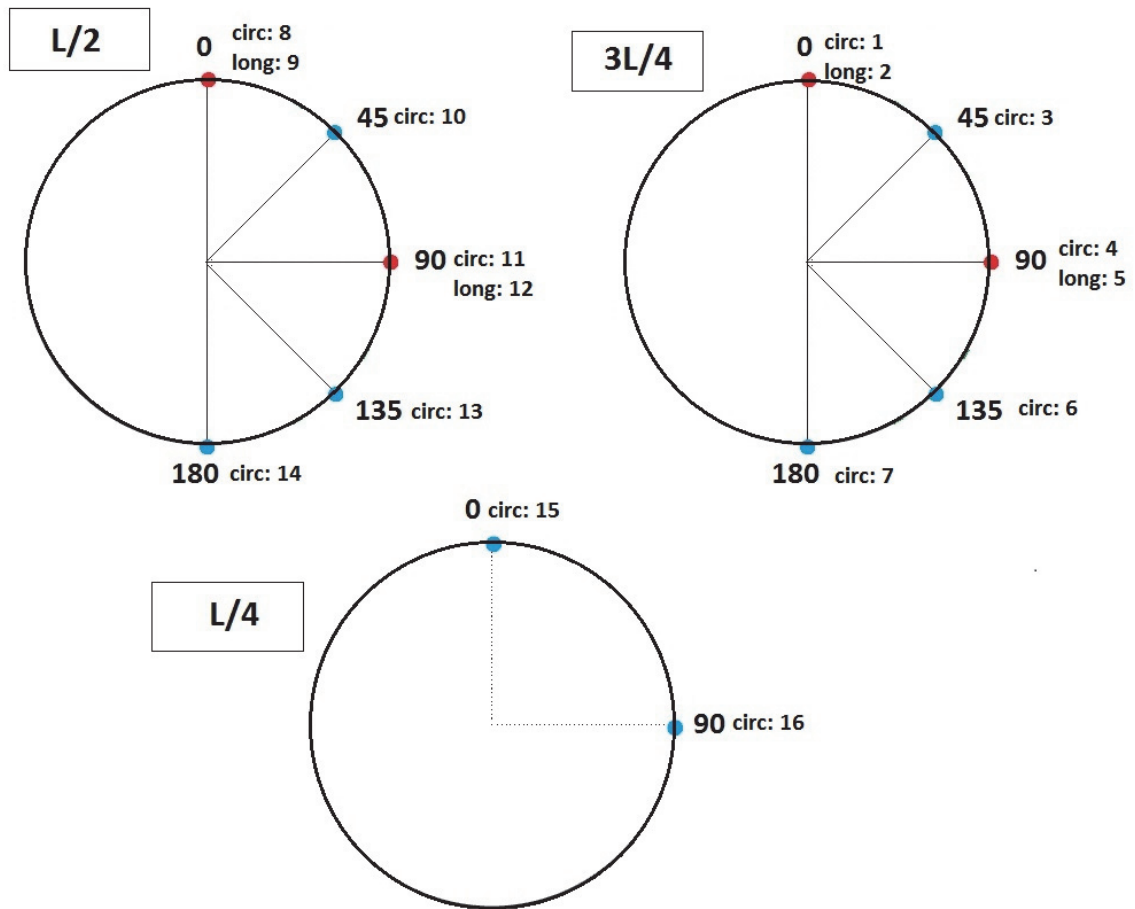
Fig. 3.5. Strain gages scheme showing the gage type and position at three cross sections of the shaft, namely L/4, L/2, 3L/4
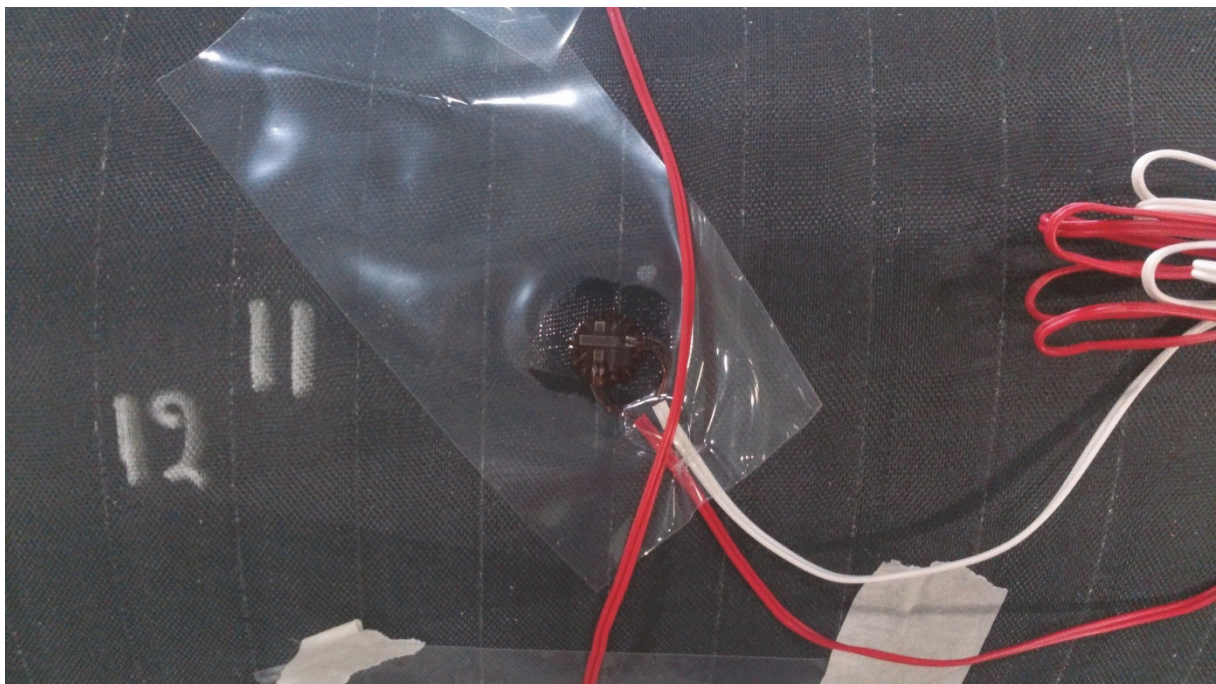

Fig. 3.6. Biaxial 0°/90° stacked rosette type strain gage

In Figure 3.5, notations "circ." and "long." refer to sensors measuring strains at the circumferential and the longitudinal direction of the shaft, respectively, whereas notations "L/4", "L/2" and "3L/4" refer to transverse sections of the shaft, in a distance of L/4 from the fixed end, at mid-length of the shaft (L/2) and in a distance of 3L/4 from the fixed end, respectively. In Figure 3.6 the wired shaft fitted to the torsion machine just before testing is presented.

Fig. 3.6. The shaft right before the beginning of the test.

After the fitting of the shaft to the torsion machine and the setting up of the measuring instruments, the torque was applied to the shaft. The lever that rotated the shaft was lifted by the hydraulic piston. Control of the lift of the lever was achieved manually by regulating the hydraulic pump that raised the piston. The loading procedure involved a force increase at the piston from 0 up to approximately 24.4 kN with an average rate of 2.60 kN/min. The corresponding torque at the shaft was 20.25 kNm and the average rate 2.14 kNm/min.

3.2.2. Experimental Results

The test was intended not to be catastrophic as per manufacturer's request. A preliminary FE analysis was conducted and showed that the failure torque of the shaft is around 42 kNm. The maximum applied torque was 20.25 kNm, as it has already been mentioned, so that the shaft would not be in risk of failing. It must be noted that the experimental results were processed in order to be presented due to complexities of the experimental set-up.

Figure 3.7 represents the evolution of the applied torque versus time. The manual application of the torque led to some variations on the rate of its increase. These variations can be seen in Figure 3.7.
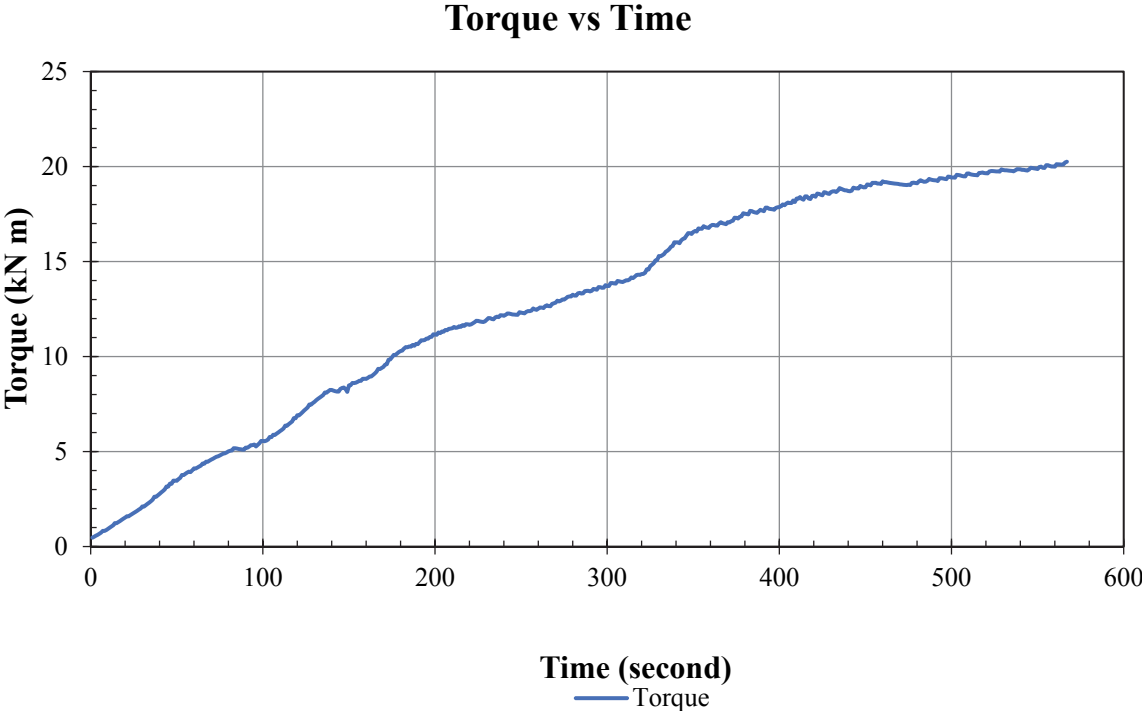
Torque vs Time

Fig. 3.7. Applied torque vs time

Figure. 3.8 represents the evolution of the angle of rotation of the rotating end of the shaft versus time. The remarks concerning the variation of the torque increase rate apply also to the angle of rotation.
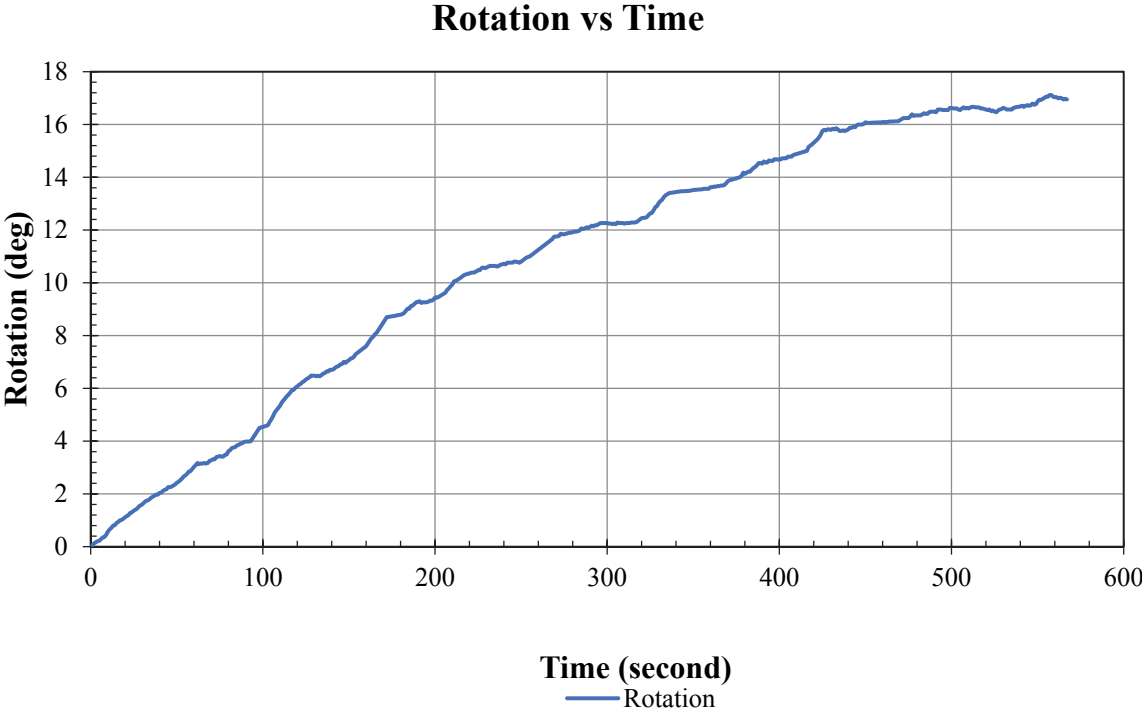
Rotation vs Time

Fig. 3.8. Rotation vs time

104

Figure 3.9 represents the torque vs rotation diagram from which the rotational stiffness of the shaft can be estimated.

Torque vs Rotation
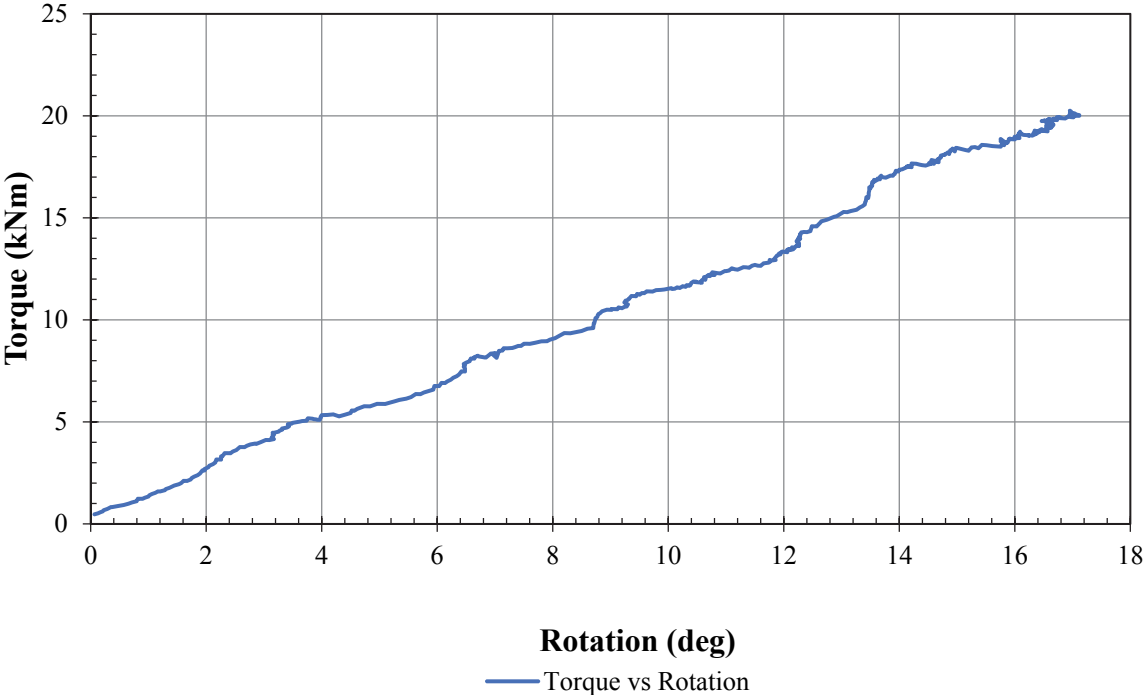
Fig. 3.9. Torque vs rotation

The rotational stiffness of the shaft is about 1.17 kNm/deg, as calculated by Figure 3.9.

The following Figures 3.10 to 3.14 present the variation of all the measured strains versus the applied torque. Each Figure corresponds to either circumferential or longitudinal strains at every cross section.

Circumferential Strains vs Torque at 3L/4
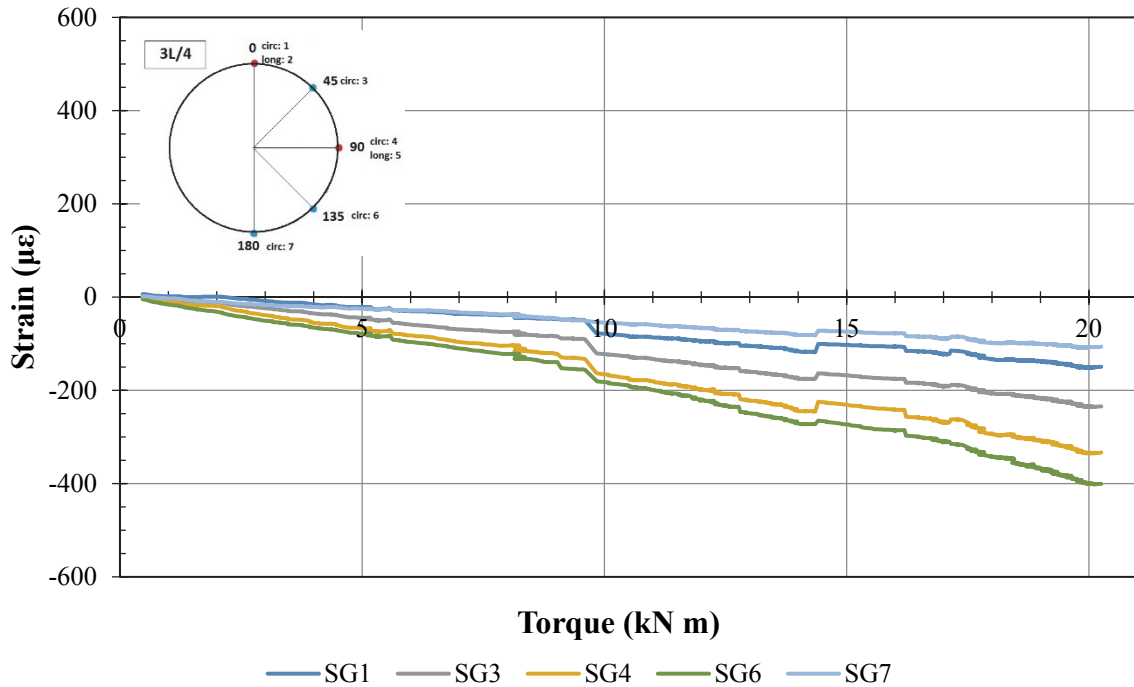
Fig. 3.10. Circumferential strain measurements at cross section 3L/4.
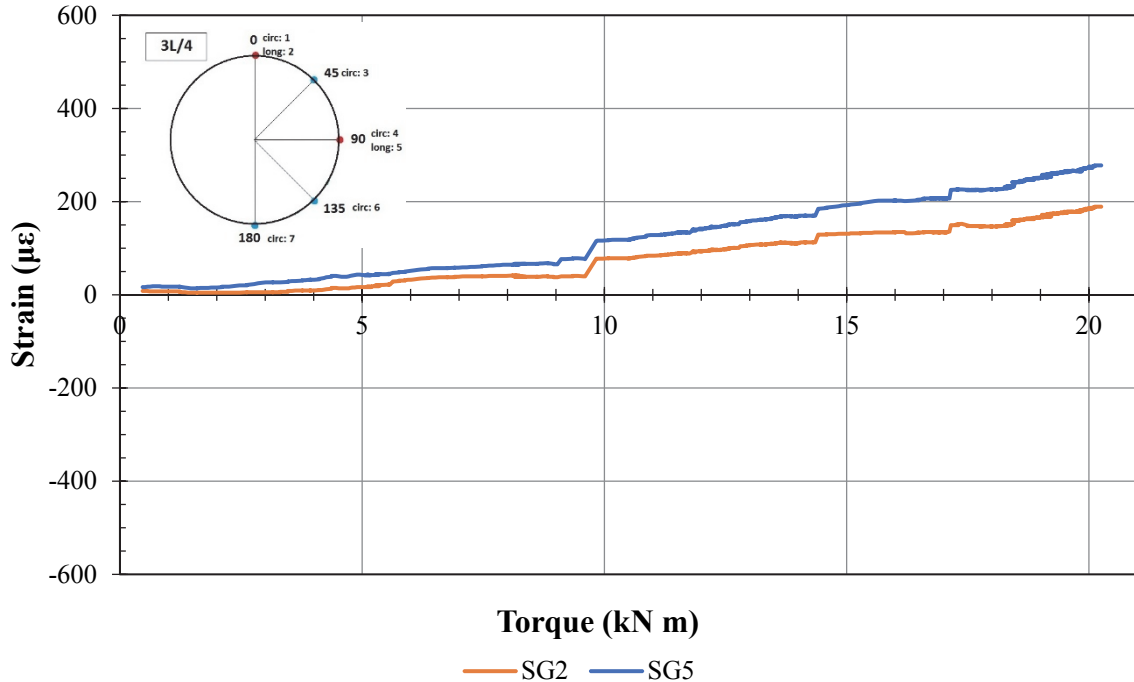
Longitudinal Strains vs Torque at 3L/4

Fig. 3.11. Longitudinal strain measurements at cross section 3L/4.

At cross section 3L/4, the minimum circumferential strains reaching -400 µε, were measured by strain gage 6, which was positioned at 135º position according to the gage scheme (Fig. 3.5). All measured circumferential strains are compressive indicating that the shaft is mainly compressed in the circumferential direction at this cross. The maximum longitudinal strains

were measured by strain gage 5 at 90 degrees and reached approximately 300 µε. Both longitudinal strain gages measured tensile strains, indicating that the shaft is mainly under tension in the axial direction as far as the 3L/4 cross section is concerned.
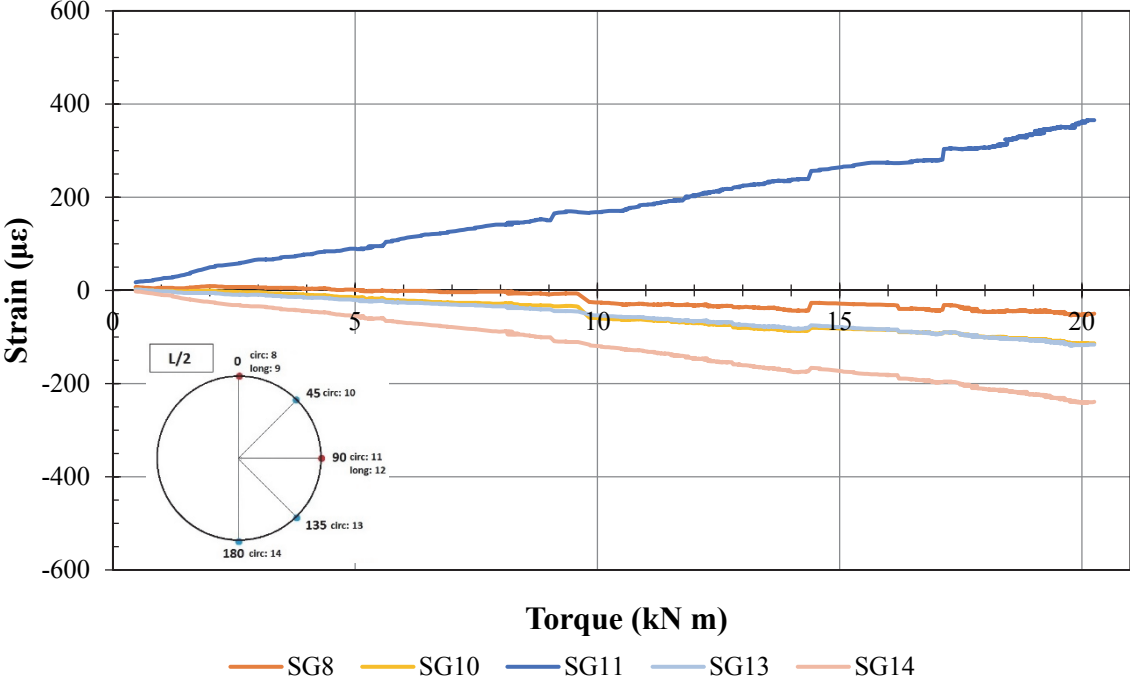
Circumferential Strains vs Torque at L/2

Fig. 3.12. Circumferential strain measurements at cross section L/2.

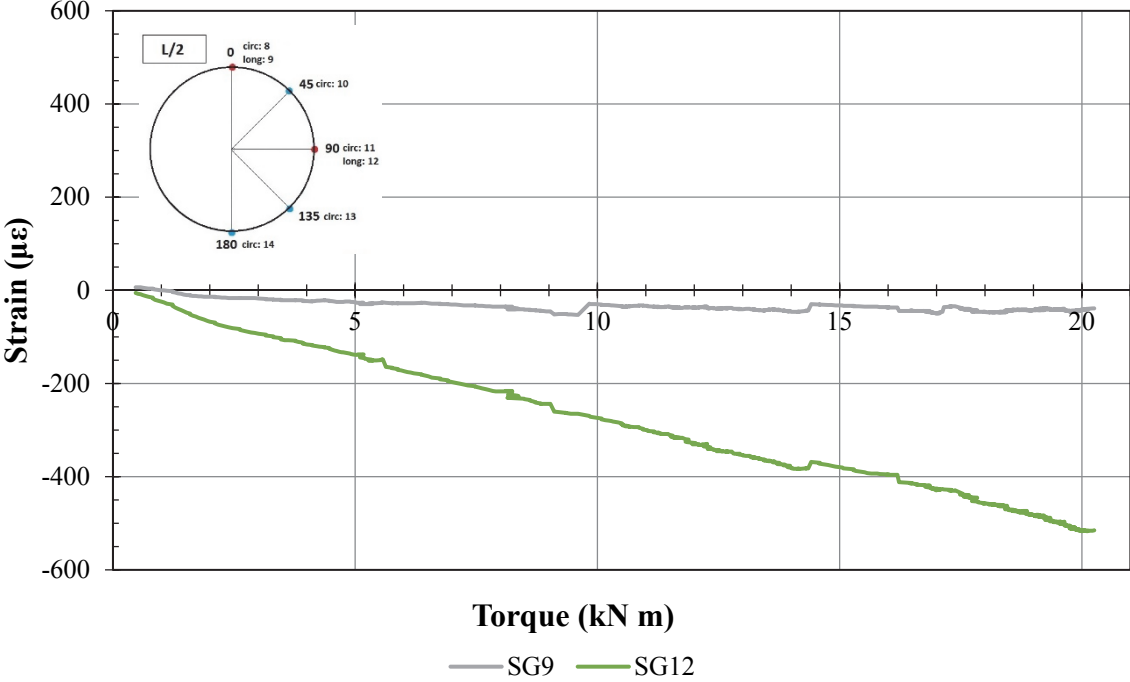## Longitudinal Strains vs Torque at L/2

Fig. 3.13. Longitudinal strain measurements at cross section L/2.

At cross section L/2, the minimum circumferential strains reaching -250 με were measured by strain gage 14, which was positioned at 180°. The maximum circumferential strains were measured by strain gage 11 at 90° and reached 350 με. All measured circumferential strains are compressive apart from strain gage 11 which measured tensile strains. This indicates that for the applied load the shaft is mainly compressed in the circumferential direction at this section. The fact that strain gage 11 measured tensile strains also implies that it is positioned near a forming crest.

The minimum longitudinal strains were measured by strain gage 12, at 90 degrees and reached approximately 500 με. Longitudinal strain gage 9, measured very low strains similarly to circumferential strain gage 8 at the same position. The last observation indicates that the position of strain gages 8 and 9 is near the cross section points that retain their initial position on the cylinder's circumference. The measurement of strain gage 12 shows that at the position of the greatest measured tensile strains in the circumferential direction, the greatest compressive strains in the axial direction are also developed.
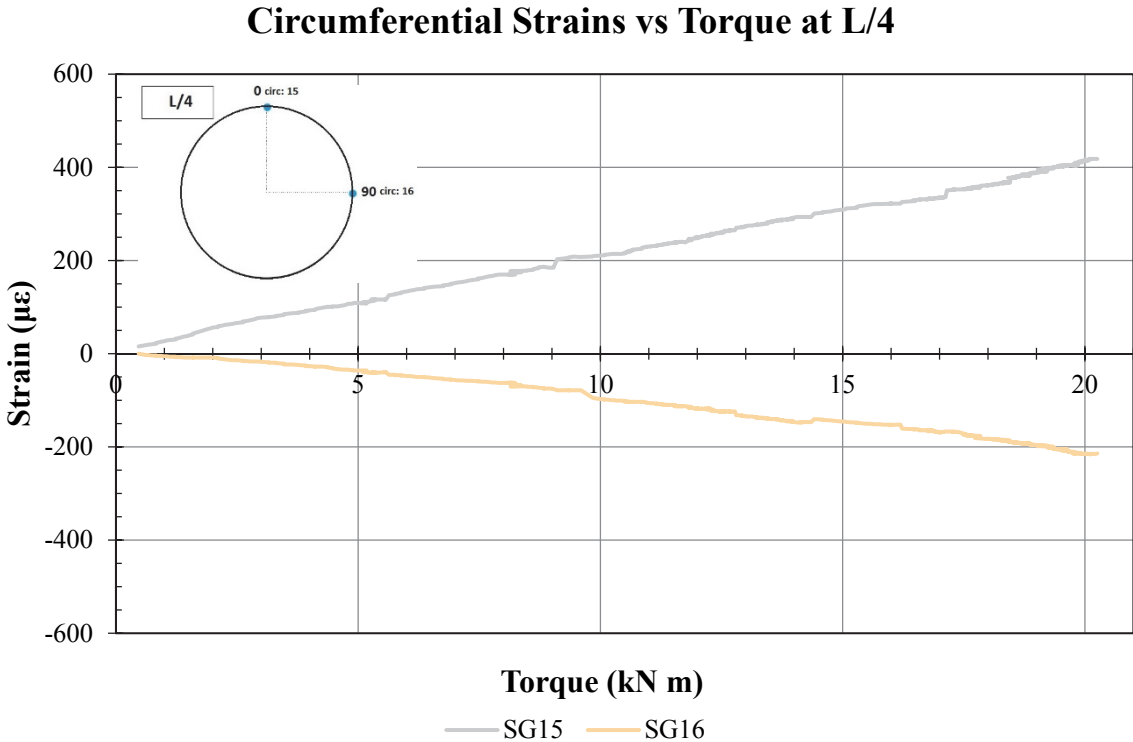

Fig. 3.14. Circumferential strain measurements at cross section L/4.

At cross section L/4, only circumferential strains at 0 and 90 degrees were measured. Strain gage 15 at 0° measured maximum tensile strain a bit higher than 400 με and strain gage 16 at 90° measured maximum strain a little lower than -200 με.

From Figures 3.10-3.14, it is confirmed that the torque applied to the shaft led to linear elastic deformations as it can be seen by the measured strains, where no signs of buckling exist. The maximum tensile circumferential strain was measured at cross section L/4 by strain gage 15 and was a little higher than 400 με and the maximum compressive was measured at cross section 3L/4 by strain gage 6 and was a little higher than -400 με. The maximum tensile longitudinal strain was measured by strain gage 5 at 3L/4 and was about 300 με and the maximum compressive was measured by strain gage 12 at mid-length and was about 500 με.

Due to the fact that the achieved torque was almost half of the predicted buckling torque, the specification of the modeshape that the shaft sustains during the evolution of the buckling phenomenon by the measured strains is quite difficult and uncertain. However, the measured circumferential strains at cross sections L/2 and L/4 provide a first indication that type 2 buckling modeshape, i.e. formation of two crests and two troughs around the circumference, is the most dominant modeshape to evolve during the buckling phenomenon. Figure 3.15 is extracted from the finite element analysis and shows a shaft buckled circumferentially in modeshape 2 and longitudinally in a wave length. It can be seen from this Figure that the circumferential strains on the external surface (as those measured) close to the two mid-length crests will have an always increasing tensile component as modeshape 2 evolves due to the local bending taking place there, whereas for exactly the same reason, strains close to the two mid-length troughs will have an always increasing compressive component as modeshape 2 evolves. It should be noted at this point that crests are circumferentially 90º apart from troughs in a type 2 modeshape buckling geometry, as it can be seen in Figure 3.15.

In Figure 3.12 that refers to cross section L/2, it can be observed that strain gage 11 has an always increasing tensile component, which means that it is in the area of a forming crest, whereas strain gage 14, that is 90º circumferentially apart from strain gage 12, has an always increasing compressive component, which means that it is in the area of a forming trough. A similar image can be seen in Figure 3.14 for strain gages 15 and 16 at cross section L/4. All the above are initial indications of the evolution of type 2 buckling modeshape.

Concerning longitudinal gage measurements, at cross section 3L/4 strain gages 2 and 5 both measured tensile strains, whereas all circumferential gages of the cross section measured compressive strains. At cross section L/2, strain gage 9 measured very low, almost insignificant compressive strains and so did its corresponding circumferential gage 8. This indicates that they are positioned at a node somewhere between a crest and a trough. Strain gage 12, measured large compressive strains of greater magnitude even from its corresponding circumferential gage 11, which was the only one from this section's gages that measured tensile strains. The fact that most measured longitudinal strains have the opposite direction of the corresponding circumferential strains was not expected, as one would expect that both would be either compressive or tensile near a forming trough or crest, respectively. However, the measurements imply that for loads much lower than the buckling load the aforementioned estimation is not true, and other global phenomena, like the axial compression of the shaft at mid-length, have a more significant effect.
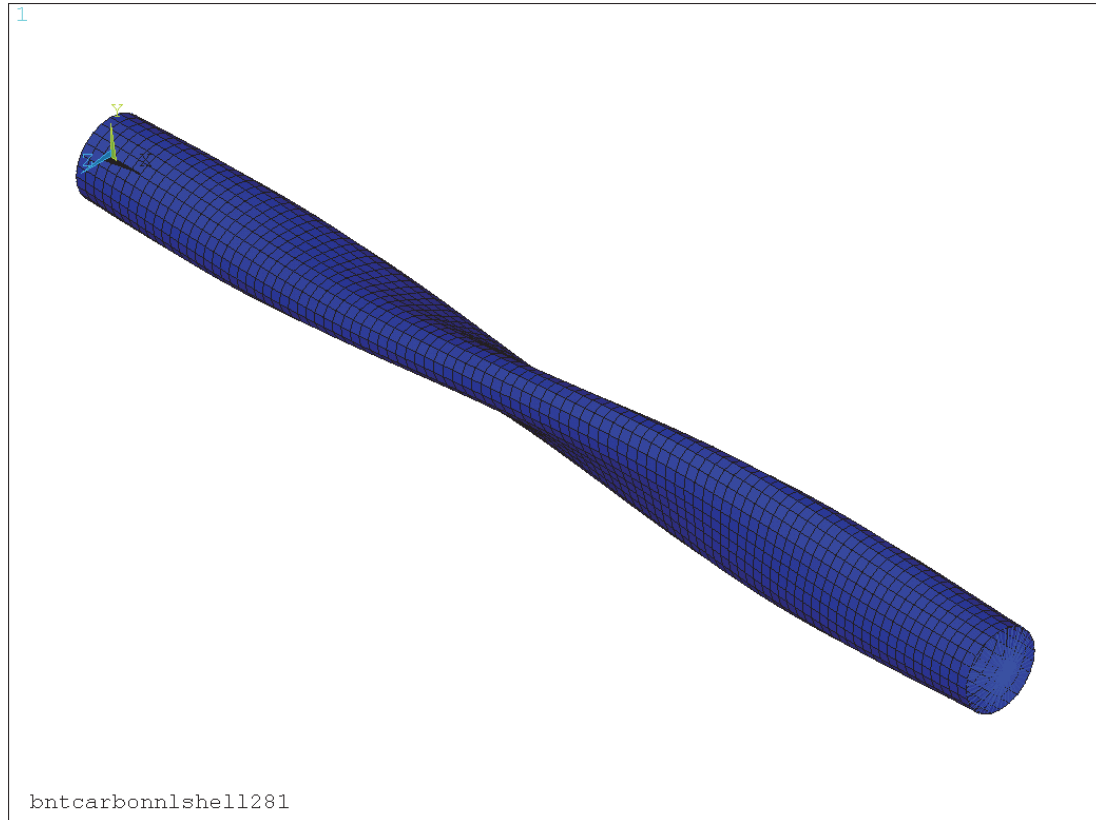
Fig. 3.15 Typical deformed shape of a shaft after modeshape 2 buckling

3.2.3. Conclusions

By the discussion of the experimental results, it is obvious that some valuable information about the mechanical behavior of the shaft can be drawn. First of all, the rotational stiffness of the shaft is calculated by the torque vs rotation diagram (Figure 3.9) and is about 1.17 kNm/deg. The strain gage measurements provide an idea of the deformations taking place. The circumferential strain gage measurements at L/2 and L/4 give a first indication that modeshape 2 is the most possible buckling modeshape that the shaft will sustain during buckling. Longitudinal strain gage measurements are in general opposite of the corresponding circumferential strains, something that was not expected but indicates that deformations other than the formation of crests or troughs, have a more significant effect for this loading level. A general conclusion is that given the opportunity, the shaft should be tested until failure in order to confirm the buckling and failure load as well as the buckling modeshape. Additionally, a useful improvement to the experimental set-up is the application of the torque by an automatic electric motor more powerful than the manual hydraulic piston in order to eliminate any variations of the rate of its increase and to increase the maximum applied torque possible.

3.3 Finite Element Analysis of the CFRP shaft

Alongside the torsion test, a numerical simulation was conducted using finite element analysis, in an effort to calibrate the numerical model by comparing its results with the experimental one. Having the experience of the finite element analysis of the GFRP shaft that was extensively discussed in the previous chapter, layered shell modeling was used for the finite element

analysis. Additionally, the CFRP shaft is relatively thin, as its thickness to diameter ratio is 2.5%, which insists on the suitability of layered shell elements. The element type used is the 8node structural shell element, SHELL281.

The developed finite element model is an evolution of the model developed for the GFRP shaft and implements both eigenvalue buckling analysis and nonlinear buckling analysis. It is reminded that there is a connection between the two, as the modeshapes of the eigenvalue buckling analysis are used as a pattern for the initial imperfections that are necessary for triggering nonlinear buckling. At first, in sections 3.3.1 and 3.3.2, the whole model will be shortly presented and only the differences from the GFRP shaft model will be further discussed. The APDL code of the model is available in appendix B. In the next sections, the results of both analyses are discussed and factors affecting these results, like for example material properties etc., are investigated.

3.3.1 Preprocessing

At first all necessary parameters were defined and the geometry of the shaft was created in the same manner as in the modelling of the GFRP shaft. The decision was taken to model the part of the shaft between its metal couplings, in order to avoid modelling the interaction between Steel and GFRP, without altering the problem.

```
/prep7              ! Enter the preprocessor
!* --------
!* GEOMETRY
!* --------
/units,si           ! Unit System SI
*SET,L,2.600        ! Length in m
*SET,Di,0.200       ! Internal diameter in m
*SET,t,0.005        ! Thickness in m
*SET,R,Di/2         ! Internal radius
*SET,Do,Di+(2*t)    ! External diameter
*SET,pi,acos(-1)    ! Set the Value of pi
```

The geometry was defined by creating 2 circles and connecting them with four lines, one for each quadrant, as it can be seen in Figure 3.16, and finally the cylindrical surface/area was created between the created lines, as it is displayed in fig 3.17.
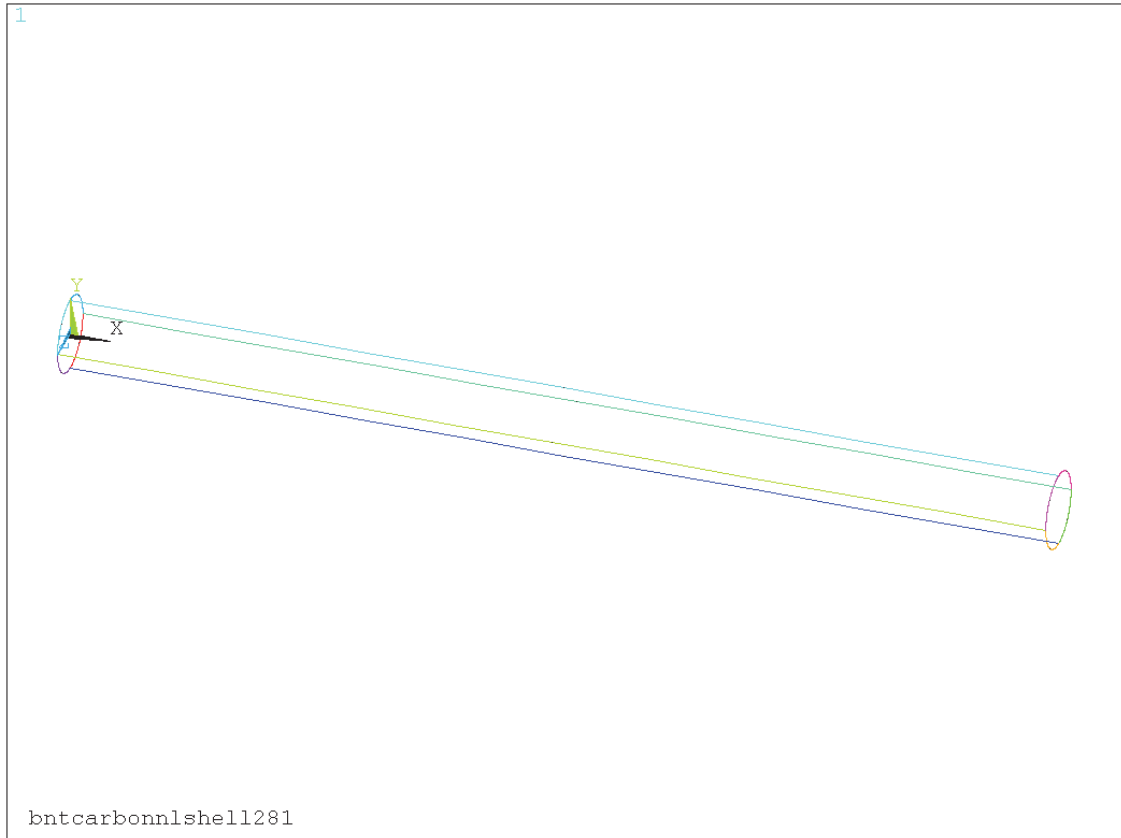
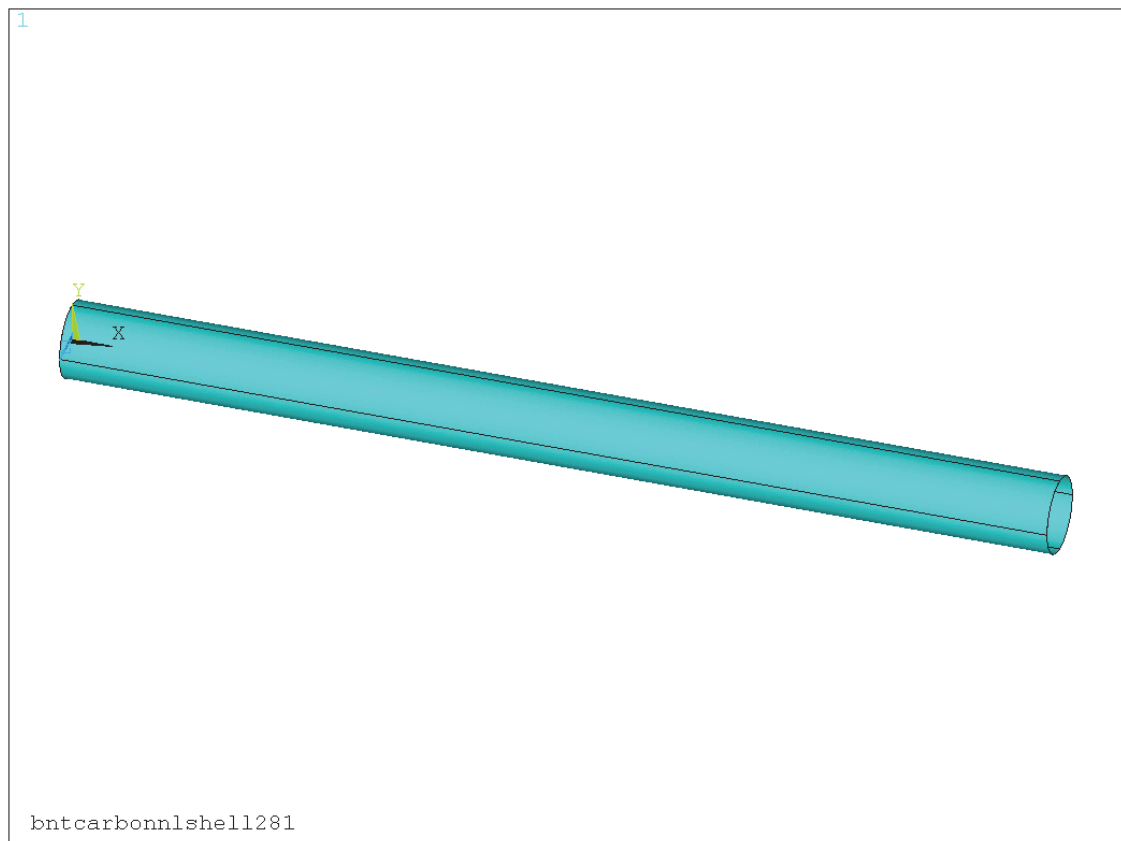Fig. 3.16. Plot of the lines that were drawn to create the areas.

Fig. 3.17. Plot of the final geometry.

112

After the creation of the geometry, the element type and its key-options were defined, as well as the material properties. As it is mentioned earlier, the chosen element type is SHELL281 and the material properties are all listed in table 3.2.

```
!* --------
!* ELEMENTS
!* --------
ET,1,SHELL281 !Define element type
ESYS,0         !Set the element coordinate system to global cartesian
!*
KEYOPT,1,1,0   !Element has both bending and membrane stiffness (default)
KEYOPT,1,8,2   !Store data for TOP, BOTTOM, and MID for all layers
KEYOPT,1,9,0   !No user subroutine to provide initial thickness (default)

!*-------------------
!* MATERIAL PROPERTIES
!*-------------------
MP,EX,1,143.7*1e9
MP,EY,1,9.2*1e9
MP,EZ,1,9.2*1e9
MP,PRXY,1,0.32
MP,PRYZ,1,0.46
MP,PRXZ,1,0.32
MP,GXY,1,3.4*1e9
MP,GYZ,1,1.7*1e9
MP,GXZ,1,3.4*1e9
```

In order to define multilayer SHELL281 elements, the shell section commands were used. As it is already mentioned in section 1.3, there are options available for specifying the thickness, material, orientation, and number of integration points through the thickness of the layers and are defined in this order by the SECDATA command. The command SECTYPE, that defines the type of the section, and SECOFFSET, that defines the starting point of the section were also used. Figure 3.18 shows the defined stacking sequence of the first 20 layers, as ANSYS cannot plot more than 20 layers. It is necessary to mention that the layup of the CFRP shaft is much more complicated than the GFRP shaft's layup, so the full section command set is listed.

```
!* --------
!* SECTIONS
!* --------

sectype,1,shell    !Defines type of section
secoffset,bot      !Starts the layup from the bottom of the section

!Stacking Sequence
![+-12/+85/-+12/-+12/-85/+-12/+-12/+85/-+12/-+12/-85/+-12/+-12/+85/-+12/-
! +12]

!Layer Thickness according to B&T Composites' measurements
tl1=0.00019    !thickness of first layer
tr=0.000145    !thickness of radial layers
tl12=0.000195  !thickness of 12deg layers
int.p=3        !number of integration points through thickness

!LAYER 1
Wangle=12
```

113

```
*do,Layer,1,2,1
   secdata,tl1,1, Wangle,int.p
   Wangle=-Wangle
*enddo

!LAYER 2
Wangle=85
*do,Layer,3,3,1
   secdata,tr,1, Wangle,int.p
   Wangle=-Wangle
*enddo
!LAYER 3-4
Wangle=-12
*do,Layer,4,7,1
   secdata,tl12,1, Wangle,int.p
   Wangle=-Wangle
*enddo

!LAYER 5
Wangle=-85
*do,Layer,8,8,1
   secdata,tr,1, Wangle,int.p
   Wangle=-Wangle
*enddo
!LAYER 6-7
Wangle=12
*do,Layer,9,12,1
   secdata,tl12,1, Wangle,int.p
   Wangle=-Wangle
*enddo

!LAYER 8
Wangle=85
*do,Layer,13,13,1
   secdata,tr,1, Wangle,int.p
   Wangle=-Wangle
*enddo
!LAYER 9-10
Wangle=-12
*do,Layer,14,17,1
   secdata,tl12,1, Wangle,int.p
   Wangle=-Wangle
*enddo

!LAYER 11
Wangle=-85
*do,Layer,18,18,1
   secdata,tr,1, Wangle,int.p
   Wangle=-Wangle
*enddo
!LAYER 12-13
Wangle=12
*do,Layer,19,22,1
   secdata,tl12,1, Wangle,int.p
   Wangle=-Wangle
*enddo

!LAYER 14
Wangle=85
*do,Layer,23,23,1
   secdata,tr,1, Wangle,int.p
```

```
    Wangle=-Wangle
*enddo
!LAYER 15-16
Wangle=-12
*do,Layer,24,27,1
    secdata,tl12,1, Wangle,int.p
    Wangle=-Wangle
*enddo
```
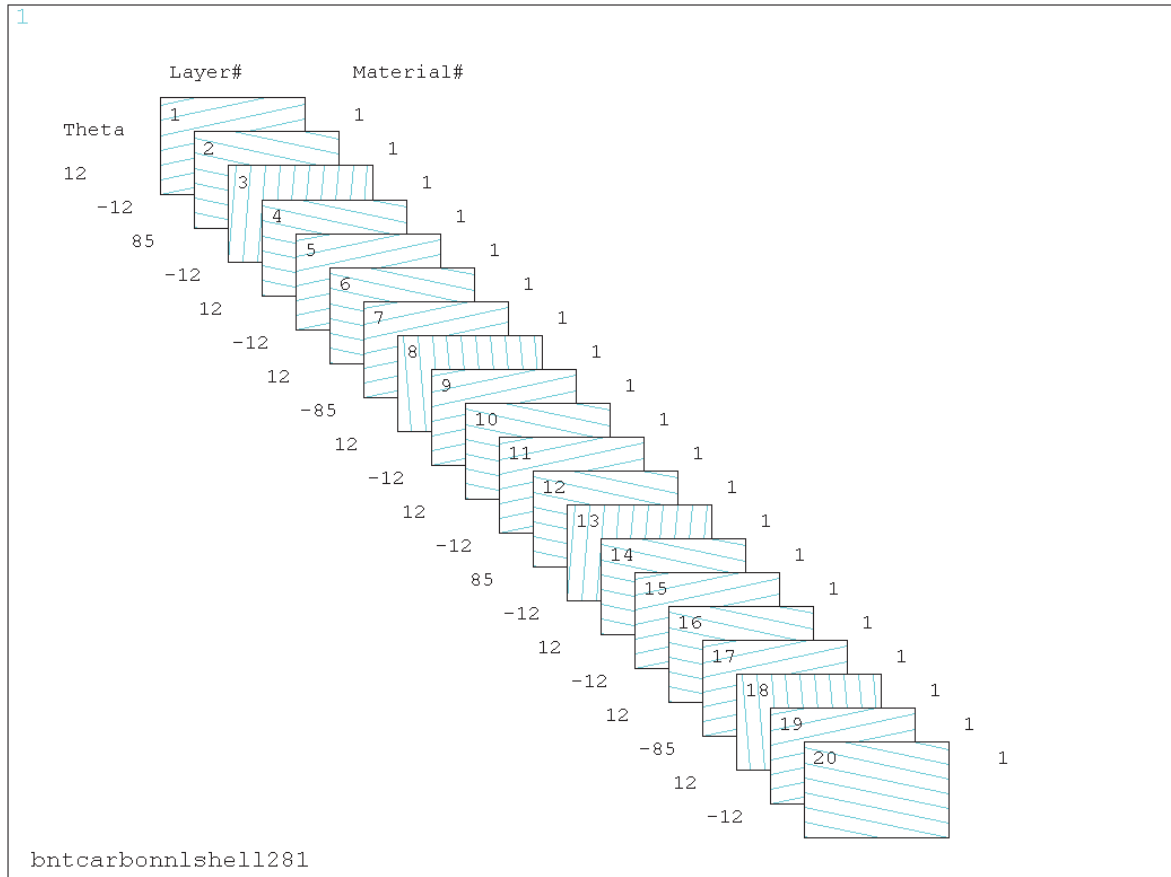

Fig. 3.18 Stacking Sequence of the first 20 layers of the Composite Material

The next task is the definition and creation of the mesh. Two parameters A and C are introduced defining the desired mesh density. The length of the shaft is divided by A and each quadrant of the circular edge by C. The aim is to create square or almost square elements. In order to achieve this, the ratios *Le=length/A* and *Ce=perimeter/(4·C)*, that correspond to the element length and width, must be almost equal. For the construction of the element mesh, an initial convergence analysis was carried out, resulting in selecting 100 equal length elements along the cylinder longitudinal axis and 24 along the circumference of the cylinder. This results in a mesh of 2400 elements. This selection leads to an element length and width equal to 0.026m. Further comment on convergence analysis is done later in, in section 3.3.4. Figure 3.19 represents the meshed geometry.

115

```
!* --------------
!* MESH DEFINITION
!* --------------
*SET,A , 100         ! Axial line mesh, Le=2.6/100=0.026m
*SET,C , 6           ! Circumferential Quadrant mesh,
                     ! Ce=2*pi*0.1/(6*4)=0.026m
!Longitudinal Lines
lesize,9 ,,,A,,,,,1 !Specifies the divisions and spacing ratio on unmeshed
lesize,10,,,A,,,,,1 !lines.
lesize,12,,,A,,,,,1
lesize,11,,,A,,,,,1
!Circumferential Lines
lesize,1,,,C,,,,,1
lesize,2,,,C,,,,,1
lesize,3,,,C,,,,,1
lesize,4,,,C,,,,,1
lesize,5,,,C,,,,,1
lesize,6,,,C,,,,,1
lesize,7,,,C,,,,,1
lesize,8,,,C,,,,,1
amesh,1,4,1 !area mesh
```
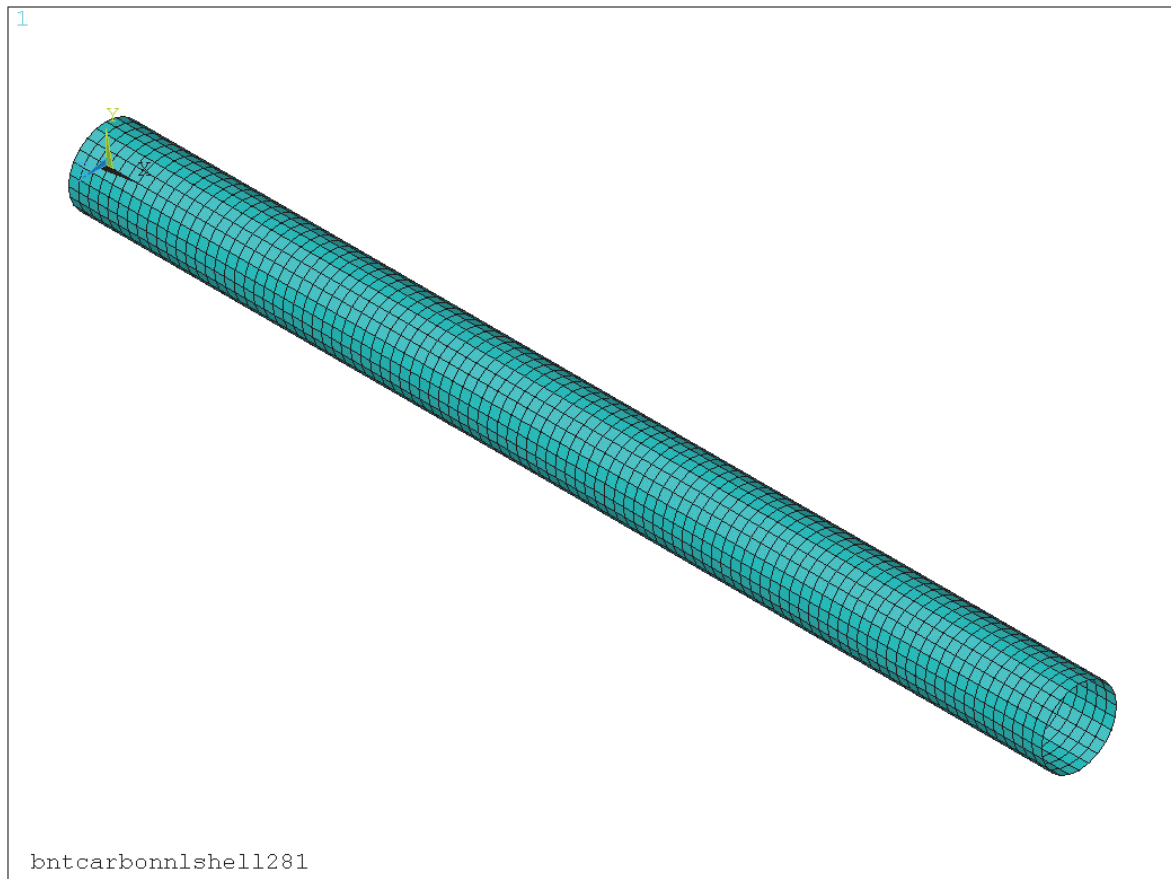

Fig. 3.19. Plot of the meshed geometry.

For the application of the torque to the one end of the shaft and for fixing the other end Multipoint Constraint elements were used. They were set to behave like rigid beams and they connected all nodes at the circumference of the one end with a master node at the center of the

circular end. This resulted in the creation of 120 MPC Elements and now the total Element number is 2520. Figure 3.20 represents the shaft with the MPC Elements.

```
!*------------------------------------------------------------
!*Creation of master node and mpc184 elements at the rotating end
!*------------------------------------------------------------
et,2,184      !Defines Element Type mpc184
keyopt,2,1,1 !Element Behaviour, K1=1 Rigid Beam, K2=1 Lagrange Multiplier
             !Method
nsel,all
csys,6
*get,nmpc,node,0,num,max  !Get the maximum node number and store it in nmpc
                          !parameter
*set,nmpc,nmpc+1          !Set parameter nmpc=nmpc+1
n,nmpc,0,0,L+0.02         !Create the master node
type,2                    !Set the Element Type to mpc184
seltol,1.0E-6             !Set the selection tolerance to 1.0e-6
nsel,s,loc,z,L            !Select all the nodes at the end of the shaft
*get,nnum,node,0,count    !Count the number of the nodes at the end
*get,ND,node,0,num,min    !Get the minimum node number at the end and store
                          !it in ND parameter

*do,i,1,nnum              !Loop for the creation of the MPC184
E,nmpc,ND                 !Create the element from nodes nmpc and ND
*SET,ND,NDNEXT(ND)        !Set ND to the next node number
*enddo

!*------------------------------------------------------------
!*Creation of master node and mpc184 elements at the fixed end
!*------------------------------------------------------------
nsel,all
csys,6
*get,nmpcf,node,0,num,max
*set,nmpcf,nmpcf+1
n,nmpcf,0,0,-0.02
type,2
nsel,s,loc,z,0
*get,nnum,node,0,count
*get,ND,node,0,num,min
*do,i,1,nnum
E,nmpcf,ND
*SET,ND,NDNEXT(ND)
*enddo
```
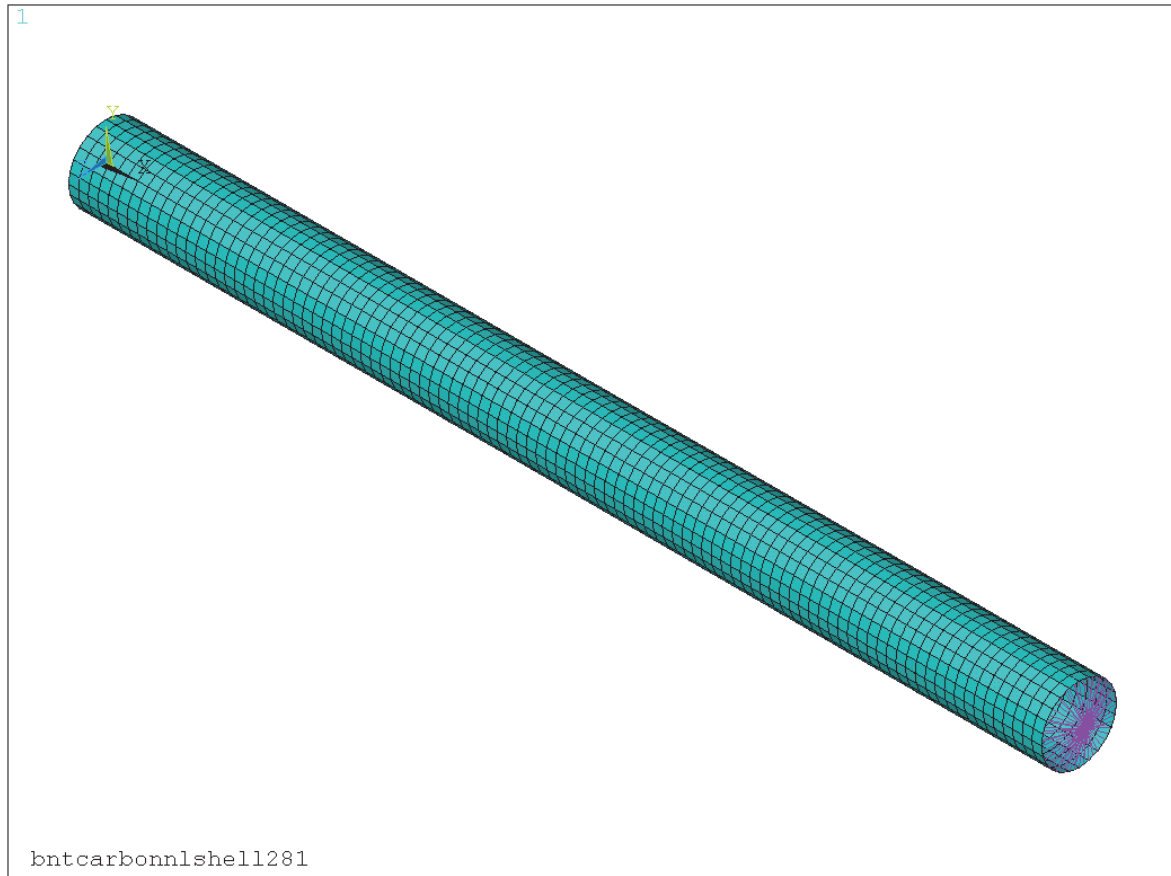
Fig. 3.20. Plot showing the MPC184 Elements.

The torque was applied to the master node and transferred through the MPC184 elements to the rest of the shaft. The master node was also constrained and allowed only to rotate around the x-axis. The other end of the shaft was considered fully fixed, by constraining all degrees of freedom (DOFs) of the second master node. All loads and constraints are shown in Figure 3.21.

```
!* ------------------
!* LOADS & CONSTRAINTS
!* ------------------
!Constraints on the fixed edge
Allsel              !Select everything
csys,0              !Set the active coordinate system to Global Cartesian
d,nmpcf,all,0       !Constrain all degrees of freedom
nsel,all            !Select all Nodes

!* --------
!* LOADS
!* --------
*SET,P , 21000    !Set the Torque to 21 kNm
!Torque
F,nmpc,MX,-P      !Apply the torque on the Master node
!Constraints on the master node
csys,0
D,nmpc,ux,0
D,nmpc,uy,0
D,nmpc,uz,0
D,nmpc,roty,0
D,nmpc,rotz,0
FINISH
```
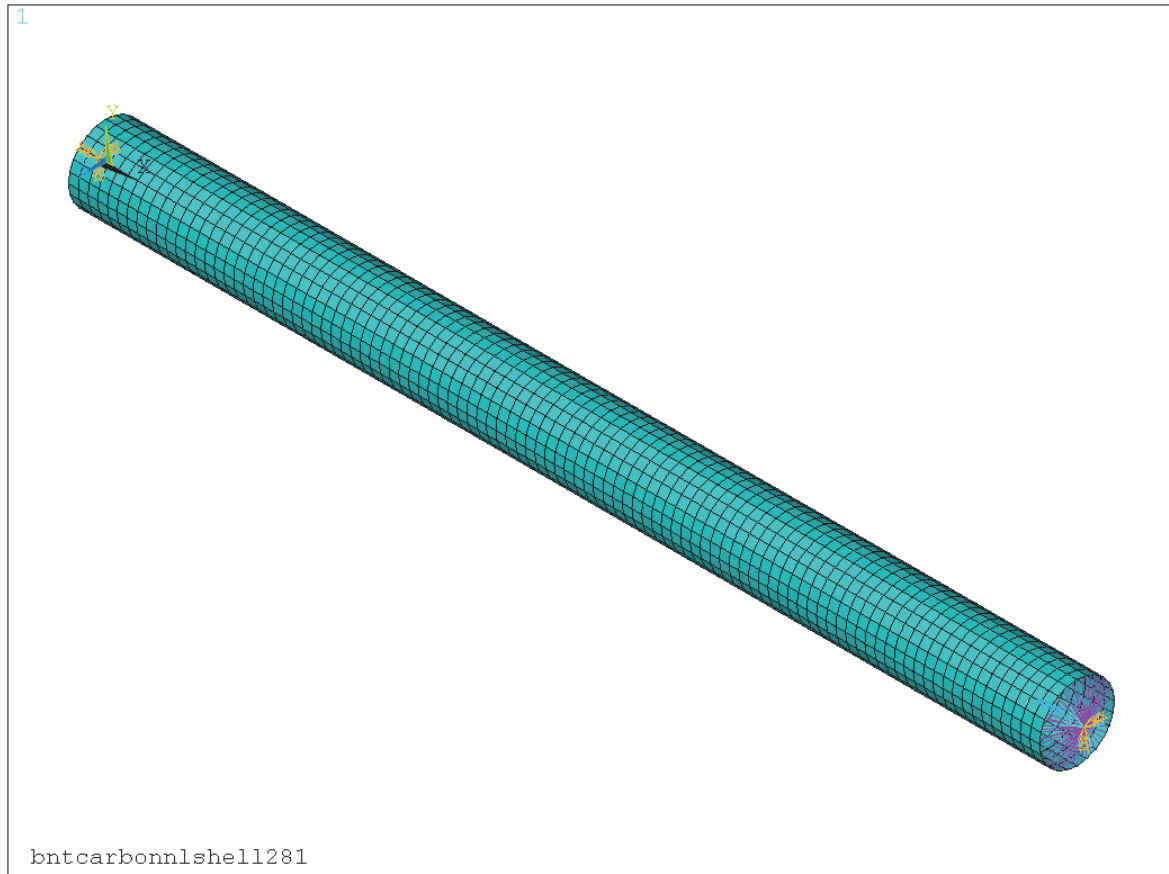
118

Fig. 3.21. Plot of the shaft with its boundary conditions and the torque applied on the master node.

3.3.2 Solution

The expected failure mode of the shaft is rotational buckling. Both eigenvalue buckling and nonlinear buckling analysis were conducted. Concerning the nonlinear buckling analysis, the chosen initial deformation pattern is the modeshape of the minimum eigenvalue and the size of the maximum imperfection is 0.1% of the internal diameter of the shaft. Different patterns and sizes of the initial imperfection are examined later in section 3.3.3.

Eigenvalue Buckling Analysis

Concerning eigenvalue buckling analysis, a random torque needs to be applied for the calculation of the eigenvalue buckling load. In the current analysis the applied torque is 21kNm, as it was mentioned in the previous section, and the buckling loads of the first 10 modeshapes are calculated. The lowest of the calculated buckling loads and the corresponding modeshape are the critical. A linear static solution is necessary prior to the eigenvalue buckling analysis.

```
!*--------
!*SOLUTION
!*--------

!FIRST STEP

!Linear Static Solution
/SOL
ANTYPE,STATIC          !Analysis Type: Static Analysis
```

119

```
NLGEOM,OFF              !Large deflection effects OFF

allsell
OUTRES,ERASE            !Resets OUTRES specifications to their default
                        !values.
OUTRES,ALL,ALL          !Writes all solution items for every substep.
SOLVE
FINISH

!Eigenvalue Buckling Analysis
/SOLU
OUTRES,ALL,ALL
ANTYPE,1                        !Analysis type: Eigenvalue Buckling Analysis.
BUCOPT,LANB,10,0,1,CENTER !Specifies buckling analysis options.
                               !10 Mode Shapes Extracted
SOLVE
FINISH

!Expansion Pass
/SOLU
!*
EXPASS,1
MXPAND,10,0,0,1,,               !Expand the 10 modes of the Buckling Analysis
SOLVE
FINISH
```

After the eigenvalue buckling analysis, the general post-processing menu is entered in order to review and assess how realistic the buckling mode shapes of the shaft and the buckling loads are. The magnitude of the displacements is also taken into account, in order to calculate the factor that will produce the desired geometric imperfections necessary for the nonlinear buckling analysis.

The results of the eigenvalue buckling analysis are listed in table 3.3. The buckling loads are the product of the applied torque (21kNm) multiplied by the buckling factor. All eigenvalue buckling factors are double which implies that the structure can buckle at the same load with a similar mode shape. After reviewing the double mode shapes, it is obvious that they are exactly the same in terms of magnitude of displacement and pattern but they differ in the angular position of their crests and troughs. In simple terms, they look like the same mode shape rotated around the x-axis. The form of the buckled shaft at the critical buckling load is displayed in Figure 3.22. The first eight modeshapes form only one crest along the longitudinal direction whereas the last two form two. The modeshape of the last two eigenvalues is displayed in Figure 3.23. Along the circumference of the shaft the number of crests varies

The critical (minimum) eigenvalue buckling load, as calculated by this analysis, is **43.6kNm**, and the buckling modeshape is modeshape 2 deformation of the structure, meaning that 2 crests are formed along the circumference of the shaft. Along the axial direction of the shaft there is only one crest, as it can be seen in Figure 3.22. These results are listed in table 3.3 in bold.

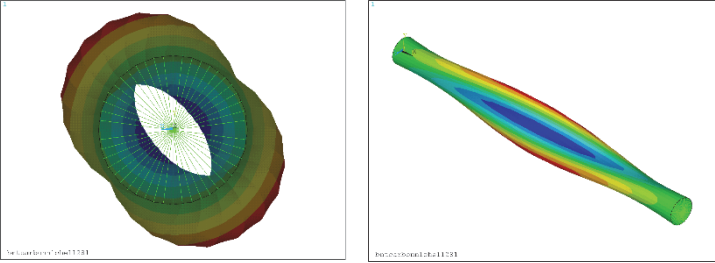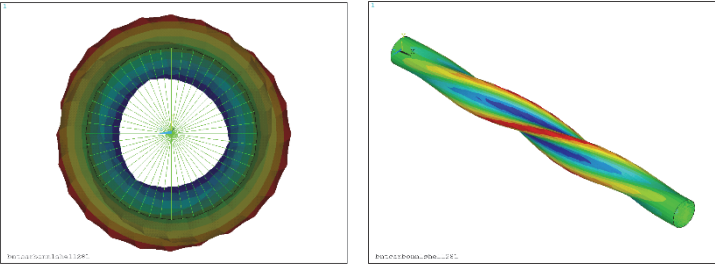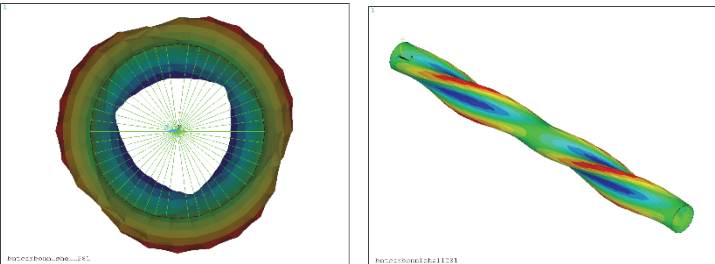Table 3.3. Results of the eigenvalue buckling analysis

Buckling load (kNm)		Buckling modeshape	
43.6	**mode 2**		
43.6	mode 2		
-44.6	mode 2		
-44.6	mode 2		
51.1	mode 3		
51.1	mode 3		
-53.1	mode 3		
-53.1	mode 3		
56.4	mode 3/2		
56.4	mode 3/2		

Figure 3.22 represents the buckled shaft with its radial displacements at the critical buckling load. The coloring represents the magnitude of the nodal radial displacement, with red representing the maximum(outwards) and blue representing the minimum(inwards) displacements.
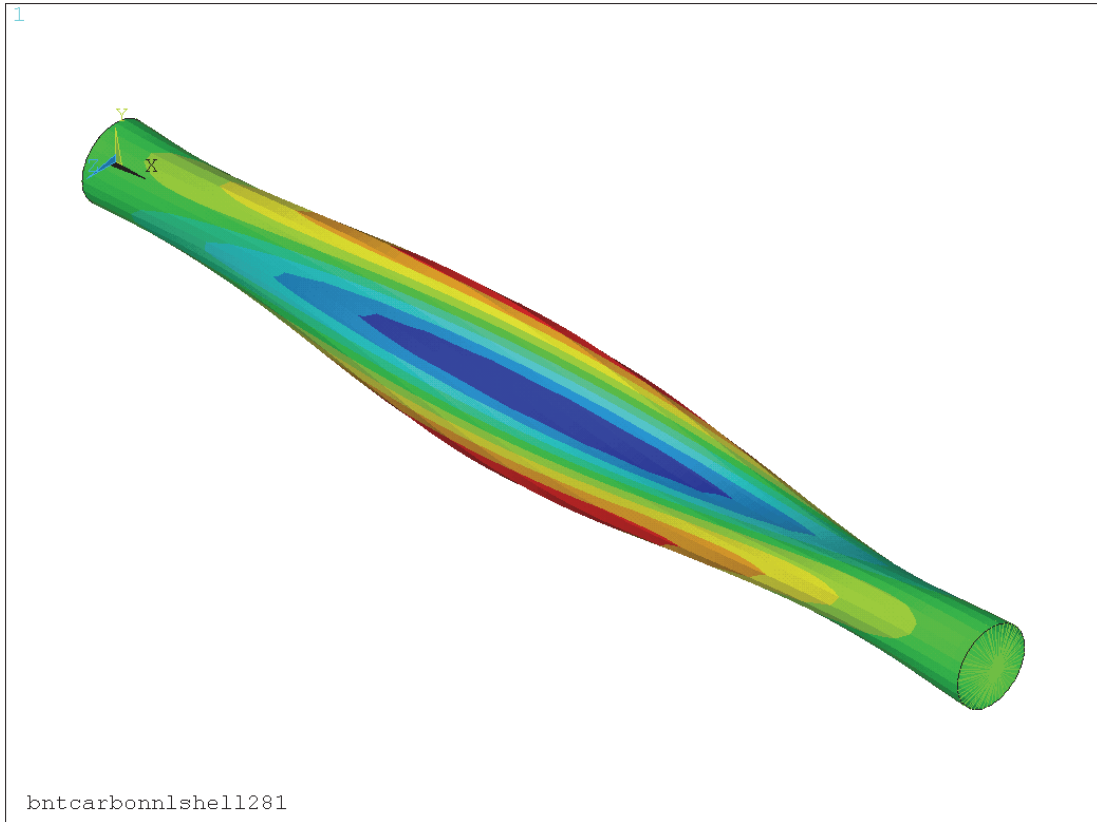
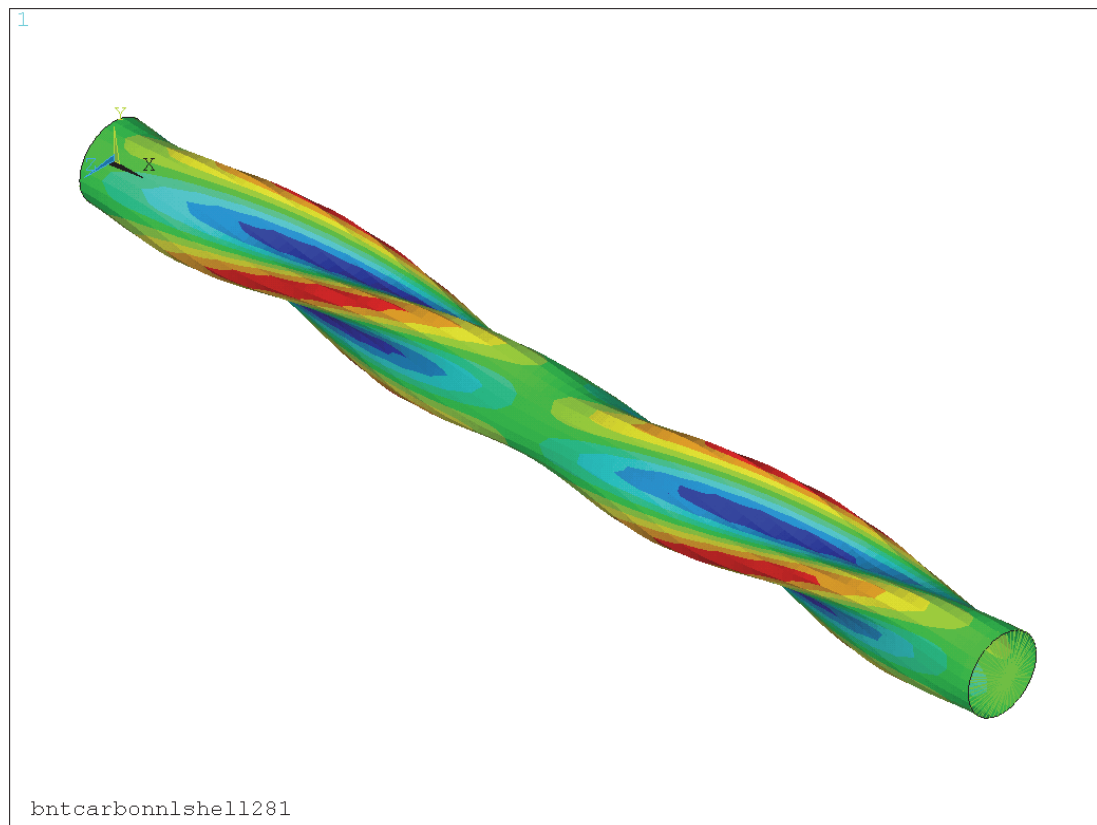Fig. 3.22. Contour plot of the radial displacements of the buckled shaft.

Fig. 3.23. Modeshape of the last two eigenvalues showing the formation of two crests along the axial direction.

Nonlinear Buckling Analysis

The nonlinear buckling analysis procedure has been extensively discussed in section 2.2.2 so it won't be repeated.

In order to generate the geometric imperfections, that are necessary for nonlinear buckling analysis, with the desired maximum magnitude equal to **0.1% of Di**, parameter **mag** is defined. Mag is equal to the desired maximum radial initial imperfection uxmax'=0.0002m (0.1% of Di) divided by the maximum absolute radial displacement uxmax.

$$mag = \frac{ux\,max'}{ux\,max}$$

(2.2)

As a result of the aforementioned values of uxmax and uxmax', **mag=0.0029**.

The preprocessor is reentered and the UPGEOM command is applied. All displacements of the critical mode-shape of the eigenvalue buckling analysis are multiplied by the parameter mag, generating this way the desired geometric imperfections. The term critical means the mode shape that corresponds to the critical (minimum) buckling load.

```
!Generate Geometric Imperfections
/prep7
*SET,mag,0.0029              !This value of the parameter "mag" results in
                            !geometric imperfections with the maximum
                            !displacement being equal to 0.1% of Di
UPGEOM,mag,1,5,bntcarbonnlshell281,rst,
FINISH
```

After the generation of the geometric imperfections, the nonlinear static analysis is run. The final Time is set equal to 1 so that every time step is a percentage of 1 and the torque applied at this time step is the same percentage of the maximum applied torque (21kNm). Automatic time stepping is used because it increases the number of time steps near the critical load and thus increases the accuracy of the results. The convergence criteria were set to default, after checking that changing them had insignificant effect in the solution of the problem.

```
!SECOND STEP

!Nonlinear Static Analysis
/SOLU
ANTYPE,STATIC
NLGEOM,ON                   !Large Displacements ON
PRED,OFF                    !No prediction occurs
TIME,1
*SET,timev,0.01             !Time step value
*SET,timn,0.001             !Minimum time step
*SET,timx,0.1               !Maximum time step
DELTIM,timev,timn,timx,     !Time step values (value, minimum, maximum)
AUTOTS,ON                   !Automatic time step on
OUTRES,all,all
SOLVE
FINISH
```

It is necessary to mention that the solution converged until the last substep, as it was expected, since the applied load was much lower than the buckling load.

3.3.3 Post-processing

At this section the results of the nonlinear buckling analysis are discussed.

Rotational Stiffness – Sensitivity Analysis

The results of the nonlinear buckling analysis concerning the rotation of the shaft are the first discussed, as they offer an overview of the global response of the finite element model, and thus should be the first considered in the calibration of the model. The node that expresses the total rotation of the shaft is the rotating master node and its angle of rotation is presented in table 3.4 and Figure 3.24. The comparison between the FE Analysis and the experimental results is also displayed in Figure 3.24.

Table 3.4. Results of the nonlinear buckling analysis

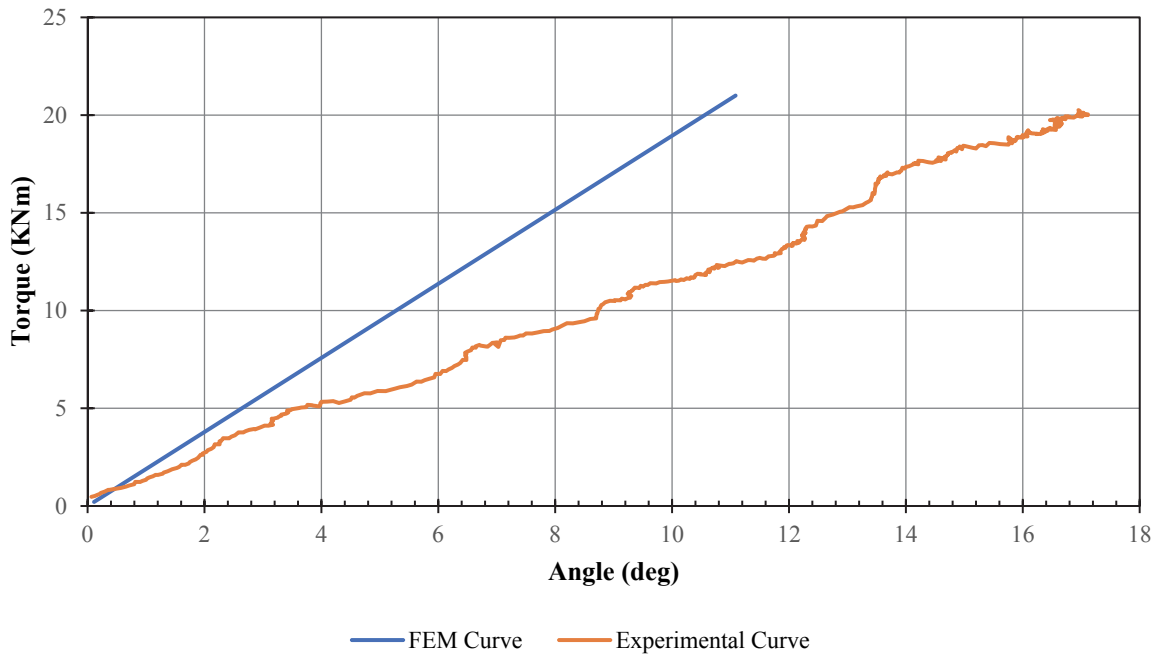| Torque (kNm)	Angle of rotation of the master node (deg)
0.2100	0.11
0.4200	0.22
0.7350	0.39
1.2075	0.64
1.9163	1.01
2.9795	1.57
4.5740	2.41
6.6740	3.52
8.7740	4.63
10.8740	5.74
12.9740	6.85
15.0740	7.96
17.1740	9.06
19.2740	10.17
21.0000	11.15

Torque vs Rotation

Fig. 3.24. Comparison between FEM Results and Experimental Curve.

It is obvious from Figure 3.24 that the finite element model predicts a higher rotational stiffness of the shaft than the experimental one. It predicts the rotational stiffness equal to 1.89 kNm/deg whereas the experimental was 1.17 kNm/deg, about 62% lower. A cross check of this result is done by applying the experimental rotation to the free end and measuring the reaction moment at the fixed end. The results of this analysis are plotted in Figure 3.25 and confirm that the model predicts a higher rotational stiffness than the experimental one. Both approaches, the application of torque and the application of rotation predict almost the same rotational stiffness equal to 1.89kNm/deg.
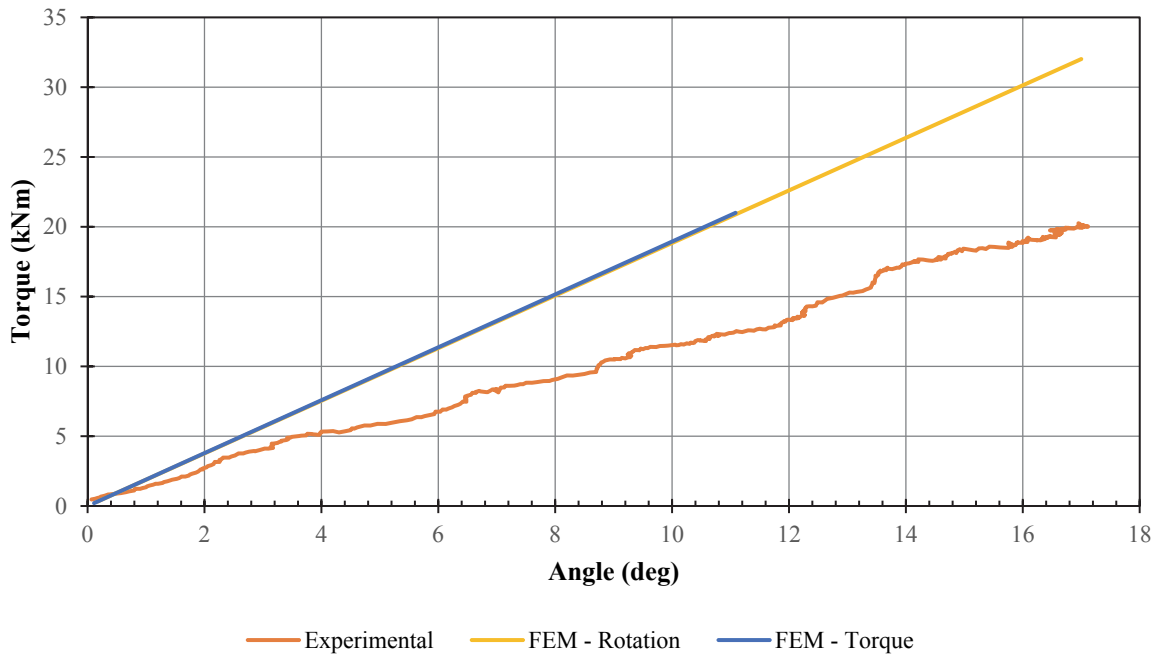
Torque vs Rotation

Fig. 3.25. Comparison between the FEM Results with the application of rotation instead of torque and the Experimental Curve.

Before any other comparison between the finite element analysis results and the experimental results is done, it should be attempted to match the finite element model rotational stiffness to the experimental.

Based on the experience gained by the finite element analysis of the GFRP shaft and especially the sensitivity analysis, E1, E2 and thickness should be reduced in the attempt to match the experimental rotational stiffness. The rest of the mechanical properties affect less the rotational stiffness and they are not investigated. Additionally, the effect of larger initial imperfections will be checked, by increasing the size of the maximum initial radial imperfection to 1% of the cylinder's internal diameter, i.e. 0.002m. In Figure 3.26, the results of the six different attempts are plotted. As in the case of the GFRP shaft, a drastic reduction of E1 by 60% is necessary in order to match the experimental rotational stiffness. This also reduces the eigenvalue buckling load to 23.6 kNm. The reduction of the thickness of the shaft by 25% was not enough to match the rotational stiffness, it dropped, however, the eigenvalue buckling load to 24 kNm. The larger initial imperfection had almost no effect to the rotational stiffness of the shaft.

It is quite unlikely that the shaft had either such a low E1 or so great thickness variations that could reduce the overall thickness by more than 25%. Additionally the calculated eigenvalue buckling loads are very low, approaching the experimental applied load, at which the shaft showed no signs of buckling, based on the measured strains, and didn't fail. If that was true the experimental measured strains would be significantly higher.
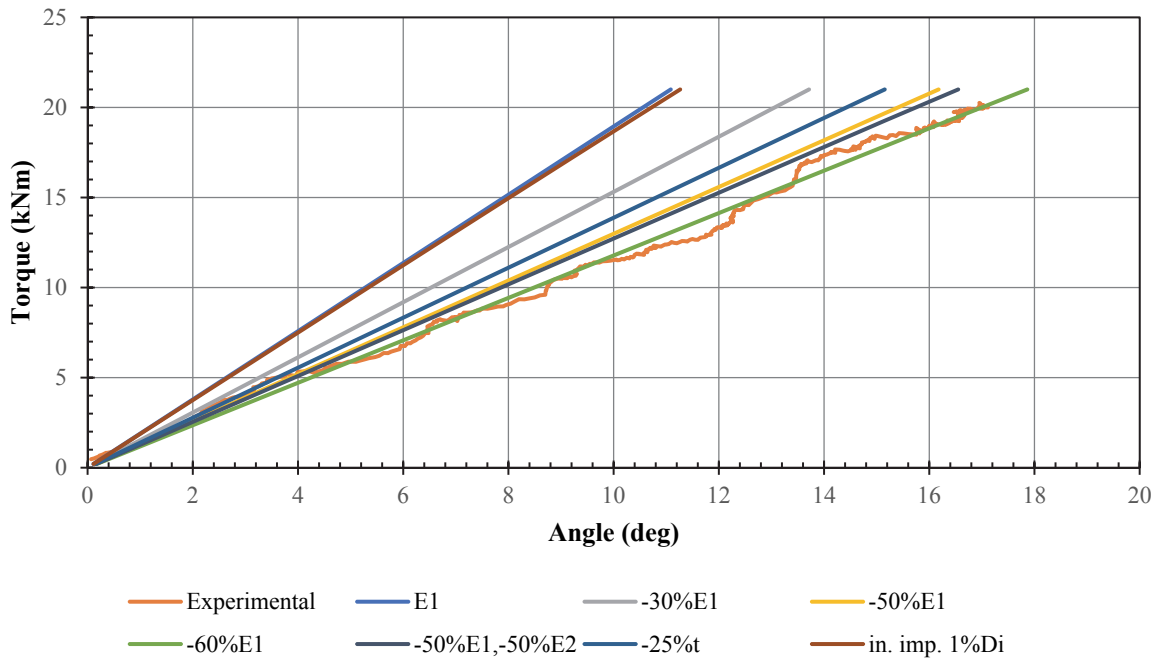
126

Torque vs Rotation

Fig. 3.26 Comparison between the layered shell model, the downgraded models and the experimental results.

Considering the results of the sensitivity analysis, and the consistency of the problem of the prediction of higher rotational stiffness that has already been encountered in the analysis of the GFRP shaft, the initial mechanical properties are considered the most realistic, and are chosen for the further comparison between the numerical and the experimental results.

Strains – Sensitivity Analysis

For the first comparison between the numerical and the experimental strains, two nodes of the finite element model were selected. The first node is the one located at the top of one crest at the mid-length cross section of the critical modeshape of the eigenvalue analysis, whereas the second node is that corresponding to the center of a trough at mid-length. These two nodes exhibit the maximum positive and the maximum negative radial displacement when buckling takes place and, consequently, external surface circumferential strains will take their maximum and minimum values at these nodes too, even prior to buckling. Circumferential strains at these two nodes constitute an upper and a lower boundary for all corresponding experimental measurements, since, in general, the locations where strains were measured will in any case fall in-between the top of a crest and the center of a trough in the shaft's deformed shape.

Several sizes of the maximum initial imperfection were tested in order to investigate the sensitivity of the numerical strains, since no information exists about the actual geometric imperfections of the shaft tested.

Figure 3.27 presents a comparison between the numerical results and the experimental measurements for the circumferential strains at mid-length of the shaft. Solid lines correspond to the experimental measured strains, whereas dashed lines correspond to the numerical results for all different initial imperfection magnitudes. Normally, the experimental curves should fall

in-between the upper and the lower numerical curves for the same initial imperfection magnitude.

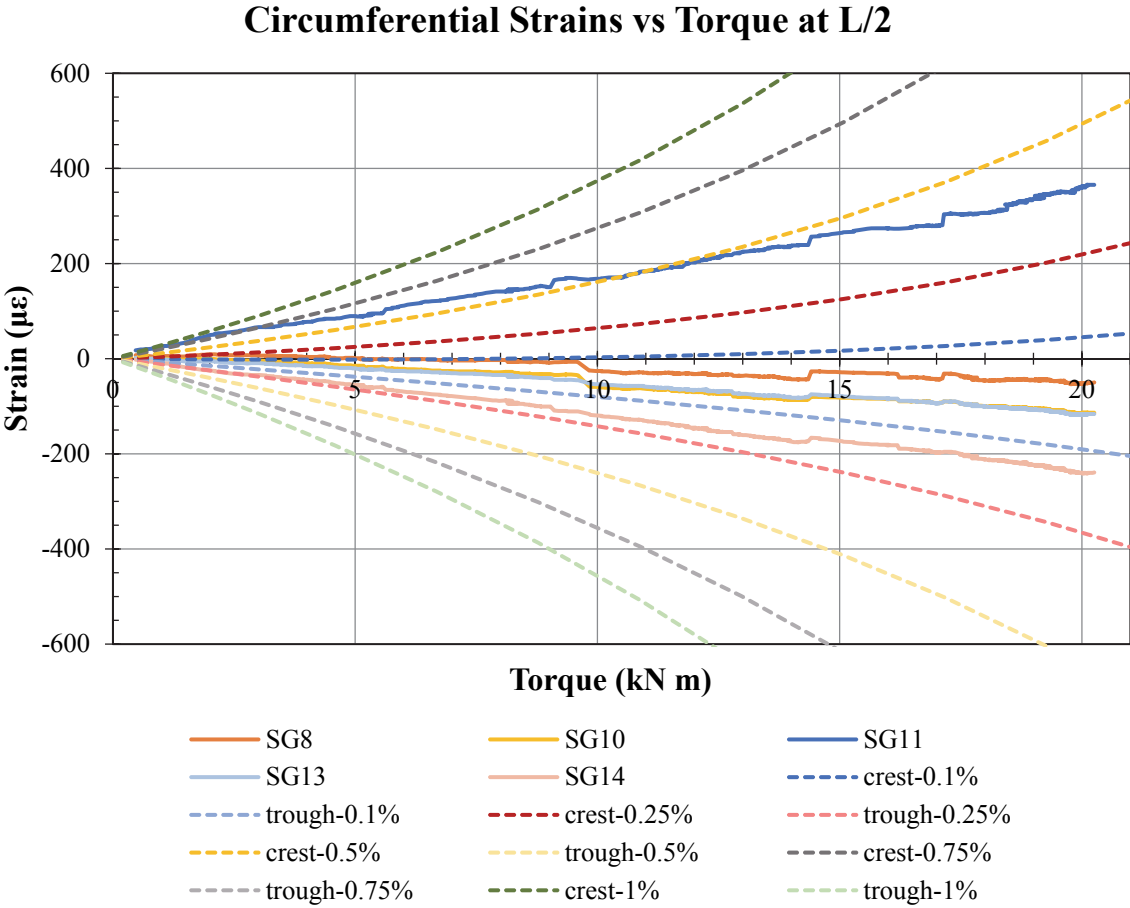**Circumferential Strains vs Torque at L/2**

Fig. 3.27. Comparison of the numerical and the experimental circumferential strains for several maximum initial imperfection sizes.

The size of the initial imperfection affects the numerical strains significantly. Initial imperfection equal to 0.1% of the internal diameter results in very small strains, whereas equal to 1% results in very large strains. These two values are the first discussed since they have already been used in the attempts to match the rotational stiffness of the shaft. The larger initial imperfection had almost no effect to the overall rotational stiffness of the shaft, however it affects greatly the calculated strains. The best fit seems to be attained for the numerical curves corresponding to an initial imperfection value of 0.5% of shaft's diameter. The gradient of these curves is close to the experimental ones' but has an increasing trend, indicating that a slightly smaller initial imperfection might produce an even better fit while the load increases.

At this point, the effect of the pattern of the initial imperfection is also investigated by using all 10 modeshapes of the eigenvalue buckling analysis in order to generate the initial imperfection. Since there is not a dominant crest or trough, two new nodes have to be selected at the mid-length cross section, from which to obtain representative strains. The first node is positioned where the maximum strain is calculated at the last substep of the nonlinear analysis, whereas

the second is positioned where the minimum strain is calculated. Two different magnitudes of the maximum initial imperfection are tested, 0.4% of the shaft's internal diameter and 1%. The numerical strains from these runs are compared with the experimental strains in Figure 3.28.

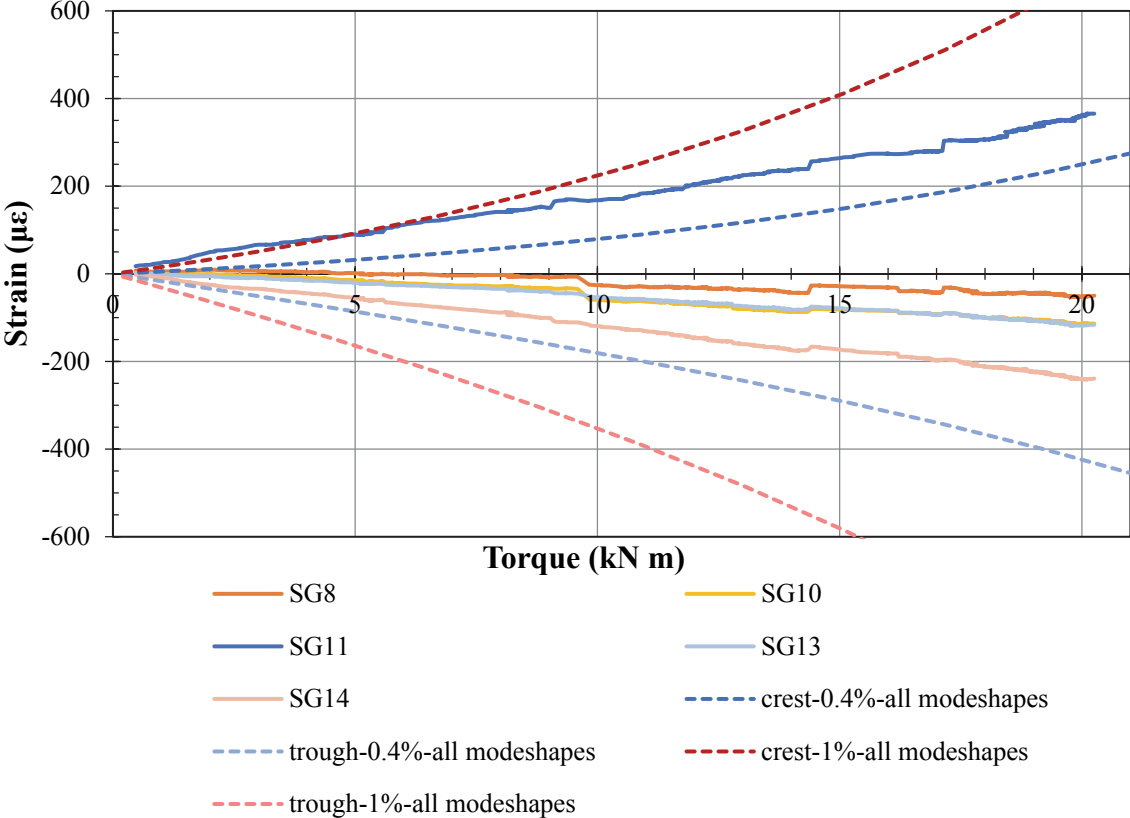**Circumferential Strains vs Torque at L/2**

Fig. 3.28. Comparison of the numerical and the experimental circumferential strains for several initial imperfection sizes and imperfection pattern from all eigenvalue modeshapes.

It can be seen by the comparison between Figures 3.27 and 3.28 that the initial imperfection pattern from all modeshapes decreases the strains for the same maximum initial imperfection size, as it was expected based on the experience of the modelling of the GFRP shaft. More specifically, for initial imperfection pattern from all modeshapes and maximum initial imperfection magnitude equal to 0.4%Di the strains are close to the ones of the case of the critical modeshape imperfection pattern and maximum initial imperfection equal to 0.25%Di. Respectively, the same applies to the cases "1%-all modeshapes" from Figure 3.28 and "0.75%" from Figure 3.27.

After assessing the aforementioned results of the several initial imperfection pattern and size cases, the one that seems to fit best the experimental results is the case of the critical modeshape initial imperfection pattern and magnitude of the maximum initial imperfection equal to 0.5% of the internal diameter of the shaft. This case will be used for the comparison between the rest measured strains and the corresponding numerical ones.

At all cross sections specific nodes of the numerical model were selected according to the strain gage scheme as it is presented in Figure 3.5. The strain gage of the mid-length cross section

129

with the maximum circumferential strain (at the top of a crest) was assigned to be strain gage 11 and starting from this position the rest were assigned.

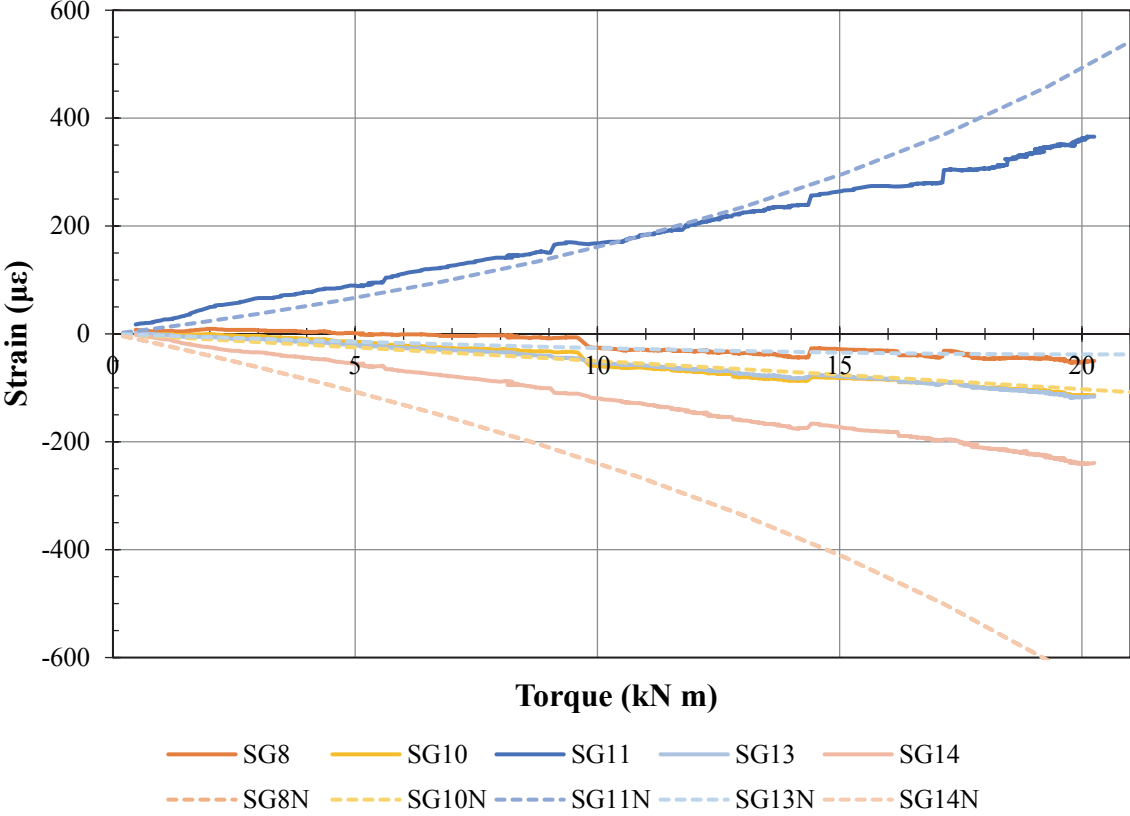**Circumferential Strains vs Torque at L/2**

Fig. 3.29. Comparison of the numerical and the experimental circumferential strains at cross section L/2

At cross section L/2, the numerical strains act like an upper and lower boundary for all experimental strains, as it has already been presented. Additionally for strain gages 10, 11 and 13 the experimental strains are very close to the numerical. However, the experimental measured strains of strain gage 8 are very low, whereas the numerical results are highly compressive (SG8N curve is exactly the same as the SG14N curve). For strain gage 14, both experimental and numerical strain values are compressive, however the numerical values are significantly higher. This comparison of the circumferential strains at cross section L/2 supports the suggestion proposed at section 3.2.2 that modeshape 2 buckling is the most dominant to evolve during the test.
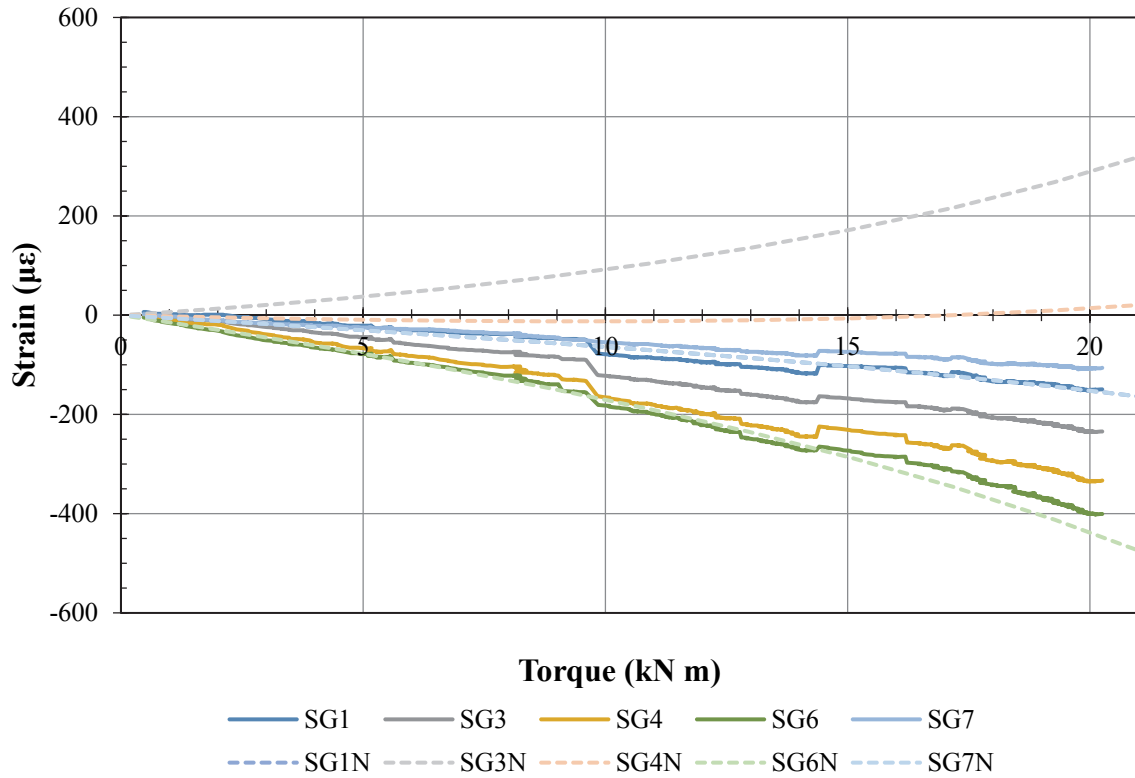
Fig. 3.30. Comparison of the numerical and the experimental circumferential strains at cross section 3L/4

At cross section 3L/4, the numerical strains act like an upper and lower boundary for all experimental strains. Additionally, for strain gages 1, 6 and 7 the experimental strains are very close to the numerical. However, for strain gage 3 the finite element model predicts tensile strains, whereas the experimental are compressive. Experimental measurements of strain gage 4 are compressive, the numerical, however, are very close to zero with a tendency to become tensile.
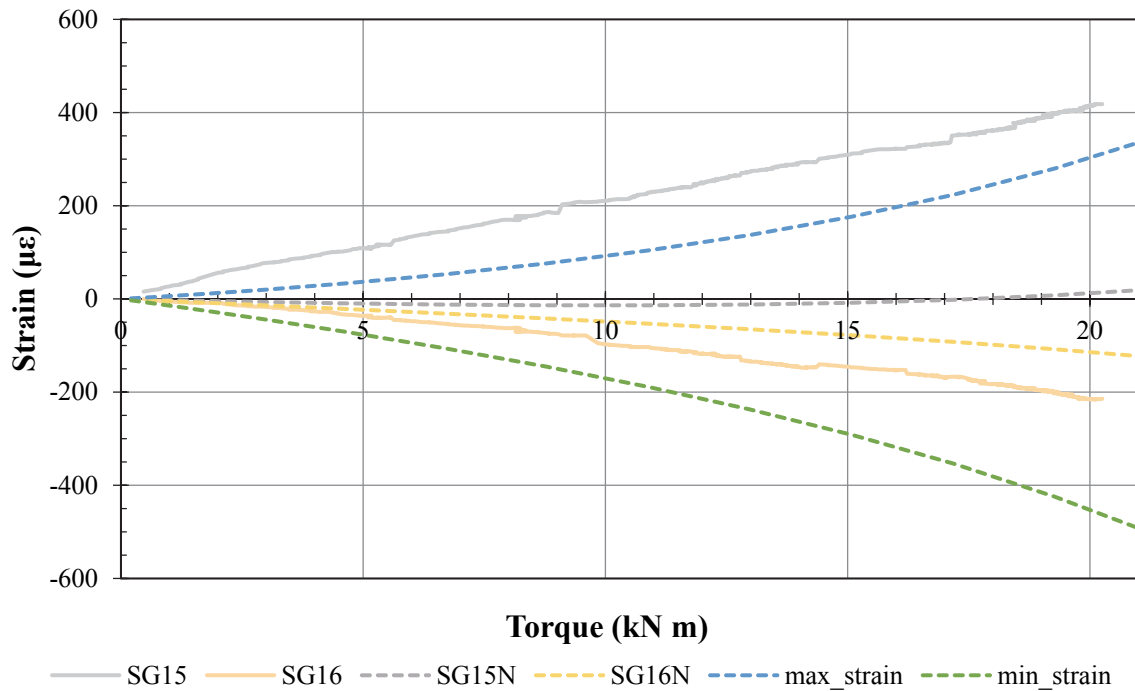
Circumferential Strains vs Torque at L/4

Fig. 3.31. Comparison of the numerical and the experimental circumferential strains at cross section L/4

At cross section L/4, the numerical strains of the chosen nodes according to the experimental strain gage scheme are significantly lower and don't act as an upper and lower boundary. Both numerical strains are compressive in contrast to the experimental. Additionally, the maximum tensile and compressive numerical strains at this section were calculated, but again the experimental tensile strain exceeded the numerical.

In Figure 3.32 an overview of the circumferential strains on the external surface of the shaft is presented. The maximum and minimum strains are concentrated near mid-length and they also seem to preserve the initial imperfection pattern.

In Figure 3.33, the radial displacements are plotted for a torque value equal to 21 kNm. There is a small decrease of the diameter of the shaft near the rotating end. Additionally, the maximum radial displacements are not positioned at mid-length but towards the fixed end. This indicates that the initial imperfection pattern has been altered during the loading.
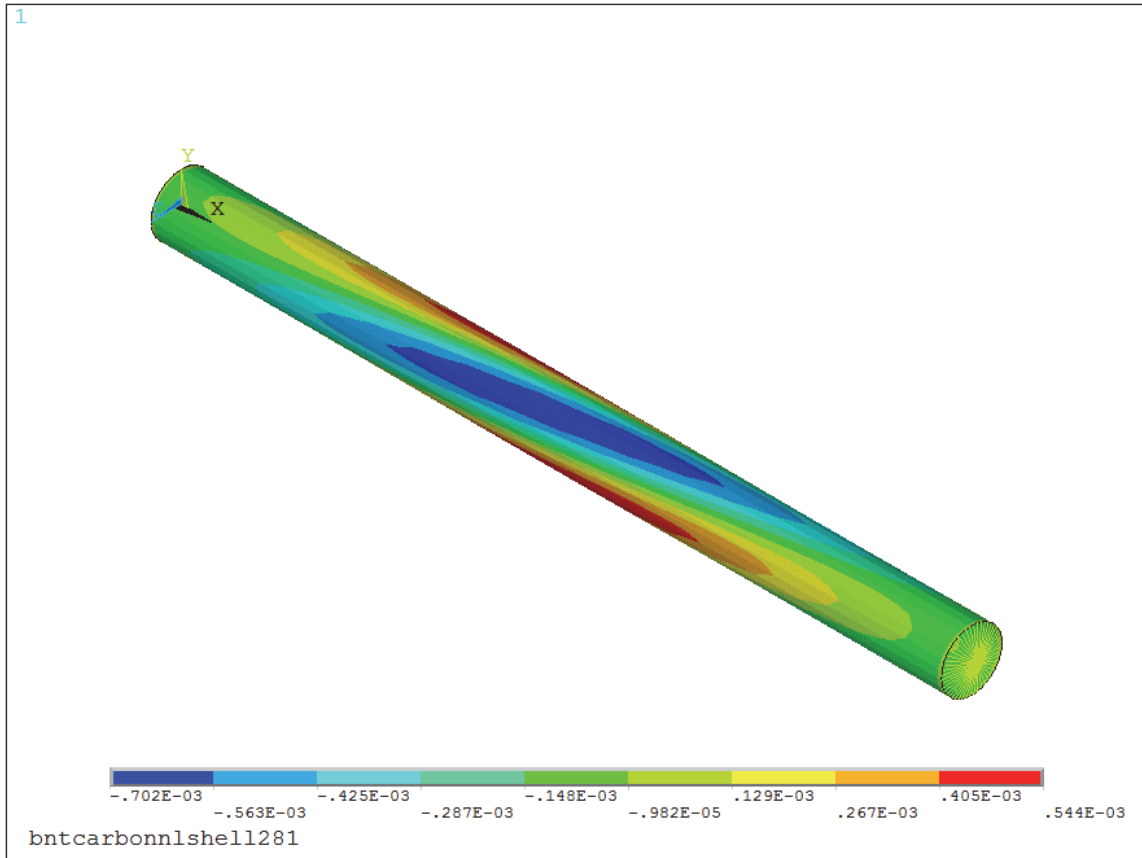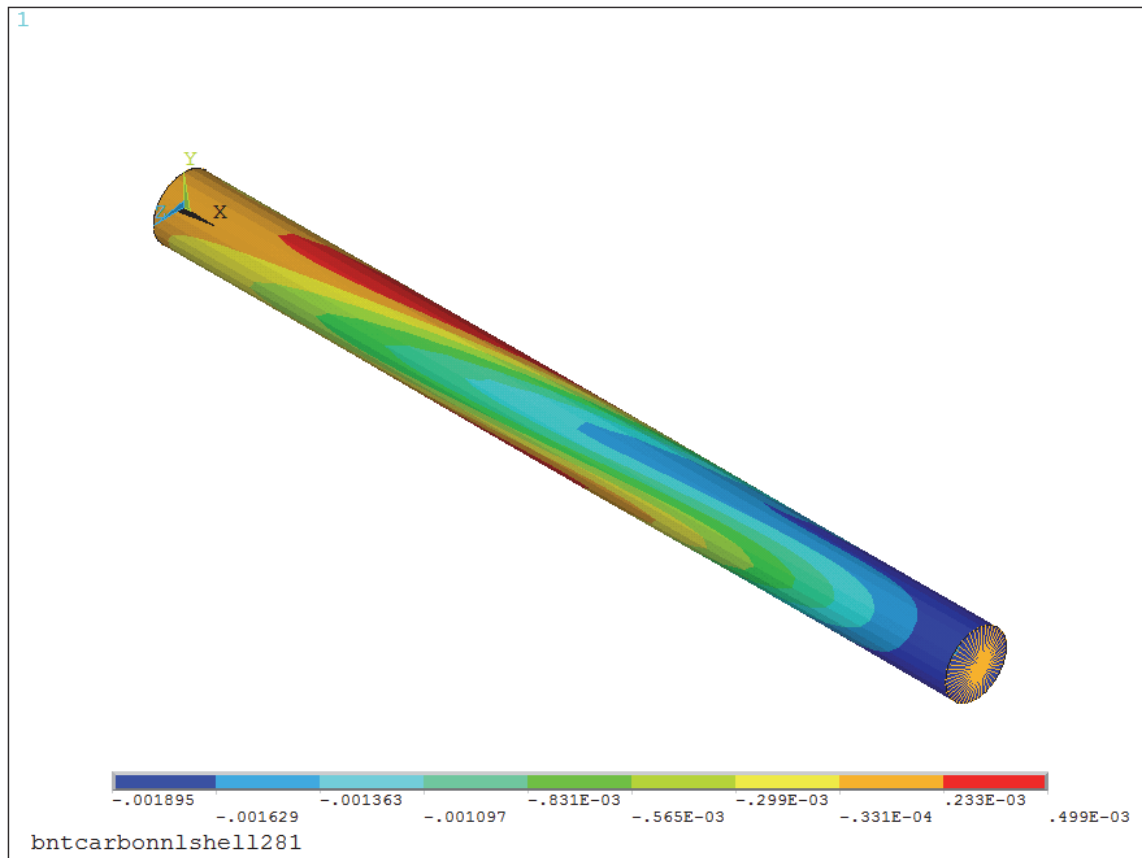
Fig. 3.32. Contour plot of the circumferential strains at the last substep of the analysis (m).

3.33. Contour plot of the radial displacements at the last substep of the analysis (m).

Concerning longitudinal strains, the numerical results are significantly lower than the experimental. Additionally, the numerical longitudinal strains are of the same sign with their corresponding circumferential strains at the same position, e.g. stain gages 11 and 12, whereas the experimental have opposite signs, as we have already discussed at section 3.2.2. This is true for all strain gages apart from 1 and 2, that both, however, measured strains of very low magnitude.

Longitudinal Strains vs Torque at L/2
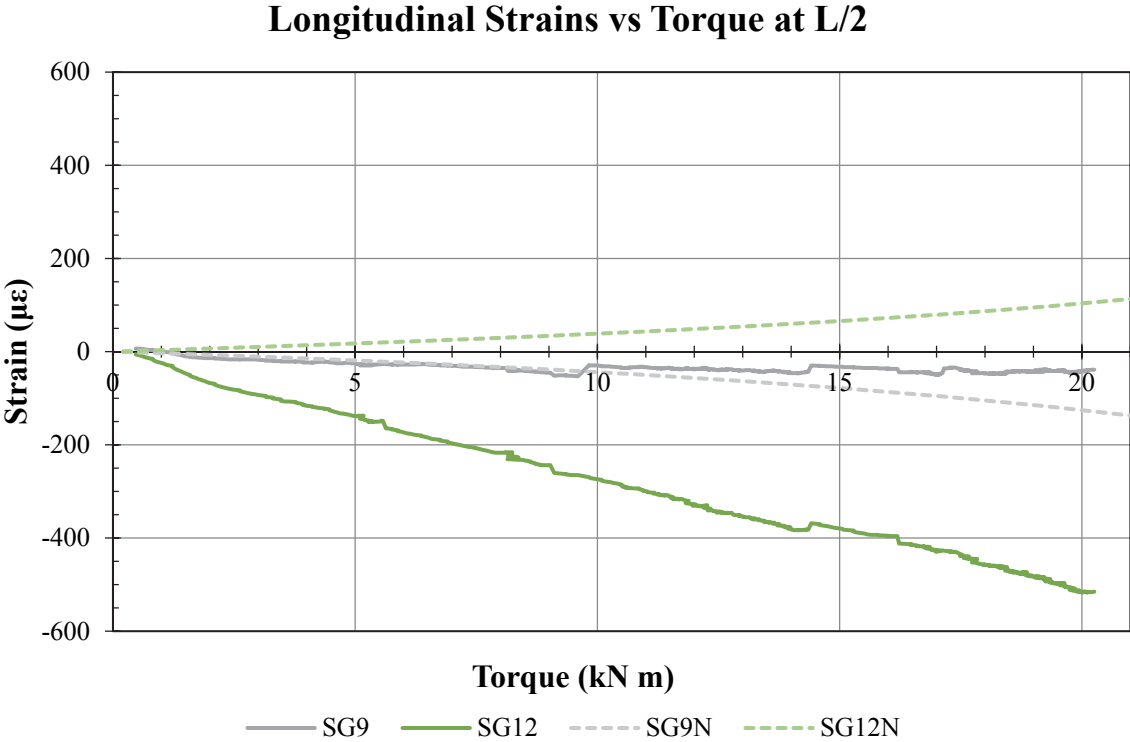
Fig. 3.34. Comparison of the numerical and the experimental longitudinal strains at cross section L/2

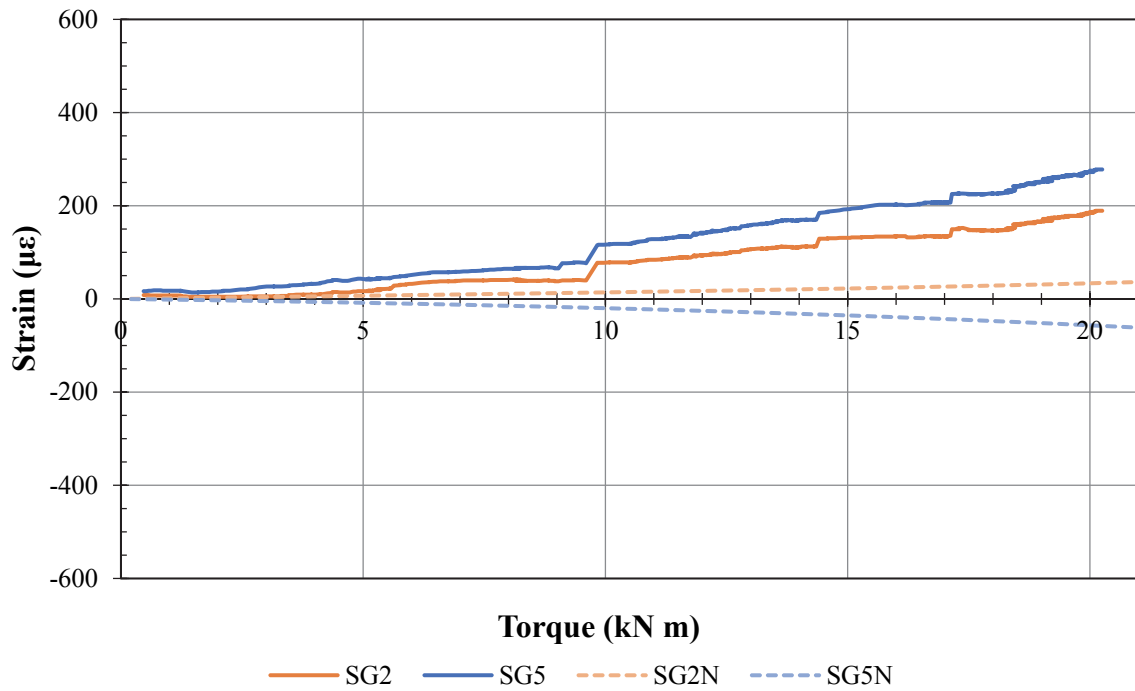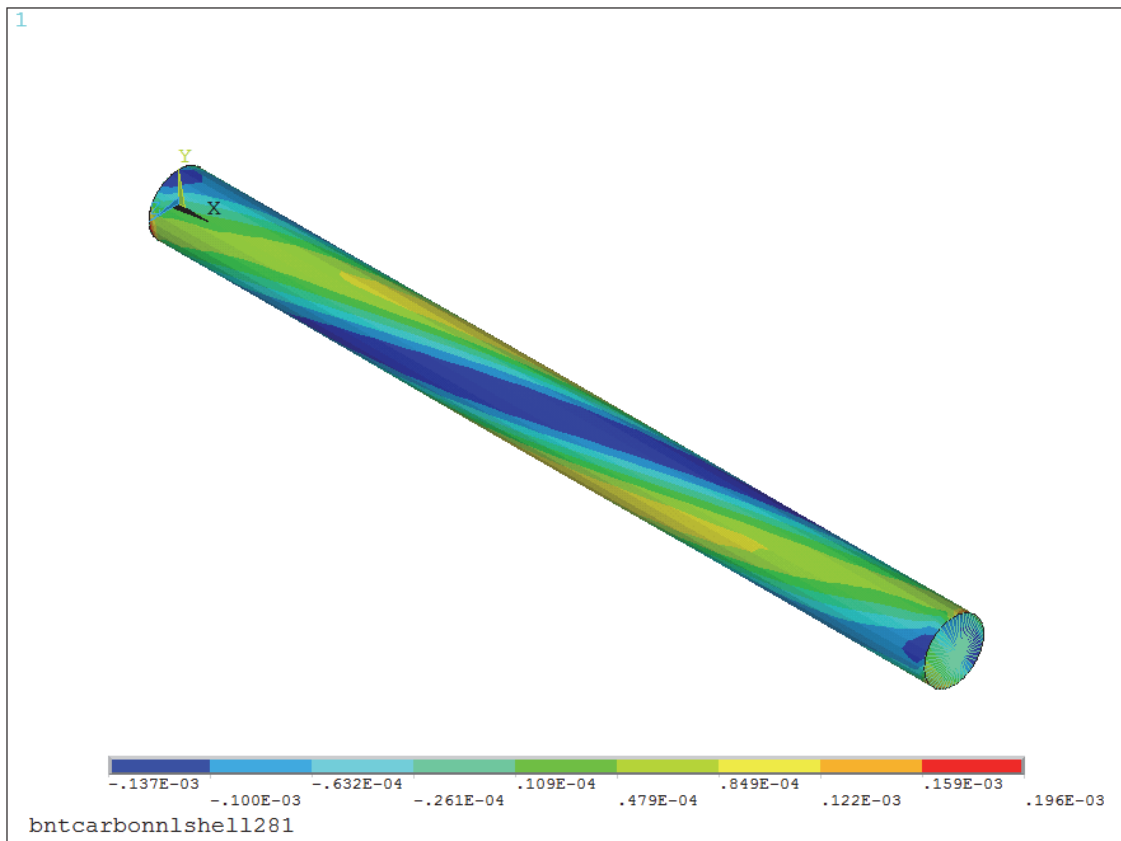## Longitudinal Strains vs Torque at 3L/4

Fig. 3.35. Comparison of the numerical and the experimental longitudinal strains at cross section 3L/4

In Figure 3.36 an overview of the longitudinal strains on the external surface of the shaft is presented.

3.36. Contour plot of the longitudinal strains at the last substep of the analysis (m).

Conclusions

The comparison between the experimental and the numerical results led to some interesting conclusions. There is a significant difference between the numerical and the experimental rotational stiffness with the former being 62% higher than the latter. This can be probably justified due to measurement inaccuracies and inaccurate knowledge of material properties, winding pattern and thickness distribution. Additionally, the model seems to accurately predict the most possible to evolve critical buckling modeshape, which is modeshape 2. The model also gives an encouraging strains prediction. Several of the discrepancies encountered between the experimental and the numerical strains could be caused by local deviations from nominal geometry and lay-up of the shaft tested.

3.3.4 Mesh Convergence Analysis

In this section, the mesh convergence analysis that was mentioned earlier in section 3.3.1 is discussed. Four different meshes were checked and the resulting eigenvalue critical buckling factors and the rotation of the master node at the ultimate load of the nonlinear solution were compared. The first mesh consisted of 1056 square elements, 66 longitudinally and 16 circumferentially, with side length 0.038m and 3 integration points through the thickness of each layer. The second mesh consisted of 2400 square elements, 100 longitudinally and 24 circumferentially, with side length 0.026m and 3 integration points through the thickness of each layer. The third mesh consisted of 2400 square elements, 100 longitudinally and 24 circumferentially and 5 integration points through the thickness of each layer. The fourth mesh consisted of 9600 square elements, 200 longitudinally and 48 circumferentially, with side length 0.013m and 5 integration points through the thickness of each element. The results are listed in table 3.5.

Table 3.5 Mesh Convergence Comparison

Mesh	Eigenvalue Buckling Load	Rotation of the Master Node at the Ultimate Load	Solution Duration
66x16 Elements, 3 integration points	43.6 kNm	11.18 deg	1.5 min
100x24 Elements, 3 integration points	43.6 kNm	11.15 deg	4 min
100x24 Elements, 5 integration points	43.6 kNm	11.15 deg	9 min
200x48 Elements, 5 integration points	43.6 kNm	11.14 deg	25 min

The difference between the coarser and the finer mesh is negligible concerning the critical eigenvalue buckling load and 0.4% concerning the maximum rotation of the master node. More integration points through the thickness of the layer offer no benefits for this problem. Considering the results and the duration of the solution the mesh of 100x24 elements and 3 integration points through the thickness of each layer was chosen. Finally, concerning the duration of the solution, it is noted that the solution was run on a personal computer with an AMD Quad Core Processor at 3.40 GHz and 8 GB RAM.
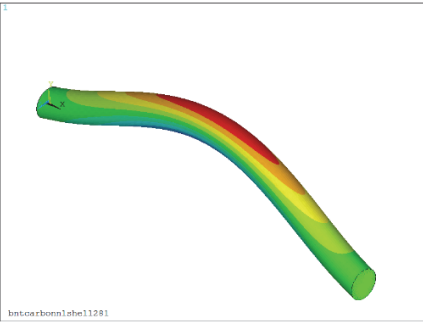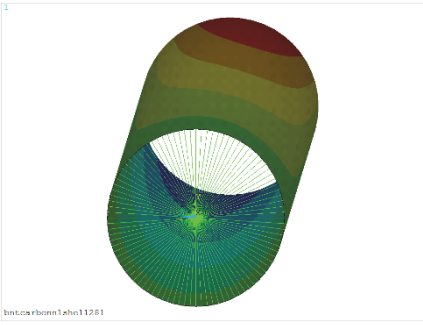
3.3.5 Modal Analysis
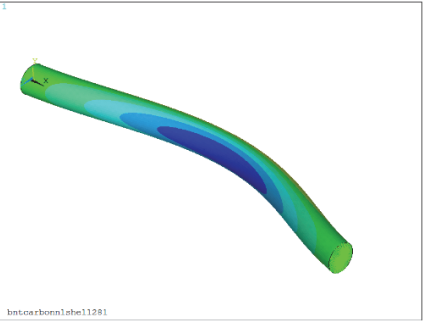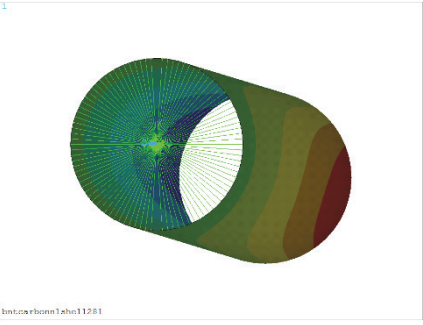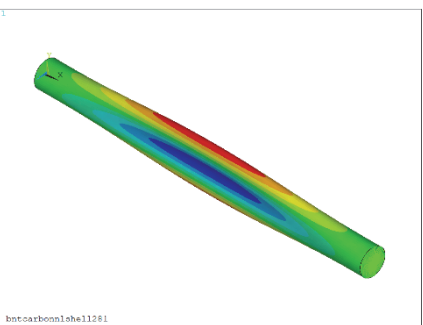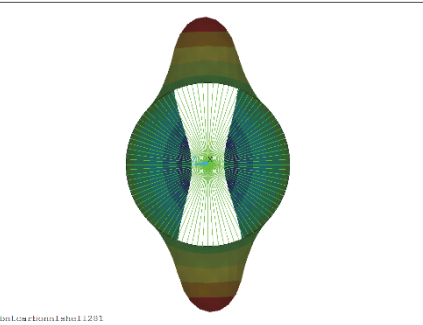
Modal analysis is used to determine the natural frequencies and mode shapes of a structure. The mode shapes are important parameters in the design of a structure for dynamic loading conditions like a shaft.
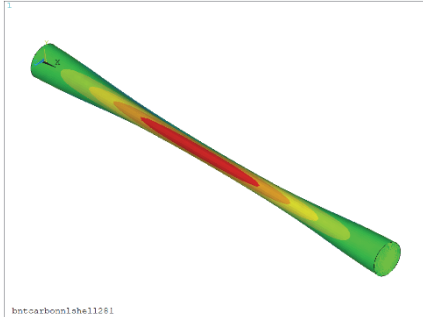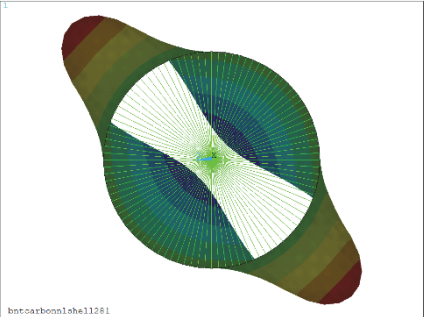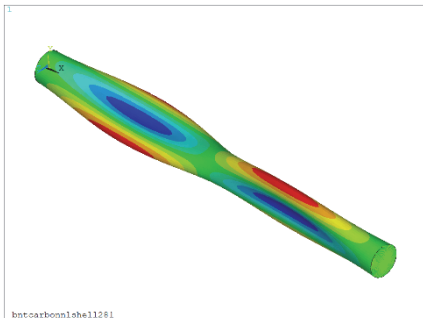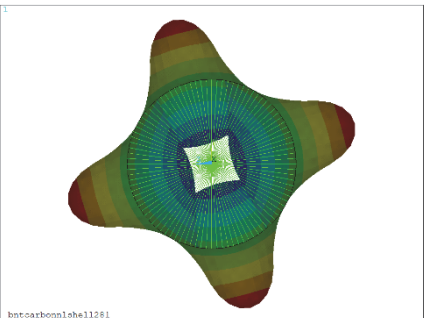
In this particular study, a modal analysis of the shaft is conducted in order to determine whether the possible in-service rotational speeds of the shaft are close to the mechanical resonance frequency (natural frequency). Mechanical resonance would lead to excessive vibrations and deformations of the shaft that could lead to failure of the shafting system components.

The density of the CFRP shaft was assumed equal to 1.6g/cc (1600kg/m^3) according to Shipbuilding Technology Laboratory measurements. Additionally, the shaft was allowed only to rotate and all other motions were restricted. The first five natural frequencies were requested.

The results of the modal analysis are summed up in table 3.7. The coloring of the modeshapes represents radial displacement.

Table 3.7. Results of the modal analysis

Frequency		Modeshape	
Hz	**RPM**		
223.91	13434.6		
223.91	13434.6		
261.92	15715.2		

137

261.92	15715.2		
335.13	20107.8		

By assessing the results of the modal analysis, it is obvious that none of the calculated natural frequencies is within the operational limits of the CFRP shaft of this study, assuming that it will be used in a marine application. Additionally, it must be underlined that the first four natural frequencies are double, and their corresponding mode shapes are similar. After reviewing the double mode shapes, it is obvious that they are the same in terms of magnitude of displacement and pattern but they differ in the angular position of their crests and troughs.

3.4 Conclusions and comments

Some interesting conclusions have been reached from the torsion test and the finite element analysis of the CFRP shaft. The experimental results offered some valuable information about the mechanical behavior of the shaft. First of all, the experimental rotational stiffness of the shaft is about 1.17 kNm/deg. The strain gage measurements provide information about the deformations taking place. The circumferential strain gage measurements at L/2 and L/4 give a first indication that modeshape 2 is the most possible buckling modeshape that the shaft will sustain during buckling. The circumferential strain gage measurements at 3L/4 are all compressive, indicating that the shaft is compressed at this section. Longitudinal strain gage measurements are in general opposite of the corresponding circumferential strains, something that was not expected but indicates that deformations other than the formation of crests or troughs, have a more significant effect for this loading level.

The finite element analysis of the CFRP shaft was conducted using layered shell elements and implemented both eigenvalue buckling analysis and nonlinear buckling analysis. Eigenvalue buckling analysis predicted that the critical buckling modeshape is modeshape 2 deformation of the structure, which agrees with the experimental results. Nonlinear buckling analysis, however, predicts a 62% higher rotational stiffness than the experimental. The sensitivity analysis conducted indicated that the aforementioned discrepancy can be probably justified due to the combination of measurement inaccuracies and inaccurate knowledge of material properties, winding pattern and thickness distribution. Additionally, the model gives an

encouraging strains prediction using the critical buckling modeshape initial imperfection pattern and maximum initial imperfection size equal to 0.5% of the shaft's diameter. Several of the discrepancies encountered between the experimental and the numerical strains could be caused by local deviations from nominal geometry and lay-up of the shaft tested.

Both experimental and numerical results underline that given the opportunity, the shaft should be tested until failure in order to confirm the FEM predicted buckling and failure load as well as the buckling modeshape.

Finally, the conducted modal analysis shows that none of the calculated natural frequencies is within the operational limits of the CFRP shaft of this study, assuming that it will be used in a marine application.

CHAPTER 4
CONCLUSIONS AND RECOMMENDED FUTURE WORK

4.1 Conclusions

After extensively discussing the finite element analysis of the GFRP shaft in chapter 2 and the torsion test and the finite element analysis of the CFRP shaft in chapter 3, a summary of the conclusions is made in this section.

- The layered shell model revealed its ability to quite accurately predict the buckling load of the GFRP shaft. The eigenvalue buckling analysis resulted in a buckling load 7% greater than the experimental one and the nonlinear buckling analysis resulted in a buckling load about 5% lower than the experimental one. The nonlinear analysis' buckling load highly depends on the chosen initial imperfection, as indicated by the sensitivity analysis. Both results can be considered as a reasonable estimation of the shaft's buckling load, with the latter being the more conservative and probably the more accurate of the two. However, the model predicted a much higher rotational stiffness of the shaft than the experimental one and this led to a thorough investigation of the factors affecting this result. Additionally, the examined stresses showed a logical pattern and reasonable magnitudes until buckling initiation which led to their rapid increase. The Tsai-Wu failure criterion was also introduced and with the initial material strengths predicted a very low failure load. The sensitivity analysis showed that a very drastic increase of the strength in the direction normal to the fibers was necessary in order to predict a failure load near the experimental.

- The modeling of the steel shaft and the comparison of its results with the analytical ones based on Young & Budynas, (2002), proved the validity of the model in the prediction of the mechanical behavior of a steel shaft.

- The homogeneous model of the GFRP shaft yielded almost the same results with the layered shell model concerning the rotational stiffness. It also predicted tensile and compressive stresses of almost the same magnitude that are symmetrically developed about the x-axis. The existence of this symmetry is an indication that homogeneous material modelling represents more accurately the real filament wound shaft. However, the homogeneous model lacked the ability to calculate stresses in the direction of the fibers as well as the ability of the direct application of failure criteria due to the lack of material strengths for the homogeneous material.

- The layered solid model of the GFRP shaft yielded almost identical results with the layered shell model, leading to the conclusion that for thin-walled layered composite shaft applications the extra computing cost of layered solid modelling offers no benefits.

- The sensitivity analysis conducted for the GFRP shaft showed that E1 had to be decreased by 60% in order to match the experimental rotational stiffness of the shaft and the buckling load dropped to about 40kNm. Reducing both E1 and E2 by 50% matched the experimental rotational stiffness and lowered the buckling load between 30 and 35 kNm. Reduction of the shear moduli had insignificant effect on the rotational

stiffness. Reducing them by 50% lowered the buckling load between 45 to 50kNm and reducing them by 90% lowered the buckling load at around 30kNm. The reduction of the thickness by 50% matched the experimental rotational stiffness and dramatically lowered the buckling load at around 10kNm. The size of the initial imperfection basically affects buckling initiation. The smaller the initial imperfection the higher the buckling load. Using all modeshapes to generate the initial imperfection triggers buckling later than considering only a same magnitude critical modeshape initial imperfection.

- By carefully assessing the results of the GFRP shaft analysis and mainly the results of its sensitivity analysis, it seems quite unlikely that any specific material mechanical property could be so much lower than the one given by the manufacturer in order to match the experimental rotational stiffness. Additionally, it is quite unfamiliar that the failure-buckling load of the shaft is approximated quite accurately whereas the rotational stiffness is almost 90% higher than the experimental. Consequently, some doubts arise mainly about the correct interpretation of the experimental data and the accurate knowledge of the material properties-winding pattern-thickness distribution combination that unfortunately could not be answered during the elaboration of the diploma thesis.

- The experimental results of the torsion test of the CFRP shaft offered some valuable information about its mechanical. First of all, the experimental rotational stiffness of the shaft is about 1.17 kNm/deg. The strain gage measurements provide information about the deformations taking place. The circumferential strain gage measurements at L/2 and L/4 give a first indication that modeshape 2 is the most possible buckling modeshape that the shaft will sustain during buckling. The circumferential strain gage measurements at 3L/4 are all compressive, indicating that the shaft is compressed at this section. Longitudinal strain gage measurements are in general opposite of the corresponding circumferential strains, something that was not expected but indicates that deformations other than the formation of crests or troughs, have a more significant effect for this loading level.

- The finite element analysis of the CFRP shaft was conducted using layered shell elements and implemented both eigenvalue buckling analysis and nonlinear buckling analysis. Eigenvalue buckling analysis predicted that the critical buckling modeshape is modeshape 2 deformation of the structure, which agrees with the experimental results. Nonlinear buckling analysis, however, predicts a 62% higher rotational stiffness than the experimental. The sensitivity analysis conducted indicated that the aforementioned discrepancy can be justified due to the combination of measurement inaccuracies and inaccurate knowledge of material properties, winding pattern and thickness distribution. Additionally, the model gives an encouraging strains prediction using the critical buckling modeshape initial imperfection pattern and maximum initial imperfection size equal to 0.5% of the shaft's diameter. Several of the discrepancies encountered between the experimental and the numerical strains could be caused by local deviations from nominal geometry and lay-up of the shaft tested.

- Finally, the conducted modal analysis shows that none of the calculated natural frequencies is within the operational limits of the CFRP shaft of this study, assuming that it will be used in a marine application.

4.2 Recommended future work

In this section, some proposals for further research are presented.

- The discrepancy between the experimental and the numerical rotational stiffness of the shaft encountered in both GFRP and CFRP finite element analyses is of particular interest. Despite the extensive sensitivity analyses conducted already, there are mechanical properties - winding pattern - thickness distribution - initial imperfection combinations that have not been tested and could lead to the elimination of the aforementioned discrepancy. However, the accurate knowledge of the true rotational stiffness of shaft is necessary.

- Both experimental and numerical results underline that the testing of the CFRP shaft until failure is an important objective, because it would offer valuable information about the buckling and failure load as well as the buckling modeshape of the shaft. Thus, the respective results of the finite element analysis could be validated.

- More sophisticated tools like Progressive Damage Modelling could be introduced to the finite element model in order to more accurately predict its mechanical behavior near buckling and failure.

- The improvement of the existing experimental set-up and the design of a new one based on the available testing machines of the Shipbuilding Technology Laboratory is a very interesting objective.

Apendix A

APDL code of the layered shell model of the GFRP shaft

```
/FILNAME,bntglassnlshell281,1
/TITLE, bntglassnlshell281
/graphics,full    !powergraphics off

/prep7           ! Enter the preprocessor
!* --------
!* GEOMETRY
!* --------
/units,si        ! Unit System SI
*SET,L,0.692     ! Length in m
*SET,Di,0.250    ! Internal diameter in m
*SET,t,0.005     ! Thickness in m
*SET,R,Di/2      ! Internal radius
*SET,Do,Di+(2*t) ! External diameter
*SET,pi,acos(-1) ! Set the Value of pi


!*---------------
!*DEFINE GEOMETRY
!*---------------
k,1,0,0,0             ! define keypoints
k,2,0,R,0
k,3,L,0,0,0
k,4,L,R,0,0

circle,1,R,3,2,360,4 ! create cicrles
circle,3,R,1,4,360,4

l,6,12               ! create lines
l,7,11
l,8,10
l,5,9

csys,6               ! activate a cylindrical coordinate system along the
                     ! main x-axis

al,9,1,12,8          ! create area from lines
al,10,2,9,7
al,11,3,10,6
al,12,4,11,5


!* --------
!* ELEMENTS
!* --------
ET,1,SHELL281 !Define element type
ESYS,0        !Set the element coordinate system to global cartesian
!*
KEYOPT,1,1,0  !Element has both bending and membrane stiffness (default)
KEYOPT,1,8,2  !Store data for TOP, BOTTOM, and MID for all layers
KEYOPT,1,9,0  !No user subroutine to provide initial thickness (default)


!*--------------------
!* MATERIAL PROPERTIES
!*--------------------
MP,EX,1,37.04*1e9
MP,EY,1,15.04*1e9
MP,EZ,1,15.04*1e9
MP,PRXY,1,0.28
```

```
MP,PRYZ,1,0.3447
MP,PRXZ,1,0.28
MP,GXY,1,5.5*1e9
MP,GYZ,1,2.75*1e9
MP,GXZ,1,5.5*1e9


!* --------
!* SECTIONS
!* --------
!*
*SET,NL , 12       !* Number of layers
*SET,tl , t/NL    !* Thickness of the layer
*SET,wangle , 45  !* Winding Angle

sectype,1,shell    !Defines the type of the section as shell
secoffset,bot      !Starts the layup from the bottom of the section

!Stacking Sequence
![+-45]12
*do,Layer,1,NL,1
   secdata,tl,1, wangle,3 !Defines the data describing the geometry of a
   wangle=-wangle         !section.
*enddo

!* ---------------
!* MESH DEFINITION
!* ---------------
*SET,A , 60        ! Axial line mesh
*SET,C , 16        ! Circumferential Quadrant mesh

!Longitudinal Lines
lesize,9 ,,,A,,,,,1 !Specifies the divisions and spacing ratio on unmeshed
lesize,10,,,A,,,,,1 !lines.
lesize,12,,,A,,,,,1
lesize,11,,,A,,,,,1
!Circumferential Lines
lesize,1,,,C,,,,,1
lesize,2,,,C,,,,,1
lesize,3,,,C,,,,,1
lesize,4,,,C,,,,,1
lesize,5,,,C,,,,,1
lesize,6,,,C,,,,,1
lesize,7,,,C,,,,,1
lesize,8,,,C,,,,,1
amesh,1,4,1 !area mesh

!*----------------------------------------------
!*Creation of master node and mpc184 elements
!*----------------------------------------------
et,2,184     !Defines Element Type mpc184
keyopt,2,1,1 !Element Behaviour, K1=1 Rigid Beam, K2=1 Lagrange Multiplier
             !Method
nsel,all
csys,6
*get,nmpc,node,0,num,max  !Get the maximum node number and store it in nmpc
                          !parameter
*set,nmpc,nmpc+1          !Set parameter nmpc=nmpc+1
n,nmpc,0,0,L+0.02         !Create the master node
type,2                    !Set the Element Type to mpc184
nsel,s,loc,z,L            !Select all the nodes at the end of the shaft
*get,nnum,node,0,count    !Count the number of the nodes at the end
```

```
*get,ND,node,0,num,min      !Get the minimum node number at the end and store
                            !it in ND parameter

*do,i,1,nnum                !Loop for the creation of the MPC184
E,nmpc,ND                   !Create the element from nodes nmpc and ND
*SET,ND,NDNEXT(ND)          !Set ND to the next node number
*enddo

!* --------------------
!* LOADS & CONSTRAINTS
!* --------------------
!Constraints on the fixed edge
Allsel           !Select everything
csys,0           !Set the active coordinate system to Global Cartesian
nsel,s,loc,x,0   !Select all nodes of the left end
d,all,all,0      !Constrain all degrees of freedom
nsel,all         !Select all Nodes
!* --------
!* LOADS
!* --------
*SET,P , 120000  !Set the Torque to 120 KNM, which is equal to the required
                 !strength of the shaft
!Torque
F,nmpc,MX,-P     !Apply the torque on the Master node
!Constraints on the master node
csys,0
D,nmpc,ux,0
D,nmpc,uy,0
D,nmpc,uz,0
D,nmpc,roty,0
D,nmpc,rotz,0
FINISH


!*--------
!*SOLUTION
!*--------

!FIRST STEP

!Linear Static Solution
/SOL
ANTYPE,STATIC           !Analysis Type: Static Analysis
NLGEOM,OFF              !Large deflection effects OFF

allsell
OUTRES,ERASE            !Resets OUTRES specifications to their default
                       !values.
OUTRES,ALL,ALL          !Writes all solution items for every substep.
SOLVE
FINISH


!Eigenvalue Buckling Analysis
/SOLU
OUTRES,ALL,ALL
ANTYPE,1                        !Analysis type: Eigenvalue Buckling Analysis.
BUCOPT,LANB,10,0,1,CENTER !Specifies buckling analysis options.
                        !10 Mode Shapes Extracted
SOLVE
FINISH


/POST1
```

```
SET,LIST
FINISH

!Expansion Pass
/SOLU
!*
EXPASS,1
MXPAND,10,0,0,1,,          !Expand the 10 modes of the Buckling Analysis
SOLVE
FINISH

!Generate Geometric Imperfections
/prep7
!*do,i,1,10
*SET,mag,0.0072           !This value of the parameter "mag" results in
                          !geometric imperfections with the maximum
                          !displacement being equal to 0.1% of Di
UPGEOM,mag,1,5,bntglassnlshell281,rst, !Change 5 to i for imperfection from
all modeshapes.
!*enddo                              !The size of the imperfection will
increase
FINISH

!SECOND STEP

!Nonlinear Static Analysis
/SOLU
ANTYPE,STATIC
NLGEOM,ON                 !Large Displacements ON
PRED,OFF                  !No prediction occurs
TIME,1
*SET,timev,0.01           !Time step value
*SET,timn,0.001           !Minimum time step
*SET,timx,0.1             !Maximum time step
DELTIM,timev,timn,timx,   !Time step values (value, minimum, maximum)
AUTOTS,ON                 !Automatic time step on
OUTRES,all,all
SOLVE
FINISH
```

Apendix B

APDL code of the layered shell model of the CFRP shaft

```
/FILNAME,bntcarbonnlshell281,1
/TITLE, bntcarbonnlshell281

/graphics,full !powergraphics off

/prep7
!* --------
!* GEOMETRY
!* --------
!*
/units,si
*SET,L , 2.600       !* Length in m
*SET,Di , 0.200      !* Internal diameter in m
*SET,t , 0.005       !* Thickness in m
*SET,R , Di/2        !* Internal radius
*SET,Do, Di+(2*t)    !External diameter
*SET,pi, acos(-1)!*
!*
!*
!*---------------
!*DEFINE GEOMETRY
!*---------------
k,1,0,0,0    !defines keypoint
k,2,0,R,0
k,3,L,0,0,0
k,4,L,R,0,0

circle,1,R,3,2,360,4 !creates circle
circle,3,R,1,4,360,4

l,6,12   !lines
l,7,11
l,8,10
l,5,9

csys,6   !Activates a previously defined coordinate system.
al,9,1,12,8 !area from lines, combination to get ESYS from the inner to the
            !outer surface
al,10,2,9,7
al,11,3,10,6
al,12,4,11,5

!* --------
!* ELEMENTS
!* --------
csys,0
ET,1,SHELL281 !element type
ESYS,0         !Sets the element coordinate system attribute pointer.
KEYOPT,1,1,0  !Bending and membrane stiffness (default)
KEYOPT,1,8,2  !Store data for TOP, BOTTOM, and MID for all layers; applies
               !to single- and multi-layer elements
KEYOPT,1,9,0
!*

!*-------------------
!* MATERIAL PROPERTIES
!*-------------------
```

```
MP,EX,1,143.7*1e9                  !Defines property data for 12K fibers
MP,EY,1,9.2*1e9
MP,EZ,1,9.2*1e9
MP,PRXY,1,0.32
MP,PRYZ,1,0.46
MP,PRXZ,1,0.32
MP,GXY,1,3.4*1e9
MP,GYZ,1,1.7*1e9
MP,GXZ,1,3.4*1e9
!*

!* --------
!* SECTIONS
!* --------

sectype,1,shell    !Defines type of section
secoffset,bot      !Starts the layup from the bottom of the section

!Stacking Sequence
![+-12/+85/-+12/-+12/-85/+-12/+-12/+85/-+12/-+12/-85/+-12/+-12/+85/-+12/-
!+12]

!Layer Thickness according to Kosmas' measurement of Do=210-210.2mm and the
!layup table
tl1=0.00019    !thickness of first layer
tr=0.000145    !thickness of radial layers
tl12=0.000195 !thickness of 12deg layers
int.p=3        !number of integration points through thickness

!LAYER 1
Wangle=12
*do,Layer,1,2,1
   secdata,tl1,1, Wangle,int.p
   Wangle=-Wangle
*enddo

!LAYER 2
Wangle=85
*do,Layer,3,3,1
   secdata,tr,1, Wangle,int.p
   Wangle=-Wangle
*enddo
!LAYER 3-4
Wangle=-12
*do,Layer,4,7,1
   secdata,tl12,1, Wangle,int.p
   Wangle=-Wangle
*enddo

!LAYER 5
Wangle=-85
*do,Layer,8,8,1
   secdata,tr,1, Wangle,int.p
   Wangle=-Wangle
*enddo
!LAYER 6-7
Wangle=12
*do,Layer,9,12,1
   secdata,tl12,1, Wangle,int.p
   Wangle=-Wangle
```

```
*enddo

!LAYER 8
Wangle=85
*do,Layer,13,13,1
    secdata,tr,1, Wangle,int.p
    Wangle=-Wangle
*enddo
!LAYER 9-10
Wangle=-12
*do,Layer,14,17,1
    secdata,tl12,1, Wangle,int.p
    Wangle=-Wangle
*enddo

!LAYER 11
Wangle=-85
*do,Layer,18,18,1
    secdata,tr,1, Wangle,int.p
    Wangle=-Wangle
*enddo
!LAYER 12-13
Wangle=12
*do,Layer,19,22,1
    secdata,tl12,1, Wangle,int.p
    Wangle=-Wangle
*enddo

!LAYER 14
Wangle=85
*do,Layer,23,23,1
    secdata,tr,1, Wangle,int.p
    Wangle=-Wangle
*enddo
!LAYER 15-16
Wangle=-12
*do,Layer,24,27,1
    secdata,tl12,1, Wangle,int.p
    Wangle=-Wangle
*enddo
!*

!* --------------
!* MESH DEFINITION
!* --------------

*SET,A , 100        !* Axial line mesh, Le=2.6/100=0.026m
*SET,C , 6          !* Circumferential Quadrant mesh Ce=
                    !* 2*pi*0.1/(6*4)=0.026m

!Longitudinal Lines
lesize,12,,,A,,,,,1 !Specifies the divisions and spacing ratio on unmeshed
                    !lines.
lesize,11,,,A,,,,,1
lesize,9,,,A,,,,,1
lesize,10,,,A,,,,,1

!Circumferential Lines
lesize,1,,,C,,,,,1
lesize,2,,,C,,,,,1
lesize,3,,,C,,,,,1
```

```
lesize,4,,,C,,,,,1
lesize,5,,,C,,,,,1
lesize,6,,,C,,,,,1
lesize,7,,,C,,,,,1
lesize,8,,,C,,,,,1

amesh,1,4,1 !area mesh
!*


!*--------------------------------
!*Creation of master node for mpc184
!*--------------------------------
et,2,184
keyopt,2,1,1 !Element Behaviour, K1=1 Rigid Beam, K2=1 Lagrange Multiplier
            !Method
nsel,all
csys,6
*get,nmpc,node,0,num,max
*set,nmpc,nmpc+1
n,nmpc,0,0,L+0.02
type,2
seltol,1.0E-6
nsel,s,loc,z,L
*get,nnum,node,0,count
*get,ND,node,0,num,min
*do,i,1,nnum
E,nmpc,ND
*SET,ND,NDNEXT(ND)
*enddo

!Second master node on the fixed end
nsel,all
csys,6
*get,nmpcf,node,0,num,max
*set,nmpcf,nmpcf+1
n,nmpcf,0,0,-0.02
type,2
nsel,s,loc,z,0
*get,nnum,node,0,count
*get,ND,node,0,num,min
*do,i,1,nnum
E,nmpcf,ND
*SET,ND,NDNEXT(ND)
*enddo

!* -------------------
!* LOADS & CONSTRAINTS
!* -------------------
*SET,P , 21000        !* Moment (NM)

!Constraints on the fixed edge
allsel
csys,0
!nsel,s,loc,x,0
!d,all,all,0
D,nmpcf,all,0

nsel,all

!Constraints on the master node (Rx free)
```

```
csys,0
D,nmpc,ux,0
D,nmpc,uy,0
D,nmpc,uz,0
D,nmpc,roty,0
D,nmpc,rotz,0

!Moment on the master node
F,nmpc,MX,-P
!Rotation = 17 degress where the max experimental moment(=21KNM) is
!reached. (Carbon Shaft)
!D,nmpc,ROTX,-0.296705973

allsel
nummrg, all

FINISH

!*-----------
!*SOLUTION
!*-----------
/SOL

ANTYPE,0
!**********
NLGEOM,OFF              !* Large deflection effects OFF
PSTRES,OFF              !* Calculate (or include) prestress effects
!*********
allsell
OUTRES,ERASE
OUTRES,ALL,ALL
SOLVE
FINISH

!Eigenvalue Buckling Analysis
/SOLU
ANTYPE,1                !Specifies the analysis type and restart status.
OUTRES,ALL,ALL
BUCOPT,LANB,10,0,10,CENTER      !Specifies buckling analysis options. 10
                                !Mode Shapes Extracted
SOLVE
FINISH

/POST1
SET,LIST
FINISH

!Expansion Pass
/SOLU
!*
EXPASS,1
MXPAND,10,0,0,1,,
SOLVE
FINISH

!Non Linear Buckling Analysis

!Initial Deformation
/prep7
csys,0
allsell
```

```
*SET,mag,0.014 !this value of mag corresponds to (max initial imperfection)
              !ux'=0.005d
!*do,i,1,10
upgeom,mag,1,5,bntcarbonnlshell281,rst,
!*enddo
FINISH

!Non Linear Static Analysis
/SOLU
!*
ANTYPE,STATIC
!*
NLGEOM,ON                 ! Large Displacements ON
!*
pred,off                  ! No prediction occurs
!*
TIME,1
*SET,timev,0.01           ! time step value
*SET,timn,0.001           ! minimum time step
*SET,timx,0.1             ! maximum time step
DELTIM,timev,timn,timx,   ! time step values (value, minimum, maximum)
AUTOTS,1                                ! automatic time step on
!
OUTRES,all,all                          ! write every substep
!
SOLVE
!
FINISH
```

Literature

Anyfantis, K. N., & Tsouvalis, N. G. (2011). Post Buckling Progressive Failure Analysis of Composite Laminated Stiffened Panels. *Applied Composite Materials*, *19*(3-4), 219–236. http://doi.org/10.1007/s10443-011-9191-1

Badie, M. A., Mahdi, E., & Hamouda, A. M. S. (2011). An investigation into hybrid carbon/glass fiber reinforced epoxy composite automotive drive shaft. *Materials and Design*, *32*(3), 1485–1500. http://doi.org/10.1016/j.matdes.2010.08.042

Bankar, H., Shinde, V., & Baskar, P. (2013). Material Optimization and Weight Reduction of Drive Shaft Using Composite Material, *10*(1), 39–46.

Barbero, E. J. (2010). *Introduction to Composite Materials Design, Second Edition*. http://doi.org/10.1017/CBO9781107415324.004

Barbero, E. J. (2013). *Finite Element Analysis of Composite Materials Using ANSYS*.

Christensen, R. M. (1979). *Mechanics of Composite Materials*.

Civgin, F. (2005). Analysis of Composite Bars in Torsion.

Cook, R. D. (1995). *Finite element modeling for stress analysis*. Retrieved from http://books.google.com/books?id=UyNEAQAAIAAJ&pgis=1

Gireesh, B., & Satwik, V. N. (2013). Finite Element & Experimental Investigation of Composite Torsion Shaft, *3*(2), 1510–1517.

Greene, E. (1999). *Marine Composites*. http://doi.org/10.1016/0010-4361(78)90325-7

Jones, R. M. (1975). *Mechanics of Composite Materials* (First).

Khoshravan, M. R., & Paykani, A. (2012). Design of a composite drive shaft and its coupling for automotive application. *Journal of Applied Research and Technology*, *10*(6), 826–834.

Khoshravan, M. R., Paykani, A., & Akbarzadeh, A. (2011). Design and Modal Analysis of composite Drive Shaft for Automotive Application. *International Journal of Engineering Science and Technology*, *3*(4), 2543–2549.

Lee, D. G., Kim, H. S., Kim, J. W., & Kim, J. K. (2004). Design and manufacture of an automotive hybrid aluminum/composite drive shaft. *Composite Structures*, *63*(1), 87–99. http://doi.org/10.1016/S0263-8223(03)00136-3

Leslie, J. C., Truong, L., Ii, J. C. L., Blank, B., & Frick, G. (1996). Composite Driveshafts : Technology and Experience. http://doi.org/10.4271/962209

Madenci, E., & Guven, I. (2006). *The Finite Element Method and Applications in Engineering Using Ansys*. http://doi.org/10.1007/978-0-387-28290-9

Moaveni, S. (2007). *Finite Element Analysis Theory and Application with ANSYS* (Vol. 2416514).

Mouritz, A. P., Gellert, E., Burchill, P., & Challis, K. (2001). Review of advanced composite structures for naval ships and submarines. *Composite Structures*, *53*(1), 21–24. http://doi.org/10.1016/S0263-8223(00)00175-6

Ooi, J. B., Wang, X., Lim, Y. P., Tan, C., Ho, J. H., & Wong, K. C. (2013). Parametric optimization of the output shaft of a portal axle using finite element analysis. *Strojniski Vestnik/Journal of Mechanical Engineering*, *59*(10), 613–619. http://doi.org/10.5545/sv-jme.2012.887

Papadakis, A. Z., & Tsouvalis, N. G. (2016). An Experimental and Numerical Study of CFRP Pressure Housings for Deep Sea Environment Research. In *Proceedings of the Twenty-sixth (2016) International Ocean and Polar Engineering Conference* (pp. 226–233).

Peters, S. T. (2011). *Composite Filament Winding*. (S. T. Peters, Ed.). Retrieved from https://books.google.com/books?hl=en&lr=&id=nciMwbQfymQC&pgis=1

Rompicharla, R. P. K., & Rambabu, K. (2012). Design and Optimization of Drive Shaft with Composite Materials. *International Journal of Modern Engineering Research*, *2*(5), 3422–3428.

Shenoi, R. A., & Wellicome, J. F. (1993). *Composite Materials in Maritime Structures, Volume 1 Fundamental Aspects*.

Shenoi, R. A., & Wellicome, J. F. (1993). *Composite Materials in Maritime Structures, Volume 2 Practical Considerations*. http://doi.org/http://dx.doi.org/10.1017/CBO9780511751844

Shokrieh, M. M., Hasani, A., & Lessard, L. B. (2004). Shear buckling of a composite drive shaft under torsion. *Composite Structures*, *64*(1), 63–69. http://doi.org/10.1016/S0263-8223(03)00214-9

Suryawanshi, B. K., & Damle, P. G. (2013). Review of Design of Hybrid Aluminum / Composite Drive Shaft for Automobile. *International Journal of Innovative Technology and Exploring Engineering (IJITEE)*, (4), 259–266.

Smith, C. (1990). Design of Marine Structures in Composite Materials. *Elsevier Applied Science, Oxford*.

Tsouvalis, N. (1998). *Analysis and Design of Composite Material Crafts*.

Young, W. C., & Budynas, R. G. (2002). *Roark's Formulas for Stress and Strain*.